Forschungszentrum Karlsruhe
Technik und Umwelt
Wissenschaftliche Berichte
FZKA 5570

Posttest Examination of the VVER-1000 Fuel Rod Bundle CORA-W2

L. Sepold (Herausgeber)

Hauptabteilung Ingenieurtechnik
Projekt Nukleare Sicherheitsforschung

Juni 1995

Forschungszentrum Karlsruhe
Technik und Umwelt

Wissenschaftliche Berichte
FZKA 5570

Posttest Examination of the VVER-1000 Fuel Rod Bundle CORA-W2

zusammengestellt von L. Sepold

Hauptabteilung Ingenieurtechnik
Projekt Nukleare Sicherheitsforschung

Forschungszentrum Karlsruhe GmbH, Karlsruhe
1995

Als Manuskript gedruckt

Forschungszentrum Karlsruhe GmbH
Postfach 3640, 76021 Karlsruhe

ISSN 0947-8620

Abstract

The bundle meltdown experiment CORA-W2, representing the behavior of a Russian type VVER-1000 fuel element, with one B_4C/stainless steel absorber rod was selected by the OECD/CSNI as International Standard Problem (ISP-36). The experimental results of CORA-W2 serve as data base for comparison with analytical predictions of the high-temperature material behavior by various code systems.

The first part of the experimental results is described in KfK 5363 (1994), the second part is documented in this report which contains the destructive post-test examination results. The metallographical and analytical (SEM/EDX) post-test examinations were performed in Germany and Russia and are summarized in five individual contributions.

The upper half of the bundle is completely oxidized, the lower half has kept the fuel rods relatively intact. The post-test examination results show the strong impact of the B_4C absorber rod and the stainless steel grid spacers on the "low-temperature" bundle damage initiation and progression. The B_4C absorber rod completely disappeared in the upper half of the bundle. The multicomponent melts relocated and formed coolant channel blockages on solidification with a maximum extent of about 30 % in the lower part of the bundle. At temperatures above the melting point of the ZrNb1 cladding extensive fuel dissolution occurred.

Nachuntersuchung des WWER-1000-Brennelementbündels CORA-W2

Kurzfassung

Das Bündel-Abschmelz-Experiment CORA-W2, das ein russisches Brennelement vom Typ WWER-1000 repräsentiert und somit auch mit einem Absorberstab aus Borkarbid/rostfreier Stahl versehen war, wurde als sog. Internationales Standardproblem (ISP-36) der OECD/CSNI ausgewählt. Die Versuchsergebnisse des Bündels CORA-W2 dienen als Datenbasis für den Vergleich mit Rechnungen mittels verschiedener Rechenprogramme im Hinblick auf das Materialverhalten bei hoher Temperatur.

Der erste Teil der experimentellen Ergebnisse liegt als KfK-Bericht 5363 (1994) vor. Den zweiten Teil stellt dieser Bericht dar. Er enthält die Ergebnisse der zerstörenden Nachuntersuchungen. Die metallografischen und analytischen (SEM/EDX) Nachuntersuchungsergebnisse wurden in Deutschland und in Rußland durchgeführt und sind in fünf eigenständigen Beiträgen dokumentiert.

Die obere Hälfte des Bündels ist stark oxidiert, in der unteren Hälfte sind die Brennstäbe relativ unversehrt. Die Ergebnisse der Nachuntersuchungen zeigen den starken Einfluß des B_4C-Absorberstabs und der Abstandshalter aus rostfreiem Stahl auf die Schadensauslösung und -ausbreitung im Bündel bei relativ niedrigen Temperaturen. In der oberen Bündelhälfte ist der Absorberstab vollständig verschwunden. Die Mehrkomponenten-Schmelze hat sich verlagert und bei der Abkühlung eine Kühlkanalblockade von maximal 30 % im unteren Teil des Bündels verursacht. Bei Temperaturen oberhalb des Schmelzpunkts der ZrNb1-Hülle kam es zu einer intensiven Brennstoffauflösung.

Contents

Extended Summary

The two VVER-CORA experiments CORA-W1 and CORA-W2 were the last ones in the series of "Severe Fuel Damage" (SFD) experiments carried out in the out-of-pile facility "CORA" at the Forschungszentrum Karlsruhe (formerly Kernforschungszentrum Karlsruhe, KfK).

The experimental program was set up to provide information on the failure mechanisms of Light Water Reactor (LWR) fuel elements in a temperature range from 1200°C to 2000°C and in one case up to 2400°C. So, a total of 17 CORA experiments with bundle configurations representing fuel elements of PWR and BWR-types used in Western countries were carried out between 1987 and 1992.

The two VVER-1000 specific tests were run in the CORA facility with identical objectives as the LWR-related experiments but with genuine VVER-type materials. The experiments were conducted on February 18, 1993 and April 21, 1993, respectively. Test bundle CORA-W1 was without absorber material whereas CORA-W2 contained one absorber rod (boron carbide/steel cladding). The design characteristics of bundle CORA-W2 can be taken from Table A and Fig. A.

The test bundles were subjected to temperature transients of a slow heatup rate in a steam environment and experienced a temperature escalation due to the exothermal zirconium-steam reaction that started at about 1200°C. The thermal response of both bundles was comparable. The test results are described in reports KfK 5212 and KfK 5363 for tests CORA-W1 and CORA-W2, respectively.

After the experiments the bundles were encapsulated with epoxy resin and cut by a saw with a 2.3 mm-thick diamond blade. Several sections selected for metallographic examinations were polished. The polished samples were distributed to the Russian laboratories and to the Karlsruhe research center according to the list in Table B.

So, this report is a joint effort of the three Russian institutions participating in the CORA-VVER program (Russian Research Center "Kurchatov Institute" Moscow, Research Institute of Atomic Reactors Dimitrovgrad, and A.A. Bochvar Research Institute of Inorganic Materials Moscow), and of the German side to document the results of the posttest examinations of CORA-W2. The report comprises five contributions:

1. Posttest material examinations at the elevations - 13, 87, 208, 221, 1098, and 1148 mm (Kurchatov Institute Moscow)

2. Microstructural posttest investigations at the elevations 327, 394, 511, 607, 726, 845, and 1083 mm (Research Institute Dimitrovgrad)

3. Posttest investigations at the elevations 141, 498, and 964 mm (A.A. Bochvar Institute Moscow)

4. Microstructural posttest investigations at the elevations 206, 392, 605, and 910 mm (Forschungszentrum Karlsruhe)

5. Posttest SEM/EDX examination results of the VVER-1000 fuel rod bundle CORA-W2 (Forschungszentrum Karlsruhe).

The contributions compiled in this report are to be understood as independent presentations supplied at the authors' responsibility. No technical editing was performed for the individual sections. However, the information of the complementary, individual contributions allows the essential results to be summarized as follows.

Extent of the oxidation of the bundle components by steam

The oxidation of the ZrNb1 fuel rod cladding and shroud and of the stainless steel absorber cladding, adsorber guide tube and grid spacers proceeded in the following way. Protective scales were established before an accelerated metal consumption was induced by scale spalling and fracture. As soon as material relocated, oxygen also was dissolved by metallic melts with the consequence of forming there an oxide scale as well. The energy release from the zirconium oxidation initiated the temperature escalation (at about 1200 °C according to temperature measurements) in the upper part of the bundle. From there the escalation front moved downward. The axial distribution of the cladding oxidation in the solid state is quantified with Fig. B. Subsequently, further oxidation took place in the molten state of the residual metallic fractions of the cladding, parallel to the dissolution of fuel and the contamination by steel melt. Finally, more than half of the bundle length - referred to the non-relocated fraction of the cladding at the original elevation - was completely oxidized.

Extent of UO_2 dissolved by molten ZrNb1

Fig. C shows the extent of UO_2 fuel dissolution by molten ZrNb1 cladding as function of the bundle elevation. UO_2 dissolution started above about 200 mm where the temperatures were high enough or relocated molten metallic cladding from higher hotter elevations initiated the chemical interactions. The maximum fuel dissolution took place in the upper half of the bundle with values between 11 and 17 %. As a result of the chemical interactions, metallic and ceramic (U, Zr, O) melts formed. Depending on the oxygen concentration the melts decomposed into α-Zr(O) which contained some U and a (U, Zr) alloy with 2 to 29 wt % U or, at higher oxygen contents (> 12 wt %), into a ceramic (U, Zr)O_2 compound with U concentrations between 10 and 44 wt %.

Chemical behavior of the B_4C/stainless steel absorber rod

Between B_4C and stainless steel eutectic chemical interactions took place with liquid phase formation around 1000°C and almost complete liquefaction above 1250°C. As a result of the axial temperature distribution within the bundle, the absorber rod which was intact below about 200 mm disappeared completely above roughly 900-mm bundle elevation. In between these two elevations, the B_4C remained partly as rod fragments and was partially dissolved (Fig. D). (The dashed line was drawn according to the results from all cross sections, whereas the data triangles represent the polished cross sections, which were studied in detail.) The boron concentration in the metallic stainless-steel-based melts varied between 7 and 10 wt %. However, one should keep in mind that in the upper half of the bundle only small B containing solidified melt droplets could be observed. The largest part of the liquefied absorber rod accumulated at the lower bundle elevations.

Chemical behavior of the stainless steel grid spacer

The eutectic chemical interactions between stainless steel and the ZrNb1 cladding material resulted in extended liquid phase formation at temperatures ≥1250°C, much below the melting point of the components, which is responsible for the localized damage initiation and damage progression. In many fuel rods, which showed still an intact cladding tube, a solidified metallic (Fe, Cr, Ni, Zr, O) melt could be detected between the UO_2 pellets and the ZrO_2 layer on the cladding outer surface. This indicates a liquefaction process of "oxygen -poor" cladding by stainless steel in axial direction over long distances. Whereas the grid spacer at

the elevation of 610 mm has completely disappeared, the two others at - 5 and 210 mm axial elevation were still present at the end of the experiment.

Melt relocation and blockage formation

Material relocated from elevations between 450 and 1150 mm and formed a coolant channel blockage between 200 and 350 mm elevation with a maximum at about 250 mm (see the axial mass profiles after the test (thick line) and before test CORA-W2 (thin line) in Fig. E). The axial position of the blockage coincides with the position of the steep axial temperature gradient at the end of the experiment. This is also the axial position of the onset of the temperature escalation at the time, when the electrical power supply was turned off. Compared to bundle CORA-W1, the axial region of fuel rod damage in bundle CORA-W2 was shifted towards the lower end of the bundle despite the fact that the input of electrical energy was smaller in test CORA-W2 compared to CORA-W1. This was caused by the liquefaction process of the absorber material, i.e. by a eutectic interaction between boron carbide and stainless steel (starting at about 1200 °C). Melting, relocation, and solidification of the materials at lower bundle elevations led to a renewed temperature increase and melt formation.

Table A: Design characteristics of test bundle CORA-W2

Bundle type:		VVER
Bundle size:		19
Number of heated rods:		13
Number of unheated rods:		5
Pitch:		12.75 mm
Cladding outside diameter		9.13 mm
Cladding inside diameter:		7.72 mm
Cladding material:		Zr-1%Nb
Heater:	- material	Tungsten (W)
	- diameter	4 mm
Fuel pellets:	- heated rods	UO_2 annular pellets
	- outer diameter (nominal)	7.57 mm
	- diameter of central void	4.2 mm
	- unheated rods	UO_2 annular pellets
	- diameter of central void	2.4 mm
Pellets stack:	- heated rods	0 to 1000 mm
	- unheated rods	-142/-192 to 1400 mm
U-235 enrichment		0.3 %
Grid spacer	- material	Stainless steel: 1.4541 (06Ch18N10T and 08Ch18N10T)
	- height	20 mm
	- number	3
	- location by elevation of upper edges (from level 0 mm)	-5; 210; 610 mm
Shroud	- material	Zr-1%Nb
	- wall thickness	1.0 mm
	- outer dimension	68 mm
	- length	1195 mm
Absorber rod	- material	B_4C
	- cladding	Stainless steel
	- cladding OD	8.2 mm
	- cladding ID	7.0 mm
Absorber rod guide tube	- material	Stainless steel
	- OD	12.6 mm
	- ID	11.0 mm

Table B: CORA-W2; Polished samples

- W2-01 bottom 141 mm → Moscow
- W2-02 bottom 208 mm → Moscow
- W2-03 bottom 327 mm → Moscow
- W2-04 bottom 498 mm → Moscow
- W2-05 bottom 607 mm → Moscow
- W2-06 bottom 726 mm → Moscow
- W2-07 bottom 845 mm → Moscow
- W2-08 bottom 964 mm → Moscow
- W2-09 bottom 1083 mm → Moscow

- W2-d top 206 mm (to be compared with W2-02 bottom) → KfK
- W2-g top 392 mm → KfK
- W2-k top 605 mm (to be compared with W2-05 bottom) → KfK
- W2-p top 910 mm → KfK

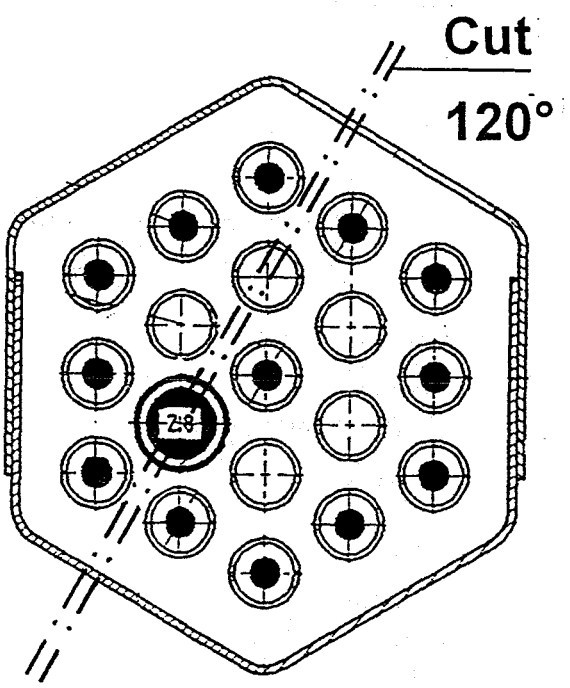

Longitudinal cut through sample CORA-W2-d

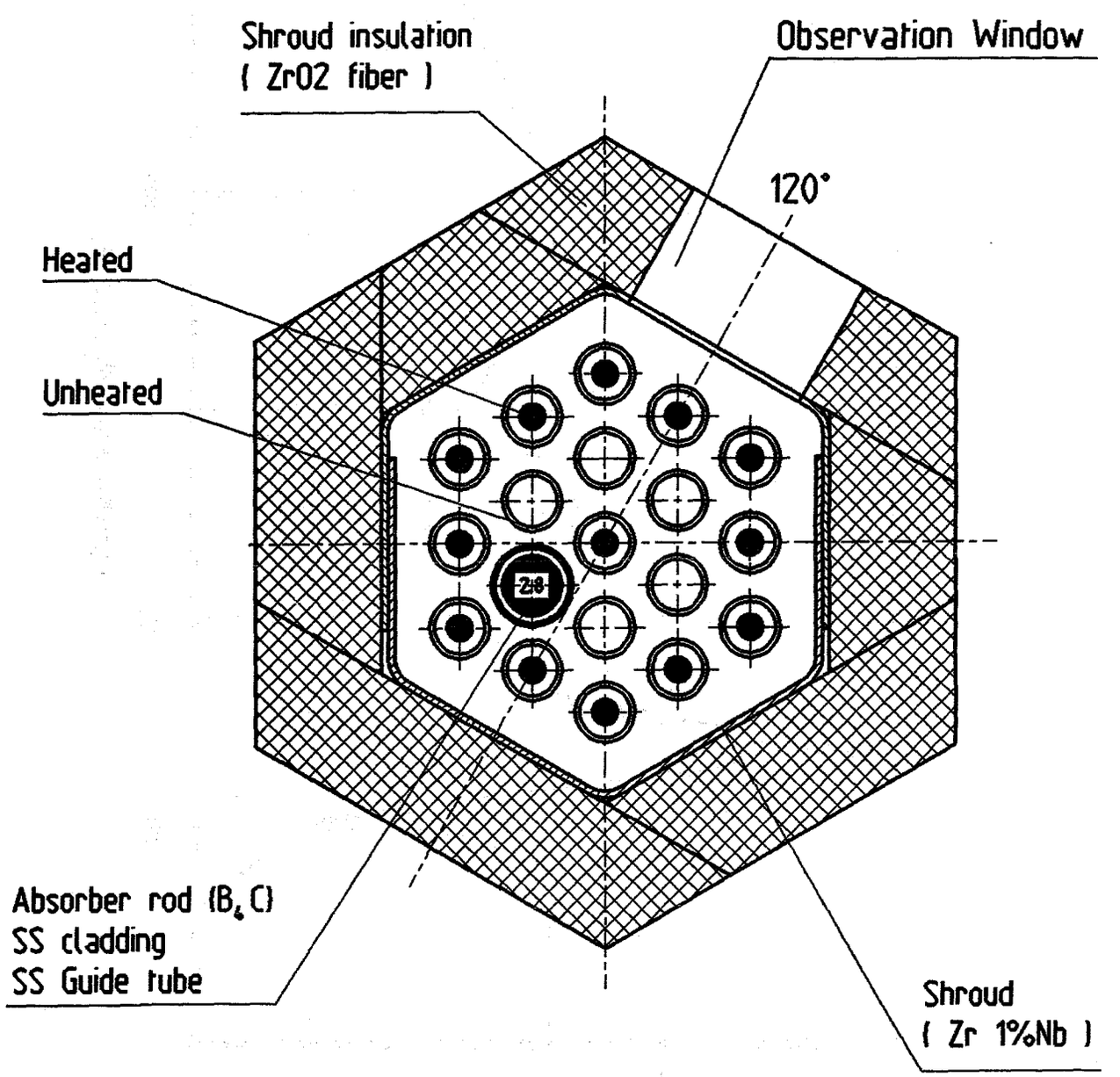

Fig. A : Rod arrangement of bundle CORA-W2

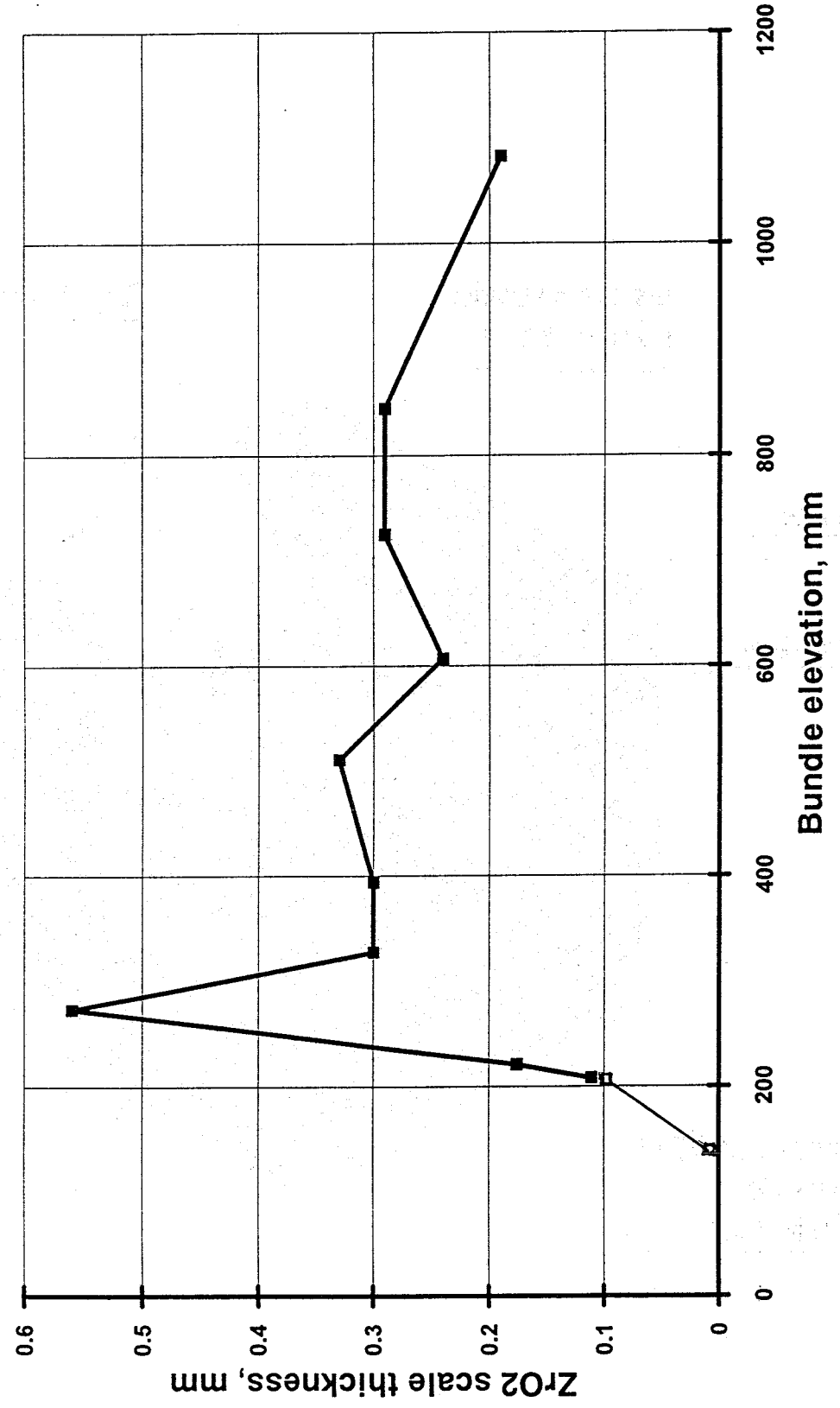

Fig. B: Axial distribution of cladding oxidation of bundle CORA-W2

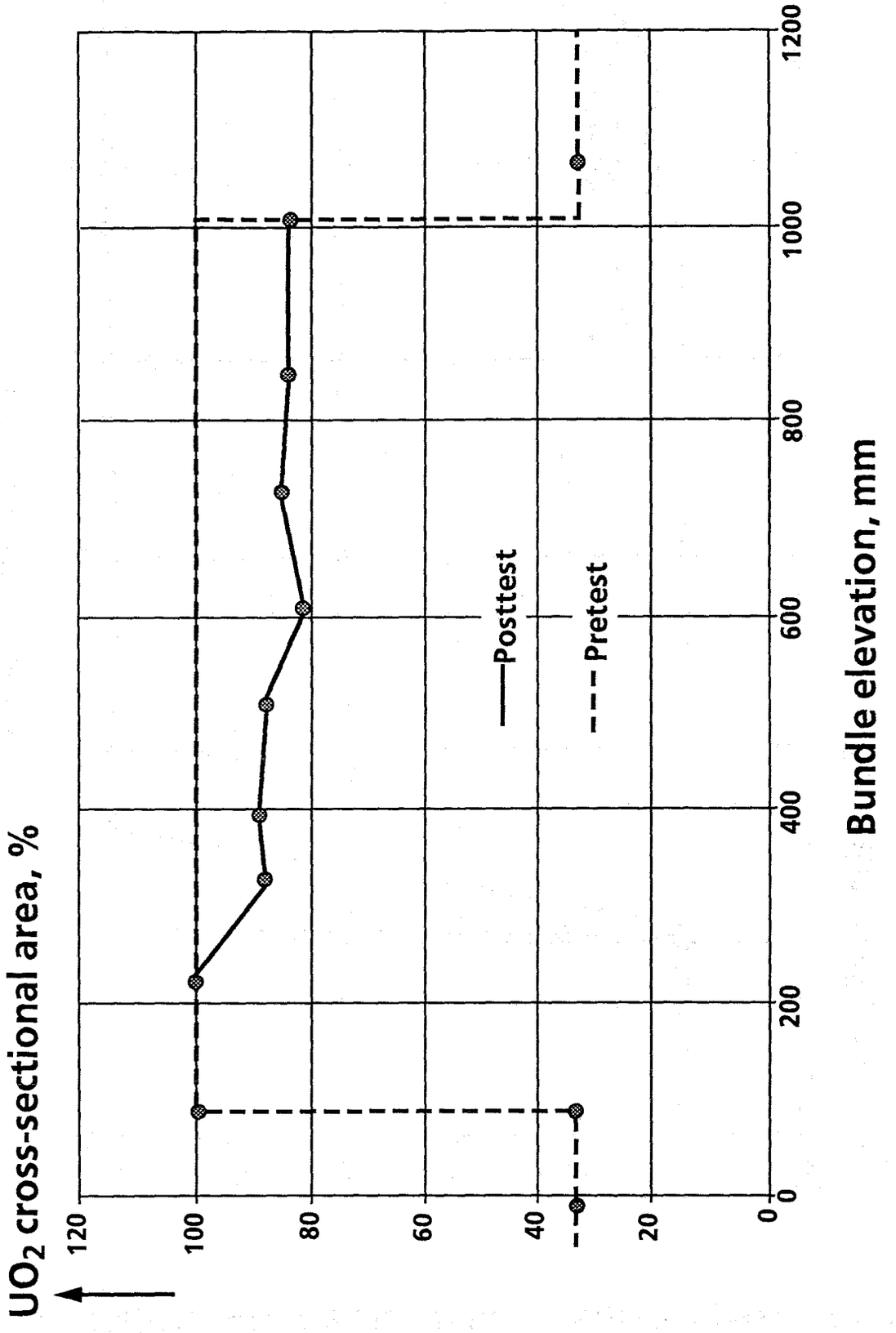

Fig. C: Axial distribution of UO_2 in the fuel rods before and after test CORA-W2

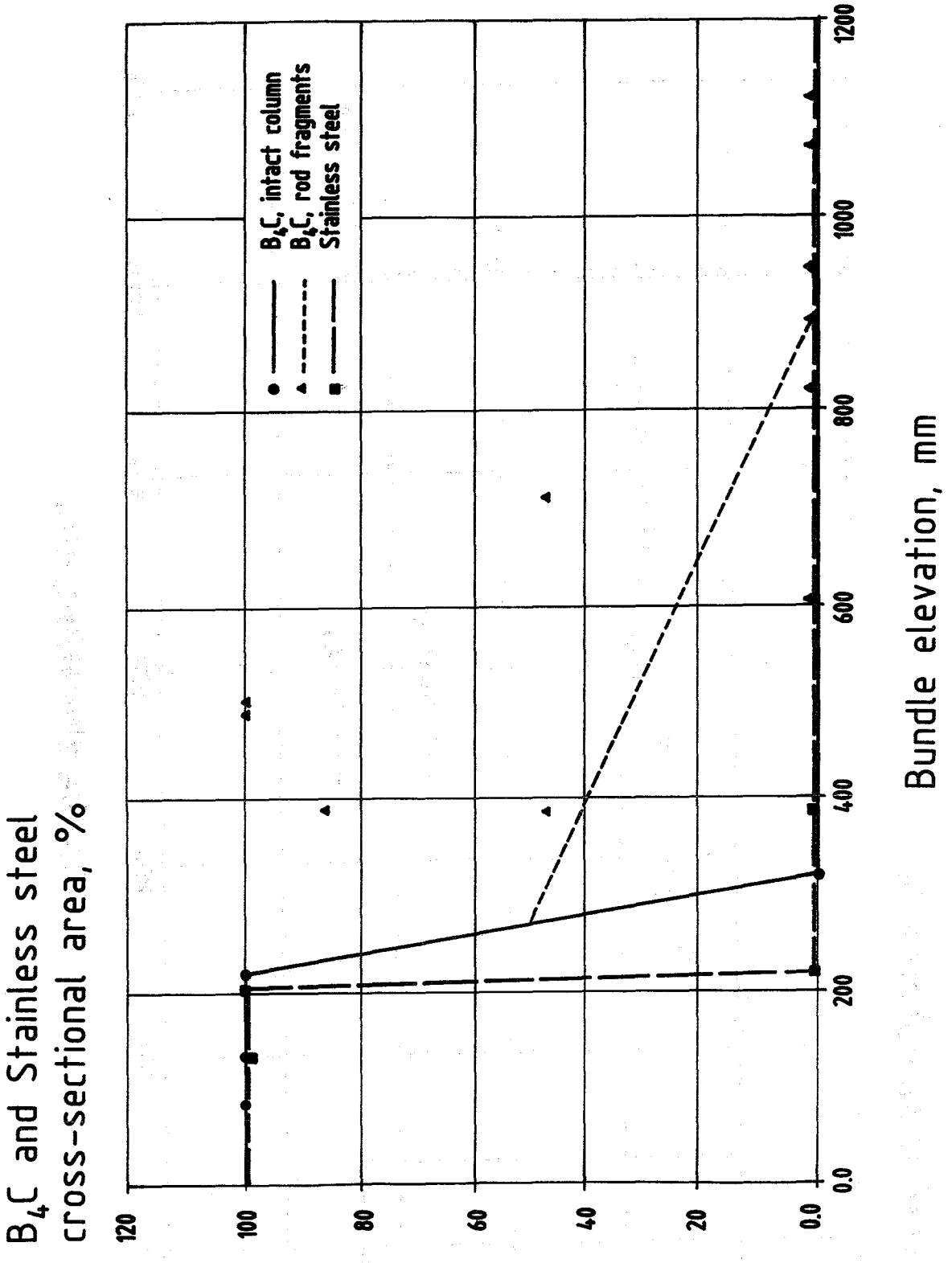

Fig. D: Axial distribution of remaining absorber rod components B_4C and stainless steel cladding

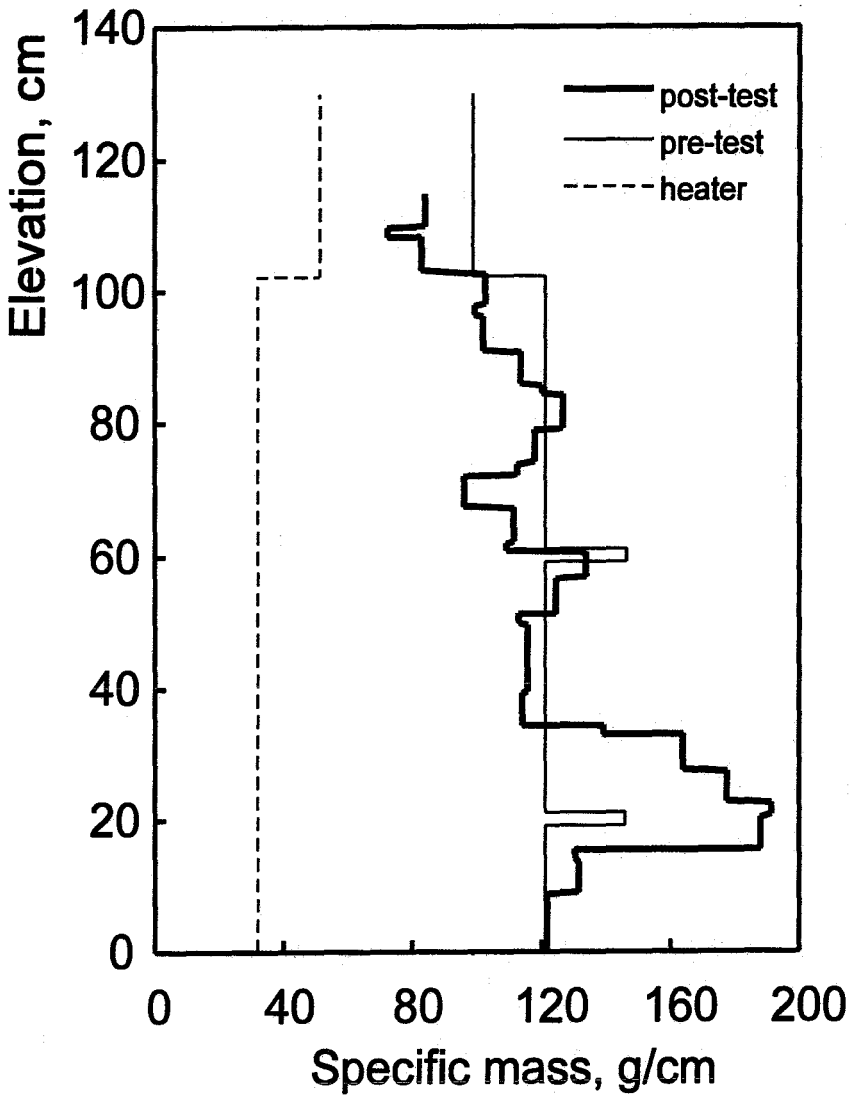

Fig. E: Posttest material distribution of bundle CORA-W2

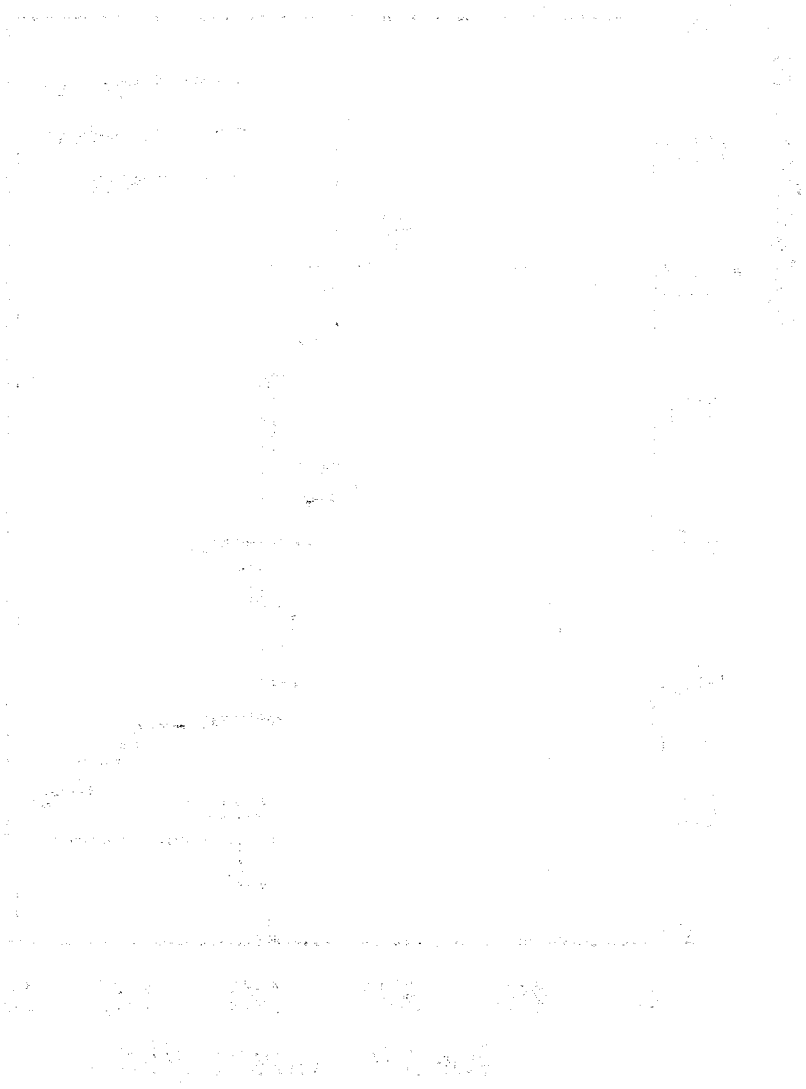

Post-test Material Examinations at the Elevations -13, 87, 208, 221, 1098 and 1148 mm.

V.Vlasov, Yu.Degaltsev

October, 1994

Russian Research Center "Kurchatov Institute",
Institute of Nuclear Reactors

Introduction.

The major purpose of the investigations is to obtain experimental data required for verification of the computational models in the framework of International "Standard Problem" ISP—36. Besides, in the course of the investigations there are determined characteristics not necessary under the "Standard Problem" procedure, but important in respect to interpretation of the degradation processes occurring in the bundles of the WWER—1000 type, verification of kinetics and criterial relationships, used for substantiation of the WWER type reactors safety, improvement of computational modeling of individual processes and phenomena taking place in the fuel bundle at accidents with melting.

The list of major parameters measured for the WWER/Cora—W2 bundle is given in [1]. The most detailed measurements of the bundle degradation parameters were taken for elevations 208 and 221 mm, included into the Summary Table on the "Standard Problem". For other elevations there were conducted investigations of local processes of physical and chemical interaction between the materials, especially of their oxidation.

Samples and Measuring Techniques

This chapter describes the results of post—test examination of the CORA—W2 bundle that has been performed at RRC "KI".

Experimentally investigated were 6 cross—sections. The samples marking, location of the sections along the bundle height and temperatures at the sections are given in Table 1. The following techniques and instruments were used in the investigations:

- metallographic microscope Neophot—30;
- qualitative and quantitative methods of microanalysis by X—ray spectrometry (scanning electron microscope DSM—960 with microprobe attachments Microspec—2A and Link AN10000, electron microscope S—800 by Hitachi with X—ray spectrometry attachment LZ—5 and computer—based data processing system by the firm "Link analytical", microanalyser Camebax SX—50) for determination of element composition of the structures observed in metallographic microsections;
- microhardness measurements with PMT—3 microhardnessmeter;
- methods of structural analysis with DRON—2 X—ray diffractometer.

When carrying out the above analyses, most attention has been concentrated on oxidation of zirconium alloys, steel and UO_2 fuel. This problem is important because the level of the material oxidation strongly affects the accident conditions: amount of hydrogen, temperatures of liquidus (T_L) and solidus (T_S), chemical activity of the materials, especially zirconium.

Quantitative measurements of the interaction zones and geometrical parameters of the bundle components, including measurements of the areas (in detail the procedure of measuring areas is described in [1]), were for the most part taken with Image analyser Quantimet QTM—720 from negatives of photomacrographs of the sections under investigation. Measurements of thicknesses of the physical and chemical interaction layers, of the fuel pellets and claddings diameters were taken with tool—room microscope ИМЦ 150x50, Б at magnification of 50:1.

In addition, in the framework of this study there was tested the method of measuring areas at elevations 208 mm and 221 mm with System for image processing IBAS—2000 by CONTON (USA) through preliminary image recording by telecamera into the system memory and computation of particular areas by a pre—arranged code.

General View of the Bundle Sections under Investigation

Photomacrographs of the general view of the bundle sections under study are given in Figs. 1—6, where the image of the lower surfaces is obtained from the overturned negative, thus simplifying comparison of the lower and upper sections at visual analysis. The figures present the results of measuring areas for all objects observed at the section.

Bundle Elevation —13 mm (Fig. 1). Missing at the section are:

— Shroud, presumably because it was removed when dismantling the bundle;

— Part of the spacer grid because the section passes along the grid end and, at possible minor shift of the section, part of the grid did not fall on it;

— B_4C in the absorber rod cladding, which is due to the powder spilling on cutting.

Observed at the elevation are individual fragments of the bundle relocated from the bundle upper part.

The flow area (S_0) at this elevation can be estimated using the value of area inside the shroud $S_1 = 3796$ mm^2 from the next section (Fig. 2). Under this estimation at the elevation —13 mm the flow area equals 2417 mm^2.

Bundle Elevation 87 mm (Fig. 2). Practically no changes to the fuel simulators and shroud are observed. B_4C powder is missing from the absorber rod cladding, the rod cladding and the guard jacket did not change.

Bundle Elevation 208 mm (Fig. 3). Observed at this elevation is hardened melt mass, relocated from the upper part of the bundle (the flow area reduced approximately by half). The bundle geometry at this section remained practically unchanged. Only fragments of the control rod are left.

Bundle Elevation 221 mm (Fig. 4). The amount of the hardened melt mass here is considerably lesser than at elevation 208 mm. Observed is destruction of the fuel rods occurring as formation of sizable voids, mostly resulting from the material melting out. For this elevation with the help of the System for image processing IBAS—2000 there were taken additional measurements of the area occupied by epoxy resin inside the shroud. The obtained value of $S_0 = 2372$ mm^2 differs little from the flow area ($S_0 = 2359$ mm^2) obtained with quantometer through measurement of the shroud interior area and the areas of all elements inside the shroud. Noted are the contours of the absorber material which had broken off in the process of the bundle dismantling.

Bundle Elevation 1098 mm (Fig. 5). Observed are the remains of the claddings in the form of "petals" adjacent to the fuel pellets and molybdenum liners. Missing are the absorber rod and, for the most part, the shroud.

Bundle Elevation 1148 mm (Fig. 6). The fuel rod claddings are partially open. Observed is partial oxidation of the claddings and the shroud to ZrO_2 ceramic phase. The absorber rod is absent.

As is seen from these results, the least flow area corresponds to the elevation 208 mm, which is defined by the presence at this elevation of the

spacer grid and hardened molten masses, flowing down from the upper elevations of the bundle.

Cladding of the Simulators and the Shroud

Prior to this investigation, the work was carried out to measure oxygen concentration in "ideal" samples, fabricated by the argon—arc melting of the mixture with the known oxygen content (mixture of Zr1%Nb with ZrO_2). The measurements of oxygen were carried out with X—ray microanalyser. The measurements of the samples microhardness were also done; microhardness being determined by oxygen content.

The curves presented in Figs. 7 and 8 were built by statistical methods with the NVP code [3]. This code is intended for mathematical description of the one—factor experiments with the approximation of the experimental results by the Forsythe orthogonal polynomials; the order of polynomial was selected based on the Fisher test for the level of significance (for this code $\alpha = 0.05$), and after that the confidence interval was established.

It is seen from Fig. 7 that the oxygen content measured by the microprobe analysis coincides with its content in the "ideal" samples with the probability of 0.95. The sensibility level is about 8 at.%.

The measurements of hardness may be used too, especially as an express method, in addition, the sensibility limit for this method is better and makes 0.2 at.% (Fig. 8).

As a rule, at metallographic analysis of the bundle sections at elevations 208 mm (Fig. 9) and 221 mm (Fig. 14) there can be identified five layers of the oxidized cladding:

— the outer layer is close to ZrO_2 in its composition;

— the other layers are oxygen stabilized $Zr(O)_x$; at the section at elevation 1098 mm the whole cladding is $(ZrU)O_2$ (Figs. 14 and 18). The linear dimensions of these layers for all simulator claddings at elevations 208 and 221 mm are given in Tables 2 and 3, and after statistical averaging they were introduced as relevant parameters into the Summary Table prepared under the "Standard Problem".

The distribution of elements over the cladding thickness was thoroughly investigated by X—ray microprobe using one central cladding at elevation 208 mm. Fig. 10 presents distribution of Zr, Fe, U and O in the oxidized cladding layers obtained by the microprobe method with linear scanning: layers I and II contain only zirconium and oxygen with nearly constant oxygen concentration in each layer; layers III and IV contain metallic component of uranium and iron, in addition to zirconium and oxygen. The uranium concentration decreases towards the outside, iron is observed as isolated inclusions. The examples of the elements distribution over the samples area are shown in Fig. 13.

The results of quantitative microprobe analysis at individual points are given in table (Fig. 11). The quantitative distribution of oxygen at the points as the average value for each layer is shown in Fig. 12.:

— at the outer surface of the cladding there is observed a thin layer of oxidized iron which most likely formed as a result of sintering of liquid steel from the higher—temperature region of the bundle. The layer character points to its good wettability by the steel melt;

— in layer I oxygen content is slightly less 66 at.% because of $Zr(O)_2$ in the main phase ZrO_2;

— in the other layers oxygen concentration does not exceed 30 at.% which is the limit of oxygen solubility in Zr;

— the curve of oxygen distribution has a minimum because the cladding is saturated by oxygen from two sources: water (H_2O) steam and uranium dioxide (UO_2);

— the total amount of oxygen in $Zr(O)_x$ phase (layers II—IV) is approximately two times more than in ZrO_2 layer. This fact should be taken into account in the model computations.

It is interesting to note that the atoms of (U, Fe) metals are located in a layer with minimum oxygen content, it seems likely that these layers also serve as the paths for migration of the metals and, in particular, this results in the metals relocation along the cladding generating line to the regions of rather low temperatures (in this case ~ 1300°C). Similar results for elevation 221 mm are presented in Figs. 15—17.

Both sides of the shroud (Fig. 19, elevation 221 mm) were oxidized to $ZrO_{0.43}$ phase. In the central zone between the oxide layers there is a layer having eutectic composition having approximately 25 at.% of oxygen. The shroud oxidation at elevation 1148 mm also proceeded from both sides to $ZrO_{0.44}$ phase.

Fuel Pellets

Change of O/U ratio in UO_2 pellet surface was measured by X—ray structural analysis on the basis of the data presented in [4]. O/U ratio increases slightly with the increase of temperature (Fig. 20).

The results of measuring areas and diameters of individual fuel pellets are given in Tables 4 and 5, the summary results for the investigated sections — in Figs. 1—6.

Spacer Grid

The spacer grid in this work is presented at two sections: at elevations — 13 mm (Fig. 1) and 208 mm (Fig. 3). In the second case the spacer grid is oxidized and as a result two layers are formed: external thin layer of FeO and the second layer of (Fe, Cr, Ni)O, enriched in Cr and depleted of Ni as compared to the initial X18H10T steel (Figs. 21 and 22).

As there are no traces of the spacer grid interaction at the section at elevation —13 mm, its measured area (329 mm^2) can be used as the initial value. The lesser area of the grid (162 mm^2, Fig. 3) for elevation 208 mm is connected with its partial absorption by the melt. With account for 27% oxidation over the grid thickness the remaining steel may be considered as occupying an area of 117 mm^2.

The spacer grid temperature was estimated using the oxide layer thickness, the thickness dependence on temperature and the time received in [5]. This temperature is close to the calculated value for CORA—W2 [2].

Absorber Rod

Structurally the absorber rod section presented the boron carbide filling in the steel cladding, surrounded on the outside by the protective jacket of

stainless steel. In the photomacrographs of the lower sections (Figs. 1 and 2) the absorber material filling is missing, which is most likely due to its spilling in the process of the bundle dismantling. That is why as the area occupied by the absorber material there was taken the area inside the cladding.

At the section at elevation 208 mm (Figs. 3 and 23) there is noted complete disappearance of the absorber rod cladding, partial meltdown of the protective jacket and sintered mass of the absorber material with internal breaking off. The detailed microprobe analysis of this zone (Figs. 23—25, Table 5) pointed to the following:

— the sintered mass fits the composition of B_4C boron carbide (points 1 and 2);

— the transition zone from boron carbide to the protective jacket is porous and presents inclusions of steel compound with boron up to 30—40 at.% (points 4, 15—20) in the steel matrix;

— in the transition zone there are found isolated inclusions of zirconium oxy—carbide (point 3) and titanium oxide (point 7);

— on the outside the steel jacket (points 8—12) is oxidized to a composition of $(Fe, Cr)_2O_3$ (points 13 and 14).

At the next section (Fig. 4) there observed only the contours occupied by the absorber rod which had broke off in the process of the bundle dismantling. At the upper sections (Figs. 5 and 6) the traces of the absorber rod presence are completely missing.

Core Blockage Formation

The integral microprobe analysis of the melts was performed with a probe of the order of 100 micrometers at the sections at elevations —13, 208 and 221 mm (Figs. 26, 27, 30). The results of this analysis indicate that at the section at elevation —13 mm the melts are based on steel with an admixture of boron. With the increase of temperature (the section at elevation 208 mm) the formation of boron compound with steel along the grain boundaries is noted. The detailed distribution of the components among the simulators /4.3/ and /4.5/ is presented in Figs. 28 and 29, the quantitative results are summarized in Table 6.

The subsequent increase of temperature (the section at elevation 221 mm) revealed formation of oxidized alloys of zirconium and steel.

Parameters for the "Standard Problem" ISP—36

The averaged experimental parameters of the CORA—W2 degradation at the sections at elevations 208 and 221 mm are given in Table 7.

Conclusion

Material analysis was performed for six sections of the CORA-W2 bundle: at sections at elevations 208 and 221 mm there were determined experimental parameters of the bundle degradation in accordance with the International "Standard Problem" ISP-36,

at other sections (-13, 87, 1098, and 1148 mm) there were performed selective investigations of local processes of physical and chemical interaction between the materials, especially of their oxidation.

Maximum damage to the bundle was observed at elevation 1098 mm. Chemical composition of the cladding fragments is close to (Zr, U)O_2 phase, of the fuel - to $UO_{2.011}$. At the section at elevation 208 mm there is observed the maximum mass of the melt relocated from the upper part of the bundle. As to its chemical composition, the melt presents steel with inclusions of boron compounds along the boundaries of the melt grains. In the oxidized cladding thickness there are found five layers. The outer layer is close in its composition to ZrO_2, the others - to $ZrO_{0.43}$. Total amount of oxygen in the phase of zirconium, stabilized with oxygen, is about twice that in ZrO_2 layer. At the section at elevation 87 mm the cladding is oxidized to the composition of $ZrO_{0.33}$.

The spacer grid survived completely in the bundle lower part (-13 mm). There was observed the grid oxidation at elevation 208 mm, the oxidized layer thickness being in correlation with predicted oxidation for temperature as recorded at this section (1300°C).

The absorber rod is retained at lower elevations (-13 and 87 mm) and is entirely absent at the upper elevations (1098 and 1148 mm). At the section at elevation 208 mm there occurred complete dissolution of the cladding and partial - of the guide tube.

Bibliography

[1] L.Yegorova, V.Vlasov, Yu.Degaltzev, N.Sokolov, A.Goriatchev. Main provisions of the post-test examination program of VVER/CORA-W2 assembly under the International "Standard Problem" (preparatory stage-selection and Validation of experimental procedures).. NSI RRC "KI" 1959, October 1993.

[2] S.Hagen, P.Hofman, V.Noack, G.Schumacher, L.Sepold. Behavior of a VVER-1000 Fuel Element with Boron Carbide/Steel Absorber Tested under Severe Fuel Damage Conditions in the Cora Facility. KfK 5363(1994).

[3] V.Nosov, I.Vorobiev, R.Petruschenko. Approximation of experimental data by orthogonal polynomails and fractionally-rational function at one-factor regression. Report KIAE-3158, 1990.

[4] W.B.Pearson. A Habdbook of Lattice Spacings and Structures of Metals and Alloys. London, New York, Paris, Los Angeles. Pergamon Press, 1958.

[5] S.Leistikow. Authorzed Priprint from Special Technical Publication 824, 1984.

List of tables:

List of figures:

Fig.12: Oxygen concentration distribution in the various reaction layers.

Fig.13: CORA-W2-02 (bottom), Elevation 208 mm.
Quantitative Microprobe Analysis, point measurements into area 128x128.

Fig.14: Cladding Oxidation. Microprobe Integral Analysis.

Fig.15: CORA-W2-02 (top), Elevation 221 mm.
Qualitative Microprobe Analysis, linear scanning.

Fig.16: CORA-W2-02 (top), Elevation 221mm.
Quantitative Microprobe Analysis in points.

Fig.17: CORA-W2-02, Elevation 221 mm.
Quantitative Microprobe Analysis, point measurements into area 256x256 mcm.

Fig.18: CORA-W2-t, Elevation 1098 mm.
Qualitative Microprobe analysis in points and linear scanning.

Fig.19: Shroud, Microprobe Integral Analysis.

Fig.20: Fuel Oxidation.

Fig.21: W2-02 bottom, Elevation 208 mm.
Microprobe integral analysis. Spacer grids.

Fig.22: Cross Section CORA-W2-02 (bottom), Elevation 208.
Spaser Grid Oxidation.

Fig.23: Absorber rod. Microprobe integral analysis.

Fig.24: Quantitative Microprobe Analysis, point measurements into area 256x256 mcm (fig.23, pos.1).

Fig.25: Quantitative Microprobe Analysis, point measurements into area 128x128 mcm (fig.23, pos.2).

Fig.26: Microprobe integral analysis of the blocage fragments within elevation-13mm.

Fig.27: Microprobe integral analysis of the blocage fragments within elevation 208mm.

Fig.28: Quantitative Microprobe Analysis, point measurements into area 256x256 mcm

Fig.29: CORA-W2-02, Elevation 208 mm
Quantitative Microprobe Analysis, point measurements into area 256x256 mcm

Fig.30: Microprobe integral analysis of the blocage fragments within elevation 221mm.

Table 1

Characteristics of samples Tested at RRC "Kurchatov Institute"

N	Marking of samples	Coordinates cross-section, mm	Temperature °C [2]	Note
1	W2-b	-13		spacer grid, blockage
		87	~700	blockage
2	W2-02	208	1300	spacer grid, blockage
		221	1550	blockage
3	W2-t	1098	1800	
		1148	1750	

Table 2.

№ of layer	Layer thickness at azimuth angle, mcm						MAX Value		MIN Value		Deviation	Average
	0	60	120	180	240	300	mcm	Angle	mcm	Angle	mcm	mcm
	cladding of simulator 1.1											
1	63	-	88	-	72	88	88	300	63	0	25	80
2	143	-	182	174	133	136	182	120	133	240	49	151
3	333	-	283	435	359	(583)*	435	180	283	120	52	352
4	-	-	181	161	146	-	181	120	146	240	35	163
5	114	102	116	98	136	113	136	240	98	180	38	111
	cladding of simulator 2.0											
1	50	-	85	60	140	128	140	240	50	0	90	95
2	165	-	177	207	166	200	207	180	165	0	42	181
3	(598)	-	205	(470)	272	(382)	272	240	205	120	67	238
4	-	-	180	-	143	-	180	120	143	240	37	161
5	127	-	151	137	157	143	157	240	127	0	30	143
	cladding of simulator 2.2											
1	64	-	52	53	42	37	42	240	64	0	27	49
2	154	129	81	148	138	125	154	0	81	120	73	135
3	(497)	(535)	(571)	248	(540)	(551)	-	-	-	-	-	-
4	-	-	-	-	-	-	-	-	-	-	-	-
5	-	-	-	-	-	-	-	-	-	-	-	-
	cladding of simulator 2.6											
1	60	80	59	61	46	-	80	60	46	240	34	60
2	141	151	124	199	142	-	199	180	124	120	75	144
3	391	302	441	268	329	-	441	120	268	180	173	340
4	177	198	188	223	202	-	223	180	177	0	46	194
5	107	121	104	113	115	-	121	60	104	120	17	112
	cladding of simulator 3.0											
1	0	-	-	-	-	-	-	-	-	-	-	-
2	182	212	215	-	145	220	220	300	145	240	75	195
3	173	(588)	211	-	(606)	347	347	300	173	0	174	244
4	349	-	195	-	-	172	349	0	172	300	177	239
5	137	153	202	105	100	158	202	120	100	240	102	138
	cladding of simulator 3.1											
1	78	-	180	75	108	96	180	120	75	180	105	106
2	249	212	-	161	179	156	249	0	156	300	93	191
3	307	(480)	(854)	(465)	274	(399)	307	0	274	240	67	290
4	197	-	-	-	177	-	197	0	177	240	20	-
5	160	170	103	97	155	166	170	60	97	180	73	146
	cladding of simulator 3.3											
1	49	48	33	71	87	48	87	240	33	120	54	54
2	184	155	263	116	(454)	141	263	120	116	180	147	170
3	375	394	279	(486)	-	401	401	300	279	120	122	362
4	86	221	-	-	153	126	221	60	86	0	135	146
5	96	148	-	-	126	100	148	60	96	0	52	113
	cladding of simulator 3.5											
1	63	-	-	-	-	52	63	0	52	300	11	57
2	160	191	157	179	-	140	191	60	140	300	51	165
3	321	286	(726)	159	275	344	344	300	159	180	180	277
4	161	130	-	-	-	115	161	0	115	300	46	135
5	103	125	73	-	-	96	125	60	73	120	52	100

* The values for several layers, vesual separation of which is impossible, are given in brackets.

Results of measurements of Interaction Zones Linear Dimensions inside Simulator Claddings W2-02 Bottom 208 mm

Table 2.(cont.)

№ of layer	Layer thickness at azimuth angle, mcm						MAX Value		MIN Value		Deviation	Average
	0	60	120	180	240	300	mcm	Angle	mcm	Angle	mcm	mcm
	cladding of simulator 3.7											
1	58	69	91	54	81	72	91	120	54	180	37	70
2	157	120	71	177	135	101	177	180	71	120	106	128
3	(541)	(502)	(700)	362	328	378	378	300	328	240	50	356
4	-	-	-	-	191	185	191	240	185	300	6	188
5	112	121	58	84	69	83	121	60	58	120	63	87
	cladding of simulator 3.9											
1	-	51	64	-	41	-	64	120	41	240	23	52
2	-	104	131	(562)	139	104	139	240	104	300	35	119
3	(698)	423	394	-	371	404	423	60	341	240	52	398
4	-	124	109	106	113	103	124	60	103	300	17	111
5	83	59	51	52	67	75	83	0	51	120	32	63
	cladding of simulator 4.1											
1	-	-	-	-	64	52	64	240	52	300	12	58
2	-	130	-	-	106	-	130	60	106	240	24	118
3	(685)	(522)	(518)	(696)	(621)	(636)	-	-	-	-	-	-
4	-	-	175	-	-	-	-	-	-	-	-	-
5	-	-	-	-	-	-	-	-	-	-	-	-
	cladding of simulator 4.3											
1	-	-	71	60	70	43	71	120	43	300	28	65
2	-	-	161	113	138	126	161	120	113	180	48	132
3	-	-	303	457	385	-	457	189	303	120	154	358
4	-	-	-	411	-	-	-	-	-	-	-	-
5	-	-	-	158	291	-	291	240	158	180	133	220
	cladding of simulator 4.5											
1	-	63	-	33	36	34	63	60	33	180	30	35
2	-	165	-	178	161	116	178	180	116	300	62	163
3	-	333	-	363	(513)	(685)	363	180	333	60	30	350
4	-	164	-	99	-	-	164	60	99	180	65	132
5	120	136	86	131	130	113	136	60	86	120	50	124
	cladding of simulator 4.7											
1	-	70	83	55	48	45	83	120	45	300	38	60
2	-	119	-	88	136	120	136	240	880	180	48	116
3	(1127)	(616)	(572)	(356)	(660)	(647)	-	-	-	-	-	-
4	-	-	188	-	-	-	-	-	-	-	-	-
5	116	92	153	81	98	94	153	120	81	180	72	100
	CLADDING OF SIMULATOR 4.9											
1	-	78	50	59	60	74	78	60	50	120	28	64
2	-	183	60	210	219	245	245	300	60	120	185	204
3	-	310	(540)	293	295	364	364	300	293	180	71	315
4	-	191	-	150	-	120	191	60	120	300	131	154
5	-	140	129	143	128	59	143	180	59	300	84	132
	cladding of simulator 5.1											
1	48	-	-	-	-	88	88	300	48	0	40	68
2	186	200	-	-	232	143	232	240	143	300	89	190
3	331	(516)	(639)	(698)	(608)	(851)	-	-	-	-	-	-
4	239	-	165	145	-	-	239	0	145	180	94	183
5	166	147	165	145	164	115	166	0	115	300	51	155
	cladding of simulator 5.3											
1	131	125	-	-	-	70	131	0	70	300	61	109
2	170	125	-	-	278	105	170	0	105	300	173	169
3	(822)	(682)	(753)	(824)	220	(484)	-	-	-	-	-	-
4	-	-	-	-	121	-	-	-	-	-	-	-
5	67	68	94	105	151	105	151	240	67	0	84	93
	Shroud											
1	-	73	41	70	41	40	73	60	40	300	33	51
2	-	192	165	116	86	125	192	60	86	240	106	135
3	(953)	135	781	(533)	(882)	(829)	135	60	62	180	73	99
4	-	135	-	-	-	-	-	-	-	-	-	-
5	-	36	-	127	-	-	127	180	36	60	91	81

Results of measurements of Interaction Zones Linear Dimensions inside Simulator Claddings W2-02 Bottom 208 mm

Table 3.

№ of layer	Layer thickness at azimuth angle, mcm						MAX Value		MIN Value		Deviation	Average
	0	60	120	180	240	300	mcm	Angle	mcm	Angle	mcm	mcm
	cladding of simulator 1.1											
1	139	136	156	192	171	165	192	180	136	60	56	157
2	(809)*	(788)	(605)	(538)	221	208	221	240	208	300	13	215
3	-	-	-	-	398	399	399	300	398	240	1	399
4	-	-	202	211	203	216	216	300	202	120	14	207
5	-	-	-	-	-	-	-	-	-	-	-	-
	cladding of simulator 2.0											
1	107	-	159	200	173	121	200	180	107	0	93	177
2	(724)	(861)	(605)	(690)	253	(1118)	-	-	-	-	-	253
3	-	-	-	-	253	-	-	-	-	-	-	253
4	-	-	-	-	193	-	-	-	-	-	-	193
5	89	127	90	-	-	-	127	60	89	0	38	90
	cladding of simulator 2.2											
1	134	72	60	75	104	66	134	0	60	120	74	78
2	155	182	154	172	155	127	182	60	127	300	55	154
3	255	257	223	324	279	-	324	240	223	180	101	203
4	157	234	202	211	125	-	234	60	125	240	109	190
5	153	319	338	112	155	115	338	120	112	180	226	185
	cladding of simulator 2.6											
1	156	137	139	165	50	89	165	180	50	240	115	130
2	205	225	285	292	156	(742)	285	120	156	240	236	238
3	381	418	-	271	510	-	510	240	271	180	239	400
4	192	203	242	230	169	-	242	120	169	240	73	132
5	-	-	-	-	-	87	-	-	-	-	-	87
	cladding of simulator 3.0											
1	-	-	83	67	(1002)	(1210)	83	120	67	180	16	75
2	-	(758)	(890)	-	-	-	-	-	-	-	-	-
3	-	-	-	157	-	-	-	-	-	-	-	-
4	-	-	-	-	-	-	-	-	-	-	-	-
5	134	136	92	105	102	162	162	300	92	120	70	119
	cladding of simulator 3.1											
1	175	206	-	34	-	131	206	60	34	180	172	153
2	(660)	(869)	(829)	(1044)	(813)	-	-	-	-	-	-	-
3	-	-	-	-	-	-	-	-	-	-	-	-
4	-	-	-	-	-	-	-	-	-	-	-	-
5	-	115	138	81	113	67	138	120	67	300	71	103
	cladding of simulator 3.3											
1	126	169	-	61	164	157	169	60	61	180	108	149
2	(655)	(787)	(683)	70	180	(673)	180	240	70	180	110	125
3	-	-	-	(584)	414	-	-	-	-	-	-	414
4	-	-	-	-	243	-	-	-	-	-	-	243
5	-	-	-	-	-	-	-	-	-	-	-	-
	cladding of simulator 3.5											
1	175	182	87	72	143	161	182	60	72	180	110	142
2	(471)	(440)	81	89	145	181	181	300	81	120	100	124
3	-	-	(378)	408	263	257	408	180	257	300	151	309
4	-	-	-	219	246	134	246	240	134	300	113	219
5	171	195	134	200	219	179	219	240	134	120	85	186

* The values for several layers, vesual separation of which is impossible, are given in brackets.

Results of measurements of Interaction Zones Linear Dimensions inside Simulator Claddings W2-02 Top 221 mm

Table 3.(cont.)

№ of layer	Layer thickness at azimuth angle, mcm						MAX Value		MIN Value		Deviation	Average
	0	60	120	180	240	300	mcm	Angle	mcm	Angle	mcm	mcm
	cladding of simulator 3.7											
1	-	138	147	86	129	121	147	120	86	180	61	129
2	(761)	(784)	138	194	177	(401)	194	180	138	120	56	170
3	-	-	(700)	227	271	-	271	240	227	180	77	249
4	-	-	-	163	130	159	163	180	130	240	33	151
5	106	77	98	154	175	177	177	300	77	60	100	133
	cladding of simulator 3.9											
1	-	122	55	56	112	-	122	60	55	120	67	89
2	166	105	123	116	121	153	166	0	105	60	61	131
3	395	(469)	397	380	316	366	397	120	316	240	81	371
4	137	-	127	138	146	137	146	240	127	120	19	137
5	-	-	74	137	95	115	167	180	74	120	63	105
	cladding of simulator 4.1											
1	44	-	46	-	121	-	121	240	44	0	77	70
2	130	159	167	126	148	210	210	300	130	0	80	150
3	(529)	(538)	(503)	(570)	(479)	(485)	-	-	-	-	-	-
4	-	-	-	-	-	-	-	-	-	-	-	-
5	-	-	-	-	-	-	-	-	-	-	-	-
	cladding of simulator 4.3											
1	105	107	154	143	123	89	154	120	89	300	65	120
2	(950)	(760)	(934)	182	210	(1037)	210	240	182	180	28	196
3	-	-	-	237	242	-	242	240	235	180	7	239
4	-	-	-	273	317	-	317	240	273	180	77	295
5	136	118	76	236	250	161	250	240	76	120	174	163
	cladding of simulator 4.5											
1	102	168	145	74	53	63	168	60	53	240	115	96
2	104	256	(906)	116	285	(719)	285	240	104	0	181	190
3	-	230	-	319	-	-	319	180	230	60	89	275
4	164	205	163	189	164	249	249	300	163	120	86	189
5	-	-	52	-	-	-	-	-	-	-	-	52
	cladding of simulator 4.7											
1	172	190	93	91	160	133	190	60	91	180	99	140
2	136	(673)	288	202	(1167)	(692)	288	120	202	180	152	209
3	(296)	-	322	314	-	-	322	120	314	180	8	318
4	-	-	197	244	-	-	244	180	197	120	47	220
5	117	99	-	-	113	107	117	0	99	60	18	110
	CLADDING OF SIMULATOR 4.9											
1	-	-	63	68	87	79	87	240	63	120	24	74
2	(991)	(937)	(851)	(754)	253	247	253	240	247	300	6	250
3	-	-	-	-	602	615	615	300	602	240	13	609
4	-	-	-	-	252	249	252	240	249	300	3	205
5	140	102	112	-	-	-	140	0	102	60	38	118
	cladding of simulator 5.1											
1	-	-	-	-	-	-	-	-	-	-	-	-
2	melt	melt	(649)	(863)	(814)	melt	-	-	-	-	-	-
3	-	-	-	-	-	-	-	-	-	-	-	-
4	-	-	-	-	-	-	-	-	-	-	-	-
5	167	135	99	173	120	123	167	0	99	120	74	136
	cladding of simulator 5.3											
1	melt	79	melt	47	-	melt	79	60	47	180	32	63
2	-	-	-	-	-	-	-	-	-	-	-	-
3	-	(857)	-	(706)	(820)	-	-	-	-	-	-	-
4	-	-	-	-	-	-	-	-	-	-	-	-
5	-	101	-	87	79	112	112	300	79	240	33	94
	Shroud											
1	86	110	71	31	188	129	188	240	31	180	157	99
2	(2998)	(1037)	235	192	121	(1117)	235	120	121	240	114	183
3	-	-	431	(747)	606	-	606	240	431	120	185	518
4	-	125	263	-	100	-	263	120	100	240	163	163
5	-	-	41	-	59	100	100	300	41	120	59	67

Results of measurements of Interaction Zones Linear Dimensions inside Simulator Claddings W2-02 Top 221 mm

Table 4.

Method of measurement	Elevation, mm	№ of Fuel Elemint Simulator																	T test, °C /2/
		1.1	2.0	2.2	2.4	2.6	3.0	3.1	3.3	3.5	3.7	3.9	4.1	4.3	4.5	4.7	4.9	5.1	5.3	
Quant.	-13		43.48	38.9	41.65	42.23	39.34												34.68	-
calc.			43.39	38.18	41.44	41.87	40.47												35.36	-
Quant.	87	32.56				39.27		33.05					31.29			29.71		31.04		700
calc.								32.9										33.45		
Quant.	208	32.56	43.8	47.9		39.27			34.2	34.5	34.4		31.29					31.04		1300
calc.		32.68				39.17						30.0	31.88					30.92		
IBAS		31.23						31.93	31.82	32.6	30.2	34.44	35.11	20.09	21.18	29.38	29.33	28.58	29.77	
Quant.	221	34.3	40.71	41.96	45.05	41.59	38.34	32.07	31.68	35.33	33.08	33.81	46.3	37.32	33.54	31.72	34.47	32.57	33.08	1550
calc.								32.56	34.36	31.86										
IBAS		28.445						28.74	30.29	30.45	31.26	13.23	33.66	30.78	28.45	29.71	31.12	30.8	31.3	
Quant.	1098		37.56	31.22	22.11	33.17	36.03													1800
Quant.	1148		36.68	37.76	43.34	41.55	37.48													1750

Quant. - (measurements were carried out at Quantimet)
calc. - (calculation was carried out due to the pellet diameter)
IBAS - (measurements were carried out at the system IBAS-2000)

Results of the Fuel Pellets Square Measurements by Different Methods

Table 5.

Elevation mm	№ of Fuel Element	Fuel Diameters at azimuth angle, mcm												Pellets calc. sq., mm^2	
		0^0		30^0		60^0		90^0		120^0		150^0		average	σ
		DIN	DEX	DIN	DEX	DIN	DEX	DIN	DEX	DIN	DEX	DIN	DEX		
-13	2.0	2069	7775	1483	7638	1637	7741	2121	7689	2259	7655	2259	7689	43.39	0.46
	2.2	3362	7620	3121	7534	2948	7655	2897	7672	3276	7638	3052	7706	38.18	0.54
	2.4	2569	7655	2275	7638	2362	7637	2655	7689	2655	7759	2724	7810	41.44	0.20
	2.6	2069	7620	2052	7672	2017	7551	2034	7689	2000	7690	2000	7758	42.87	0.36
	3.0	2810	7879	2759	7759	2758	7638	2672	7586	2844	7500	2828	7827	40.47	0.70
	5.3	3828	7706	3966	7638	3810	7775	3707	7741	3724	7655	3724	7741	35.36	0.43
87	3.1	4259	7707	4086	7724	4121	7724	4172	7622	4190	7655	4138	7741	31.90	0.32
	5.1	4224	7793	4069	7707	4207	7759	4207	7690	4121	7672	4207	7862	33.45	0.29
208	1.1	3963	7566	3945	7498	3963	7600	3946	7600	3998	7600	3963	7566	32.68	0.17
	1.1M		7481				7484				7520				
	3.9	4221	7463		7532		7515	4169	7480		7480		7480	30.0	0.27
	3.9M		7764				7756				7736		7736		
	4.1	4083	7618	4135	7600	4152	7583	4152	7549	4066	7583			31.88	0.22
	4.1M		7563				7578				7572				
	5.1	3963	7515	3998	7498	4169	7515	4118	7429	4100	7463	4135	7498	30.92	0.29
	5.1M		7486				7481				7474				
	2.6	2574	7515		7532		7515	2539	7498		7532		7498	39.17	0.08
221	3.1	4068	7517	4034	7552	3982	7586	3948	7689	4120	7724	4103	7603	32.56	0.43
	3.1M		7431				7389				7413				
	3.3	4310	7982	4190	7845	4155	7534	4051	7568	4344	8034	4293	8120	34.36	0.97
	3.3M		7531				7493				7524				
	3.5	4413	7758	4138	7828	4206	7672	4051	7500	4137	7465	4327	7603	31.86	0.63
	3.5M		7488				7434				7425				

DIN - internal diameter
DEX - external diameter

Measurements were carried out at Quantimet (with the index "m" - at the tool-room microscope)

Results of the Fuel Pellets Diameter Measurement by Different Methods

Table 6

Point (Fig 23, Fig 24, Fig 25)	Concentration in at%										
	Fe	Cr	Ni	B	C	O	Zr	Nb	Ti	Si	Mo
1	0.01	0.004	-	78.49	21.496	-	-	-	-	-	-
2	0.046	0.009	0.011	79.658	20.264	-	0.01	-	-	-	0.002
3	-	-	-	-	-8.492	73.361	18.132	-	-	-	0.015
4	35.288	25.557	0.904	37.878	-	-	0.008	-	0.008	0.013	0.344
5	54.651	16.426	4.048	14.483	7.805	-	0.041	0.015	0.069	-	2.462
6	74.176	7.418	14.579	-	1.702	-	-	-	0.023	1.653	0.449
7	0.919	0.682	0.119	1.985	4.079	23.214	-	0.005	68.973	-	0.024
8	75.132	9.978	13.032	-	-	-	0.08	-	0.023	1.335	0.42
9	69.957	17.145	9.878	-	1.566	-	0.085	-	0.404	0.965	-
10	71.45	17.281	10.239	-	-	-	0.025	-	0.423	0.582	-
11	70.837	17.01	9.99	0.666	-	-	0.055	0.125	0.37	0.947	-
12	71.812	8.587	9.154	-	-	8.439	0.051	-	1.047	0.262	0.648
13	13.025	22.433	0.02	1.724	-	61.54	0.049	-	1.198	0.011	-
14	14.323	18.772	0.029	1.944	-	63.004	0.158	0.012	1.707	-	0.051
15	45.509	11.963	4.08	38.034	-	-	0.021	-	-	-	0.393
16	60.203	2.56	31.268	-	-	-	0.115	-	-	5.624	0.23
16	60.203	2.56	31.268	-	-	-	0.115	-	-	5.624	0.23
17	42.364	17.871	4.843	33.832	-	-	-	0.064	0.025	0.438	0.563
18	75.07	7.573	15.283	-	-	-	0.012	-	0.035	1.595	0.432
19	36.973	24.541	1.078	36.965	-	-	-	0.033	0.024	-	0.386
20	35.161	25.272	0.914	38.129	-	-	-	-	0.023	-	0.501

CORA-W2-02 /1.1/ 210°, Elevation 208 mm
Quantitative Microprobe analysis in points

Russian Research Center "Kurchatov Institute",

Table 7

Material Interaction Parameters in the Cross-section of the Elevation Speciment W2-O2

№№	Parameters	Parameter Value Elevation	
		208 mm	221 mm
1.	Thickness of ZrO_2 ceramic phase:		
	Average within cladding	0.111 mm	0.176 mm
	Average within ahroud	0.136 mm	0.172 mm
2.	Thickness of oxide phase α-Zr(O):		
	Average within cladding	0.357 mm	0.577 mm
	Average within shroud	0.327 mm	0.518 mm
3.	Dissolved B_4C thickness	0.141 mm	-
4.	Disapperance:		
	of absorber cladding	total	total
	of absorber guide tube	partial	total
5.	Melting of cladding	no	no
6.	Melting of shroud	no	no
7.	Total fuel square	553 mm^2	657mm^2
8.	Total square of ZrO_2 ceramic phase:		
	cladding	73 mm^2	61 mm^2
	shroud	125 mm^2	142 mm^2
9.	Total square of α-Zr(O) oxidized phase:		
	cladding	294 mm^2	216 mm^2
	shroud	213 mm^2	212 mm^2
10.	B_4C total square	34 mm^2	33 mm^2 (fell down during cutting)
11.	Square of spacer grid:		
	(Fe,Cr,Ni)O	45 mm^2	-
	steel	117 mm^2	-
12.	Melts:		
	steel X18H10T	964 mm^2	-
	(Fe,Cr,Ni)O	-	12 mm^2
	alloy X18H10T+6.5 wt% Zr	-	61 mm^2
	$(Fe,Cr,Ni)_3Zr$	-	52 mm^2
	$(Fe,Cr,Ni)_2Zr$	-	56 mm^2
	Fe-Cr-Ni-Zr-O-B	-	116 mm^2
13.	Total square of materials within cross-section		
	without shroud	2335 mm^2	1502 mm^2
	with shroud	2673 mm^2	1858 mm^2

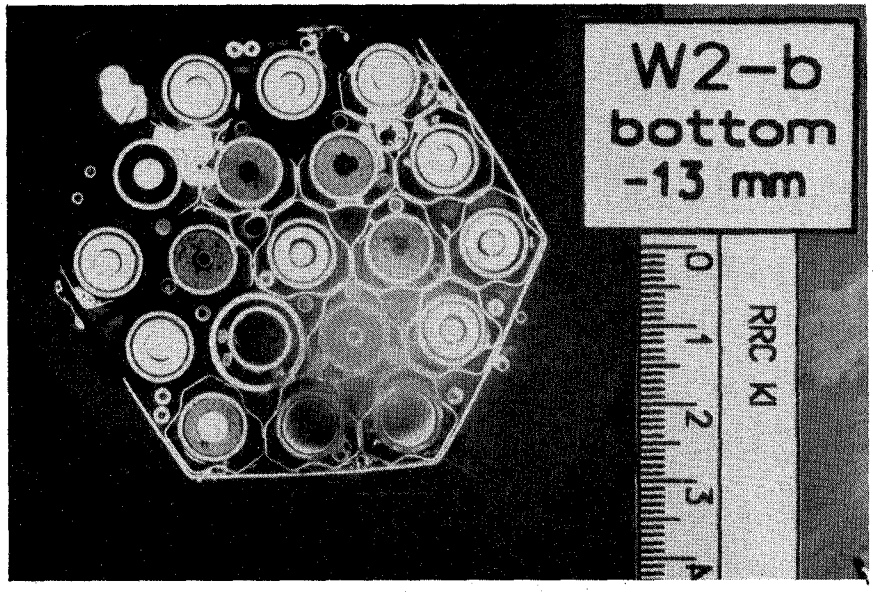

Square of the fuel S_2=240 mm^2;
Square of the simulator claddings
S_3=331 mm^2;
Square of the spacer grids
S_4=329 mm^2
Square of the heaters S_5=178 mm^2
Square of the thermocouples
S_6=73 mm^2
Square of the melts S_8=85 mm^2

Square inside the cladding of the absorber rod cladding S_9=38 mm^2
Square of absorber rod cladding S_{10}=16 mm^2
Square of the absorber rod guide tube S_{11}=31 mm^2

Fig.1. Cross Section CORA-W2-b (bottom), Elevation - 13 mm. Overview, results of measurement

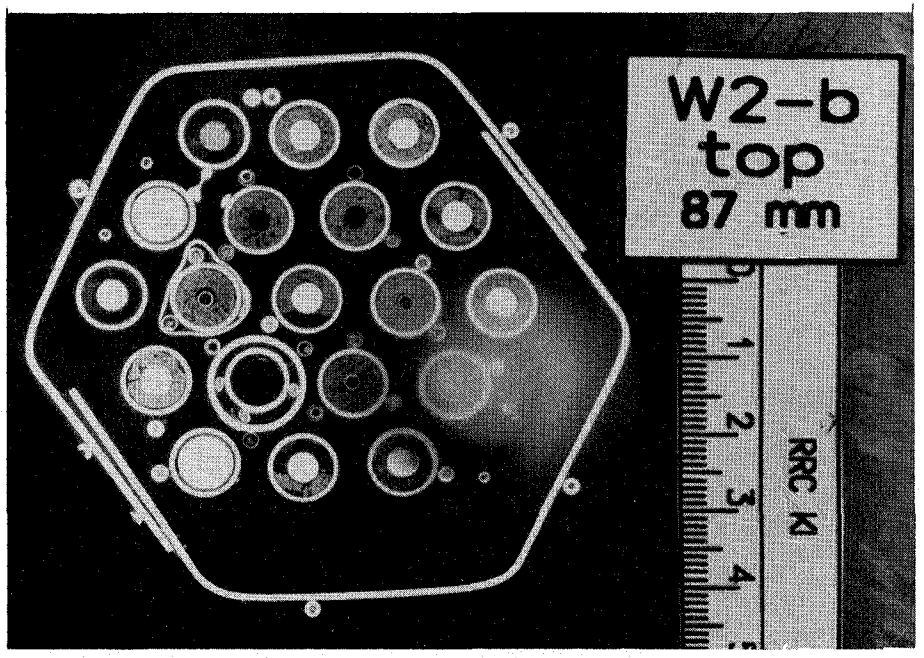

Square inside the shroud S_1=3796 mm^2
Square of the fuel S_2=133 mm^2;
Square of the simulator claddings S_3=338 mm^2;
Square of the heaters S_5=171 mm^2
Square of the thermocouples S_6=67 mm^2
Square of the bandage S_7=24 mm^2
Square of the melts S_8=43 mm^2

Square inside the cladding of the absorber rod cladding S_9=37 mm^2

Square of absorber rod cladding S_{10}=15 mm^2
Square of the absorber rod guide tube S_{11}=30 mm^2
Square of the shroud S_{12}=310 mm^2
Square of the flow cross-section S_0=2940 mm^2

Fig.2. **Cross Section CORA-W2-b (top), Elevation - 87 mm. Overview, results of measurement**

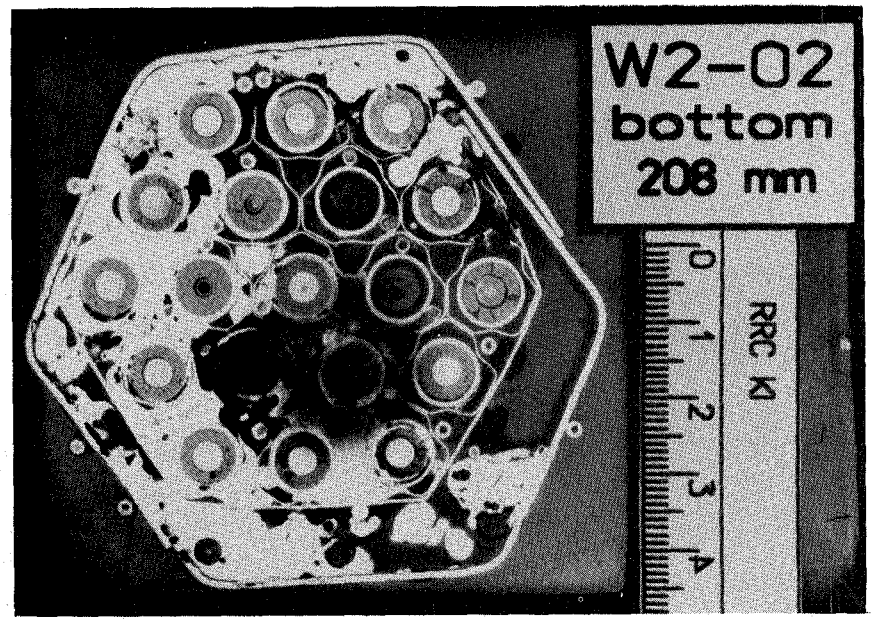

Square inside the shroud S_1=3880 mm^2
Square of the fuel S_2=553 mm^2;
Square of the simulator claddings S_3=367 mm^2;
Square of the spacer grids S_4=162 mm^2
Square of the heaters S_5=159 mm^2
Square of the thermocouples S_6=88 mm^2
Square of the melts S_8=964 mm^2
Square inside the cladding of the absorber rod S_9=34 mm^2
Square of the absorber rod guide tube S_{11}=8 mm^2

Square of the shroud S_{12}=338 mm^2
Square of the flow cross-section S_0=1545 mm^2

Fig.3. **Cross Section CORA-W2-02 (bottom), Elevation 208 mm. Overview, results of measurement**

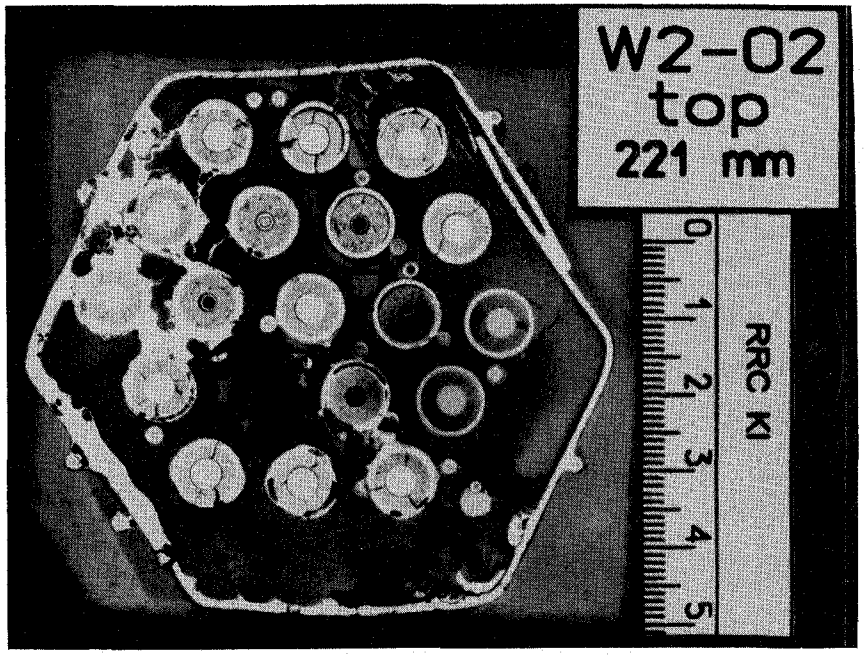

Square inside
the shroud S_1=3861 mm^2
Square of the fuel S_2=657 mm^2;
Square of the simulator claddings
S_3=277 mm^2;
Square of the heaters S_5=173 mm^2
Square of the thermocouples
S_6=65 mm^2
Square of the melts S_8=247 mm^2

Square inside the cladding of the absorber rod S_9=33 mm^2
Square of the shroud S_{12}=354 mm^2
Square of the flow cross-section S_0=2359 mm^2

Fig.4. **Cross Section CORA-W2-02 (top), Elevation 221 mm. Overview, results of measurement**

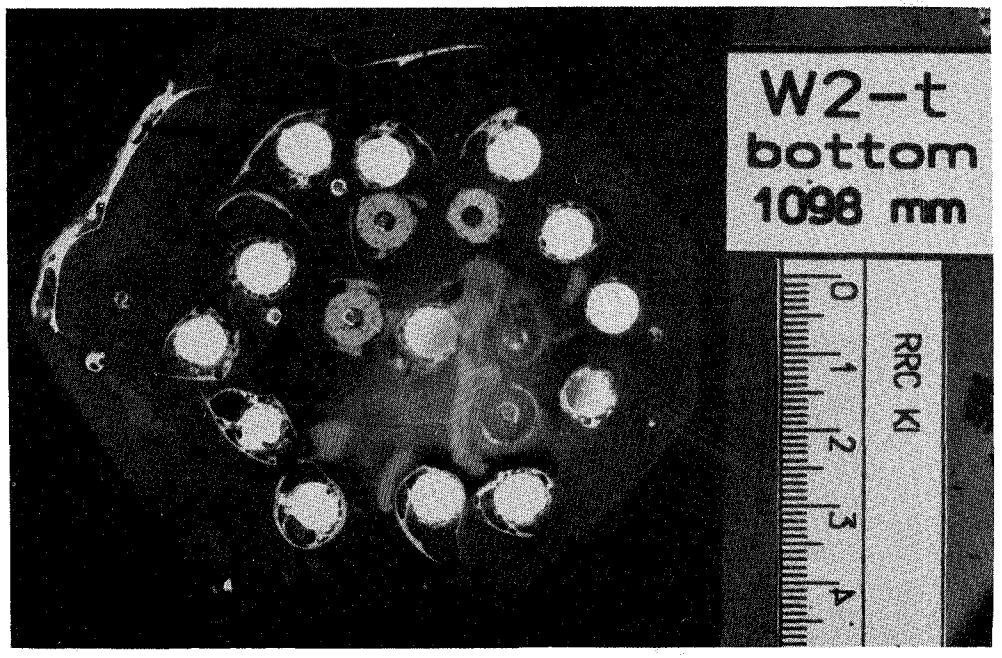

Square of the fuel S_2=160 mm^2;
Square of the simulator claddings
S_3=216 mm^2;
Square of the heaters S_5=405 mm^2
Square of the thermocouples
S_6=12 mm^2
Square of the shroud S_{12}=96 mm^2

Fig.5. Cross Section CORA-W2-t (bottom),
Elevation 1098 mm.
Overview, results of measurement

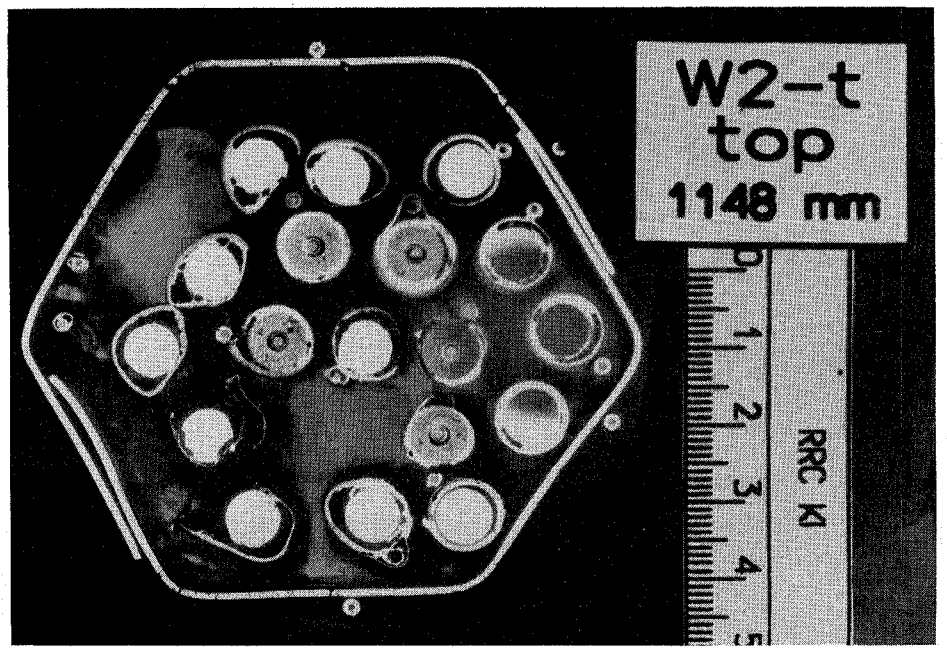

Square inside the shroud
S_1=3910 mm^2
Square of the fuel S_2=233 mm^2;
Square of the simulator claddings
S_3=389 mm^2;
Square of the heaters S_5=469 mm^2
Square of the thermocouples
S_6=72 mm^2
Square of the bandage S_7=14 mm^2
Square of the shroud S_{12}=326 mm^2
Square of the flow cross-section S_0=2734 mm^2

Fig.6. **Cross Section CORA-W2-t (top), Elevation 1148 mm. Overview, results of measurement**

Post-Test Material Examination of the Model Bundle WWER/CORA-W2

Correlation of the Oxigen Concentration in Zr1%Nb Measured by Integral Microprobe Analysis due to "Ideal" Samples, Obtained by Ar-Arc Melting of the Mixture with the Known Oxigen Content (mixture of Zr1%Nb with ZrO_2)

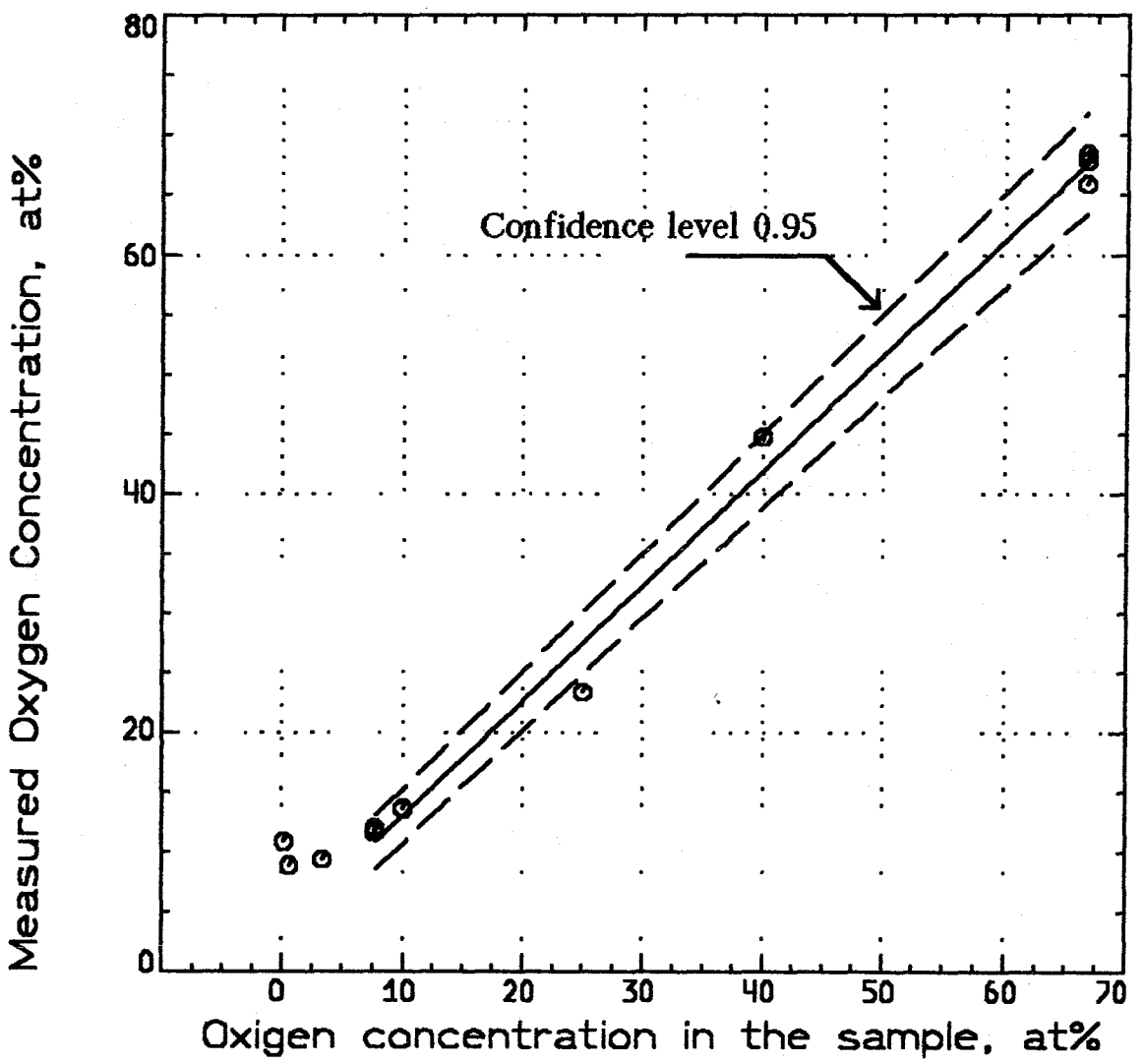

Fig. 7

Cladding oxidation

Russian Research Center "Kurchatov Institute",
Institute of Nuclear Reactors

Post-Test Material Examination of the Model Bundle WWER/CORA-W2

Microhardness Correlation and Oxygen Concentration in "Ideal" Samples

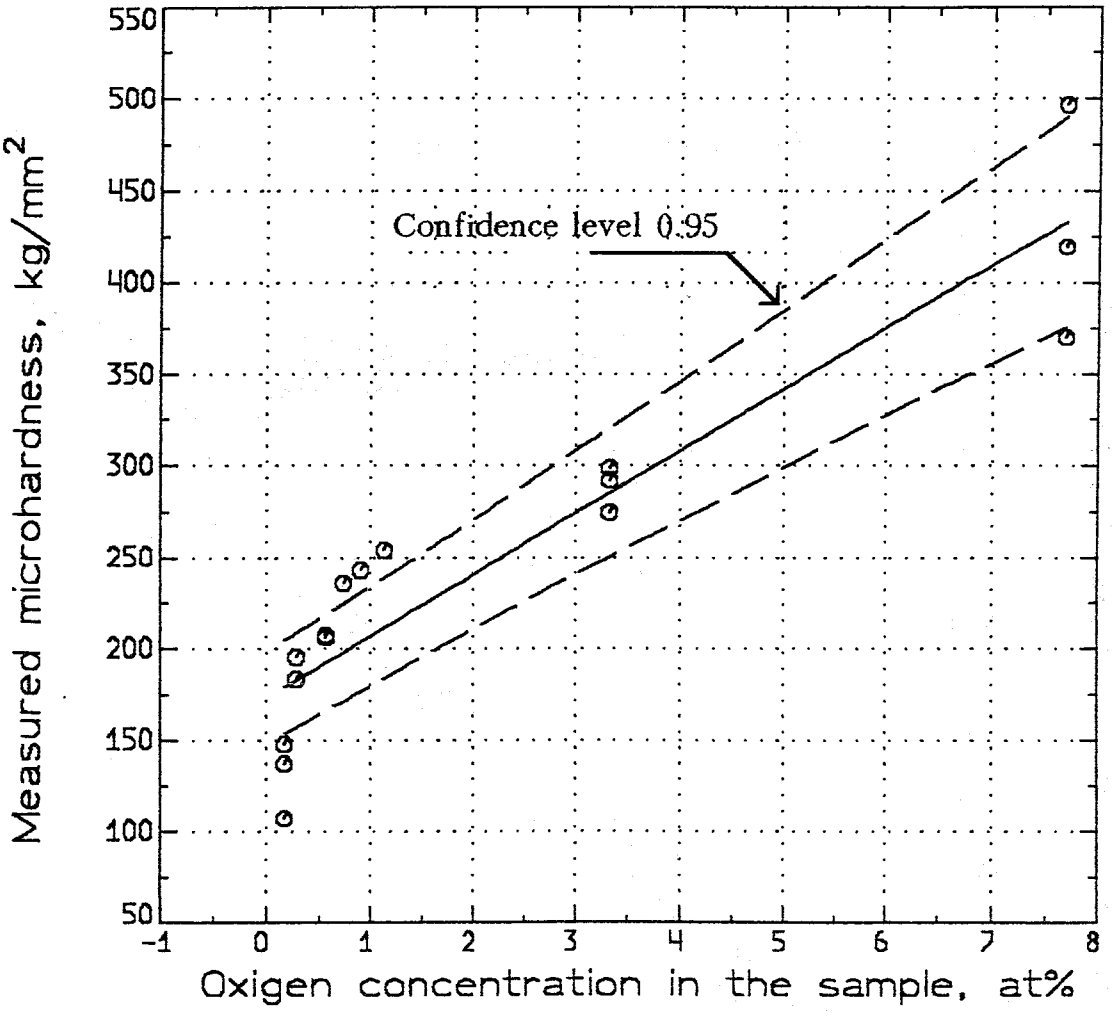

Fig. 8

Cladding oxidation

Russian Research Center "Kurchatov Institute",
Institute of Nuclear Reactors

W2-b bottom /4.9/, Elevation -13 mm.

H_V= 97 ± 12 kg/mm^2 --- Zr1%Nb

W2-b top /3.0/, Elevation 87 mm.

Element	Zr	O
Conc. in at%	74.999	25.001
Phase	$ZrO_{0.33}$	

W2-02 bottom /1.1/ 210°, Elevation 208 mm.

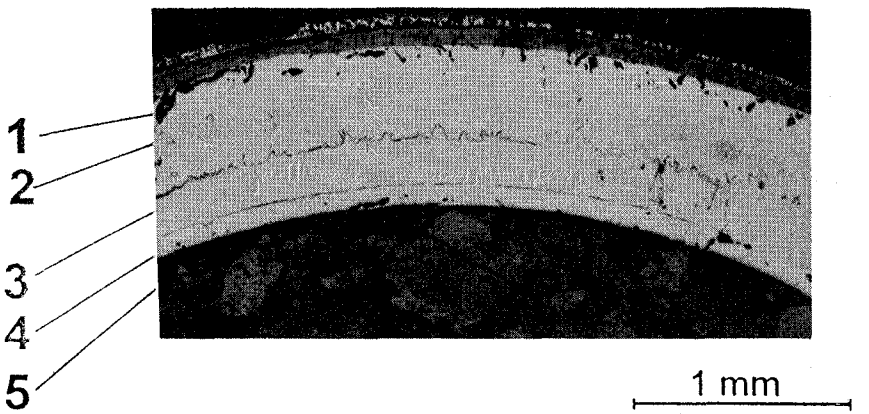

Pos	Conc. in at %.		
	Zr	O	U
1	35.3	64.4	0.08
2	65.8	34.2	---
3	64.2	33.0	2.8
4	71.8	27.6	0.6
5	69.0	31	---

Fig.9. **Cladding Oxidation. Microprobe Integral Analysis.**

Russian Research Center "Kurchatov Institute", Institute of Nuclear Reactors

Post-Test Material Examination of the Model Bundle WWER/CORA-W2

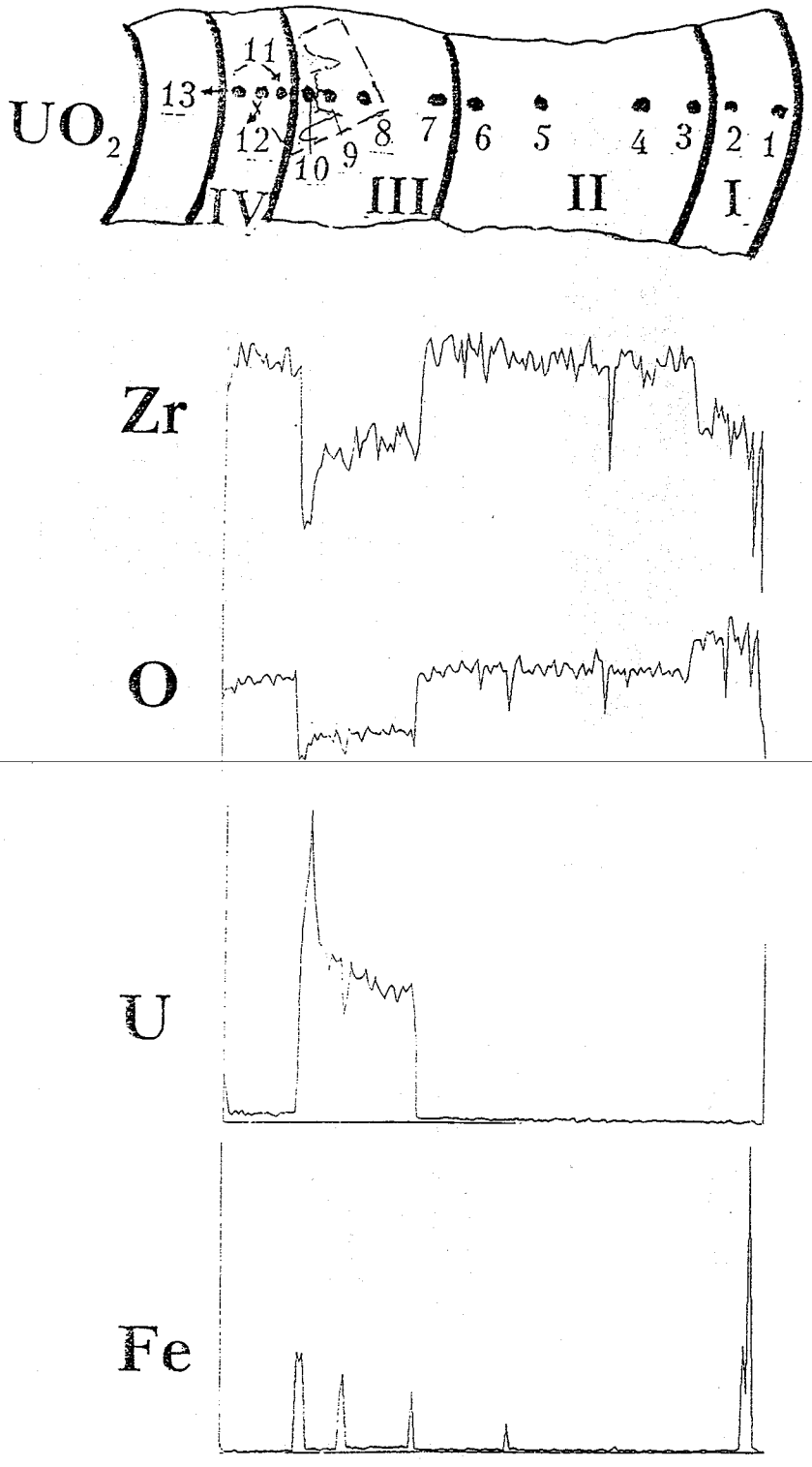

Fig.10. CORA-W2-02 (bottom), Elevation 208 mm
Qualitative Microprobe analysis, linear scanning

Post-Test Material Examination of the Model Bundle WWER/CORA-W2

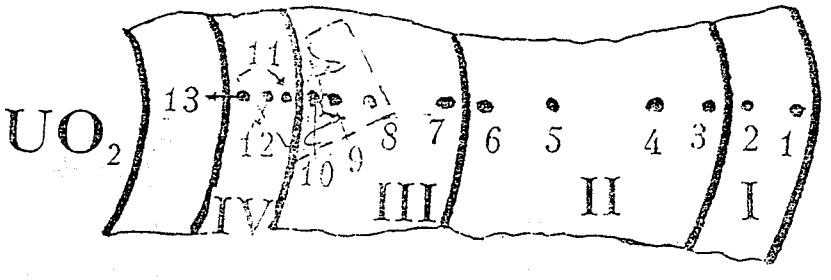

Layer	Point	Point measurements, (zond 1 mcm) Concentration in at%			
		Zr	U	Fe	O
I	1	34.1	~0	0	65.9
	2	34.1	0	0.2	65.7
II	3	68.8	0	0	31.2
	4	77.9	0	~0	22.0
	5	81.1	0	~0	18.8
	6	77.5	~0	0	22.5
III	7	72.3	12.4	0.4	14.9
	8	70.8	13.5	0.5	15.2
	9	64.5	16.0	0.3	19.2
	10	49.3	16.4	24.4	9.9
IV	11	72.9	0.3	0	26.8
	12	70.5	0.3	0	29.2
	13	68.8	0.4	0	30.8

Fig.11. CORA-W2-02 (bottom), Elevation 208 mm
Quantitative Microprobe analysis

Russian Research Center "Kurchatov Institute", Institute of Nuclear Reactors

Post-Test Material Examination of the Model Bundle WWER/CORA-W2

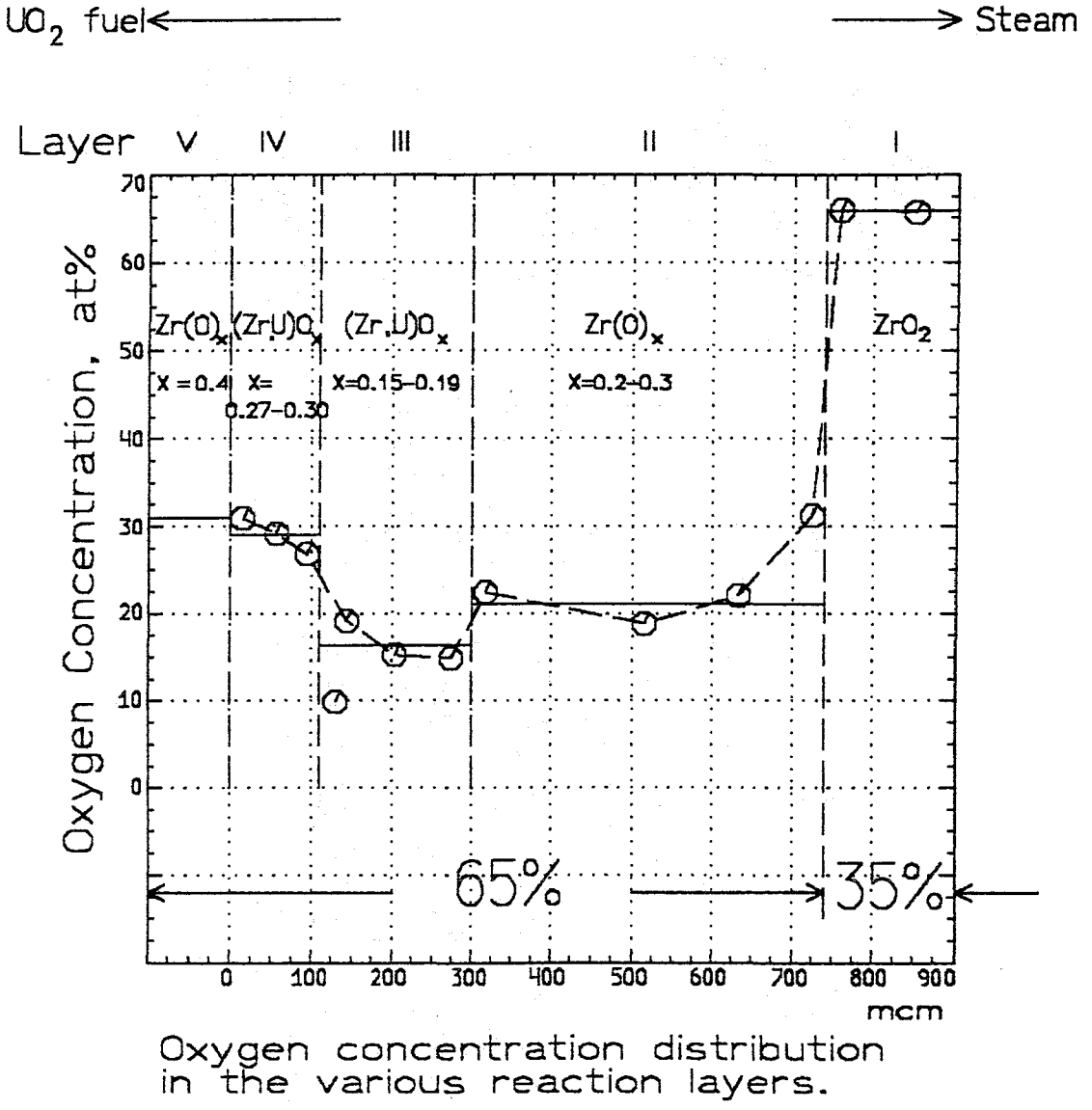

Fig. 12

The percentage of oxygen of the total amount of oxygen absorbed by the cladding in phases $Zr(O)_X$ and ZrO_2 - 65% and 35% respectively

CORA-W2-02 /1.1/ 210°, Elevation 208 mm Quantitative Microprobe analysis in points

Russian Research Center "Kurchatov Institute",
Institute of Nuclear Reactors

Post-Test Material Examination of the Model Bundle WWER/CORA-W2

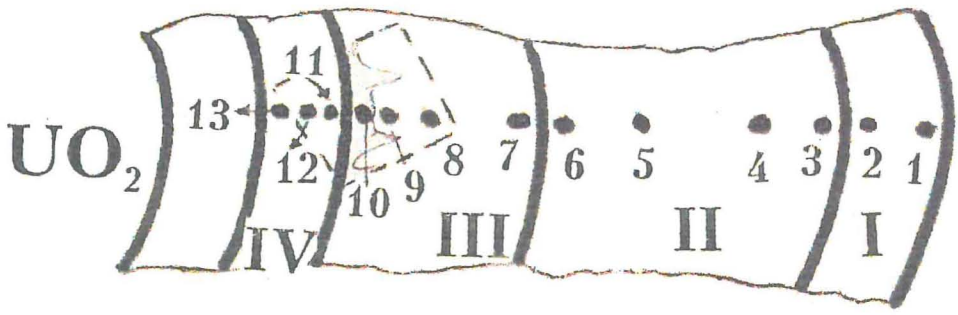

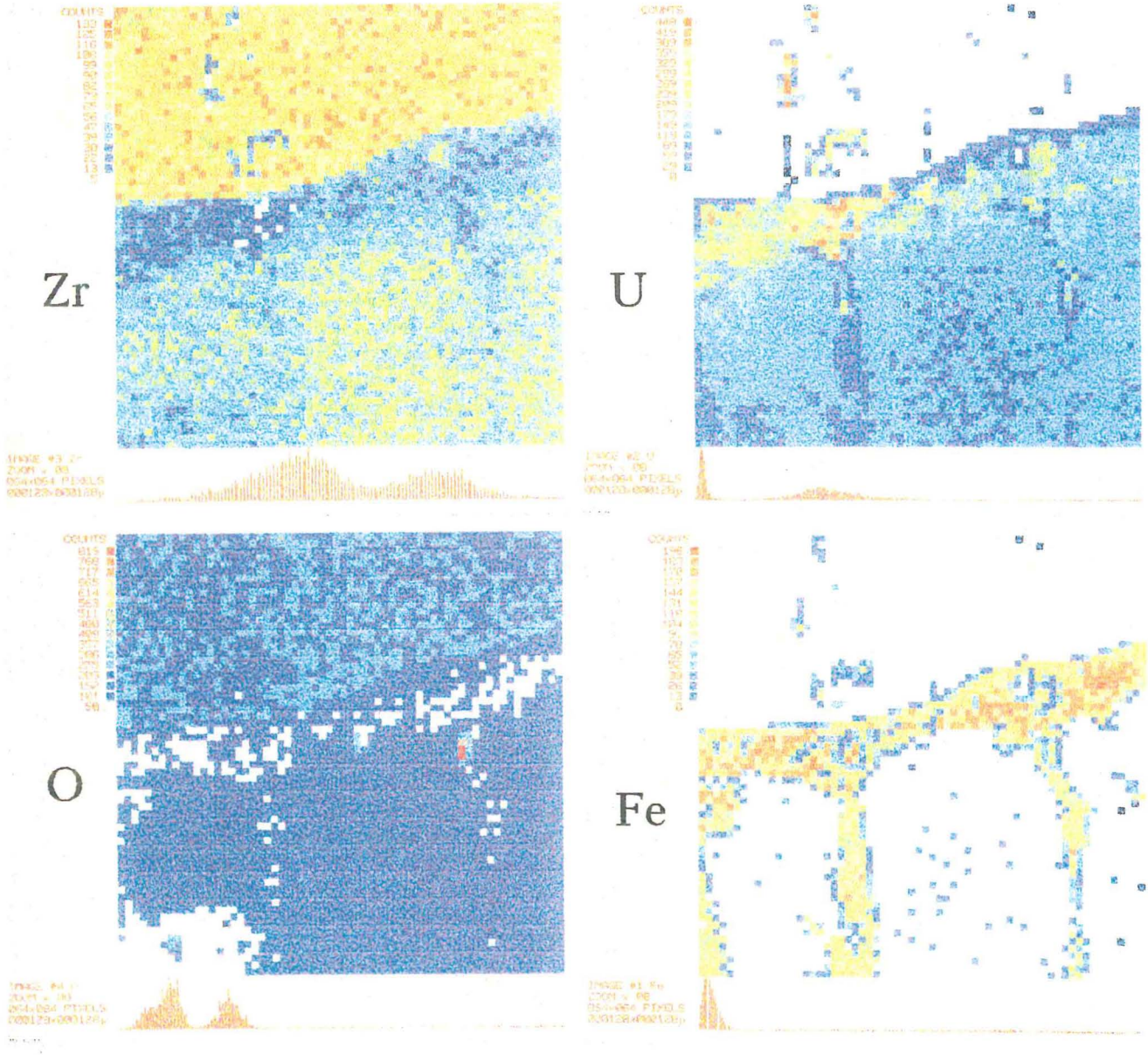

Fig.13: CORA-W2-02 (bottom), Elevation 208 mm

Quantitative Microprobe Analysis, point measurements into area 128x128 mcm

W2-02 top /2.4/ 240°, Elevation 221 mm. W2-t bottom /2.6/ 270°, Elevation 1098 mm.

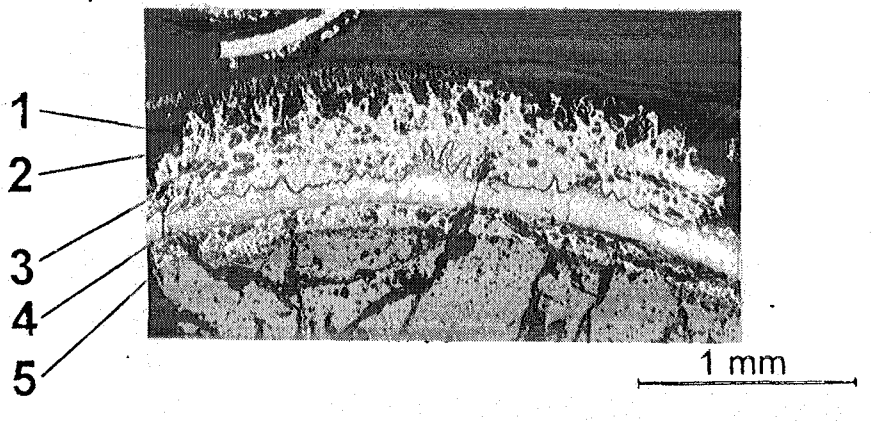

Pos	Conc. in at %.		
	Zr	O	U
1	33.2	66.8	---
3	63.2	36.8	---
4	48.6	37.1	14.3
5	60.9	38.1	1.0

Element	Zr	O	U
Conc. in at%	31.4	62.9	5.7

All the claddings of this elevation are damaged.

W2-t top /3.5/ 120°, Elevation 1148 mm.

Pos	Conc. in at %.	
	Zr	O
1	37.8	62.2
2	69.3	30.7

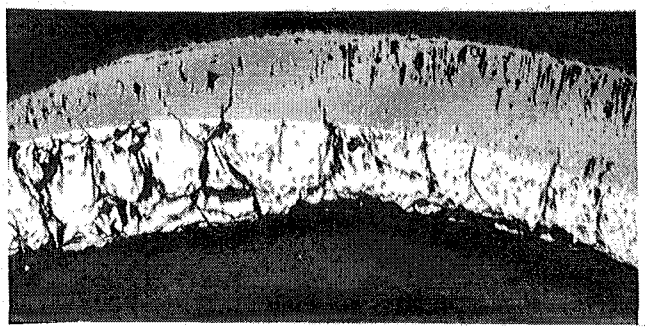

The claddings are less damaged than within the elevation 1098 mm.

Fig.14. Cladding Oxidation. Microprobe Integral Analysis.

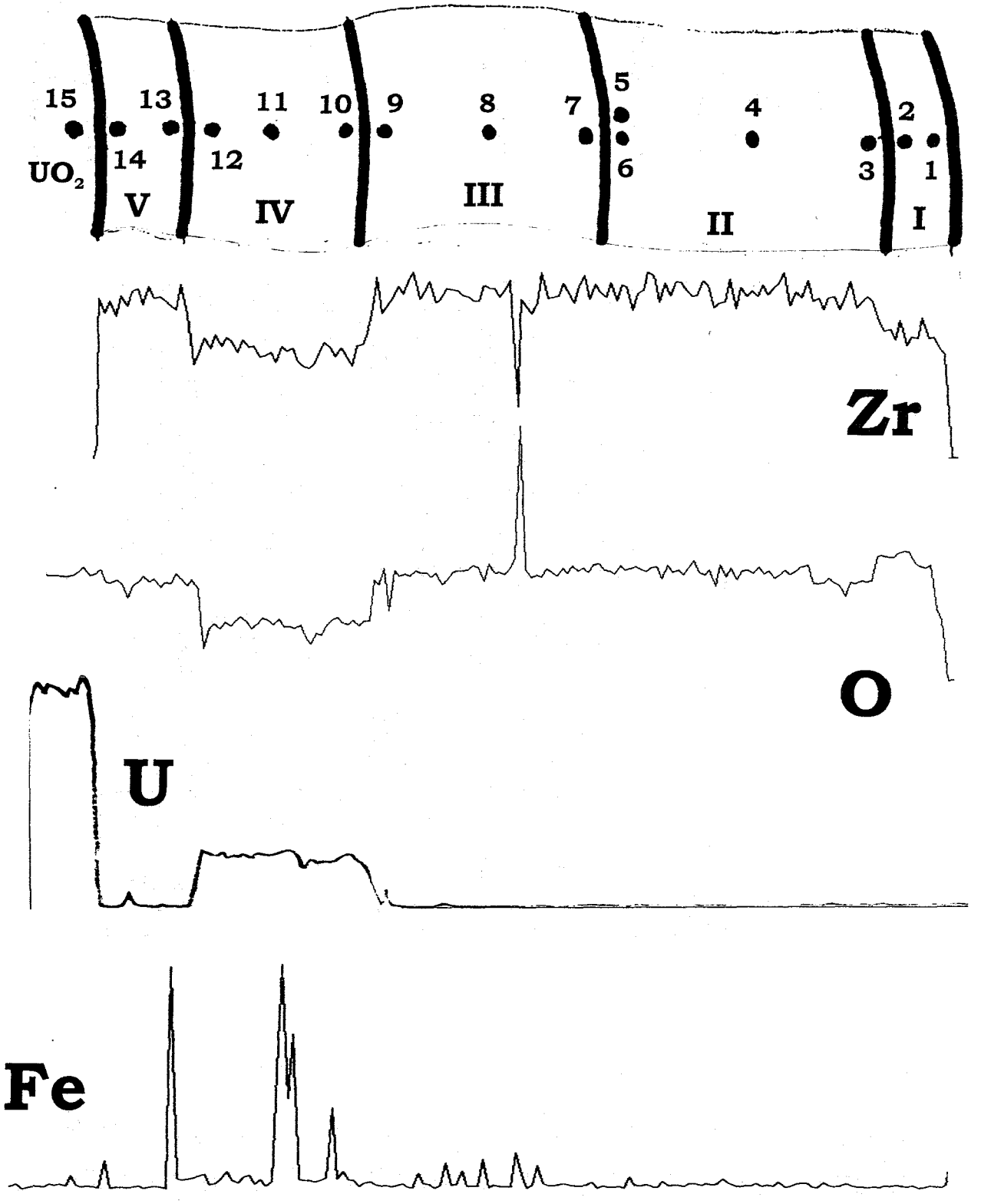

Fig. 15: CORA-W2-02 (top), Elevation 221mm
Qualitative Microprobe analysis, linear scanning

Post-Test Material Examination of the Model Bundle WWER/CORA-W2

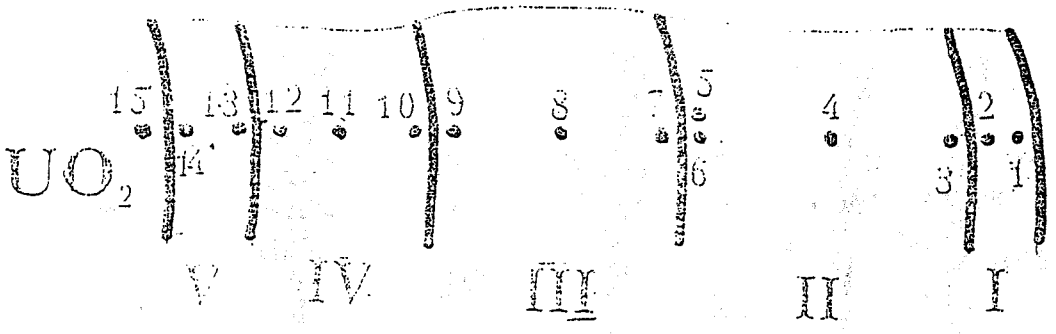

Layer	Point	Point measurements, (zond 1 mcm) Concentration in at%			
		Zr	U	Fe	O
I	1	34.776	0	0.023	65.201
	2	34.699	0	0.008	65.293
II	3	69.787	0	0.049	30.164
	4	81.315	0	0	18.685
	5	83.866	0	0.282	15.852
	6	86.778	0	0.105	13.117
III	7	82.651	0	0	17.349
	8	81.715	0	0.014	18.271
	9	81.104	0.045	0.027	18.824
IV	10	72.86	9.777	0.618	16.745
	17	59.536	7.585	22.723	10.156
	11	73.174	10.324	0.558	15.944
	16	56.91	6.25	21.941	14.899
	12	70.754	12.674	0.666	15.906
V	13	69.604	0.67	0	29.726
	14	70.243	0.773	0	28.984
UO_2	15	0	31.918	0	68.082

Fig.16 CORA-W2-02 (top), Elevation 221 mm
Quantitative Microprobe analysis in points

Russian Research Center "Kurchatov Institute",
Institute of Nuclear Reactors

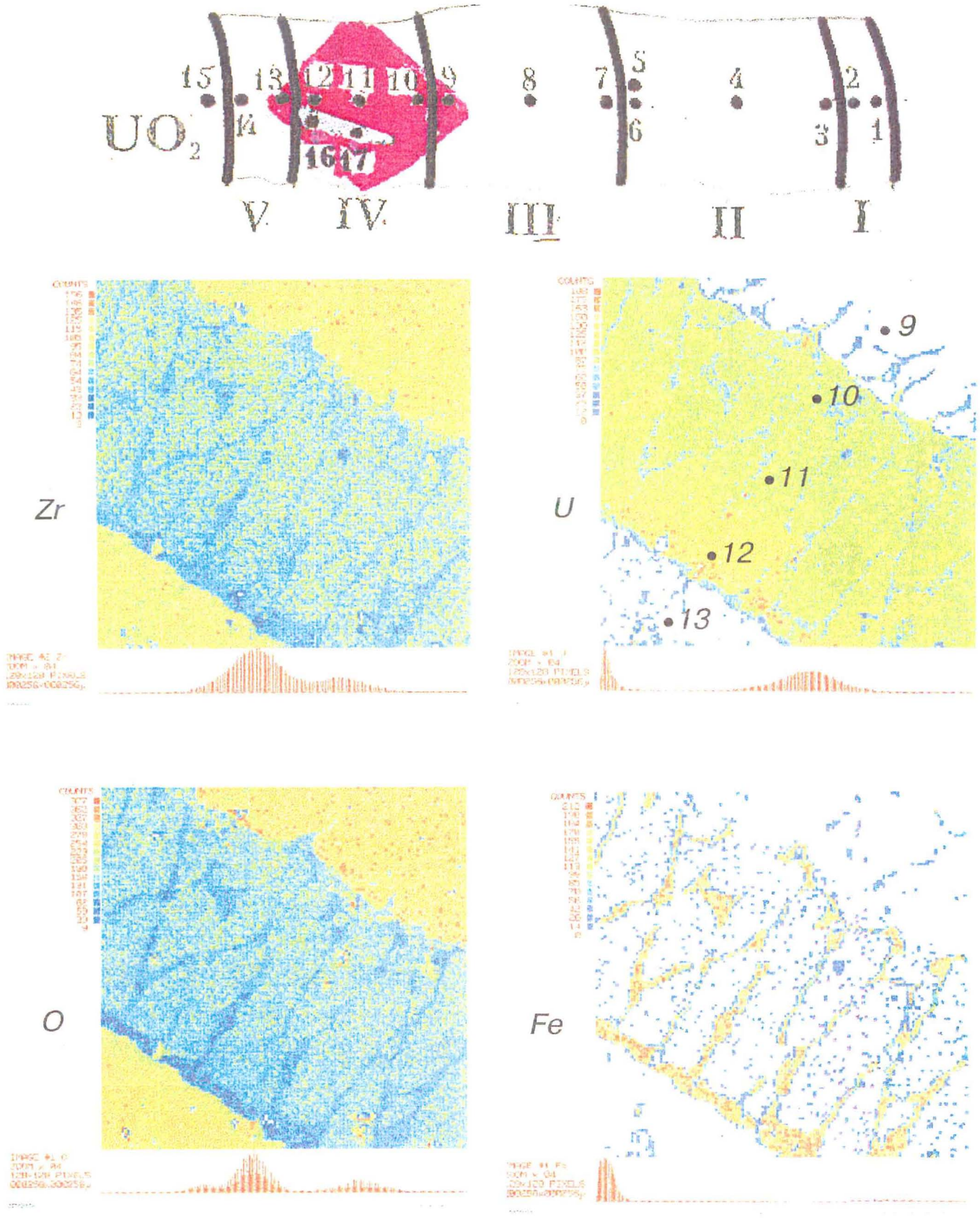

Fig.17: CORA-W2-02, ELEVATION 221 mm
Quntitative Microprobe Analysis, point measurements into area 256x256 mcm

Post-Test Material Examination of the Model Bundle WWER/CORA-W2

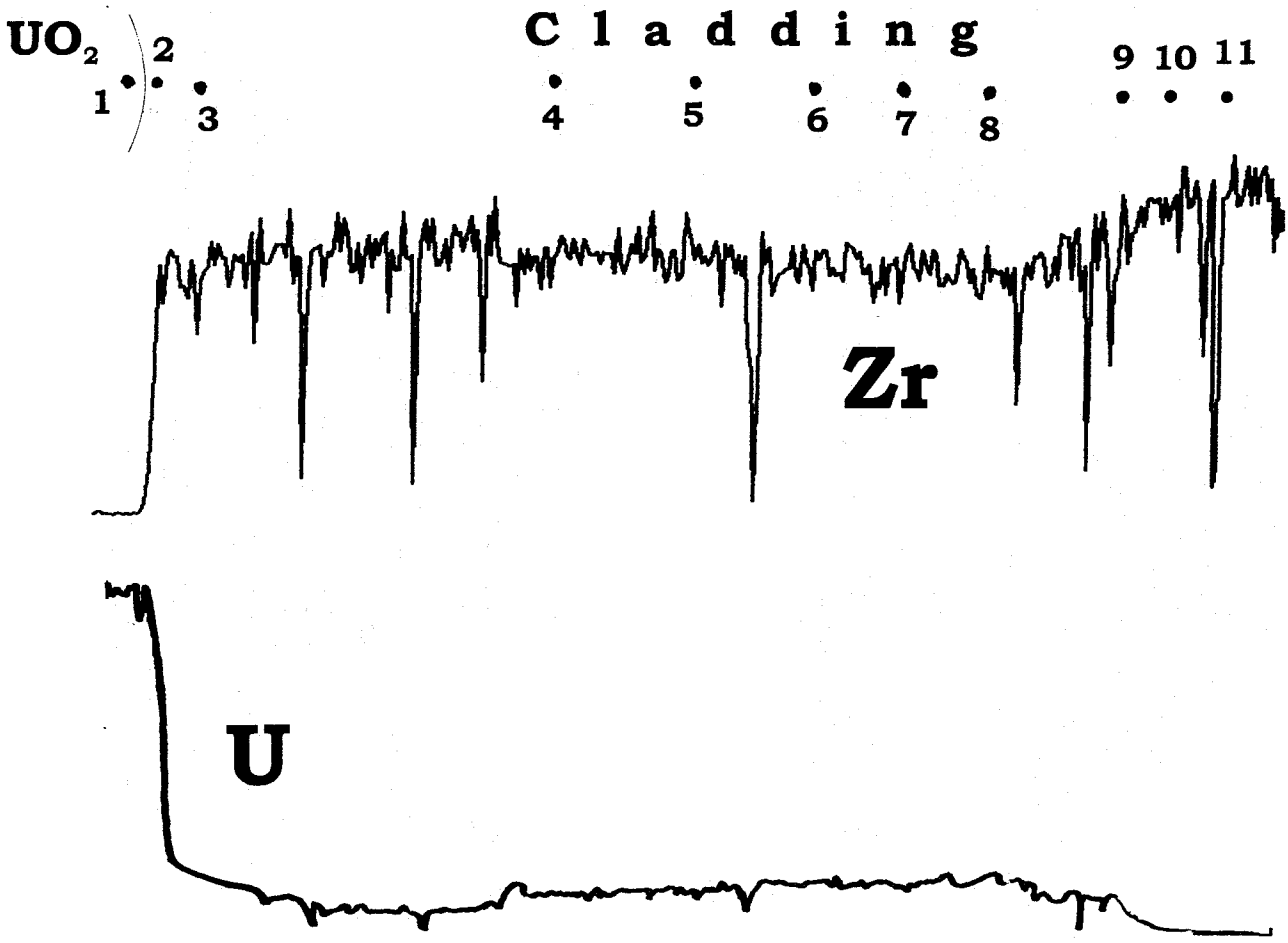

Point			1	2	3	4	5	6	7	8	9	10	11
Point measurements, (zond 1 mcm)	Concentration in at%	Fe	—	—	0.01	0.05	0.02	—	—	—	—	0.05	—
		U	30.0	3.9	3.59	1.3	2.5	3.0	3.0	4.0	0.8	0.1	0.01
		Zr	0.07	29.3	30.4	31.4	30.6	30.4	30.6	29.6	32.9	33.2	33.8
		O	69.93	66.8	66.0	67.25	66.88	66.6	66.4	66.4	66.3	66.65	66.19

Fig. 18: CORA-W2-t, Elevation 1098 mm
Quantitative Microprobe analysis in points and linear scanning

W2-02 top /Shr/ 120°. Elevation 221 mm

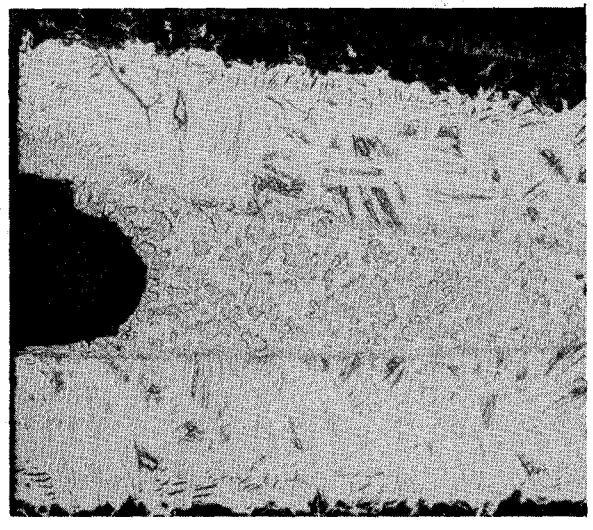

Pos.	Composition, at. %					Phase
	Fe	Cr	Ni	Zr	O	
1	---	---	---	69.9	30.1	$ZrO_{0.43}$
2	13.4	1.9	1.7	58.0	25.0	$[(Fe,Cr,Ni)Zr_3]O_{0.43}$
3	---	---	---	69.7	30.3	$ZrO_{0.43}$

W2-02 top /Shr/ 30°, Elevation 1148 mm

Fig.19. Shroud, Microprobe Integral Analysis.

Russian Research Center "Kurchatov Institute", Institute of Nuclear Reactors

Change of O/U Ratio in the fuel upon the results of X-Ray Structural Analysis (System Дрон−2)

Elevation	*Initial*	*1148 mm*	*1098 mm*
Temperature, °C*	---	1750	1800
a, Å	5.4704	5.4701	5.4691
O/U **	2.000	2.003	2.011

*) based on KfK data (Results of experiment CORA-W2)

**) based on W.B. Pearson data (A Handbook of Lattice Spacings and Structures of Metals and Alloys. London, New York, Paris, Los Angeles. Pergamon Press, 1958).

Fig.20. Fuel Oxidation

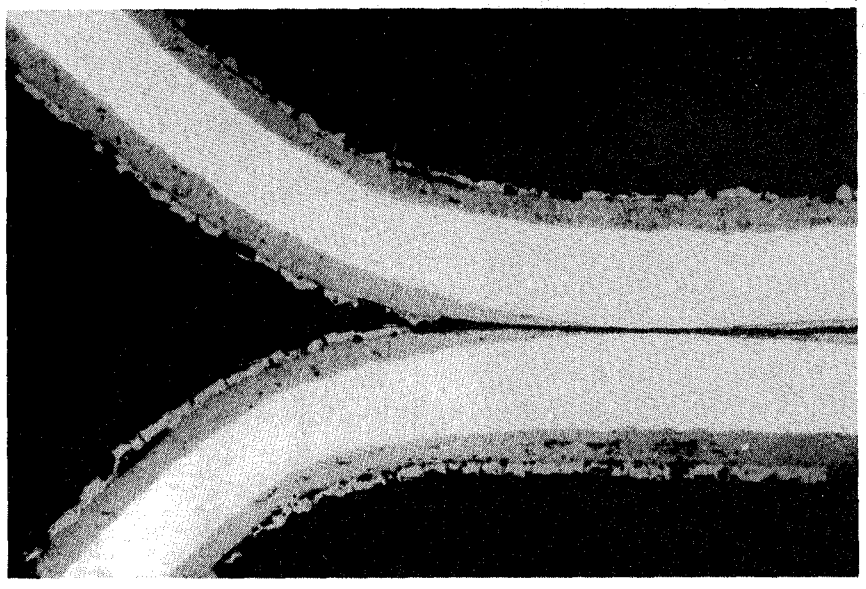

1 mm

Sample fragment	Composition, at. %					Phase
	Fe	Cr	Ni	Mo, Mn, Si	O	
Steel	69.5	18.6	9.5	2.4	---	SS
Oxide	25.8	19.8	0.8	0.8	52.8	(Fe, Cr, Ni) O
External layer	47.5	1.1	---	1.5	49.9	FeO

Temperature within the elevation, calculated due to the grid oxidation (data by S. Leistikow . Authorzed Priprint from Special Technical Publication 824, 1984) corresponds to KfK experimental results (Results of Experiment CORA-W2).

Fig.21. W2-02 bottom, Elevation 208 mm.
Microprobe integral analysis.
Spacer grids.

Russian Research Center "Kurchatov Institute", Institute of Nuclear Reactors

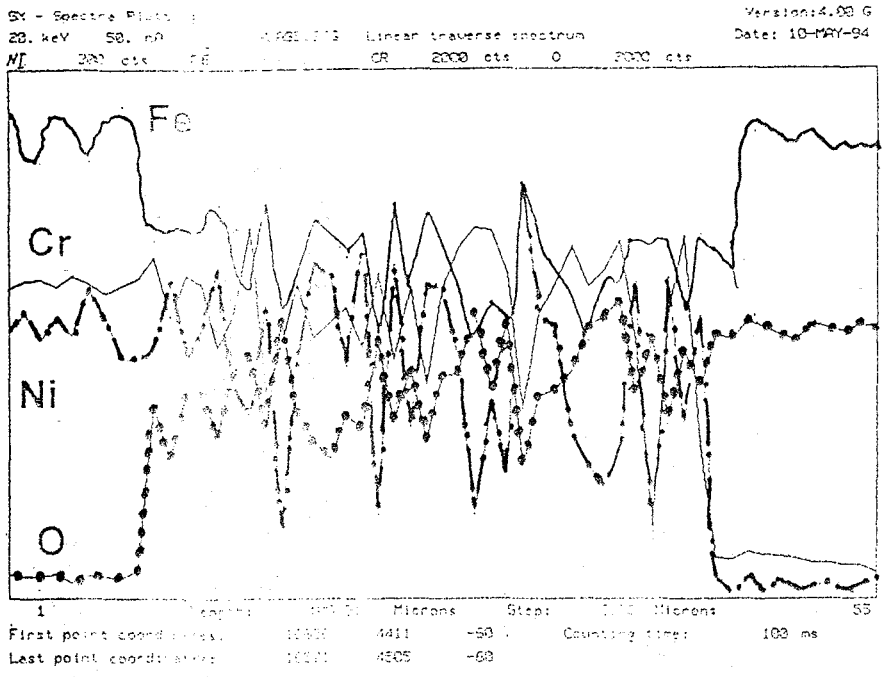

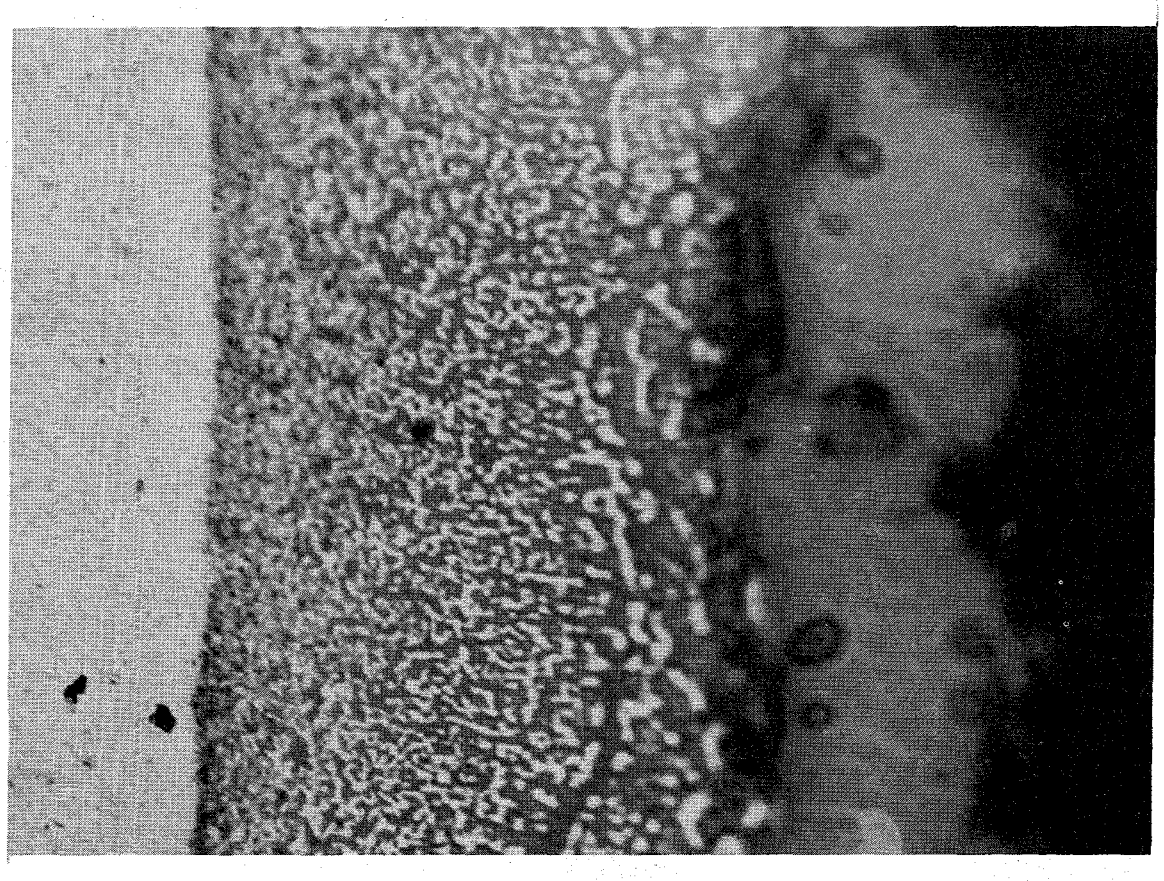

Fig.22. Cross Sectiom CORA-W2-02 (bottom), Elevation 208
Spaser Grid Oxidation

W2-b bottom -13 mm
/2.6/ 120°

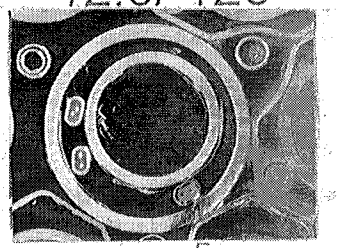

5 mm

W2-b bottom 208 mm
/2.6/ 210°

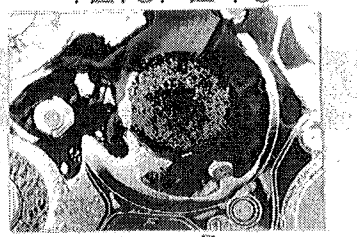

5 mm

W2-02 top 221 mm
/2.6/ 120°

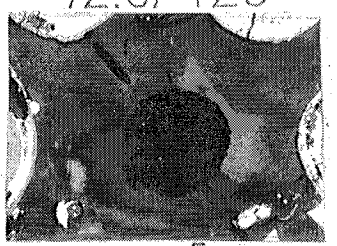

5 mm

W2-02 bottom 208 mm /2.6/ 240°

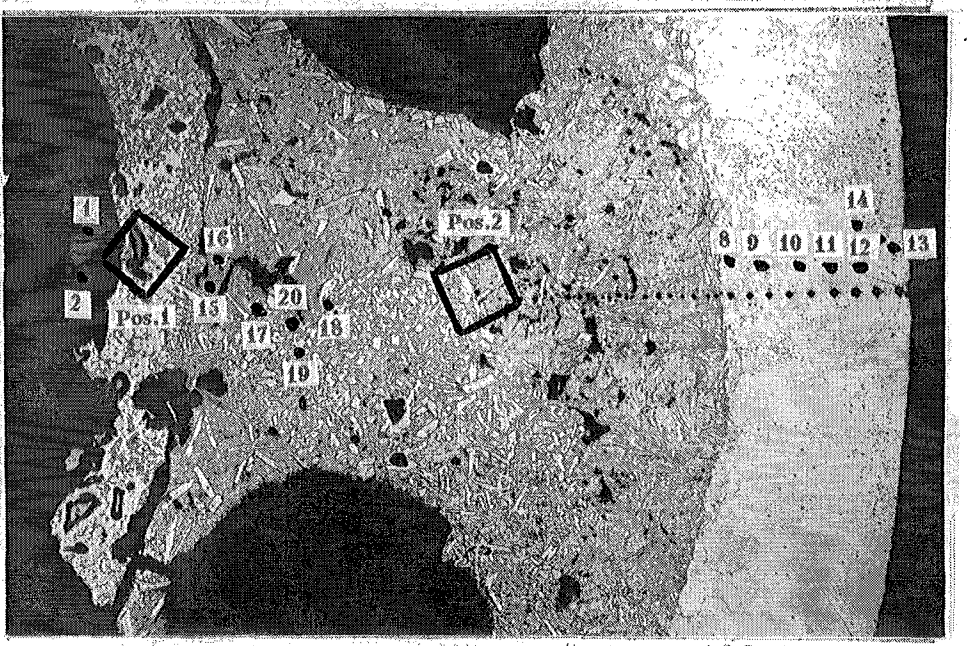

100 mcm

Quantative analysis of melt

Element	Fe	Cr	Ni	O	Mo
Conc. in at %	63.7	24.2	8.8	2.6	0.7

Fig.23. Absorber rod. Microprobe integral analysis

Russian Research Center "Kurchatov Institute", Institute of Nuclear Reactors

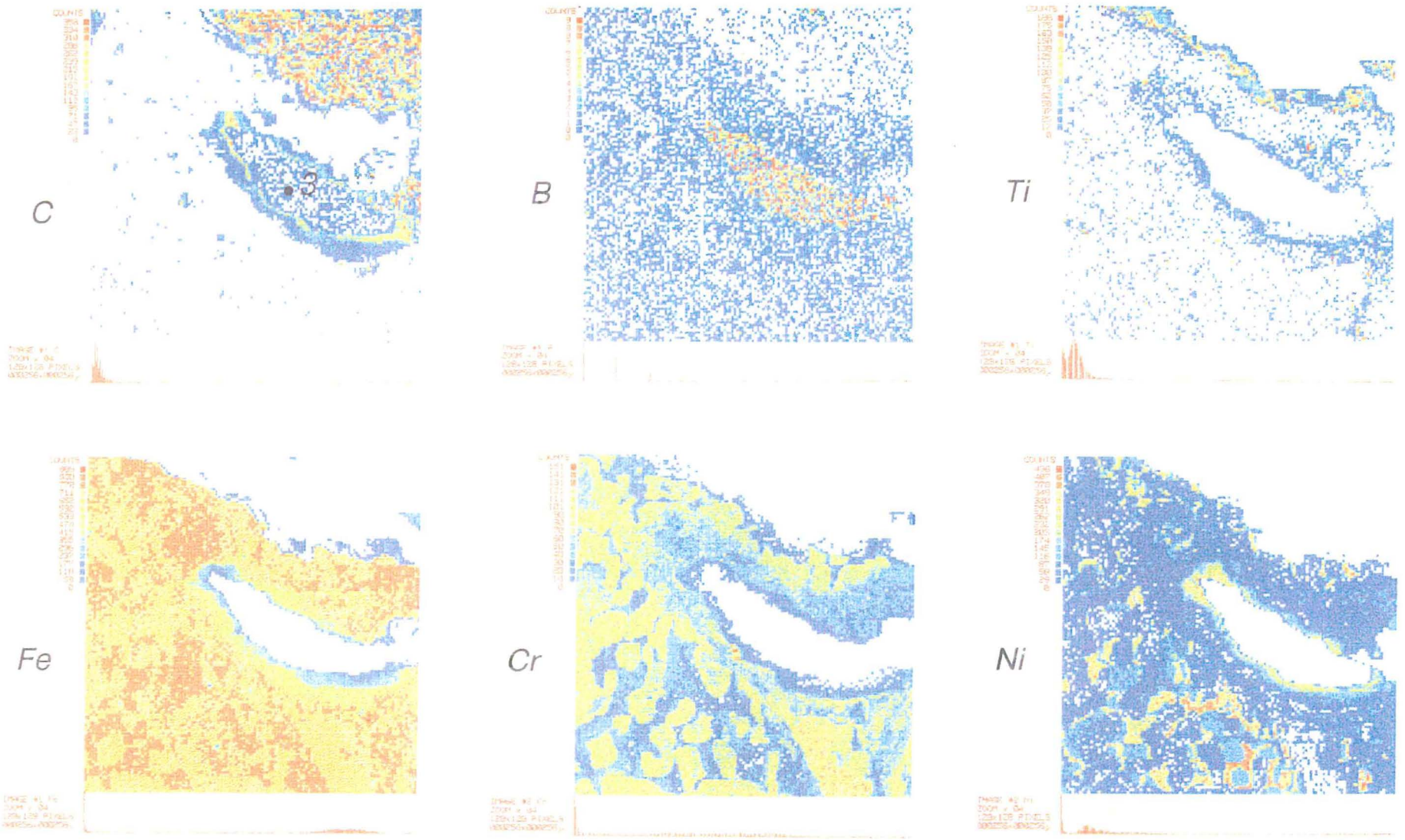

Fig.24: Quantitative Microprobe Analysis, point measurements into area 256x256 mcm (fig.23, pos.1)

Russian Research Center "Kurchatov Institute", Institute of Nuclear Reactor

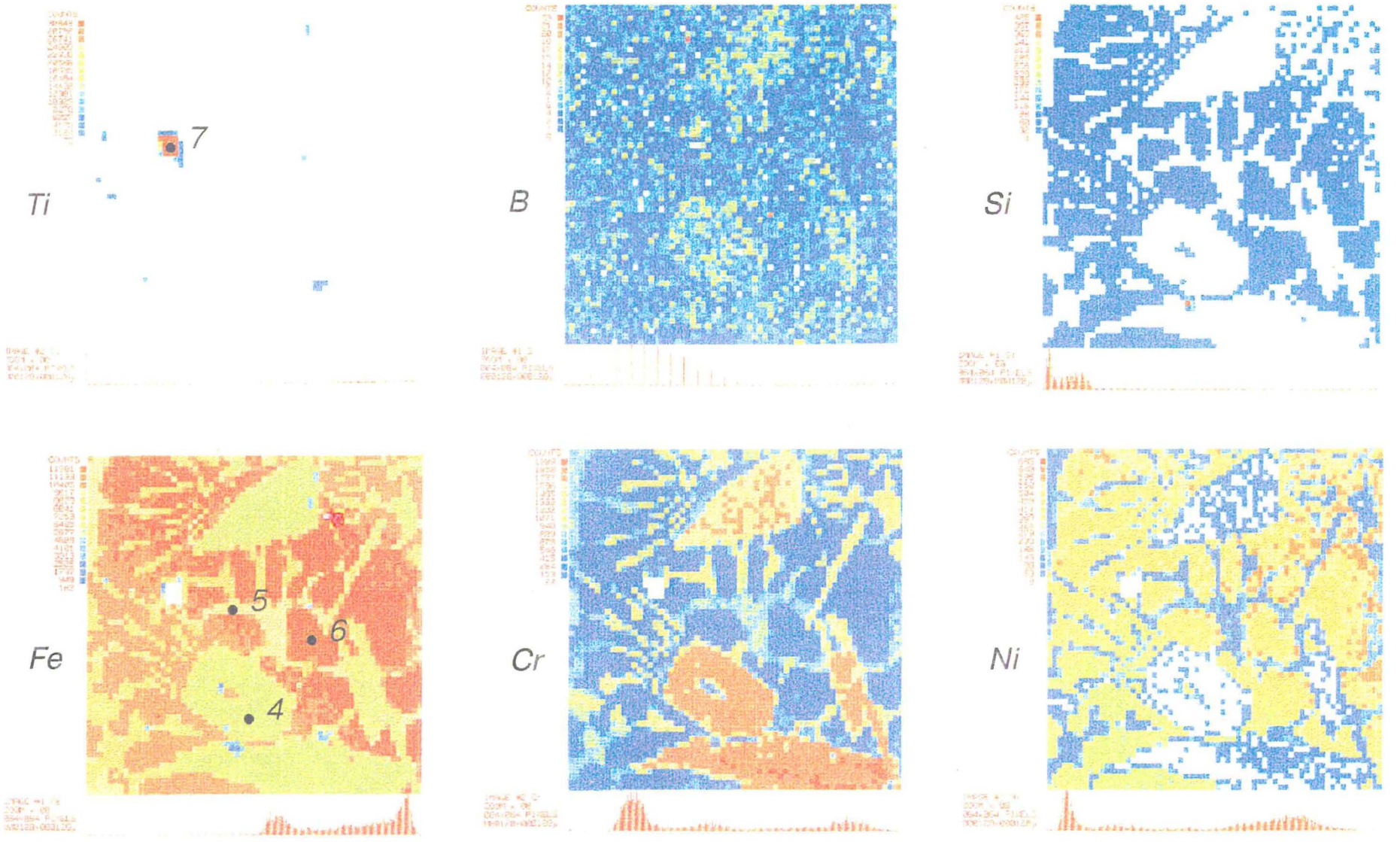

Fig.25: Quantitative Microprobe Analysis, point measurements into area 128x128 mcm (fig.23, pos.2)

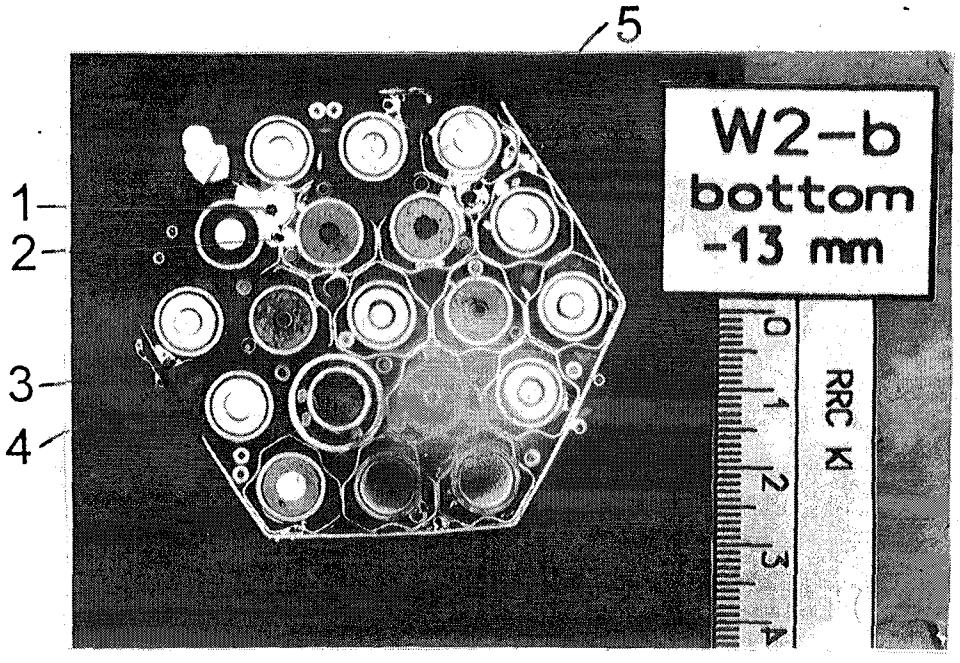

Pos.	Conc in at. %									Phase
	Fe	Cr	Ni	Si	O	Mo	Zr	Re	B	
1	67.7	15.9	9.8	0.7	0.8	2.5	0.7	0.04	1.8	Steel+B
2	68.5	15.7	10.3	0.8	1.0	2.8	0.8	---	---	Steel
3	66.2	12.4	10.2	0.2	1.3	0.3	1.1	---	8.2	Steel+B
4	64.8	12.2	9.9	0.3	1.3	0.4	1.1	0.02	9.9	Steel+B
5	63.8	14.3	9.6	0.8	1.4	1.9	1.4	---	6.8	Steel+B

Fig.26. Microprobe integral analysis of the blocage fragments within elevation -13 mm

Russian Research Center "Kurchatov Institute", Institute of Nuclear Reactors

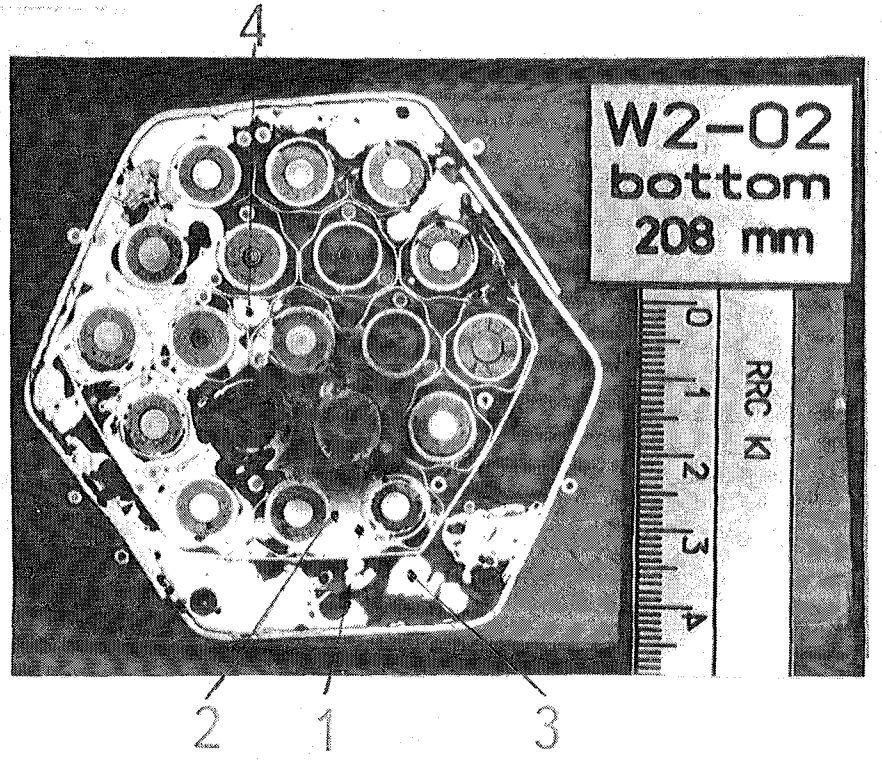

Pos.	Conc in at. %										Ratio of the elements
	Fe	Cr	Ni	Mn	Si	O	Mo	Zr	Re	B	
1	71.5	16.3	10.4	0.04	0.8	---	0.8	0.1	0.006	---	Steel
2	66.8	15.9	10.0	0.05	0.5	---	1.3	0.1	0.02	5.2	Steel+B
2*	71.0	12.4	11.2	---	0.5	0.5	0.3	---	---	4.1	Steel+B
2**	29.0	30.8	0.6	---	---	---	0.6	0.05	---	39.0	$(Fe,Cr,Ni)_3/B_2$
3	68.2	13.5	11.9	---	---	6.3	---	---	---	---	Steel
4	67.3	12.4	11.4	---	---	6.5	2.4	---	---	---	Steel

* grain - zond - 1 mcm
** grain boundary, zond - 10 mcm

Fig.27. Microprobe integral analysis of the blocage fragments within elevation 208 mm.

Russian Research Center "Kurchatov Institute", Institute of Nuclear Reactors

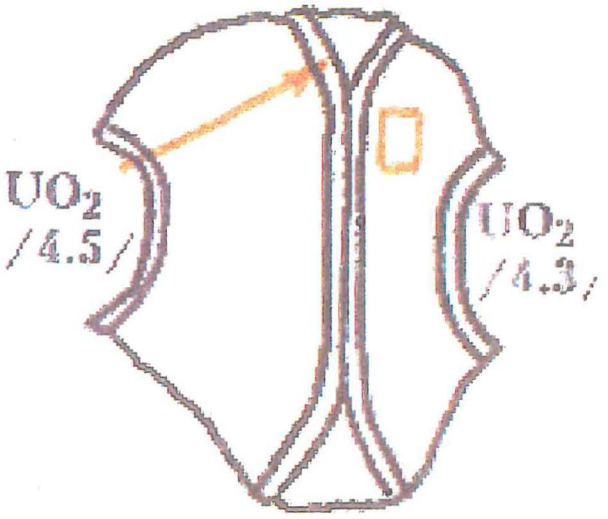

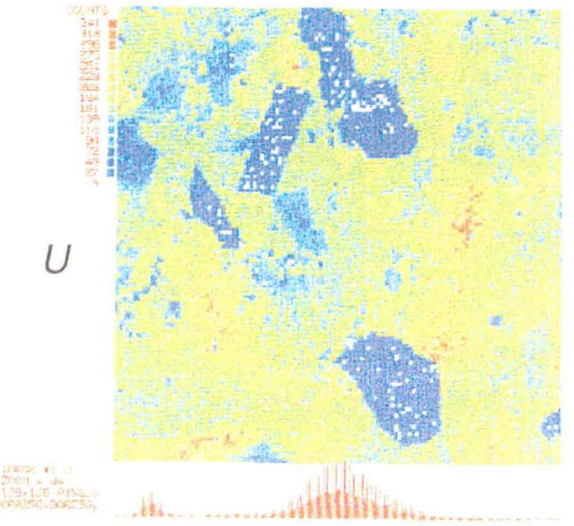

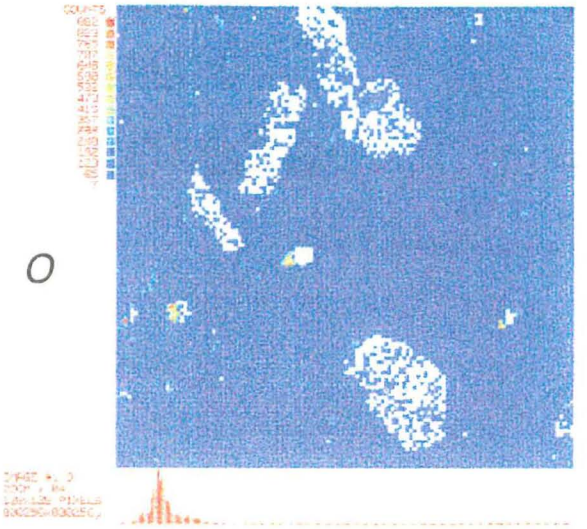

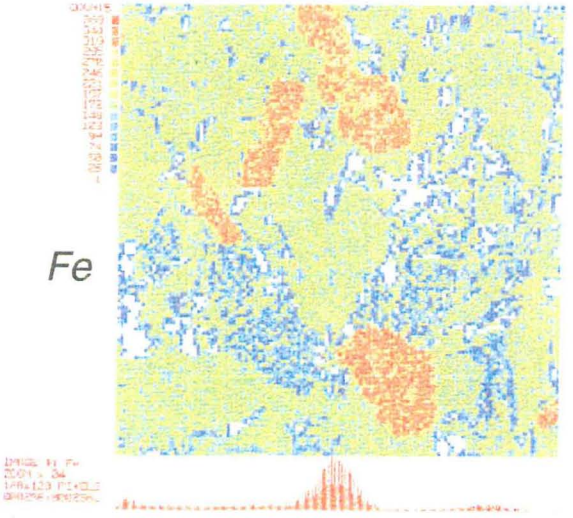

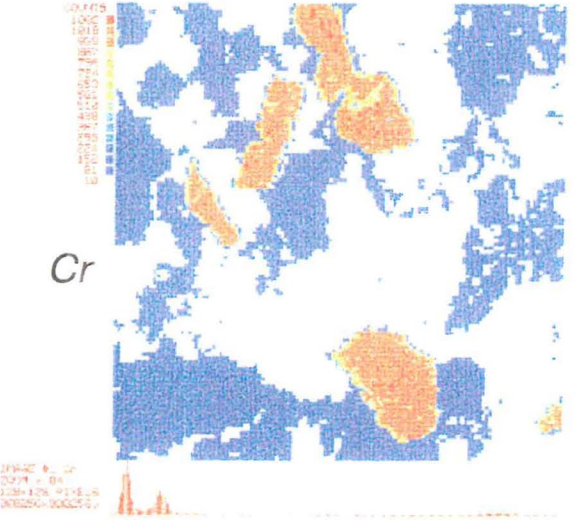

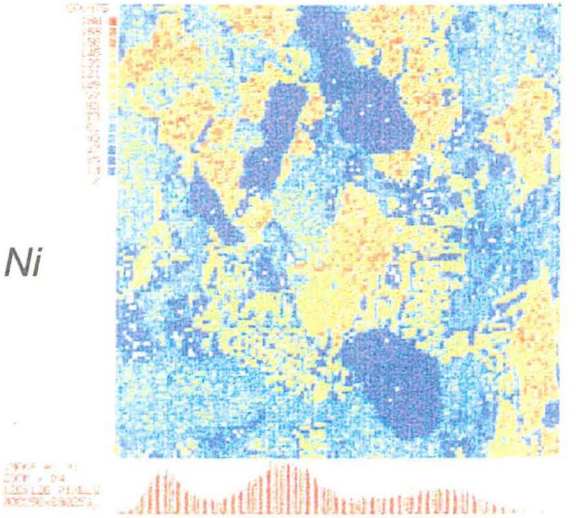

Fig.28: Quantitative Microprobe Analysis, point measurements into area 256x256 mcm

Russian Research Center "Kurchatov Institute", Institute of Nuclear Reactor

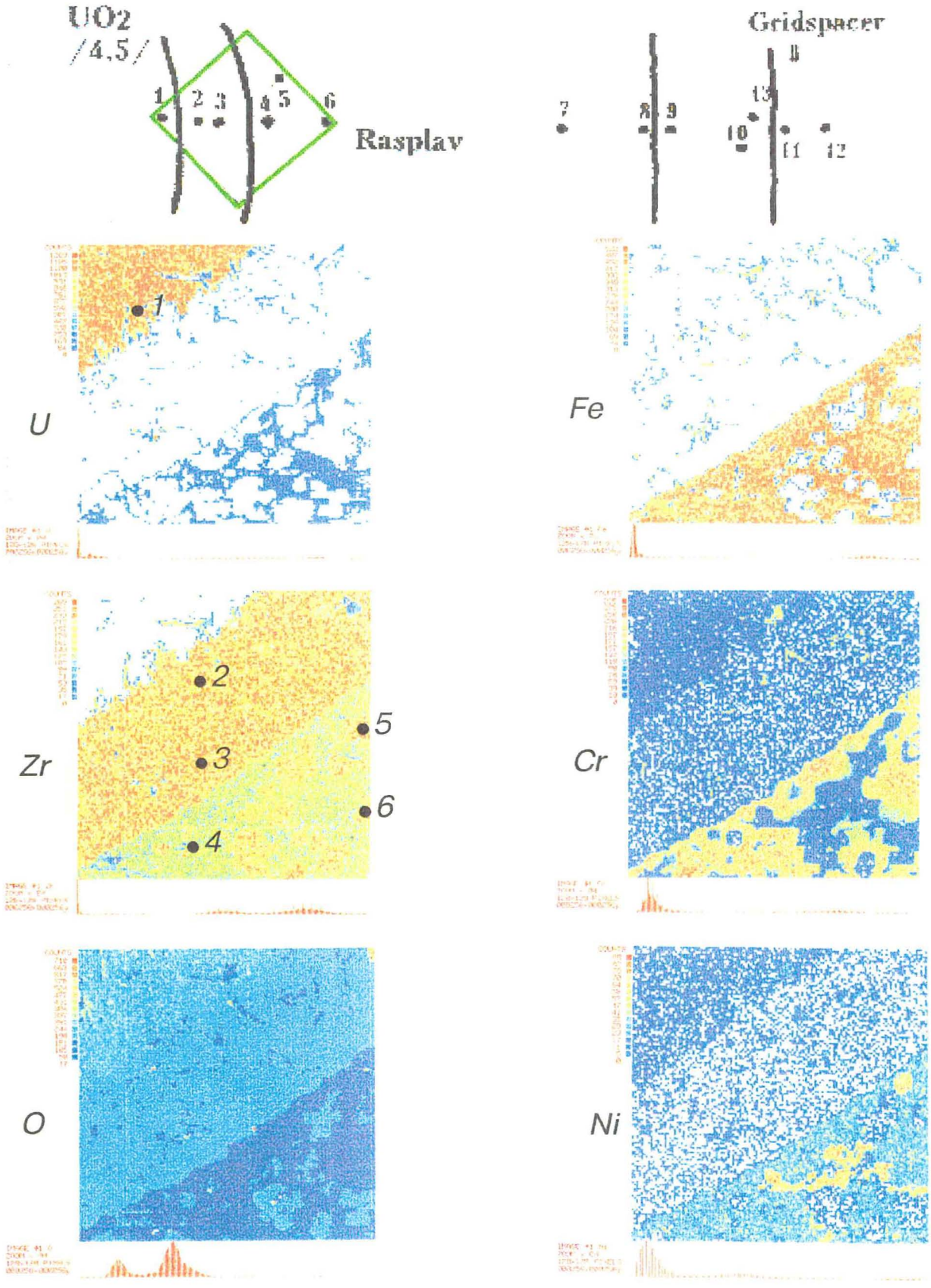

Fig.29: CORA-W2-02, ELEVATION 208 mm
Quantitative Microprobe Analysis, point measurements into area 256x256 mcm

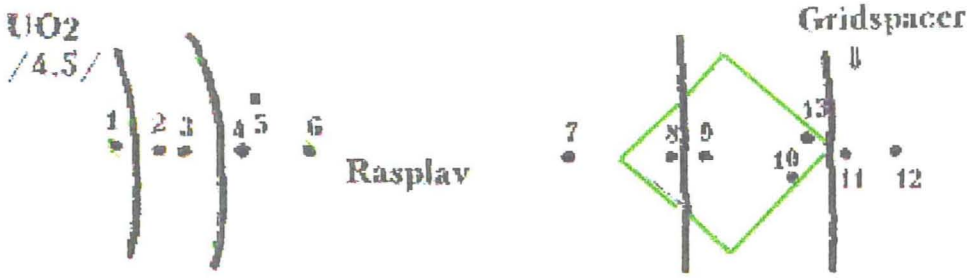

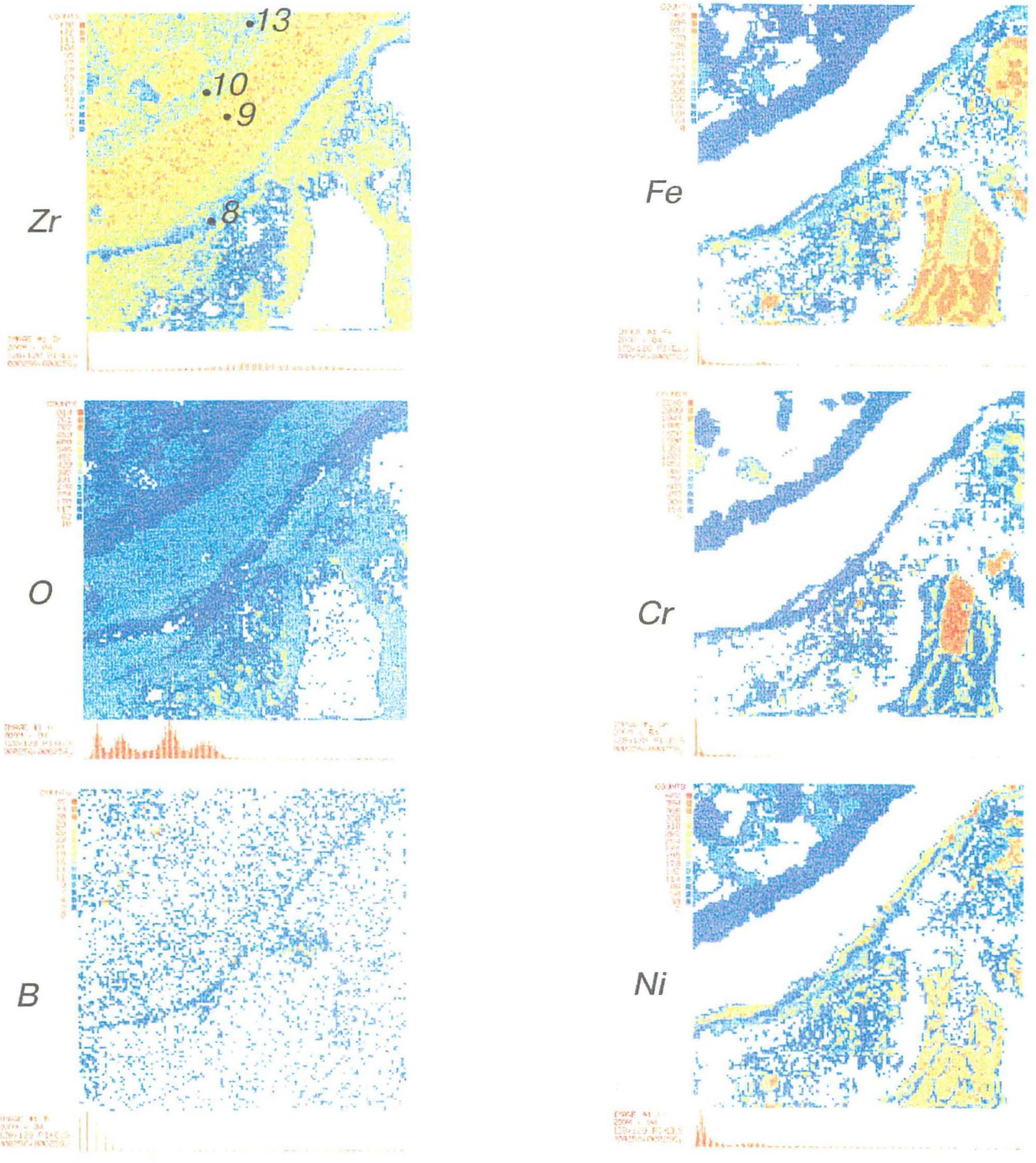

Fig.29 (cont.): CORA-W2-02, ELEVATION 208 mm
Quantitative Microprobe Analysis, point measurements into area 256x256 mcm

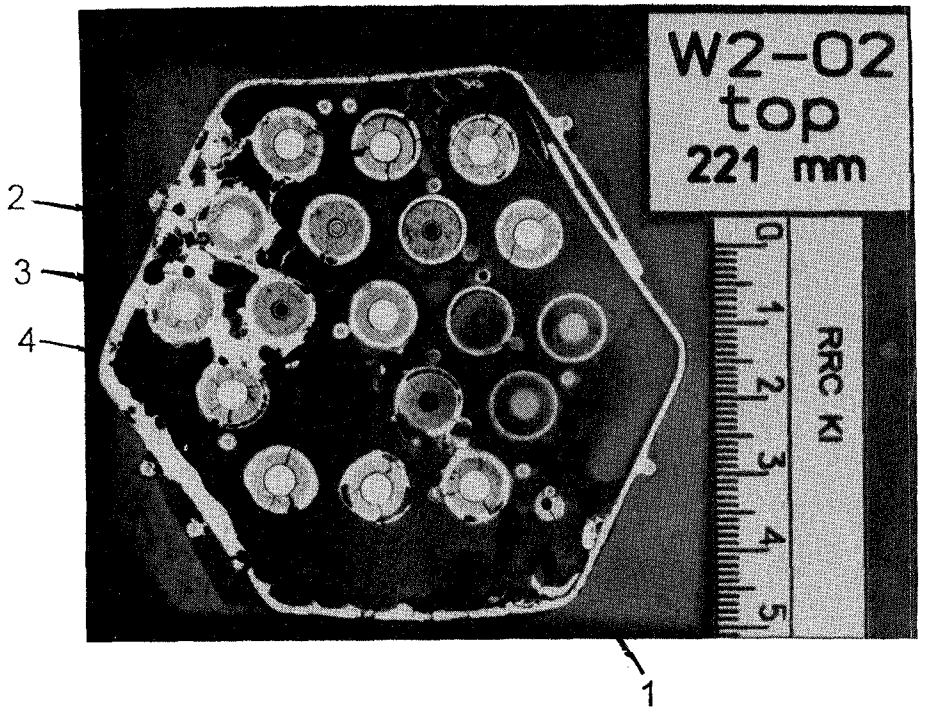

Pos.	Conc in at. %						Ratio of the elements
	Fe	Cr	Ni	O	Zr	U	
1	37.8	5.0	7.1	50	---	---	(Fe, Cr, Ni)/O
2	64.7	14.7	10.7	6.1	3.8	---	Steel
3	43.7	8.1	9.0	11.2	26.9	1.1	$(Fe, Cr, Ni)_2/Zr/O_{0.4}$
4	47.3	11.0	9.3	9.1	22.6	0.7	$(Fe, Cr, Ni)_3/Zr/O_{0.4}$

Fig.30. Microprobe integral analysis of the blocage fragments within elevation 221 mm

Microstructural Post-test-Investigation at the Elevations 327, 394, 511, 607, 726, 845 and 1083 mm.

A. Goryachev, Yu. Shtuckert, E. Zwir,
L. Stupina, V. Yakovlev

October, 1994

Research Institute of Atomic Reactors

Introduction

This chapter describes the results of post-test examination of the CORA-W2 bundle that has been fulfilled at RIAR. W2-03, W2-05, W2-06, W2-07, W2-09 cross-sections were subjected to metallographic investigations. Also the quantitative parameters of the core degradation have been measured on this cross-sections.

Only quantitative parameters have been measured on the W2-j and W2-h cross-sections, because the detailed metallographic investigations on neighbour to these cross-sections have been made at KfK and RIIM.

Core blockage measurements have been done on W2-k, W2-l and W2-m, cross-sections also the average oxide layers thickness has been measured on one half of the W2-e cross-section to clearify a picture of the blocage formation and the cladding oxidation. Below the obtained result are described.

Bundle elevation 327 mm

The cross-section W2-03 is shown in (Fig. 1). At this elevation the bundle is characterized by significant destruction of the fuel rod claddings. The cladding and guide tube of the absorber rod are completely melted and flowed down. The central part of the absorber rod in form of the pole consists of sintered powder, which may be observed inside the epoxy resin up to 511 mm elevation, is broken and abcent at this cross-section. Some amount of the relocated melt is accumulated in the space between the fuel rods. The shroud is significantly ballooned and slightly tilted with respect to the position of the fuel rods.

The fuel rod claddings are completely oxidized (Fig. 2). Outer ZrO_2 layers formed during solid state oxidation of the claddings followed by oxidized cladding melt reacted with the fuel pellet (Pos. 1,2). Flowing of the liquid (Zr,U)O melt led to deformation of the outer ZrO_2 layer and typical voids formation (Pos. 3). Small metallic inclusions inside the oxidized cladding material (Pos.4) and thin metallic layers formation are observed at several positions of the cross-section (Fig. 3 pos. 1 and 4) and attributed to the contamination of the (Zr,U)O melt by more oxidation resistant bundle materials such as SS components or TC shroud materials.

The residual relocated melt accumulated at this elevation shows different degree of oxidation (Fig. 3, Pos.2 and 3). Location of the not completely oxidized parts of the melt around the position of the melted absorber rod shows that the most probable reason for such oxidation resistance of the melt was its contamination by the SS components from the absorber rod cladding and guide tube. Such lightly oxidized parts of the melt must be in liquid state during heating stage of the test. It led to a strong interaction of the liquid melt with the oxide layers of the claddings (Fig. 4) , whereas dissolution of fuel pellets by such kind of the melt seems relatively low (Fig. 3, Pos.1 and 4; Fig. 4, Pos. 2).

Shroud oxidation led to formation of the oxide layers at the inner and outer surfaces. The outer oxide layer remained over the whole surface of the shroud, whereas the inner oxide layer is completely abcent at some positions (Fig. 5, Pos. 1 and 2). The abcence of the inner

oxide layer at some positions on the shroud may be refered to the effect of the inner oxide layer spalling of the metallic base (Pos. 1 and 3), that may lead to missing of the spalled parts of the inner oxide layer. The thickness of the residual inner oxide layers shows that oxidation of the shroud at the inner surface was more intensive than that at the outer one. The oxygen concentration in the remained metallic parts of the shroud is not uniform. In the different azimutal orientations the metallic layer microstructure changes from a-Zr(O) phase to the duplex a-Zr(O) + ZrO_2 structure (Pos. 4).

Strong degradation of the thermocouples as a result of their dissolution by the core materials melt is observed at this elevation (Fig. 6).

Bundle elevation 607 mm

Cross-section W2-05 is shown in (Fig. 7). At this elevation the bundle is characterized by severe damage of the fuel rod claddings, which remained only partially. The absorber rod and the spacer grid are completely absent. A great amount of the melt contains numerous metallic inclusions accumulated at this elevation of the bundle. The fuel pellets are significantly dissolved by the melt. Separated particles of oxidized core materials are observed at several locations of the cross-section. The shroud is ballooned. About one third of the shroud is missed.

The remained cladding fragments are completely oxidized. Two oxide layers and thin metallic layers were formed during the claddings oxidation, as it has already been described for the cross-section W2-03 (Fig.8, Pos.2 and 4). The SEM WDX examinations of the formed phases element contents have prooved, that the metallic layers on the surface of the fuel pellets were formed due to contamination of the fuel-cladding melt by the SS components (Fig. 9, Tabl. 1).

The relocated melt oxidation changes from the completely oxidized parts (Fig. 10, Pos 1) to the duplex structure (Fig.8, Pos. 1,3,5; Fig 10, Pos. 2-4).The metallic parts of the melt contain a significant amount of the SS components (Fig. 9. Tabl. 1), whereas the oxidized part of the melt consists mainly of the oxidized Zr-U alloy. Therefore, the availability of a relatively great amount of the metallic melt at this elevation may be attributed to the uptake of the SS components by the melt from the melted grid spacer. The small metallic inclusions in the almost completely oxidized parts of the melt may be also attributed to the contamination of the (Zr,U)O melt by the SS components (Fig.11, Pos. 1-3). In this figure positions 4 and 5 show the separated particles consists of the oxidized layers of the cladding and the melt. The partially oxidized melt dissolved both the oxidized claddings and the fuel pellets (Fig. 12, Pos. 1,2). A great amount of the trapped melt seems to be the main reason of the severe cladding and fuel pellet degradation at this elevation of the bundle.

The state of the residual shroud is very similar to that of the cross-section W2-03.

Bundle elevation 726 mm

Cross-section W2-06 is shown in (Fig. 13). At this elevation a strong oxidation of the bundle material is observed. Only a little quantity of small metallic inclusions remained. These inclusions look like the SS droplets of the melted absorber rod or the residual parts of the thermocouples (Fig. 14, Pos. 1 and 3; Fig. 16, Pos 1). Small remnant of the B_4C powder is retained at this cross-section (Fig. 13,Pos. 1 and 4). The fuel rod remnants of the first ring moved from the initial position and show a very strong degradation of the claddings and fuel pellets together with the neighbouring fuel rods of the second ring (Fig. 15, Pos. 1-4), whereas some fuel rods of the second ring remained relatively intact (Fig. 16). At these positions the typycal oxide layers are formed.

Insignificant amount of the melt retained at this elevation. The fuel rod claddings and the retained melt are completely oxidized, except of the above mentioned small metallic droplets.

Only a small remnant of the shroud is retained at this cross-section. However, it was found not entirely oxidized (Fig. 17). A thin metallic layer of the shroud consists of the a-Zr(O) + ZrO_2 phase (Pos. 1). Also small metallic inclusions were found in the oxidized part of the shroud (Pos. 2).

Bundle elevation 845 mm

Cross-section W2-07 is shown in the (Fig. 18). The state of this cross-section is very similar to that of above cross-section W2-06, with an exception that no absorber materials and shroud remnants were find. Only thin oxidized films around the cross-section were identified as the spalled shroud oxide layers. Also, more metallic inclusions were found at this cross-section, that were identified as the SS melt sprayed from the melted absorber rod. The microstructure of these SS droplets and some typical microstructures of the oxide layers and relocated melt are shown in (Fig. 19-21).

Bundle elevation 1085 mm.

Cross-section W2-09 (Fig. 22) is situated above the upper end of the heated rods fuel stack and the upper end of the W heaters. Only five unheated fuel rods represent real reactor core materials. The claddings of these rods is completely failed and missed. Only a small amount of the oxidized melt retained on the surface of fuel pellets (Fig.23, Pos. 1). Some of the melt remnants contain metallic inclusions (Pos. 2), which are most probably molibdenium inclusions. The heated rod claddings show a formation of the outer zirconia layers (Fig. 24, Pos. 1) followed by once molten layers, that create eutectic with Mo-electrodes (Pos. 2 and 3). Such melted eutectic layers may serve as a source of the molybdenum-rich droplets for the lower parts of the bundle.

A small remnant of the shroud is not completely oxidized. A typical a-Zr(O) + ZrO_2 microstructure of this shroud remnant is shown in (Fig. 25).

Quantitative results of the bundle degradation parameters measurements

In order to ensure the possibility of the comparison of the calculated core degradation parameters with the real state of the tested bundle, some parameters have been measured on the bundle cross-sections under examination. Quantitative parameters of the bundle degradation have been evaluated by digital image processing of the bundle cross-sections.

Core blockage formation

To evaluate the core blockage formation, all areas of the core materials have been measured on each of the tested cross-sections. Materials, that were identified as belonging to the shroud, were not taken into account. The total area of the core materials is listed in the (Table 2). These data reflect an area occupied by the solid core materials at the bundle cross-sections. However, the cross-sectional area available for the vapour flow, that may be calculated using these data, might be overestimated, because of the materials porosity was not taken into account. Some of the pores, that may be seen on the cross-section, may appear to be closed pores inside the material and their cross-sections are not available for the heat transfer flow. Because of this assumption, additional calculations have been made. In this case the area of pores, which look like closed in the cross-section, i.e. have no visible leakage to the area among the fuel rods, have been added to the measured core materials area. The resulting data is also listed in the (Table 2). Obviously, these data are conservative for the free cross-sectional area calculation. The real value should be somwhere between the described data.

Fuel pellets degradation

In order to evaluate the final distribution of the uranium along the bundle the fuel pellet remnants cross-sectional area have been measured on each of the tested cross-sections. The results are listed in (Table 3).

ZrO_2 axial distribution

The measured areas of the zirconia layers formed on the fuel rod claddings during solid state oxidation are listed in (Table 4). It should be taken into account, that only zirconia layers retained in the cross-section and their retained fragments have been measured, so these data reflect only final distribution of the material.

Cladding oxidation profile

In order to evaluate the zirconia layer thickness formed during solid-state oxidation of the claddings the thickness of the cladding zirconia layers or their remnants were calculated as a ratio of the measured object area to a half of its perimeter. As a result the average thickness of each measured layer or fragment have been obtained. The results is not sensitive to the missing of some parts of the oxide layers from the fuel rod claddings, but possible thinning of the oxide layers as a result of their partial dissolution by the cladding metallic melt may be a sourse of error. The zirconia layer thickness of the claddings are listed in (Table 5).

Relocated core melt distribution

The cross-sectional area of the melted materials, that have not been definitely attributed to any of initial materials of the bundle and consists usually of the complex mixture of the core materials have been measured in oder to evaluate the core blockage formation and final core materials redistribution. The results are listed in (Table 6). The cross-sectional areas of the metallic and oxidized phases of this "undefined melt" are listed separetely. In the case the measured phase was a mixture of the ceramic and metallic grains, its area was divided between the oxidized and metallic phases of the melt by image processing of the microstructure.

Absorber material redistribution

The absorber material remnants were observed in three of seven tested cross-sections. Above the core elevation 511 mm the boron carbide remained in form of the small remnants of sintered powder glued to the fuel rods by the solidified SS droplets. Results of the absorber material cross-sectional area measurements are listed in (Table 7).

Constructive elements cross-sectional area measurements

Additionally to the core materials cross-sectional area measurements the cross-sectional areas of the W-heaters and termocouple remnants have been made. These data were used for the core blockage calculations. The results are listed in the (Tables 8 and 9).

Summary

At the examined elevations the fuel rod claddings are completely oxidized. Two partial oxide layers have formed: outer oxide layer corresponds to solid state oxidation and internal one corresponds to oxidation of the liquid cladding material with dissolved UO2.

Before the cladding material was completely oxidized it had dissolved some part of the fuel pellets. No other mechanisms of fuel pellets damaging were found.

Stainless steel structural elements of the bundle have completely disappeared at the examined cross sections. Only small remnants of the stainless steel remained in form of droplets inside the core materials melt.

B4C partially remained in form of poles consisting of sintered powder up to elevation 511 mm. This shows that the mechanism of B4C disintegration at the upper elevations may be different with its sole dissolution by the SS cladding and guide tube melt.

Core materials melt relocation led to local core blockage formation at the position of the upper spacer grid.

List of figures:

List of tables:

Table 1. SEM/WDX results of the reacted materials composition measurements

Element		Zr	U	Fe	Cr	Ni	Nb	Mo
Line		L	M	K	K	K	L	L
Pos.	Phase	wt(%)						
1.1	Metallic inclusions		15.3	35	8.3	4.7	20.7	16
1.2	Inner oxidized part	77.7	23.3					
1.3	Outer oxidized part	100						
2	Oxidized melt	57.2	42.8					
3	Oxidized melt	51.3	48.7					
4	Oxidized melt	47.9	52.1					
5	Oxidized melt	49.3	50.7					
6	Oxidized melt	52.6	47.4					
7	Oxidized melt	77.4	21.3	~0.7	~0.3			
8	Oxidized melt	43.5	56.5					
9.1	Metallic part of the melt	66.1	12.2	10.3	3.2	1.7	2.7	
9.2	Oxidized part of the melt	81.4	18.6					

Table 2. Blockage formation

Bundle Elevation (mm)	Cross-section	Core materials area Sm, (mm*mm)	Blockage (Sm-So)/(Ssh-So) *100%	Core materials area including closed pores area Sm+p, (mm*mm)	Blockage (Sm+p-So)/(Ssh-So) *100%
327	W2-03	1256	-0.7	1574	12.0
394	W2h	1112	-6.4	1305	1.3
511	W2j	1129	-5.8	1330	2.3
565	W2k	1433	6.4	1577	12.2
607	W2-05	1431	6.3	1737	18.6
622	W2l	1383	4.4	1486	8.5
674	W2m	1174	-4.0	1261	-0.5
726	W2-06	1104	-6.8	1290	0.7
845	W2-07	1186	-3.5	1426	6.1
1083	W2-09	812	-18.4	1060	-8.5

Area inside the shroud Ssh=3772 mm*mm

Initial cross-section of the fuel and absorber rods So=1273 mm*mm

Table 3. UO2 remnants cross-sectional area

Cross-section	Bundle Elevation (mm)	UO2 remnants area at the fuel rods, (mm*mm)																		
			2.0	2.2	2.4	2.6	3.0													total
W2-03	327	21.1	34.6	38.1	36.3	35.6	36.4	24.9	28.5	27.2	29.9	24.5	27.7	28.2	27.7	28.2	30.1	26.8	26.9	533
W2h	394	29.3	35.1	34.8	34.3	33.6	30.4	27.6	26.5	30.6	29.0	30.2	29.0	26.5	30.1	28.0	28.4	27.7	27.8	539
W2j	511	28.2	34.0	25.1	34.2	35.4	32.0	23.8	26.9	28.7	26.2	30.1	30.2	31.4	29.8	29.0	27.9	27.6	26.2	527
W2-05	607	27.4	31.2	32.2	19.6	30.3	34.6	26.8	27.5	28.7	29.7	30.0	17.3	31.4	29.5	17.7	28.7	28.7	27.0	498
W2-06	726	29.6	38.2	36.1	4.7	32.2	37.9	28.2	27.1	26.1	21.5	29.8	29.7	27.9	29.7	30.2	31.0	29.6	28.7	518
W2-07	845	30.0	36.9	34.5	38.0	28.0	38.1	21.1	22.5	24.1	20.8	26.0	26.5	24.6	27.1	26.1	28.0	27.6	31.0	511
W2-09	1083		33.9	27.9	30.6	33.6	38.4													164

Table 4. ZrO2 layers cross-sectional area

Cross-section	Bundle Elevation (mm)	ZrO2 area at the fuel rods, (mm*mm)																		
		1.8	2.0	2.2	2.4	2.6	3.0	3.1	3.3	3.5	3.7	3.9								total
W2-03	327	7.2	3.0	7.7	8.6	7.3	8.1	6.2	9.8	6.9	10.1	11.3	10.6	5.7	3.6		10.9	5.6		122.5
W2h	394		3.2	1.9	6.9	2.1		8.0	2.3	3.2	5.8	9.6	5.8	5.4			7.9	8.5		70.8
W2j	511				1.9				2.3	7.3	6.8		7.4	11.7	9.7	7.3	4.3	6.8	2.9	68.5
W2-05	607	4.7			1.8	3.4	0.9	4.4	3.5	5.1	4.3		1.5	1.5	2.6	3.6	2.5	2.0		41.9
W2-06	726	3.4	4.1	4.3				9.7	7.7	9.3	12.6	9.2	6.4	2.5	3.3	3.8	3.3		8.4	88.1
W2-07	845	7.4	5.5	8.1			2.9	7.3	6.9	10.3	7.5	5.1	5.4	5.5	4.4	4.3		2.3	7.9	91.0
W2-09	1083		2.1				1.0													3.0

Table 5. Average thickness of the ZrO2 layers

Cross-section	Bundle Elevation (mm)	ZrO2 thickness at the fuel rods, (μm)																		
			2.0	2.2	2.4	2.6	3.0													average
W2-03	327	325	202	268	246	365	263	270	297	229	324	429	393	320	263		336	227		297
W2h	394		391	322	282	247		412	253	205	293	281	328	277			310	305		300
W2j	511								283	351	269		351	476	404	355	340	297	278	340
W2-05	607	309.9			234.4	288		330.4		251.8	231		187	207.2	203	238	194	228		242
W2-06	726		349.5	212.4				366.7	266.3	278.9	388	265.1	240	193.2	203	387	233		336	288
W2-07	845	354.6	221	343.2			293	266.1	256.6	309.5	351	260.9	252	231.1	285	345			284	289
W2-09	1083		196				181													189

Table 6. Oxidation of the core relocated melt and shroud

Cross-section	Bundle Elevation (mm)	Relocated melt area, (mm*mm)			Shroud area, (mm*mm)		
		Ox phase	Me phase	Total	ZrO2	aZr(O)	Total
W2-03	327	355.8	55.7	411.5	366.7	196.9	563.6
W2h	394	284.3	21.8	306.1	631.3	90.5	721.8
W2j	511	308.6	21.6	330.2	436.6	64.7	501.4
W2-05	607	661.3	71.4	732.7	387.9	48.9	436.8
W2-06	726	264.4	5.5	269.9	-	-	-
W2-07	845	328.1	71.8	399.9	18.5	-	18.5
W2-09	1083	269.4	1.8	271.2	-	-	-

Table 7. B4C area measurement results

Cross-section	W2-03	W2h	W2j	W2-05	W2-06	W2-07	W2-09
Bundle elevation (mm)	327	394	511	607	726	845	1083
B4C area (mm*mm)	-	18.2	40.5	-	17.9	-	-

Table 8. Thermocouple area measurement results

Cross-section	W2-03	W2h	W2j	W2-05	W2-06	W2-07	W2-09
Bundle elevation (mm)	327	394	511	607	726	845	1083
TC area (mm*mm)	16.1	22.6	11.4	5.5	0.5	2.6	12.1

Table 9. W-heaters area measurement results.

Cross-section	Bundle Elevation (mm)	Heater area in the fuel rod (mm*mm)													
		1.1	3.1	3.3	3.5	3.7	3.9	4.1	4.3	4.5	4.7	4.9	5.1	5.3	total
W2-03	327	12.8	11.4	11.5	11.3	11.6	10.2	11.8	11.5	11.3	11.5	12.3	12.1	12.1	151
W2h	394	11.1	11.8	11.6	11.5	11.5	10.7	12.2	11.7	12.1	10.7	12.4	11.4	11.9	150
W2j	511	11.8	12.1	11.8	11.8	11.8	11.7	11.5	11.7	11.0	11.6	11.5	11.7	11.8	152
W2-05	607	11.4	12.1	12.5	12.4	12.6	12.3	9.3	11.8	11.8	11.3	11.1	12.3	11.9	153
W2-06	726	12.2	11.8	11.9	11.5	11.7	12.0	12.1	11.8	11.6	12.1	11.8	11.7	11.6	154
W2-07	845	12.8	11.9	12.4	11.8	13.0	11.9	12.2	12.0	11.5	11.5	12.4	11.7	12.3	157
	1083	30.4	31.4	29.0	34.9	26.9	32.2	24.4	30.2	13.8	24.8	25.8	30.7	26.4	361

-W heaters

-Mo electrodes

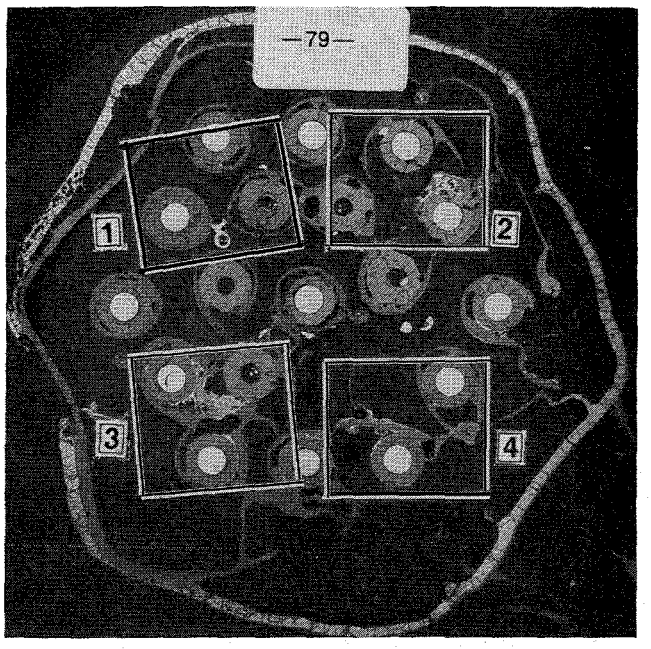

Position 1

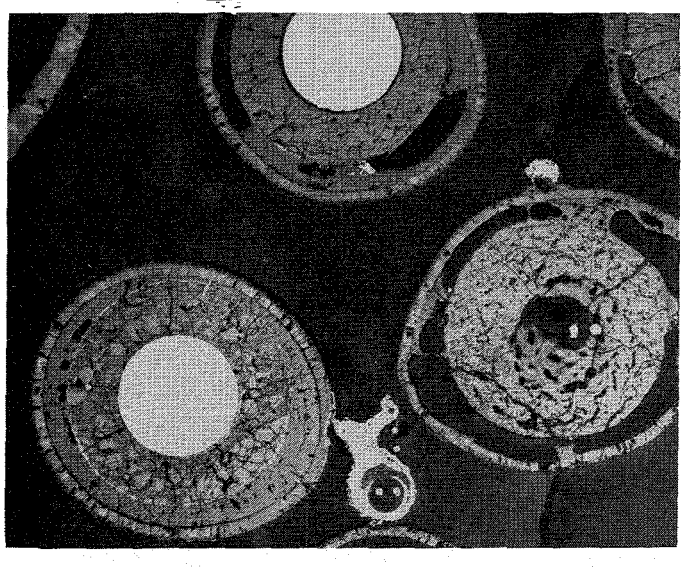

Position 2

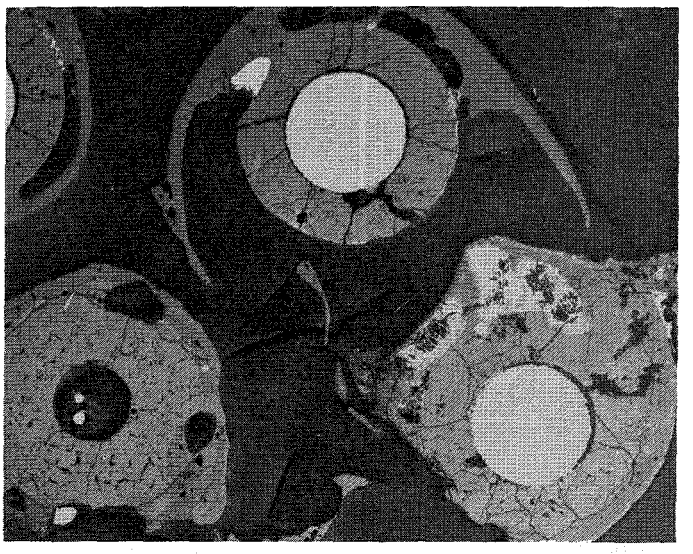

Position 3

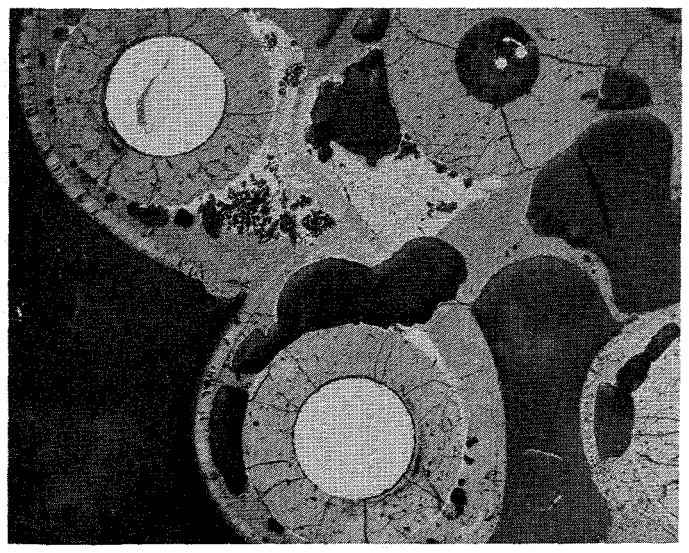

Position 4

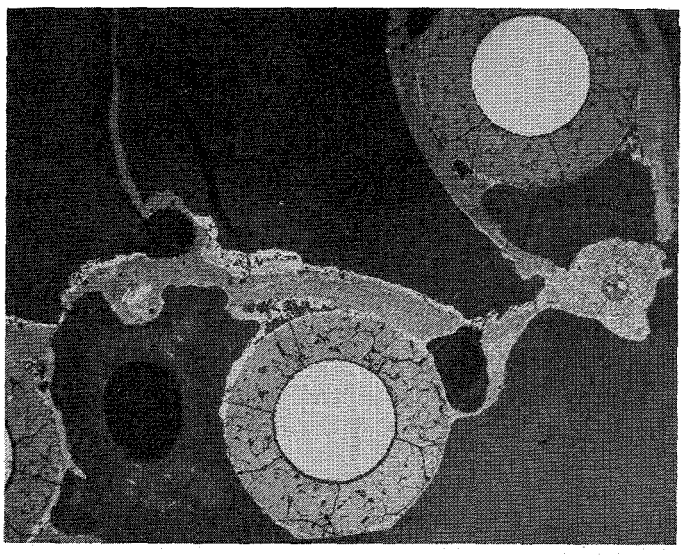

Fig.1. Cross-section W2-03 (bottom view). Elevation 327mm.

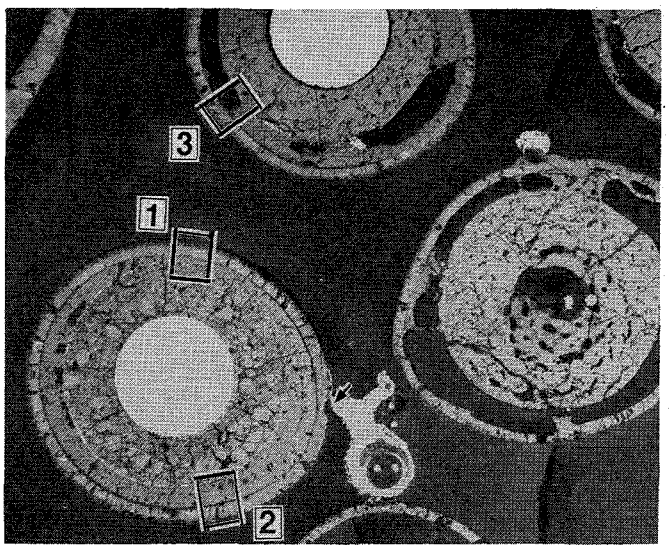

Position 1

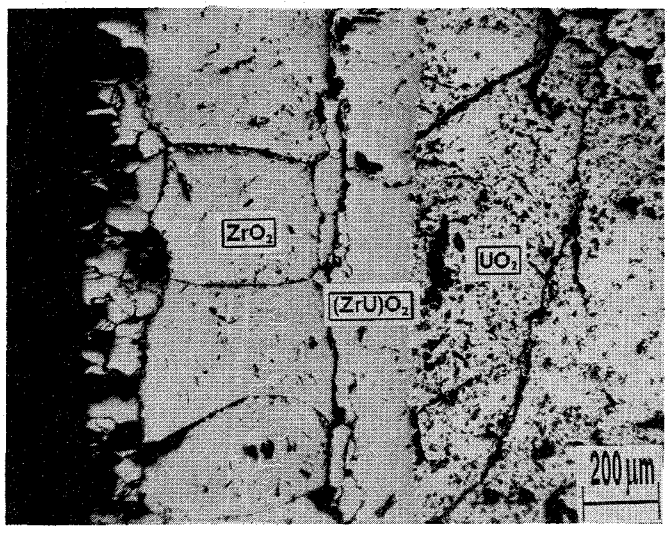

Position 2

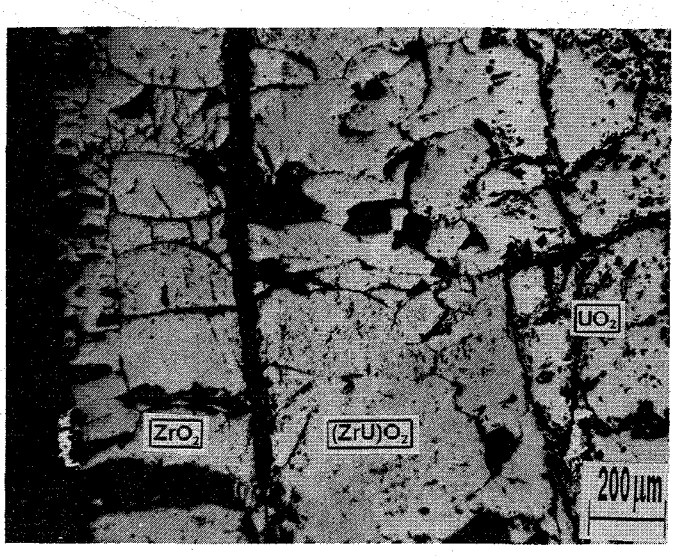

Position 3

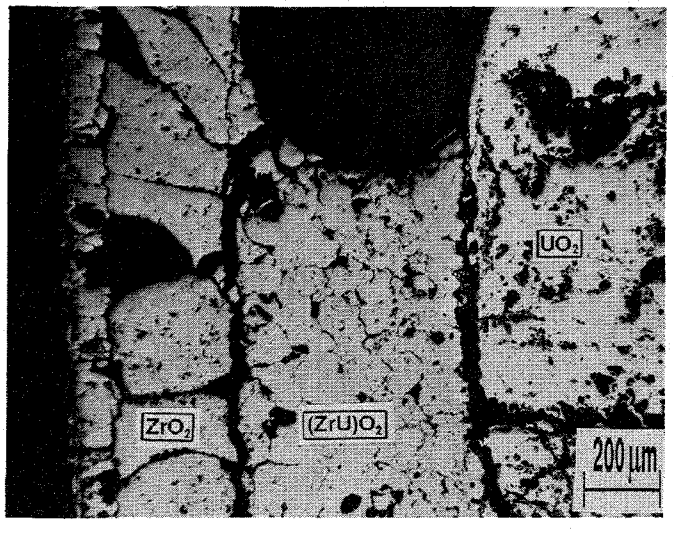

Position 4

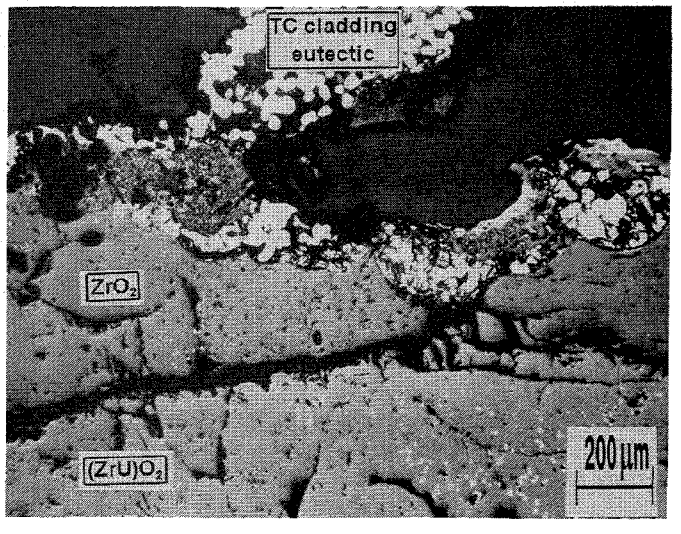

Fig.2. Cross section W2-03.
ZrO_2 and $(Zr,U)O_2$ layers formation.

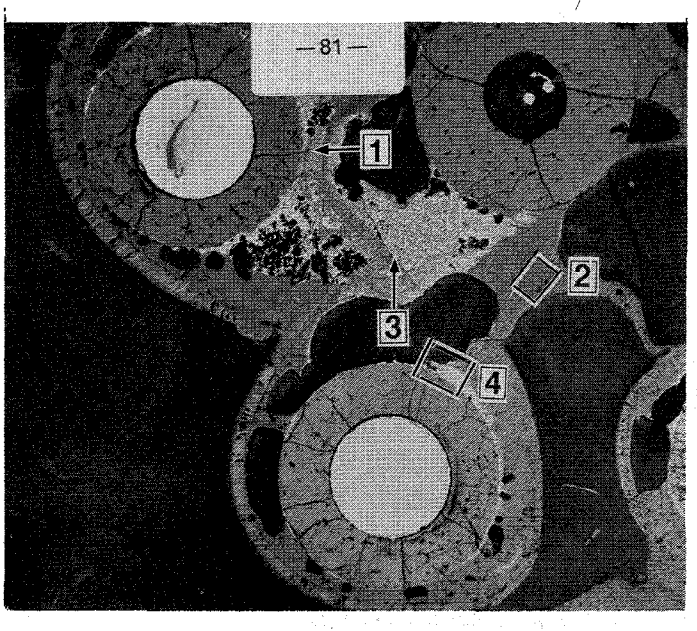

Position 1

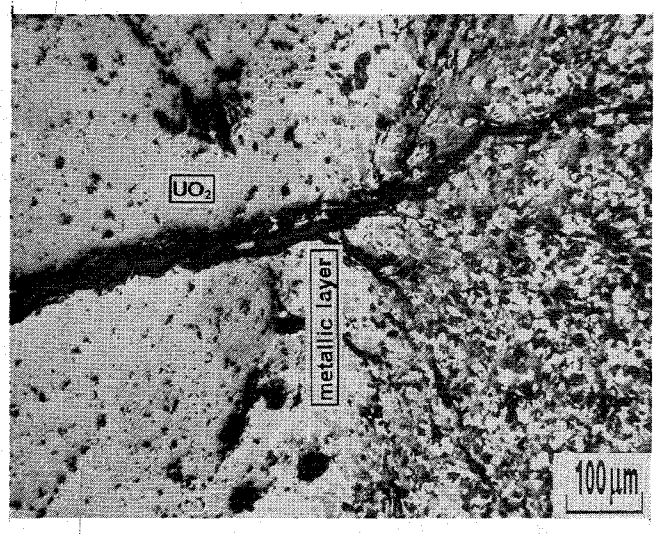

Position 2

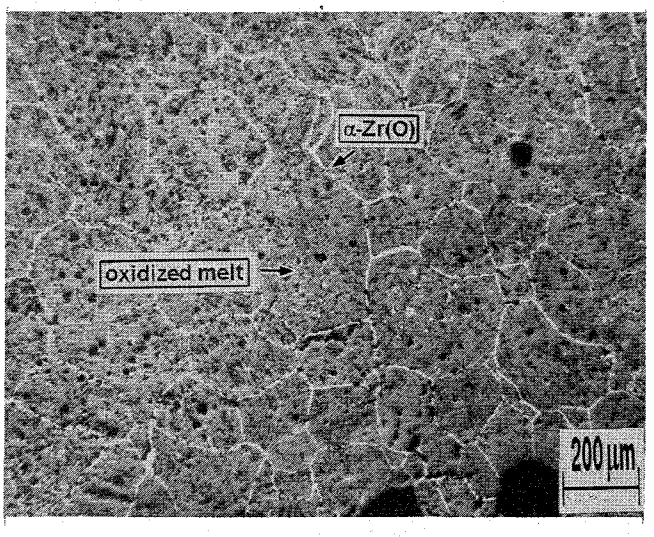

Position 3

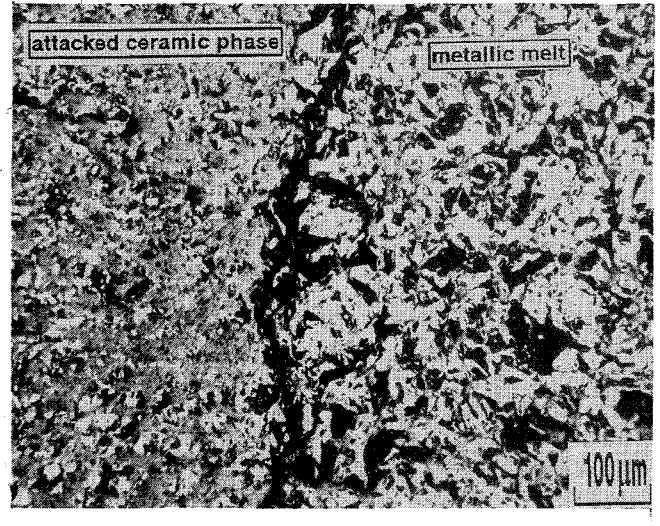

Position 4

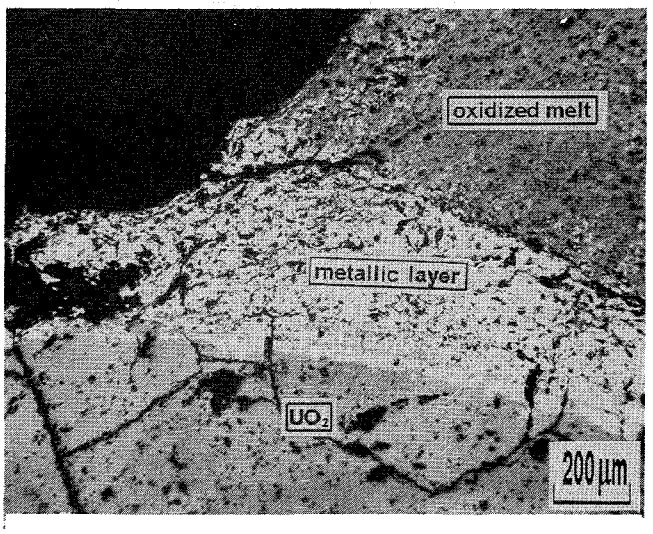

Fig.3. Cross section W2-03. Oxidation of the relocated Melt. Formation of the thin metallic layers on the fuel-cladding boundaries.

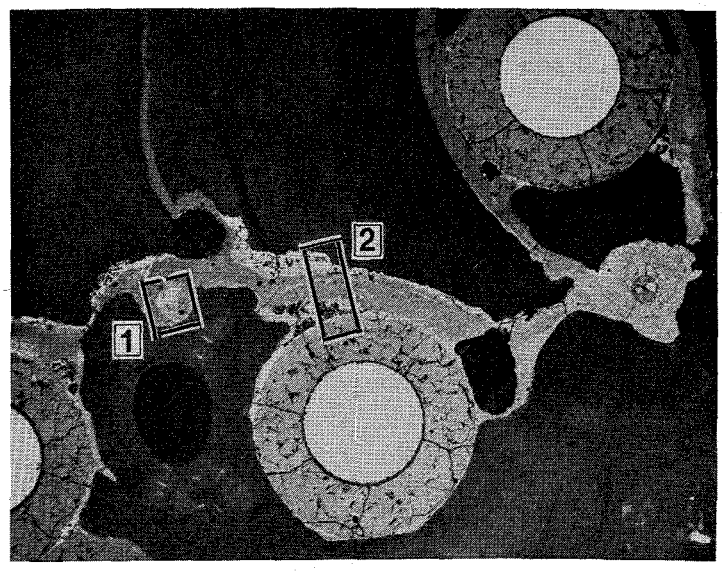

Position 1

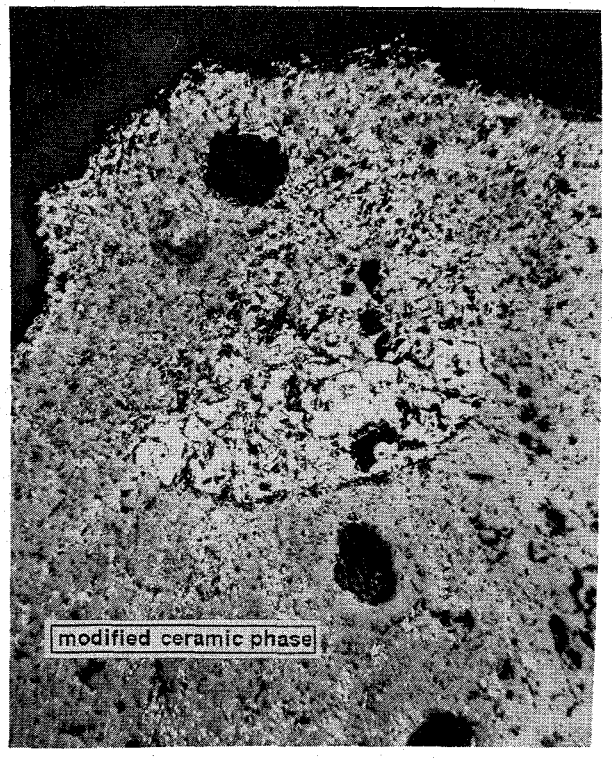

Position 2

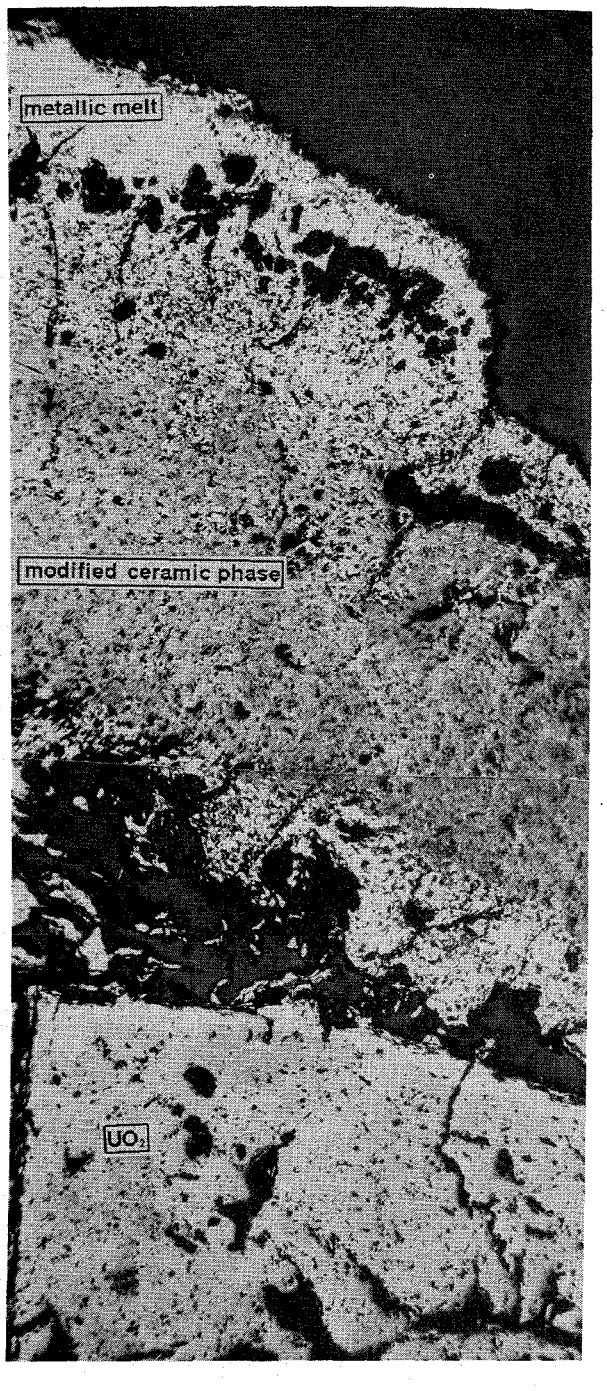

Fig.4. Cross section W2-03. Interaction of the metallic melt with the oxidized cladding.

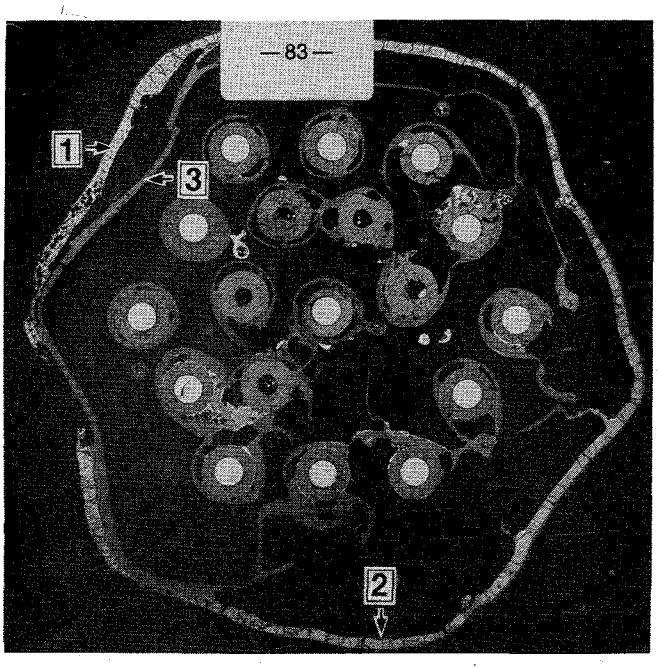

Position 1

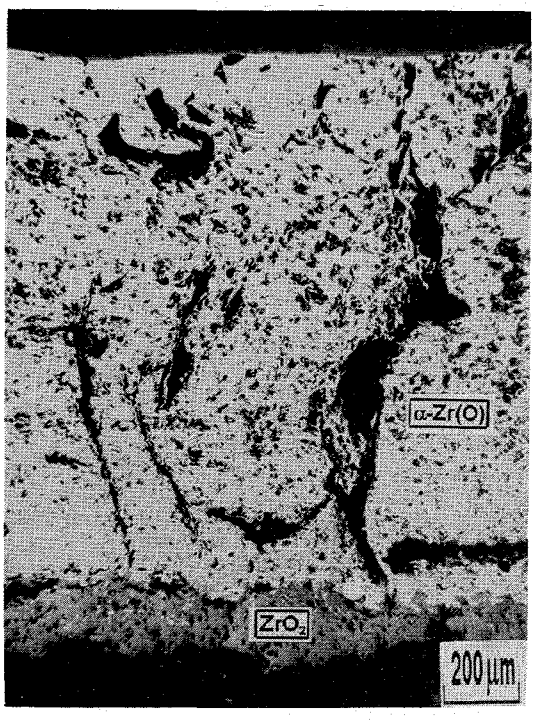

Position 2

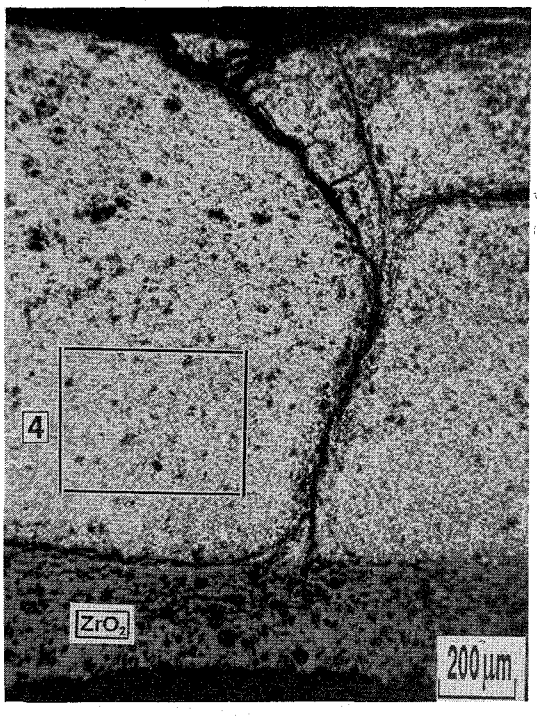

Position 3

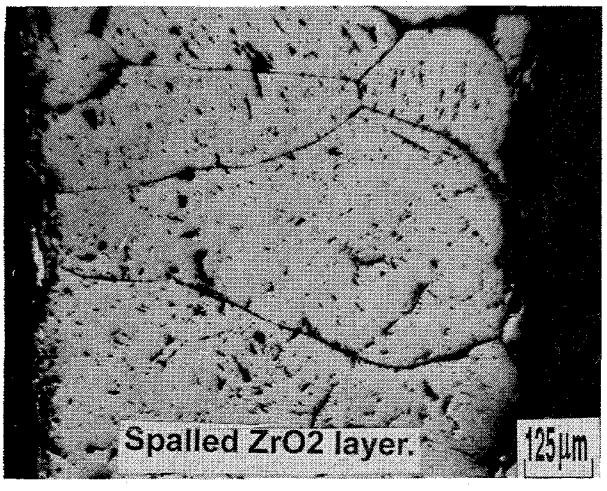

Position 4

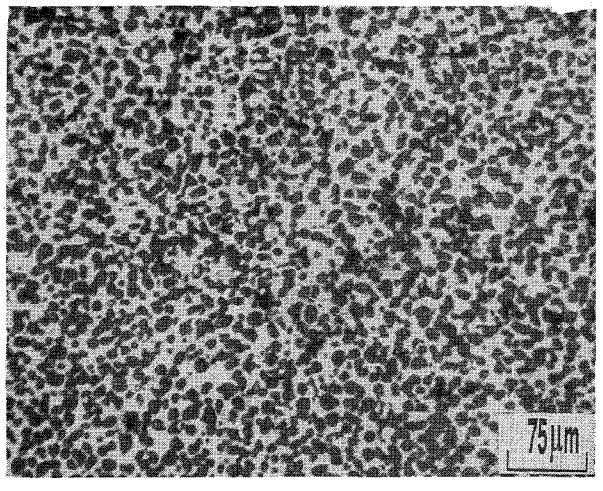

Fig.5. Cross section W2-03. Oxidation of the shroud.

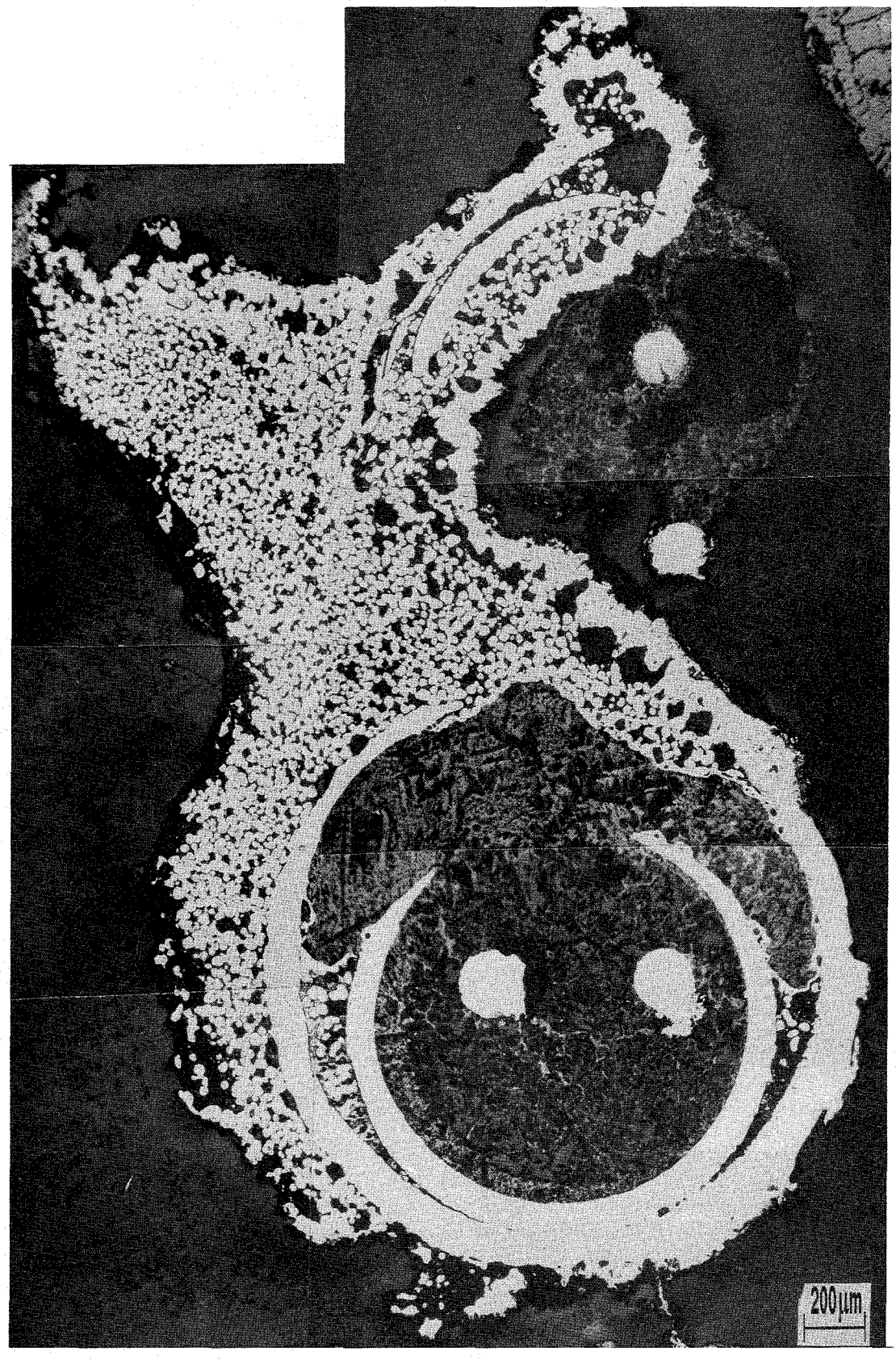

Fig.6. TC shroud dissolution by the melt.

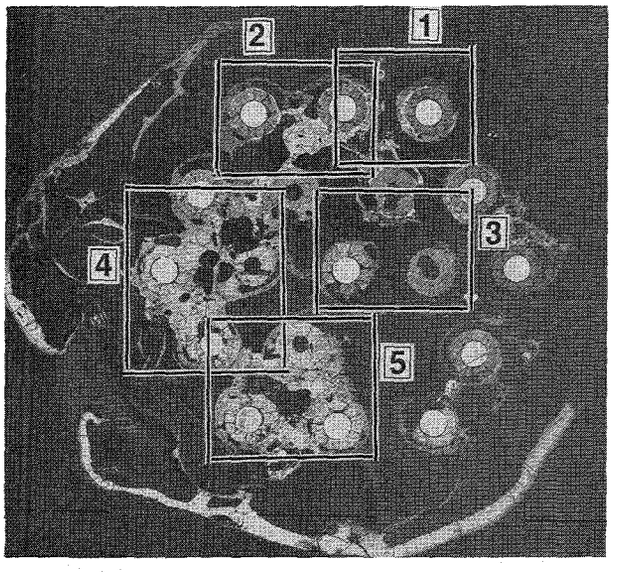

Position 1

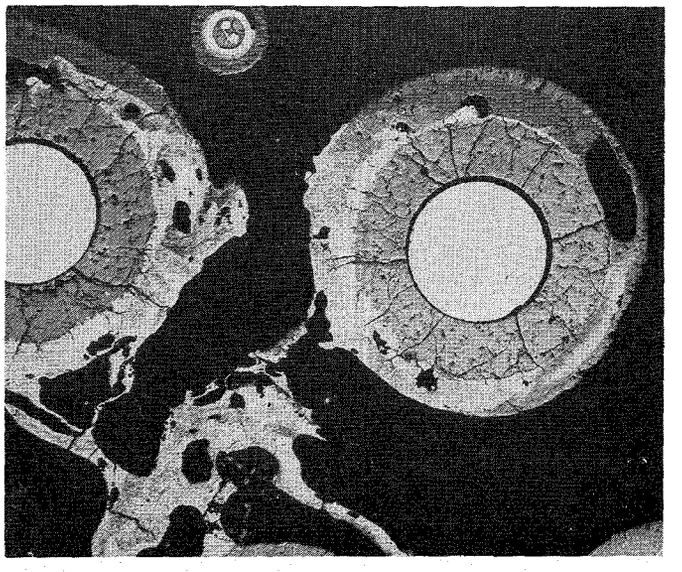

Position 2

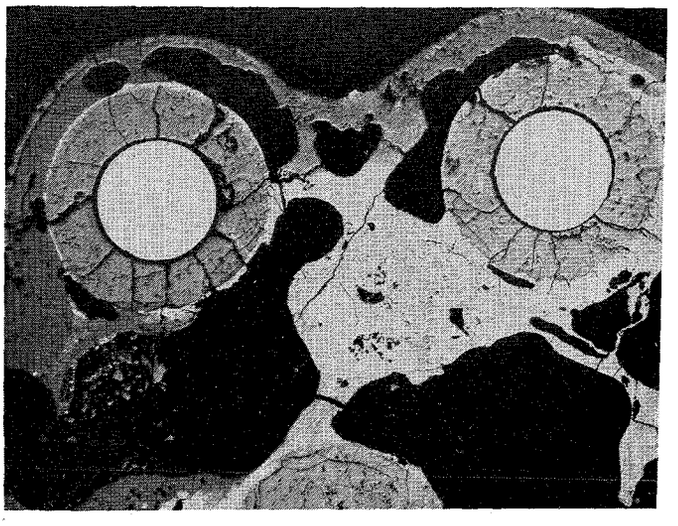

Position 3

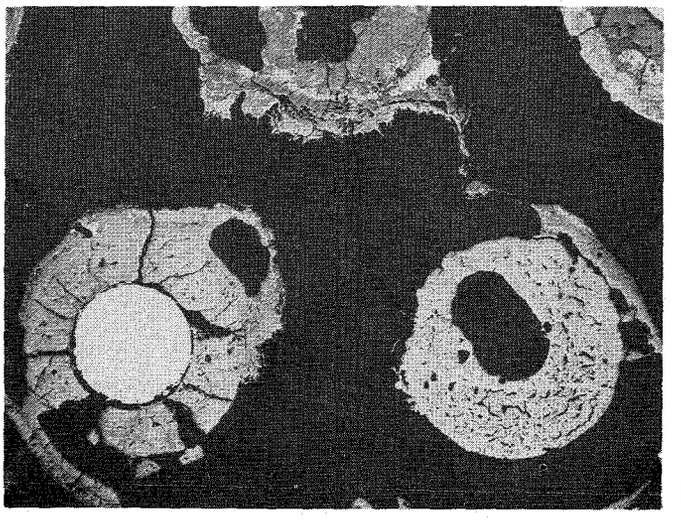

Position 4

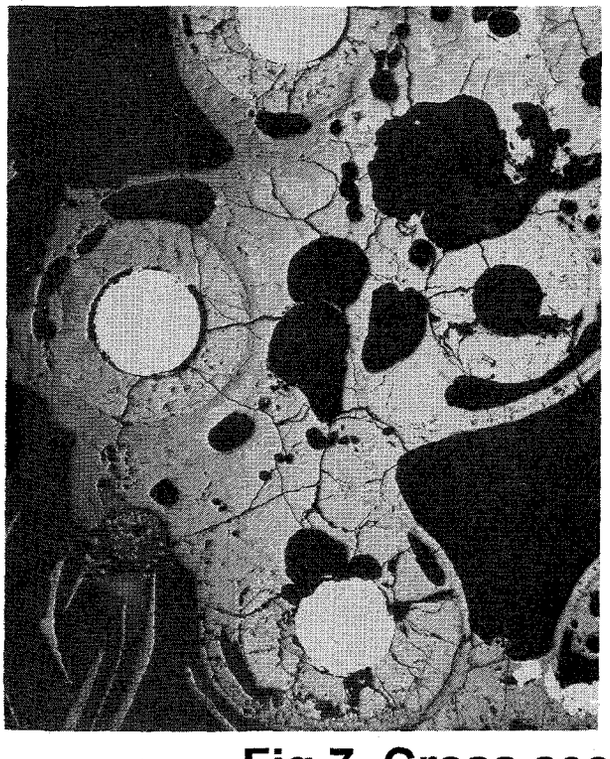

Position 5

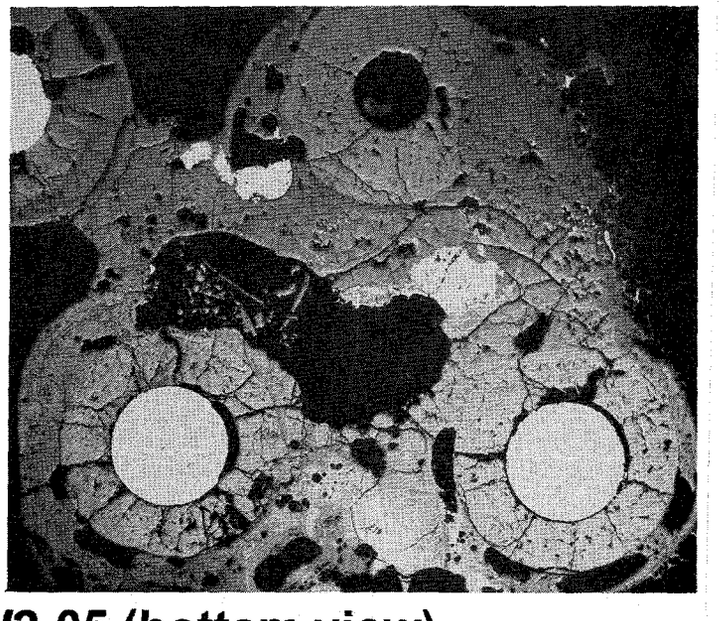

Fig.7. Cross section W2-05 (bottom view). Elevation 607 mm.

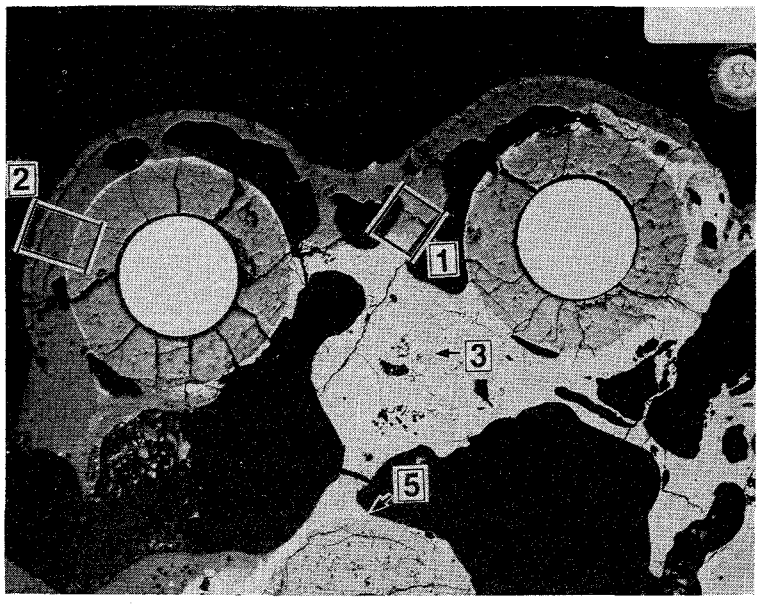

Position 1

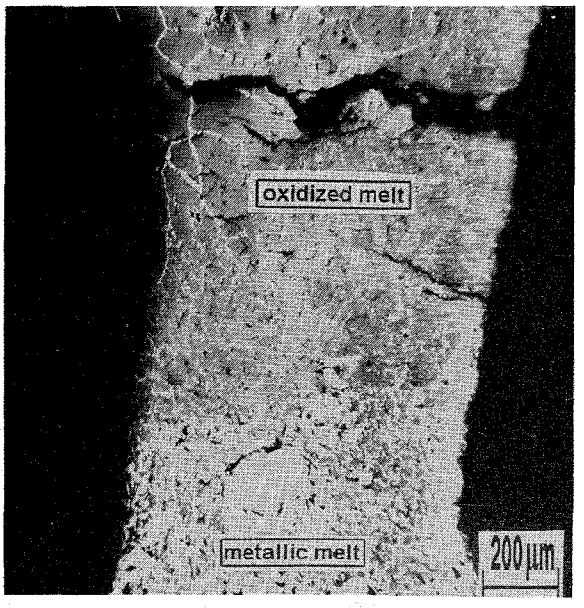

Position 2

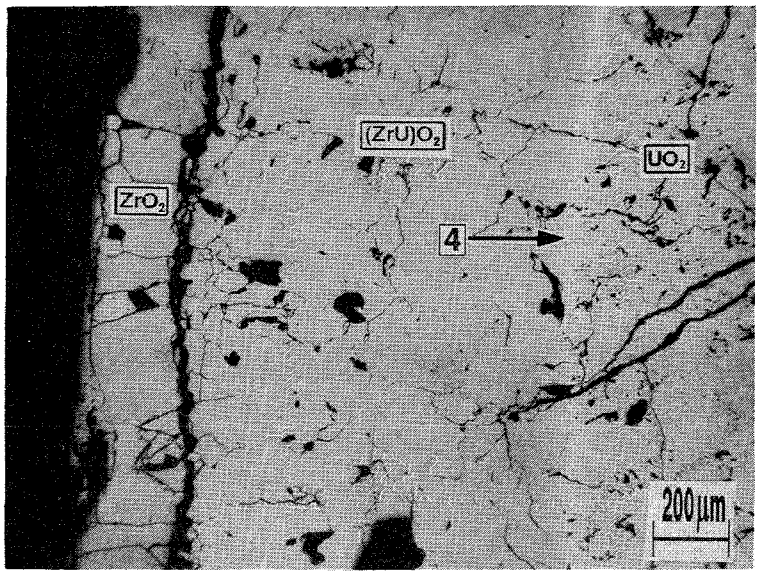

Position 3

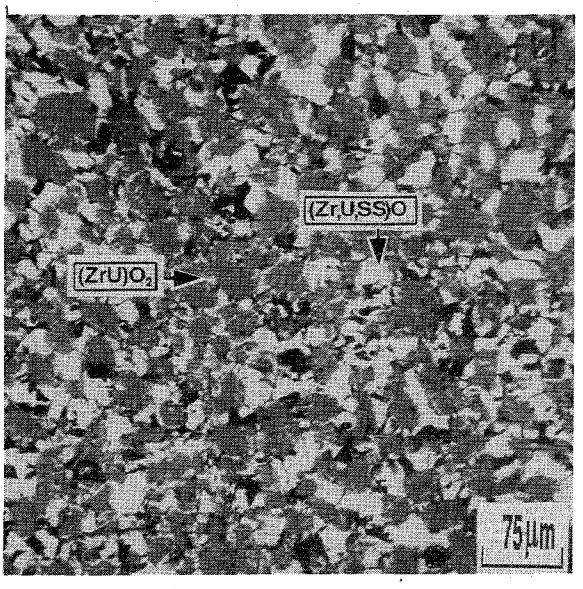

Position 4

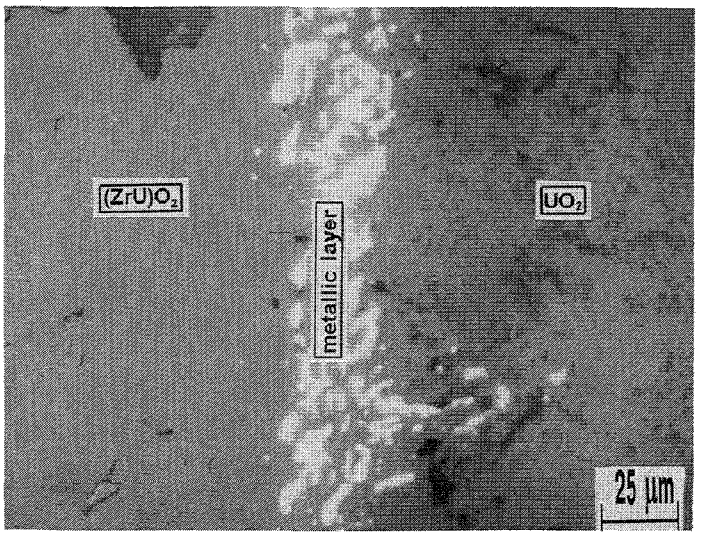

Position 5

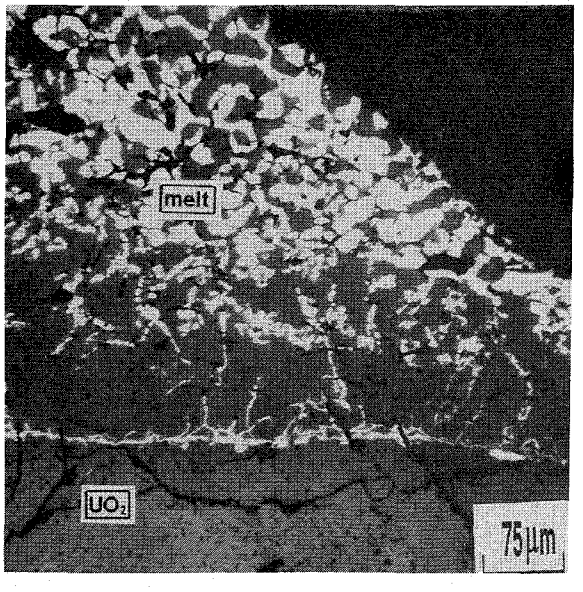

Fig.8. Cross section W2-05. Oxidation of the relocated melt. Metallic layers formation on the fuel-cladding bondaries.

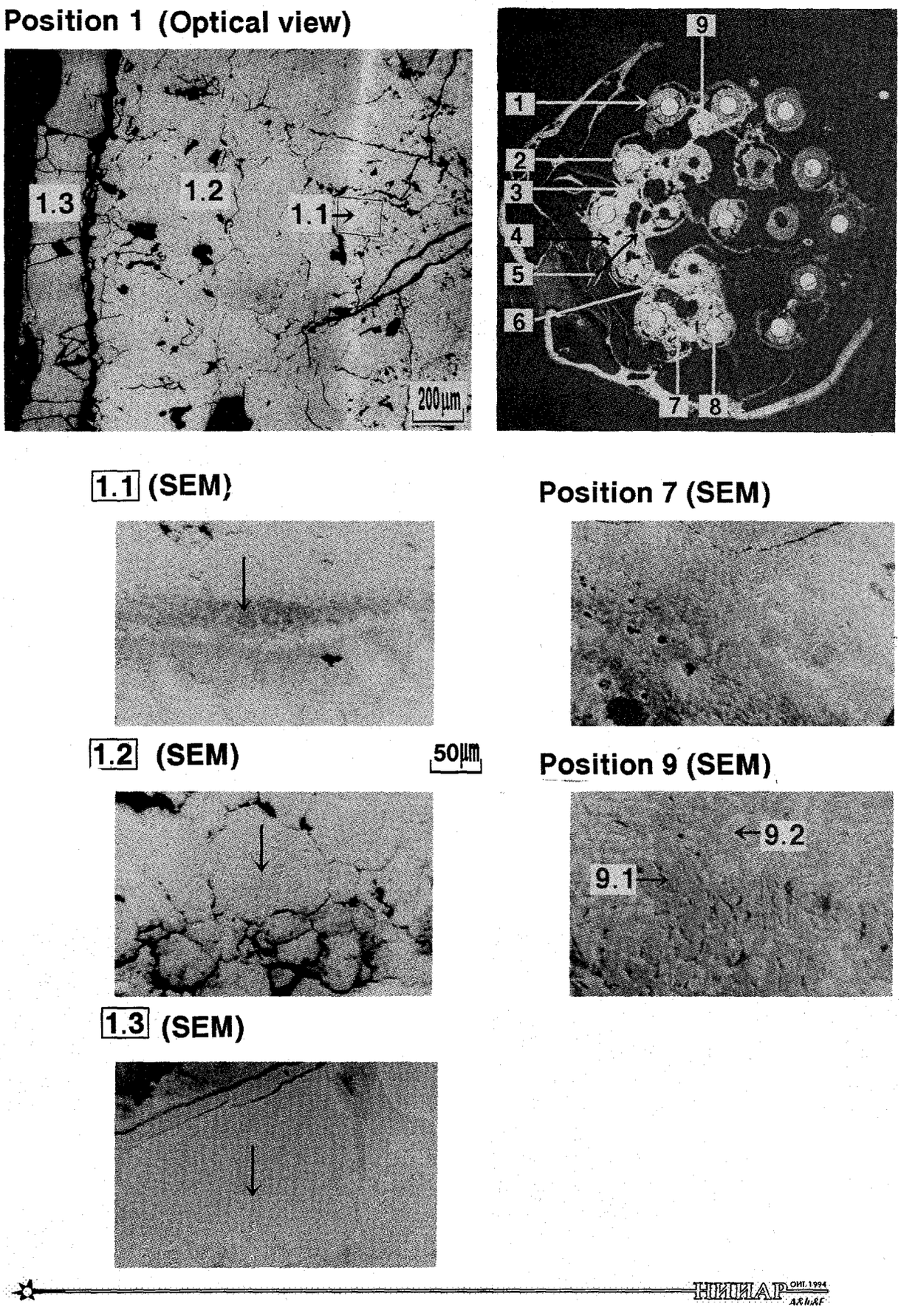

Fig. 9. Cross section W2-05. Elevation 607 mm SEM/WDX analyse positions.

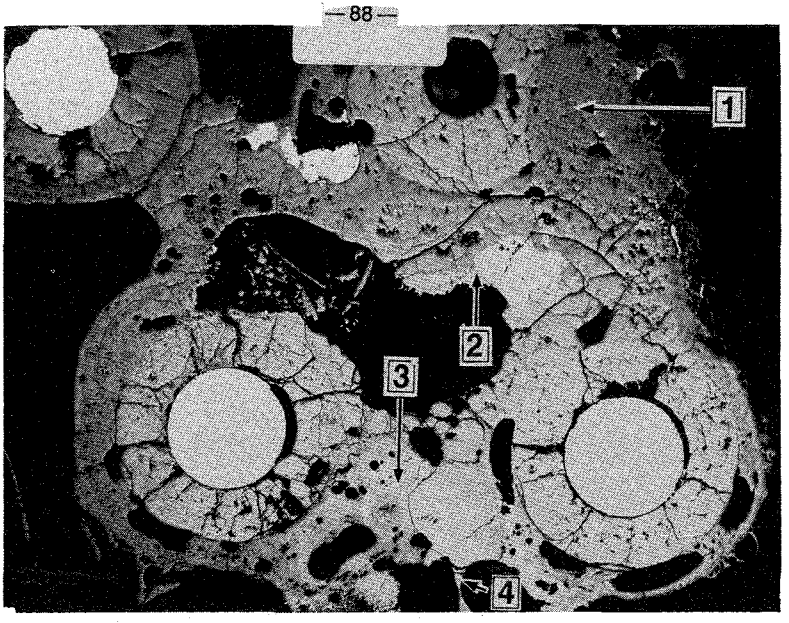

Position 1

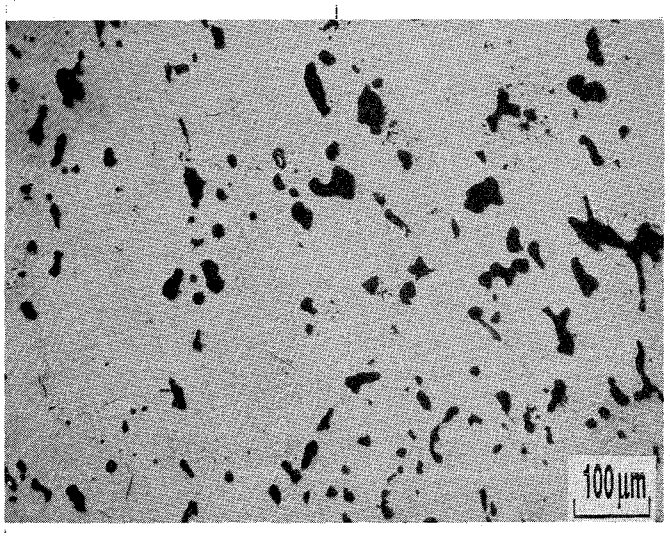

Oxidized melt

Position 2

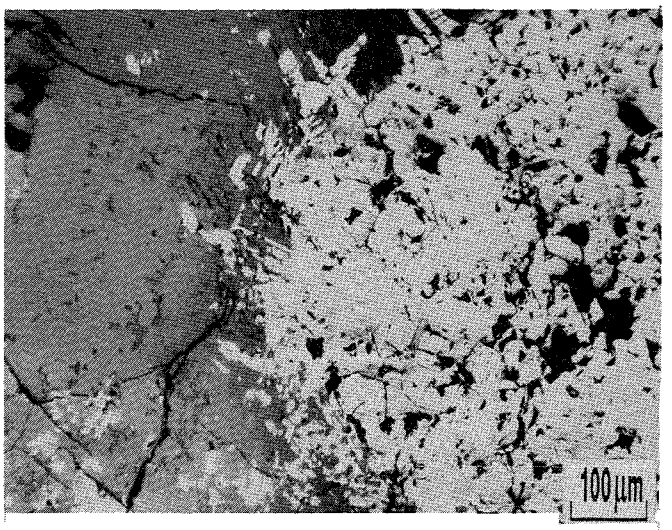

Metallic inclusion in the oxidized melt

Position 3

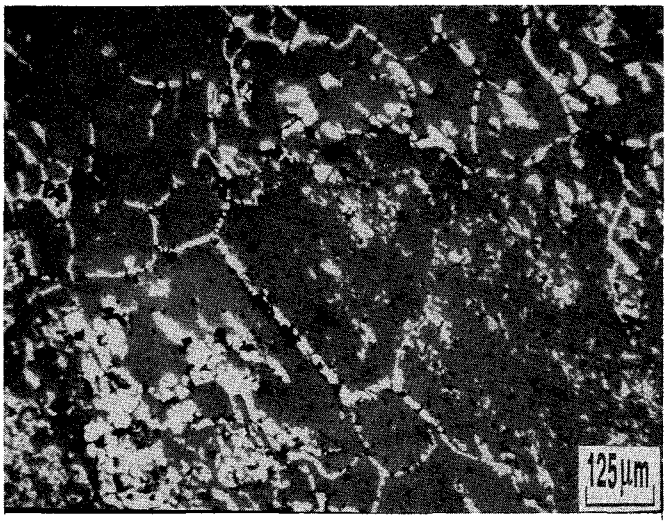

Partially oxidized melt

Position 4

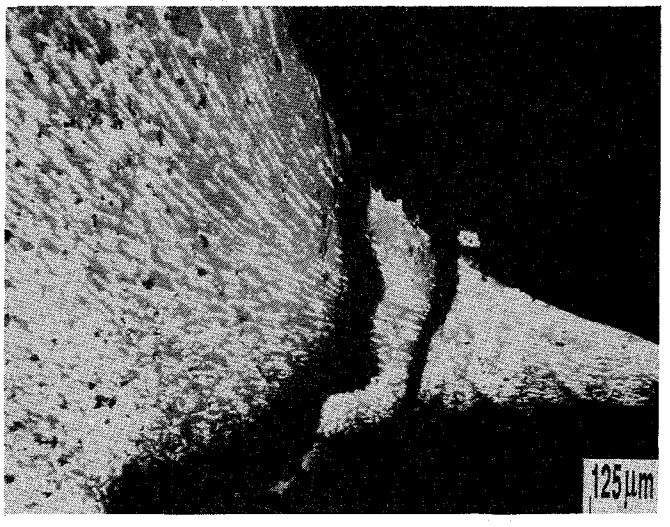

Partially oxidized melt

Fig.10. Cross section W2-05.
Oxidation of the residual melt.

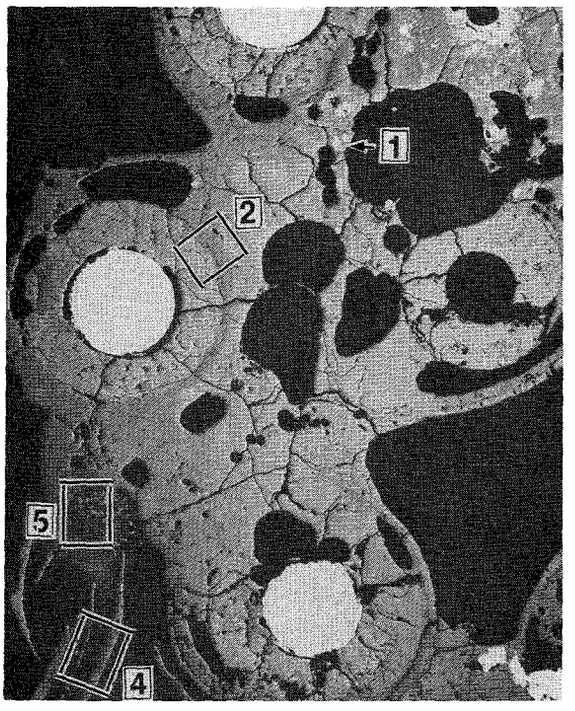

Position 1

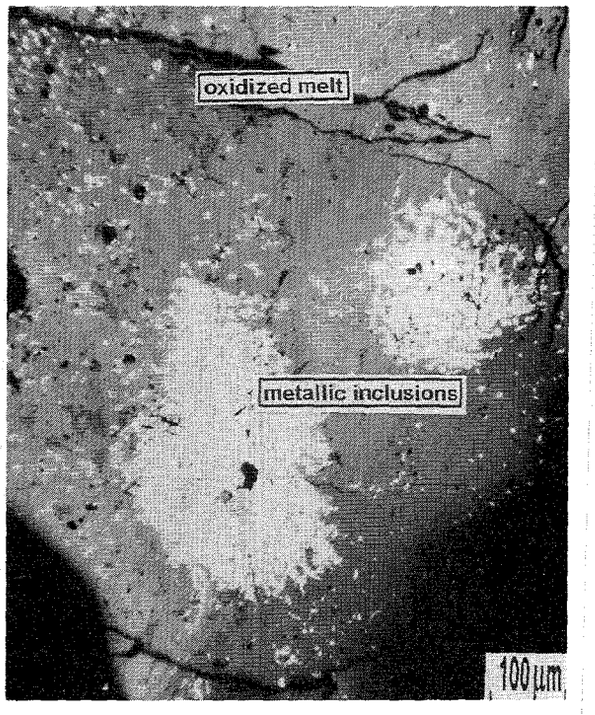

Position 2

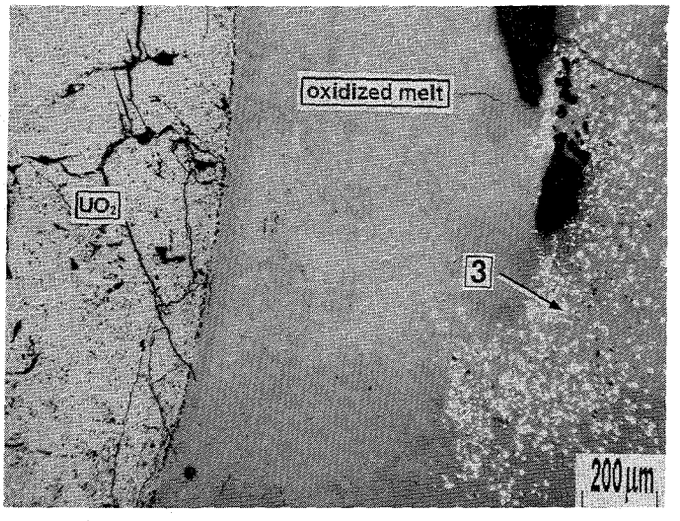

Position 3

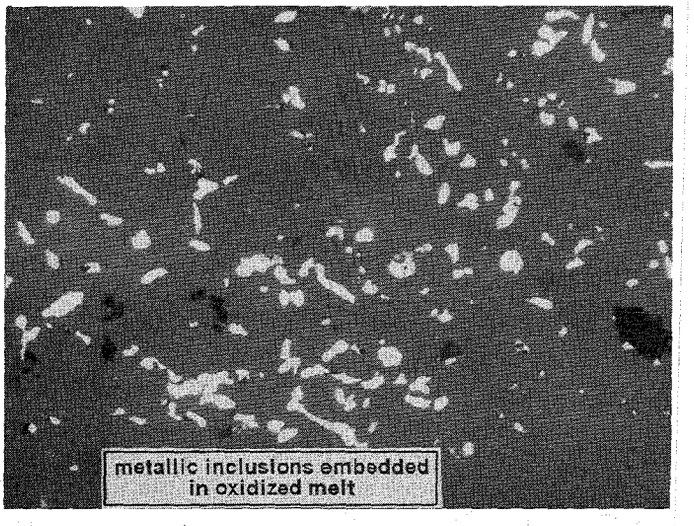

Position 4

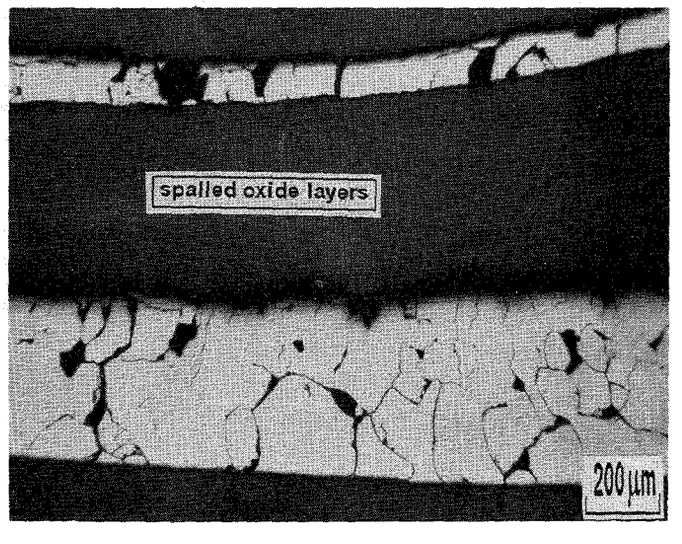

Position 5

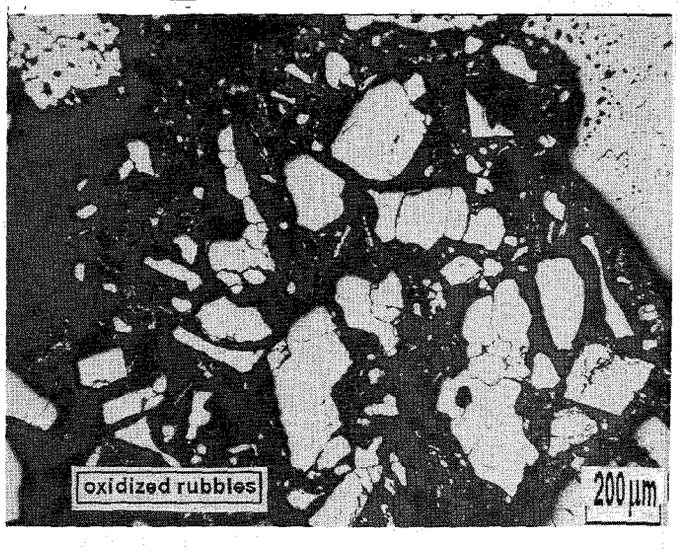

Fig.11. Oxidation of the relocated melt.

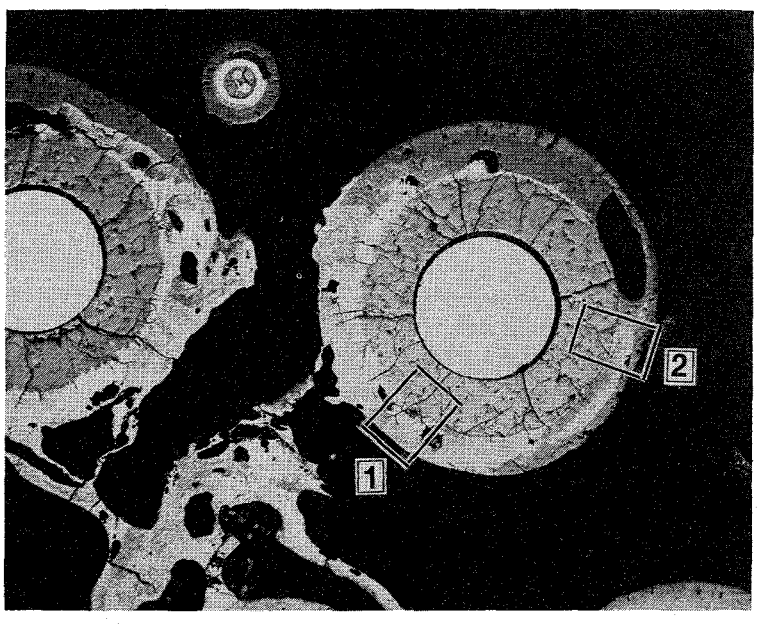

Position 1

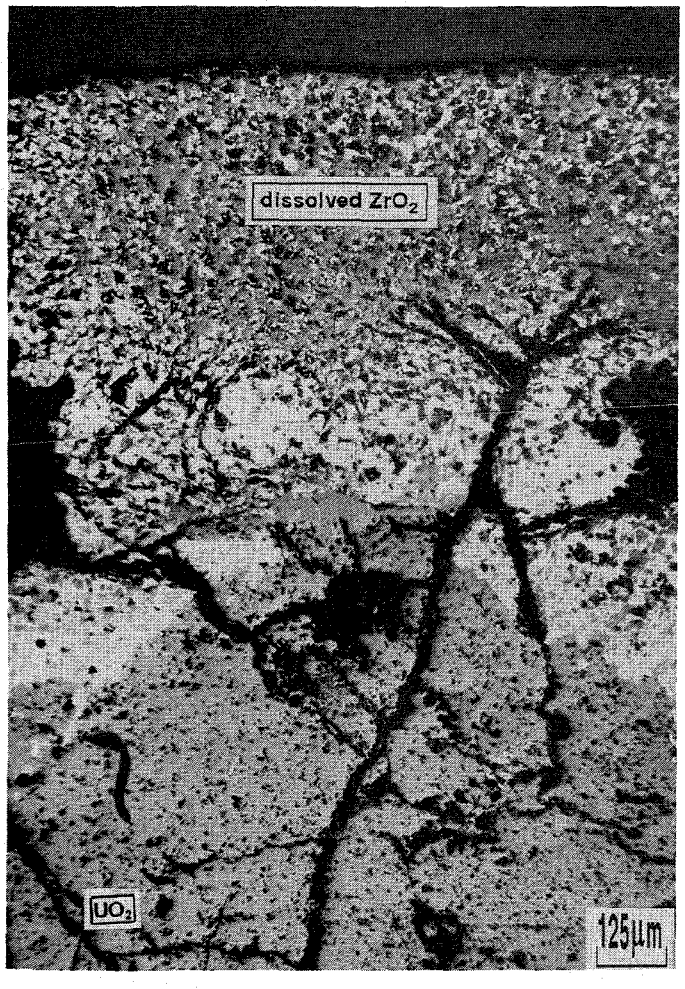

Position 2

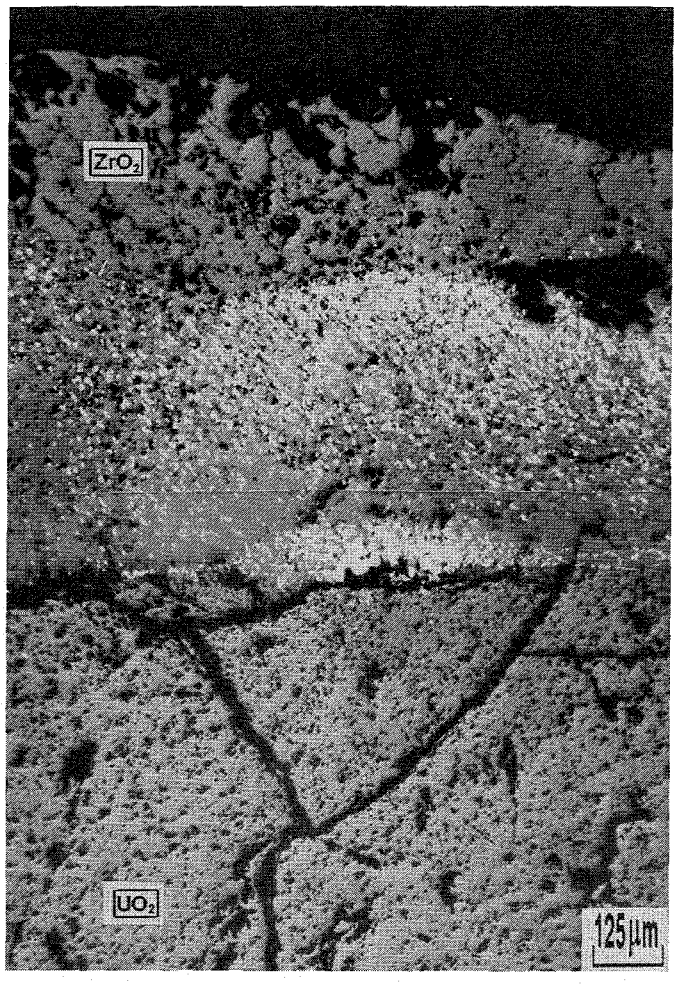

Fig.12. Cross section W2-05. Dissolution of the ZrO2 and UO2 by the metallic melt.

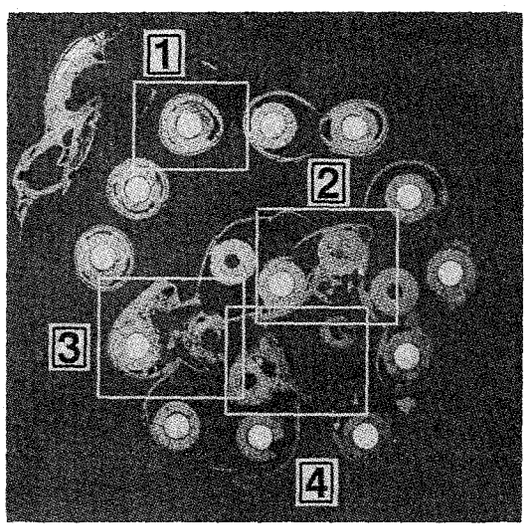

Position 1

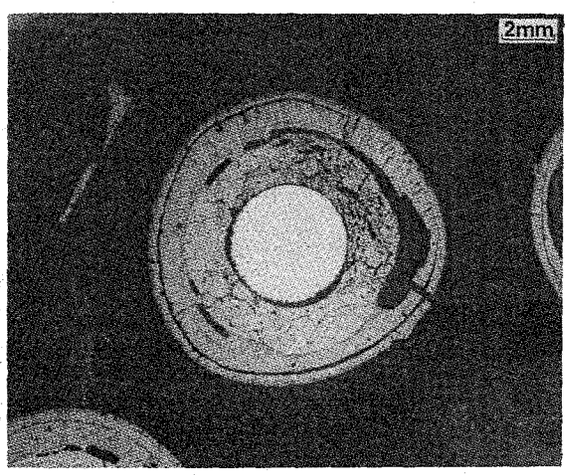

Position 2

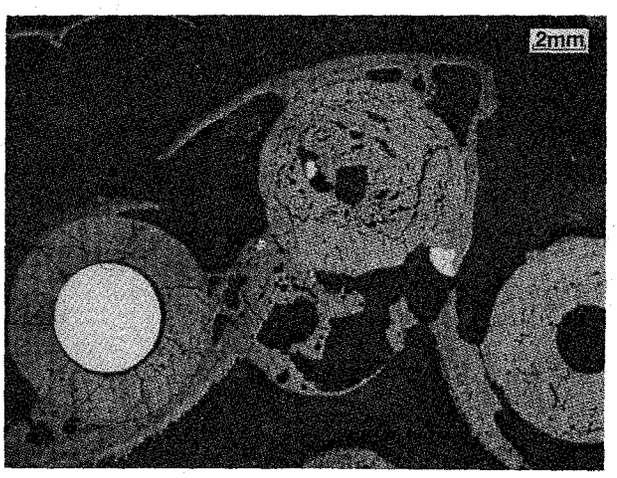

Position 3

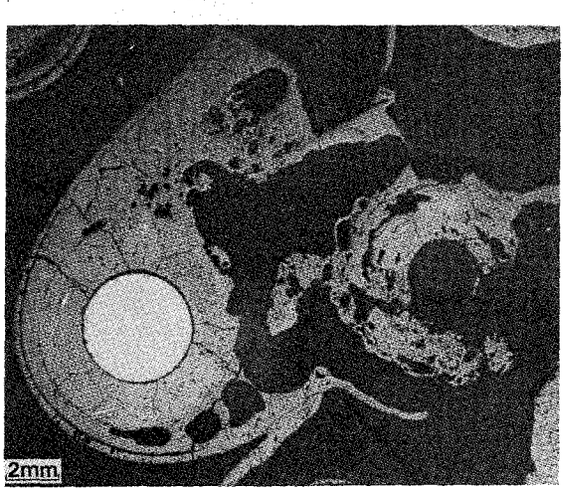

Position 4

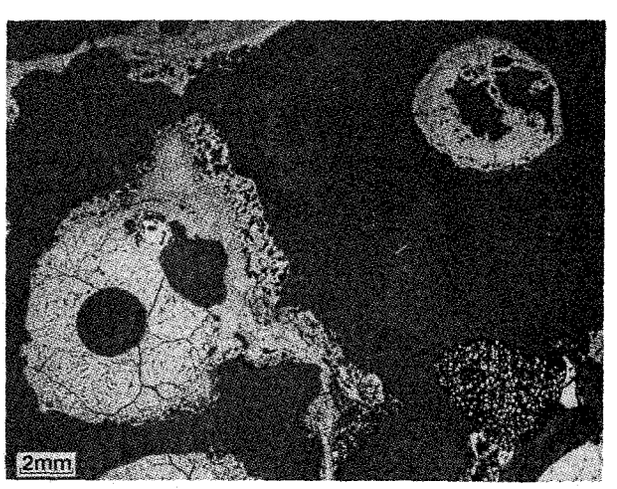

Fig.13. Cross section W2-06 (bottom view). Elevation 726 mm.

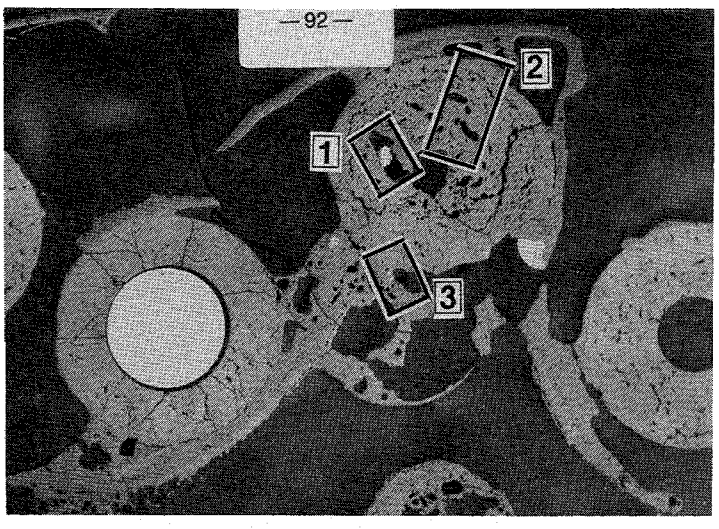

Position 1

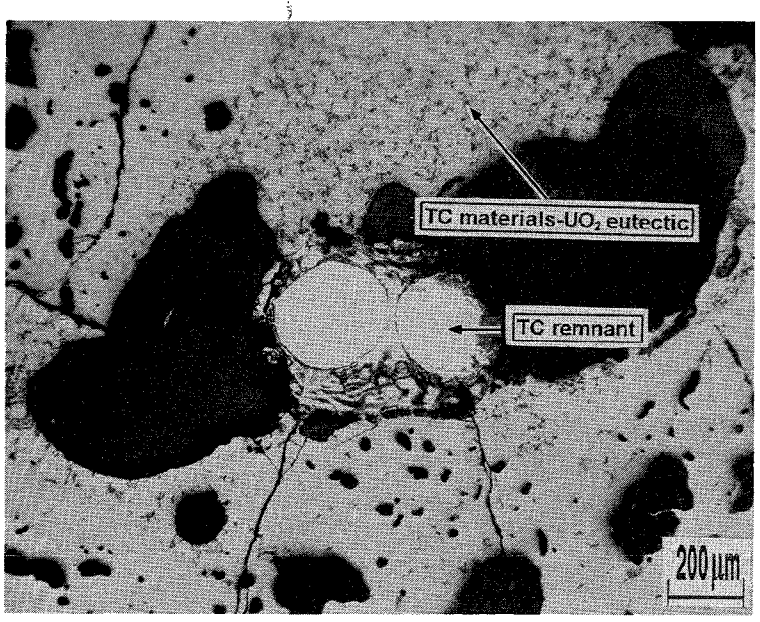

Position 2

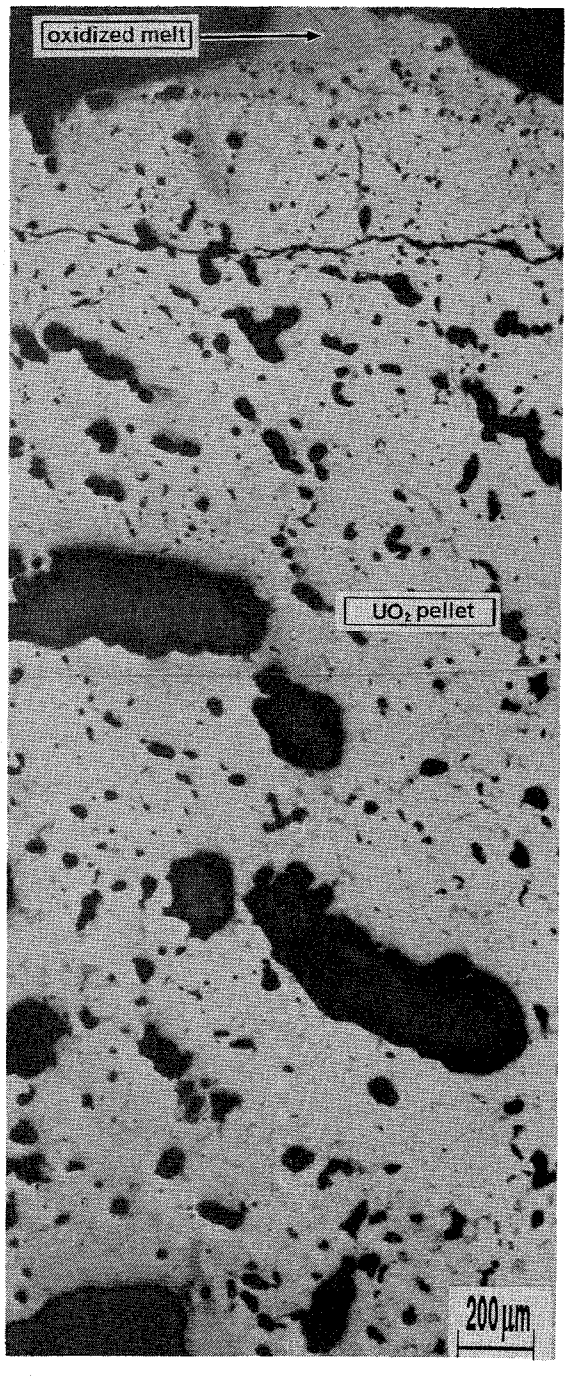

Position 3

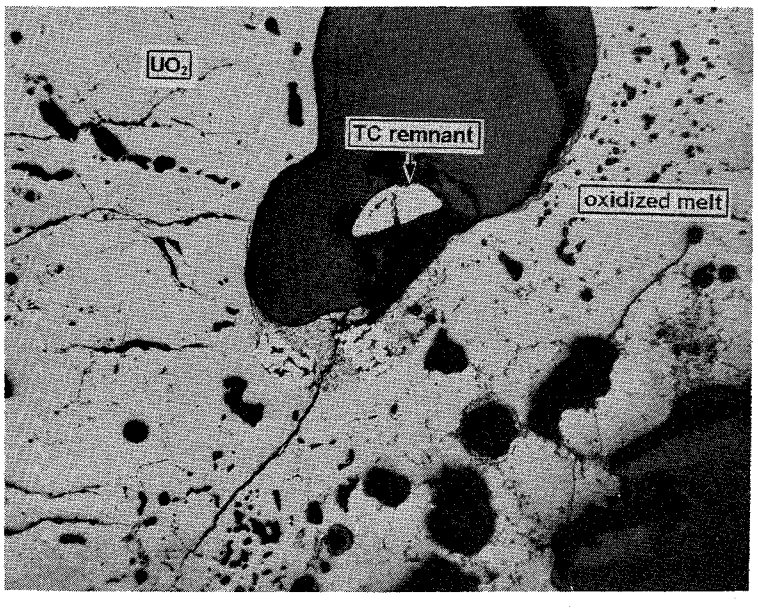

Fig.14. Modified microstructure of the UO_2 pellet. TC destructure.

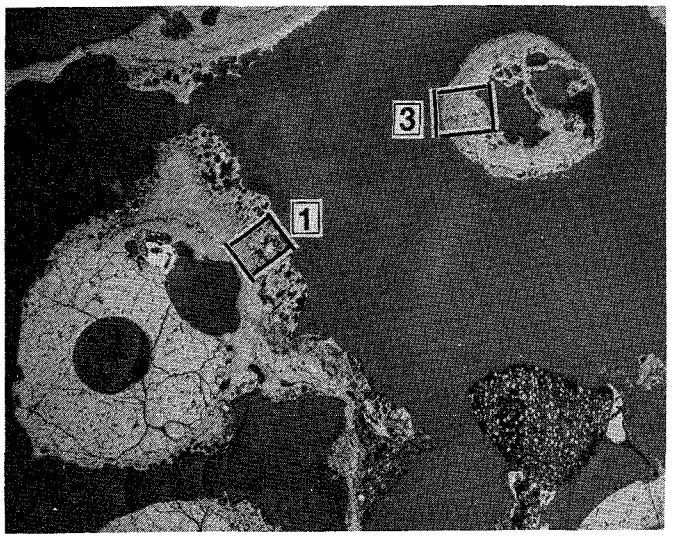

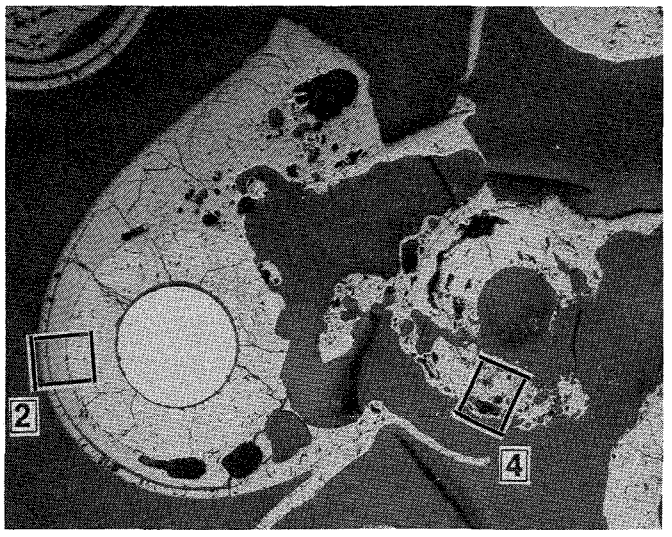

Position 1

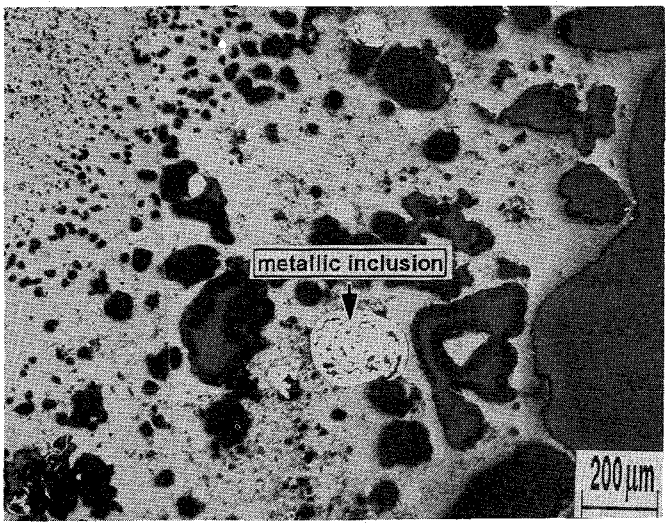

Position 2

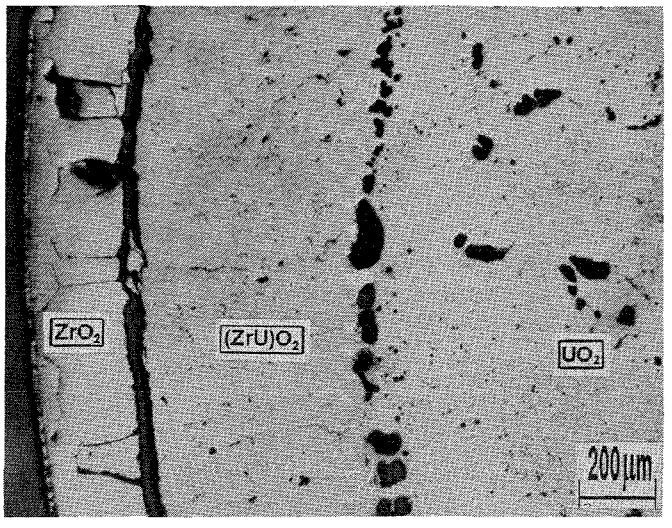

Position 3

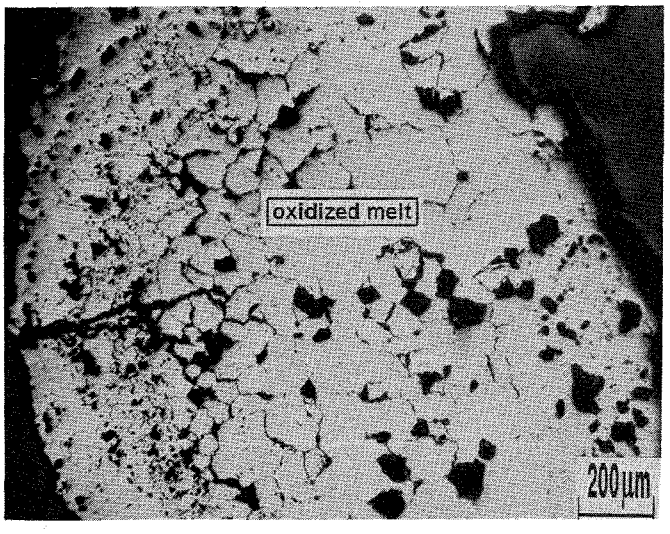

Position 4

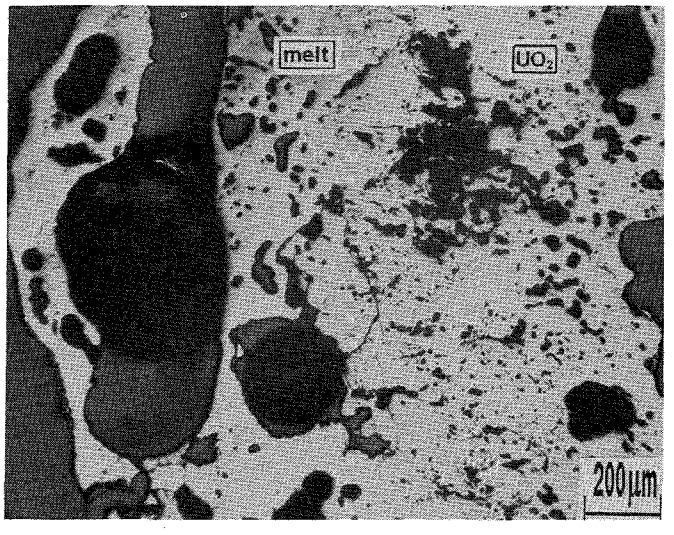

Fig.15. Oxidized melt microsructures. Modified microstructure of the UO_2 pellets.

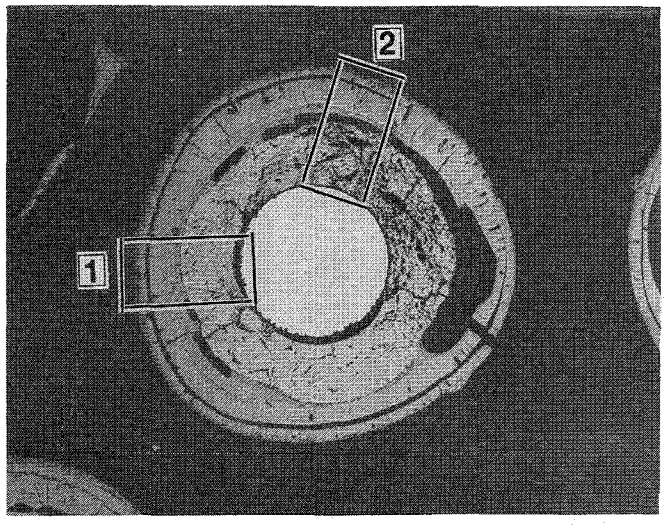

Position 1

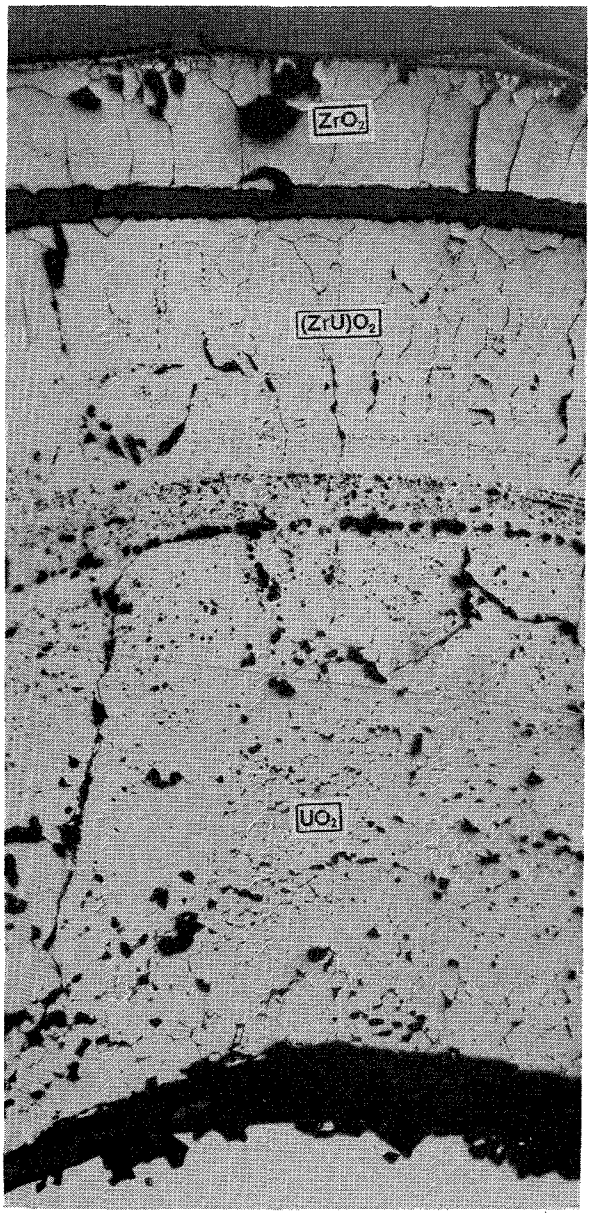

Position 2

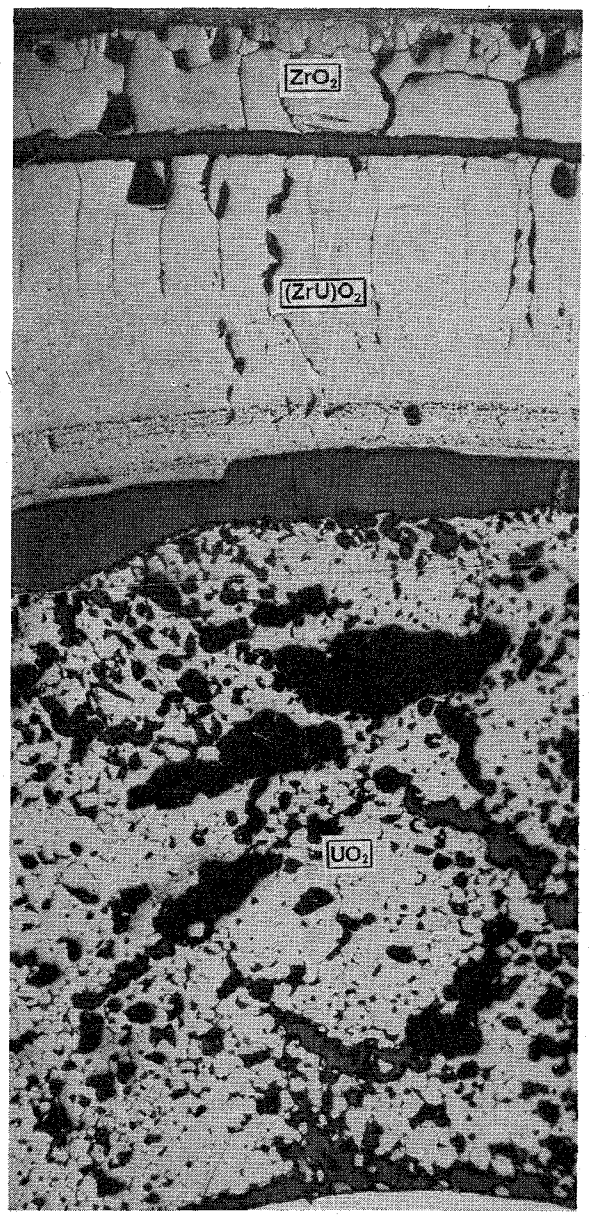

Fig.16. Oxidized cladding microstructure.

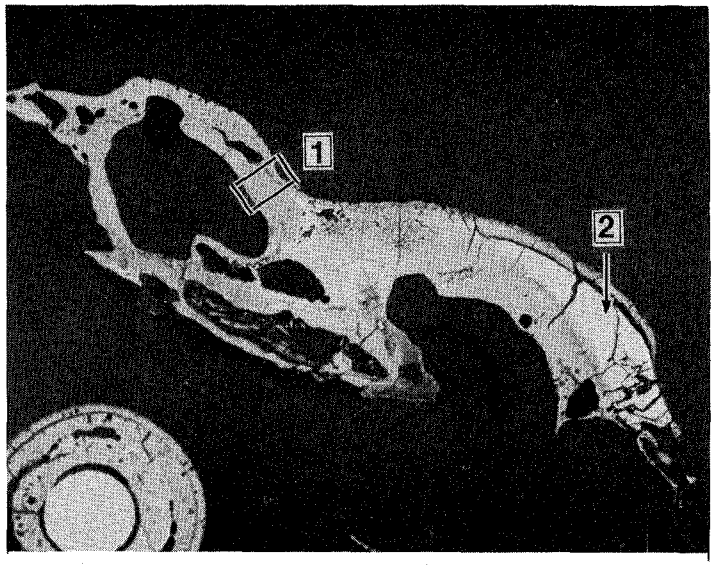

Position 1

Position 2

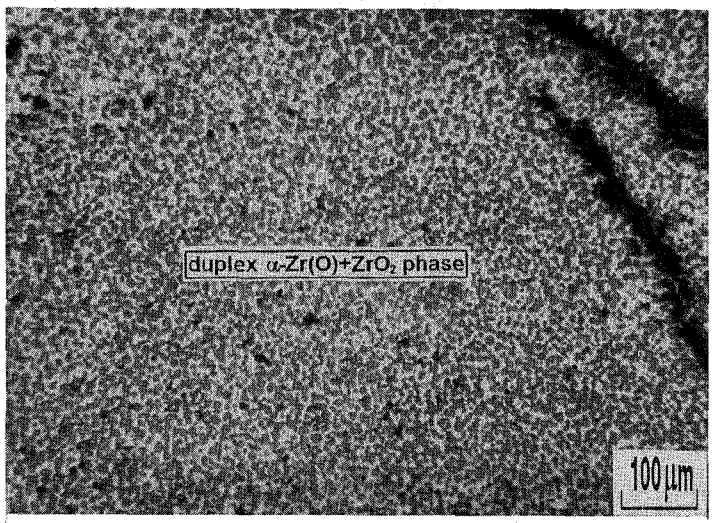

Fig.17. Microstructure of the shroud remnant.

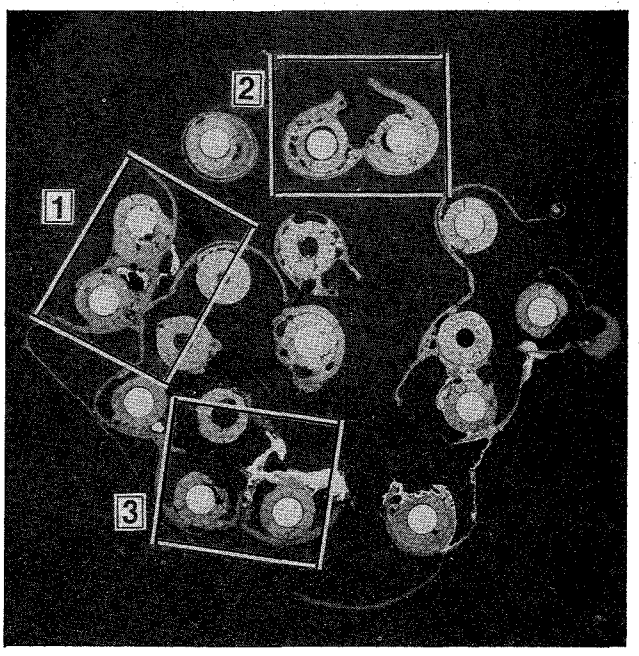

Position 1

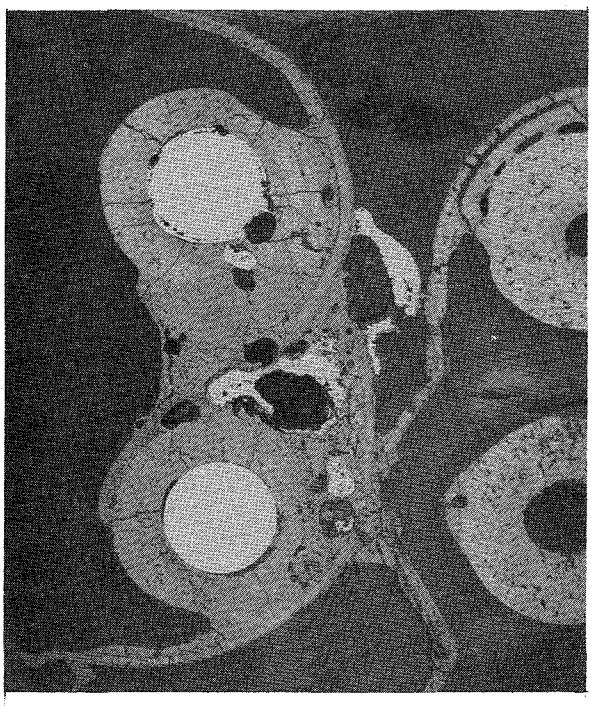

Position 3

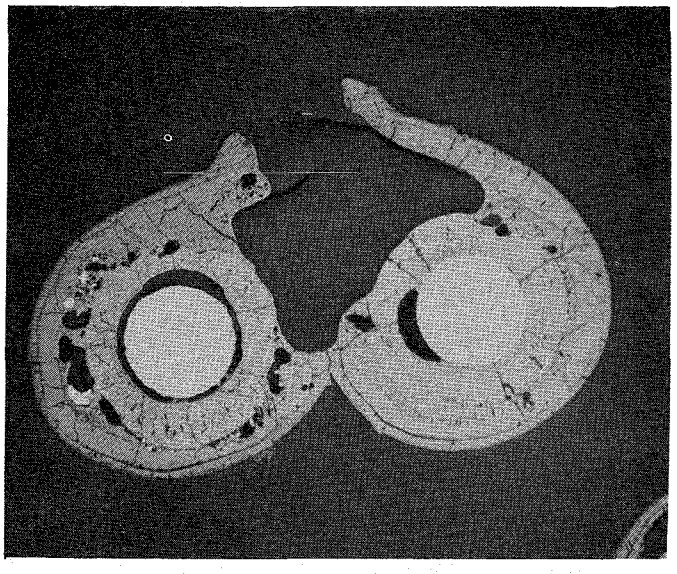

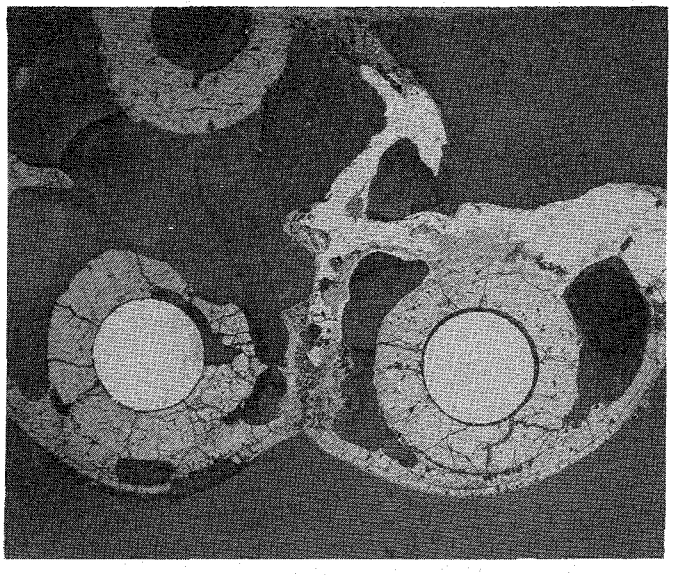

Fig.18. Cross section W2-07 (bottom view). Elevation 845 mm.

Position 1

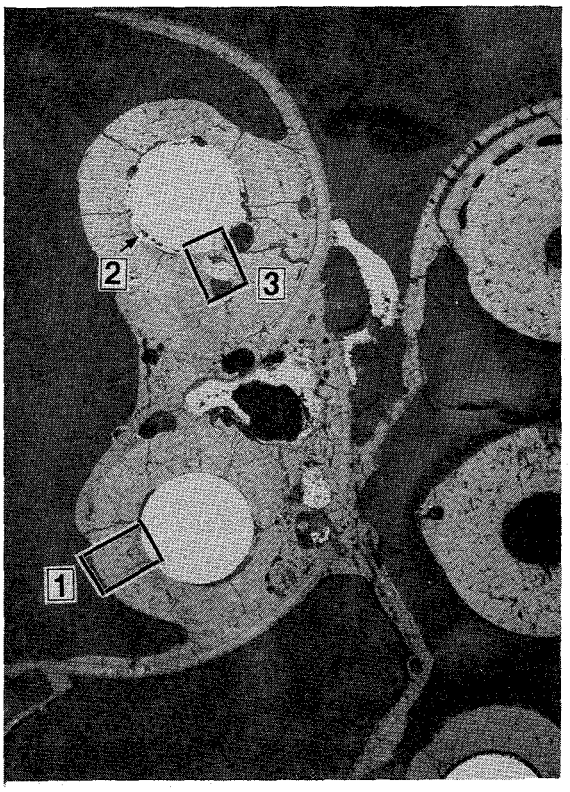

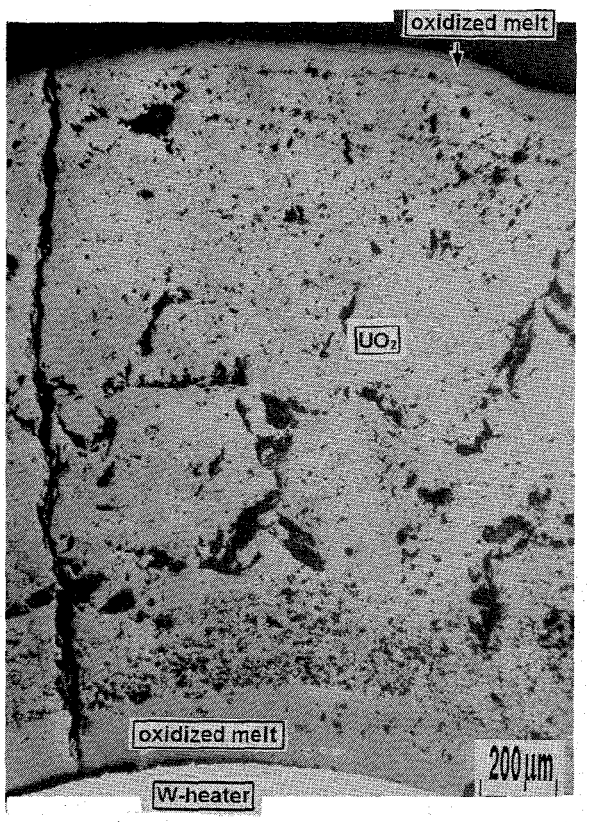

Position 2

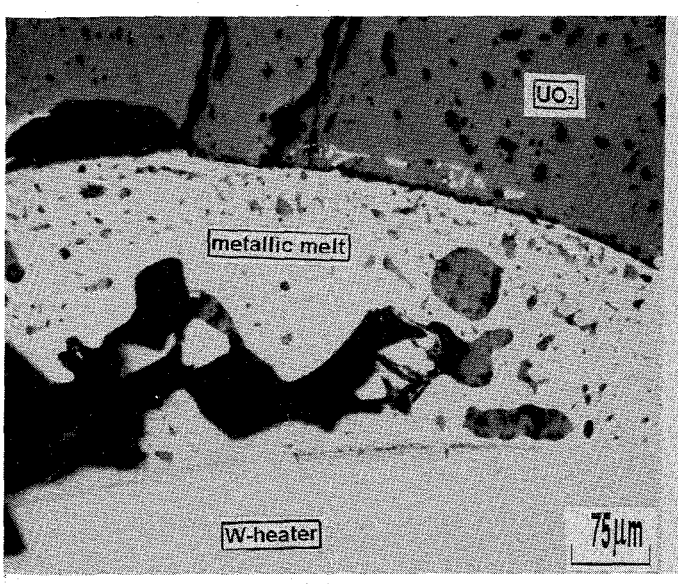

Position 3

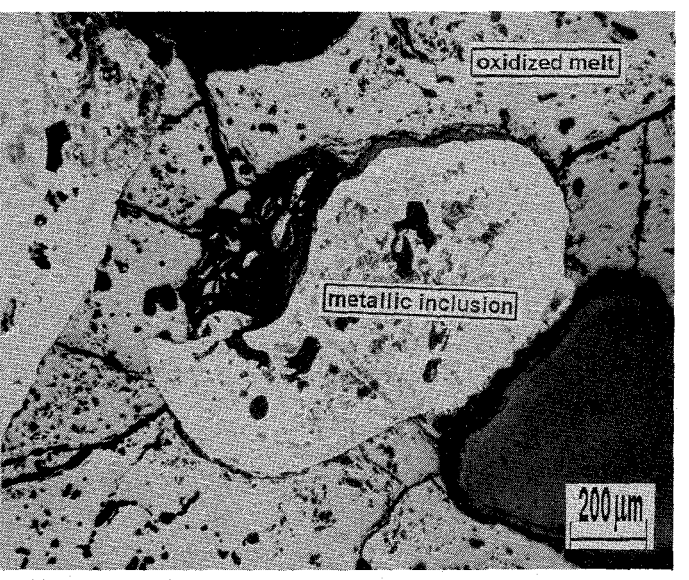

Fig.19. Relocated melt in the W-UO_2 gap between W-heaters and UO_2 pellets. Metallic inclusions in the oxidized melt.

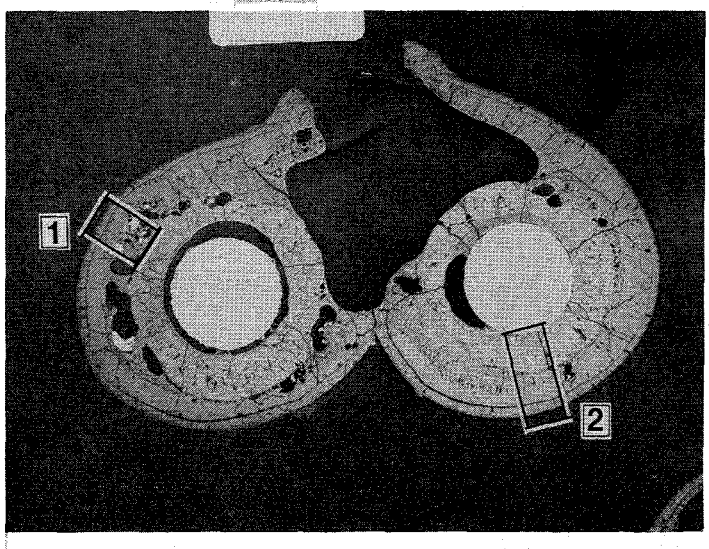

Position 1

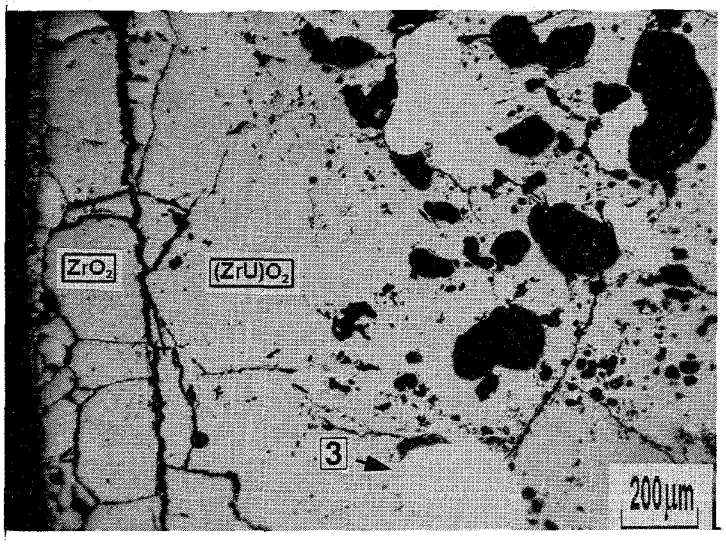

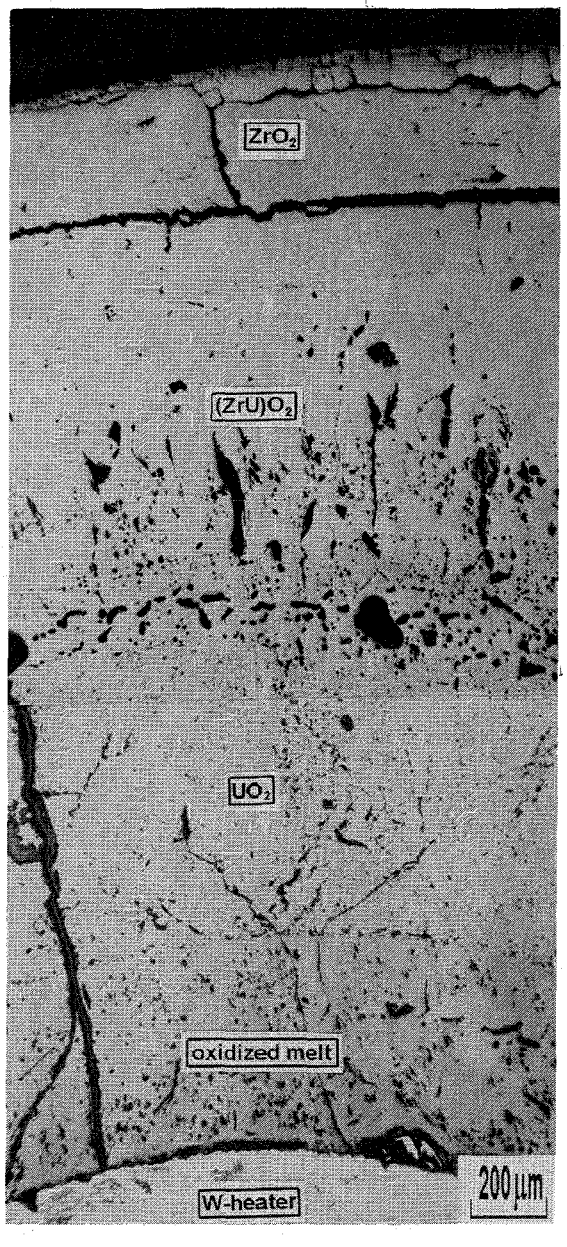

Position 3

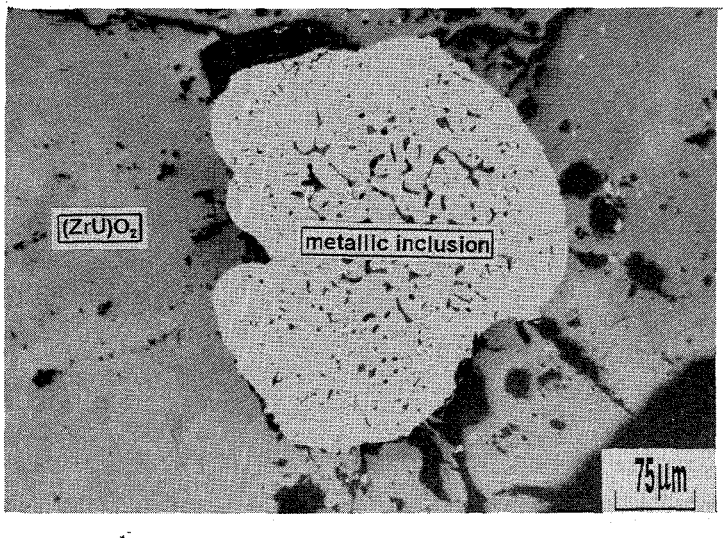

Fig.20. Metallic inclusion inside oxidized cladding area. Dissolution of the UO_2 pellet by the cladding melt.

W2-07

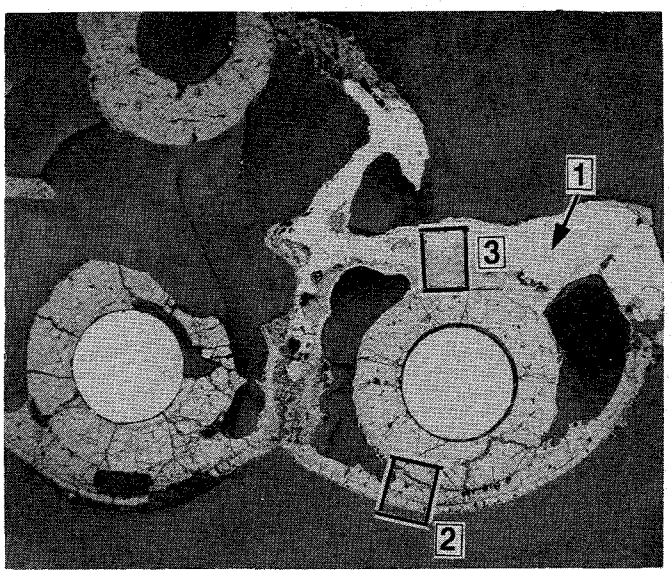

Position 1

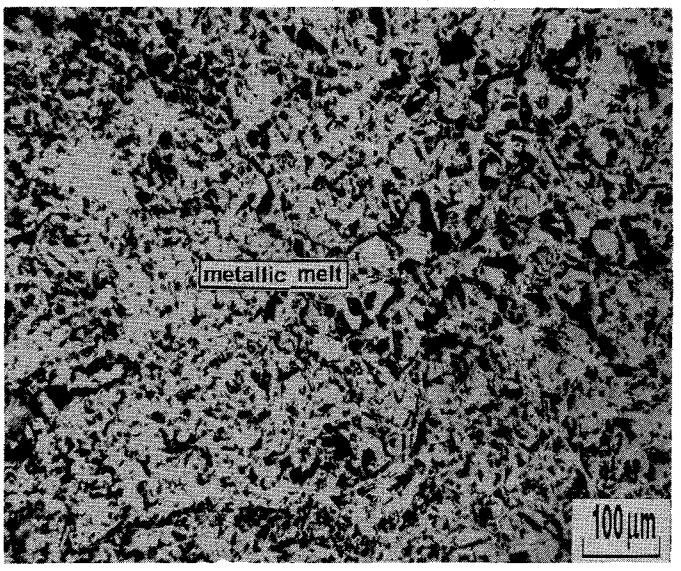

Position 2

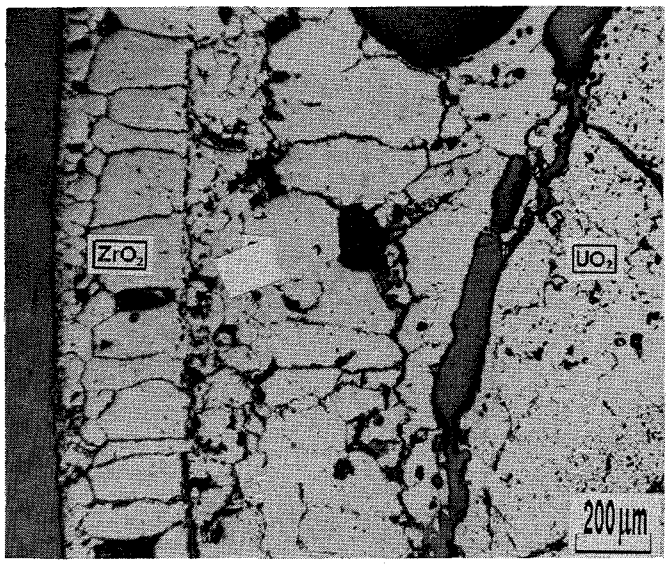

Position 3

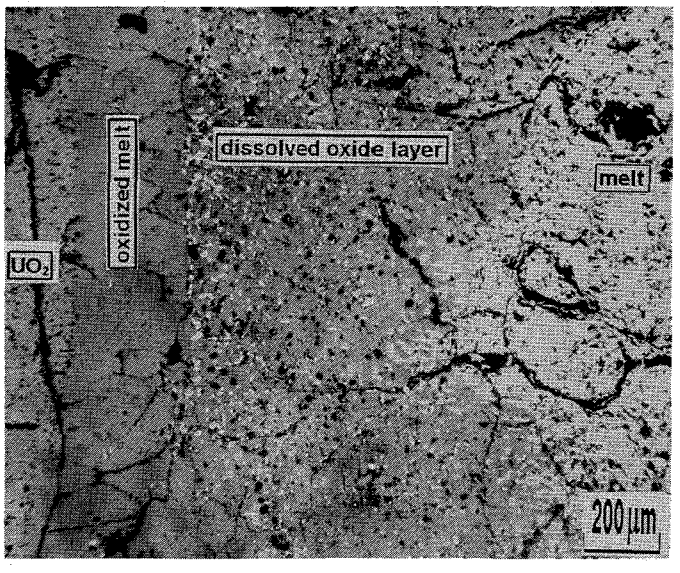

Fig.21. Metallic and oxidized melt. Oxidation of metallic melt by oxigen consumption from UO_2 pellet.

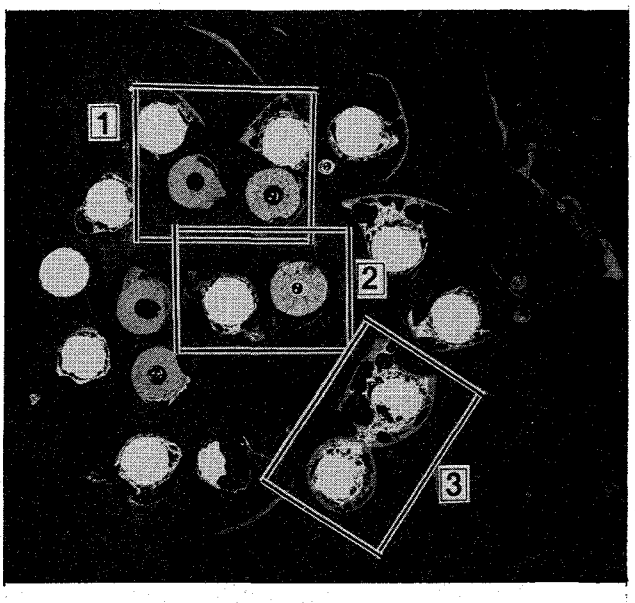

Position 1

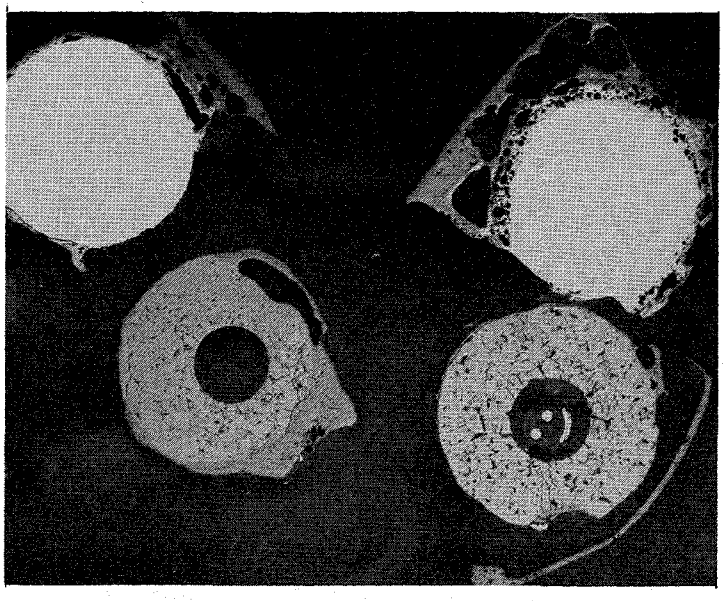

Position 2

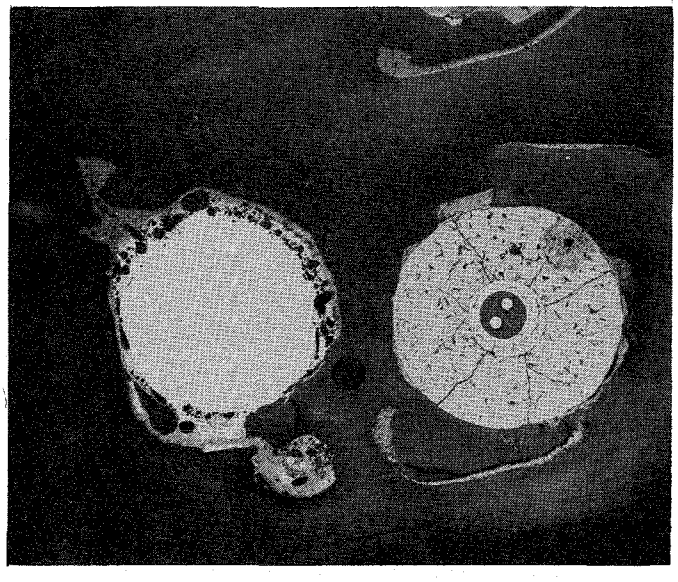

Position 3

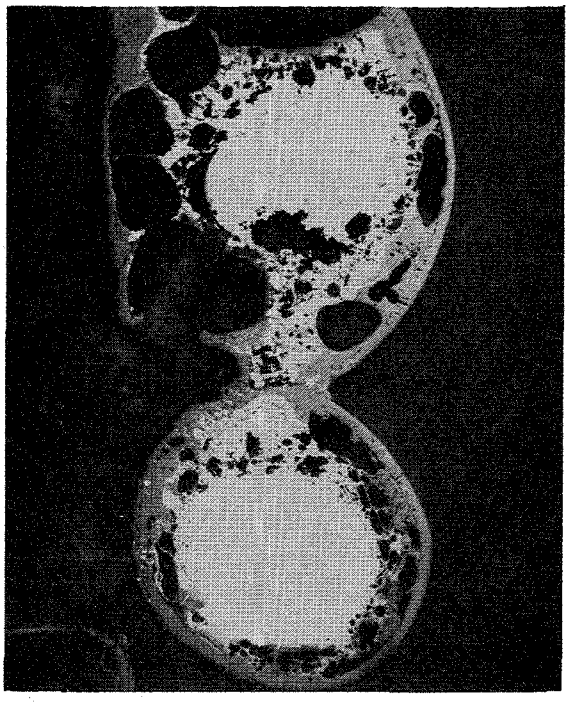

Fig.22. Cross section W2-09 (bottom view). Elevation 1085 mm.

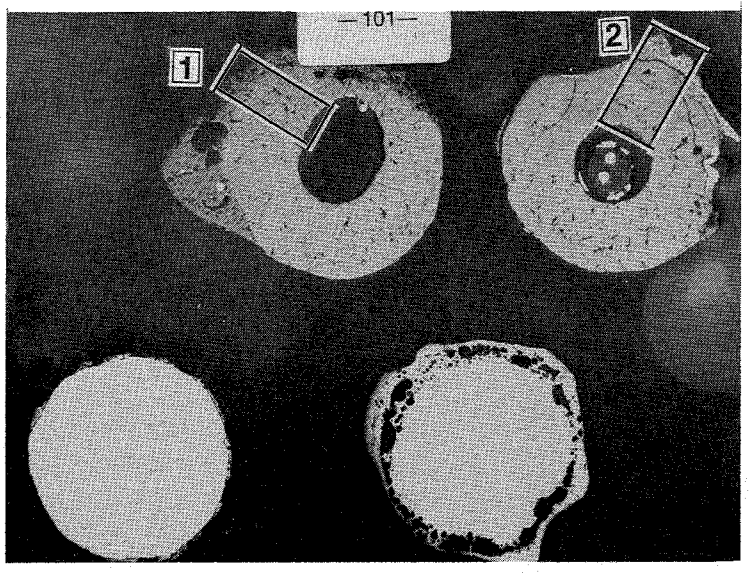

Position 1

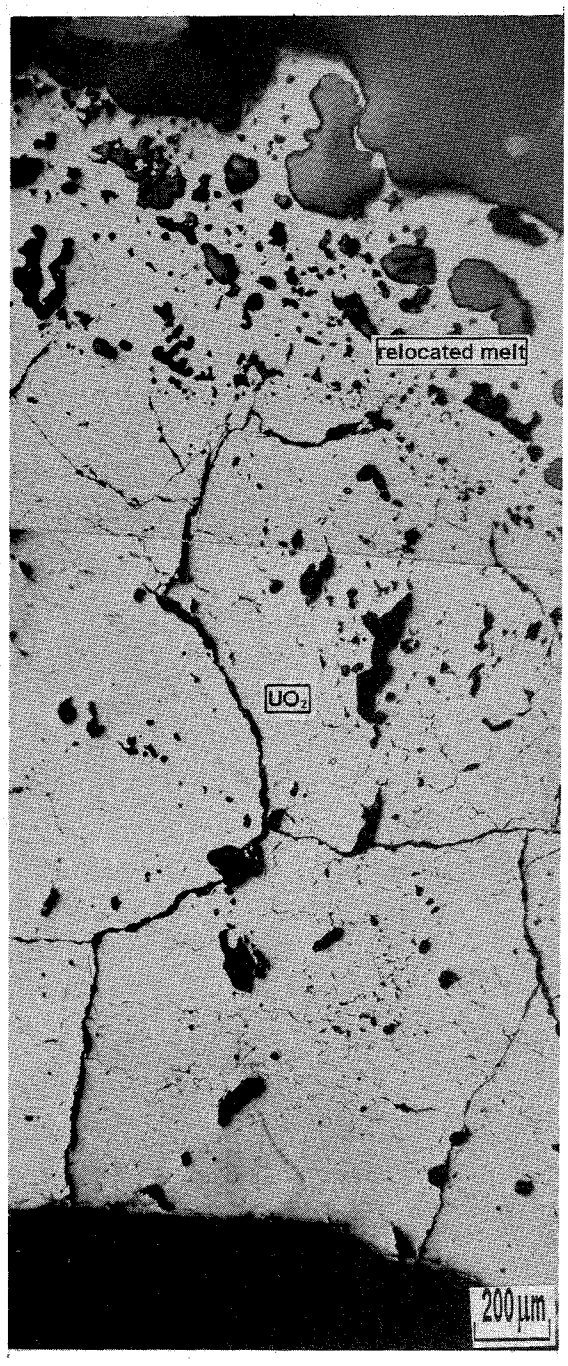

Position 2

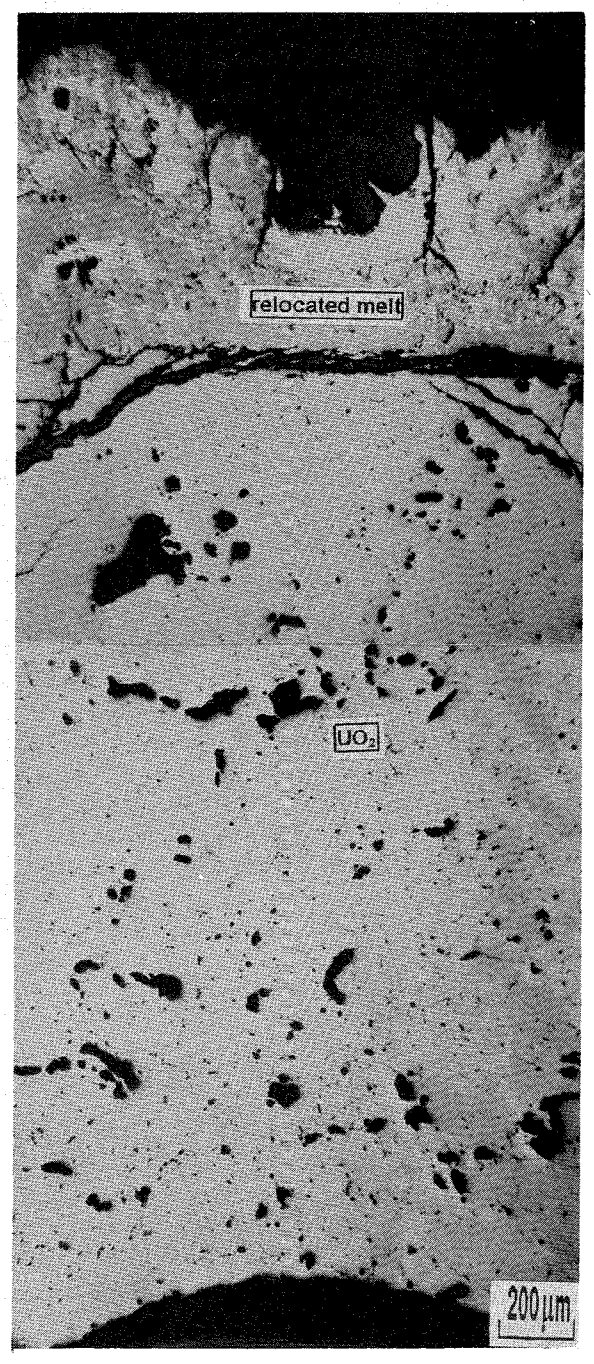

Fig.23. Relocated melt remnants on the surface of the UO_2 pellets.

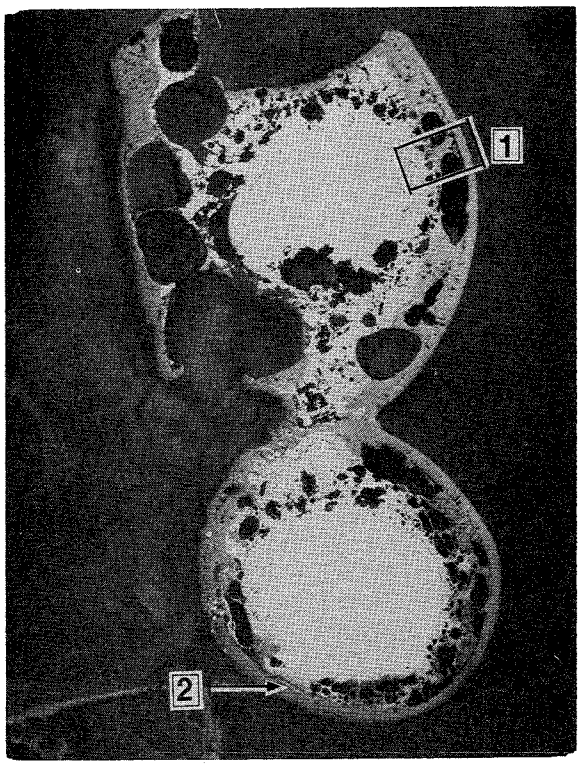

Position 2

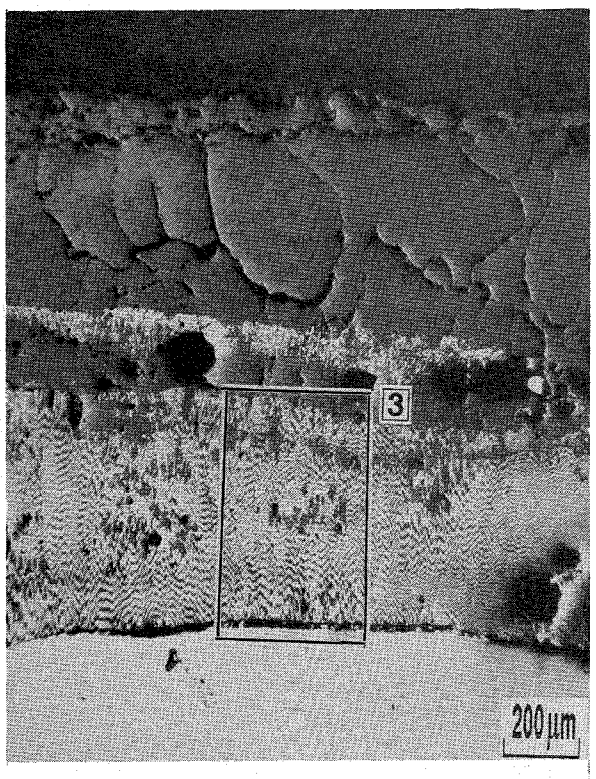

Position 1

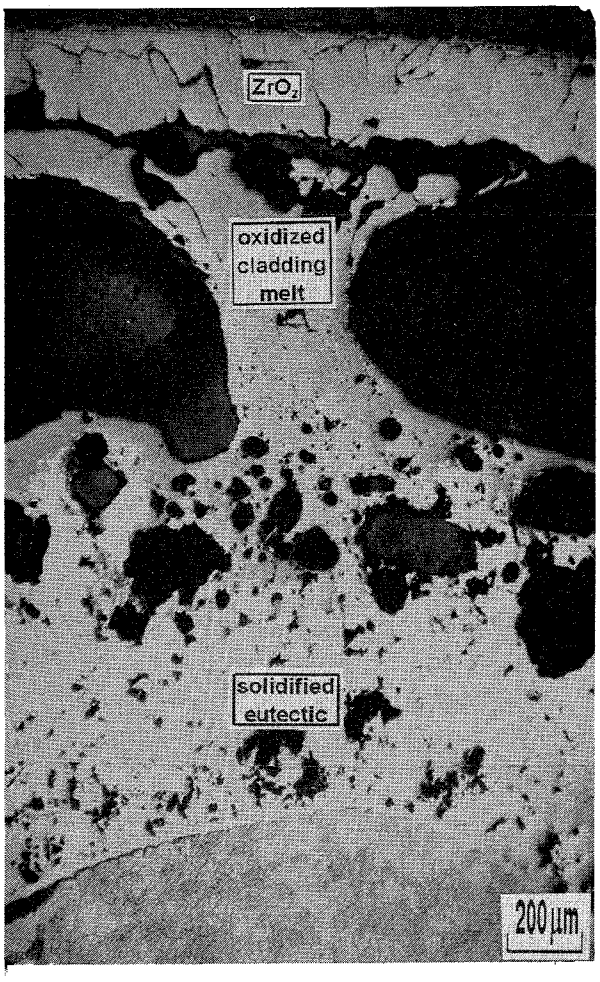

Position 3

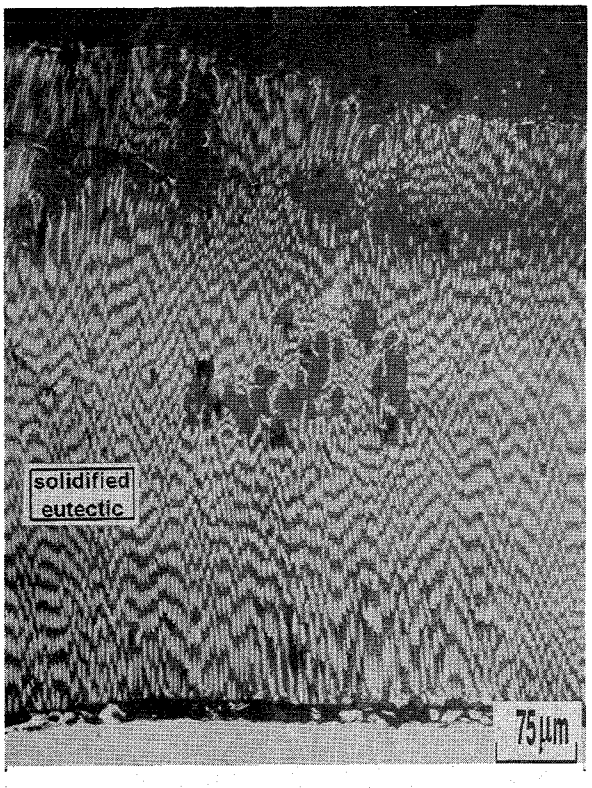

Fig.24. Mo-electrode - cladding interaction.

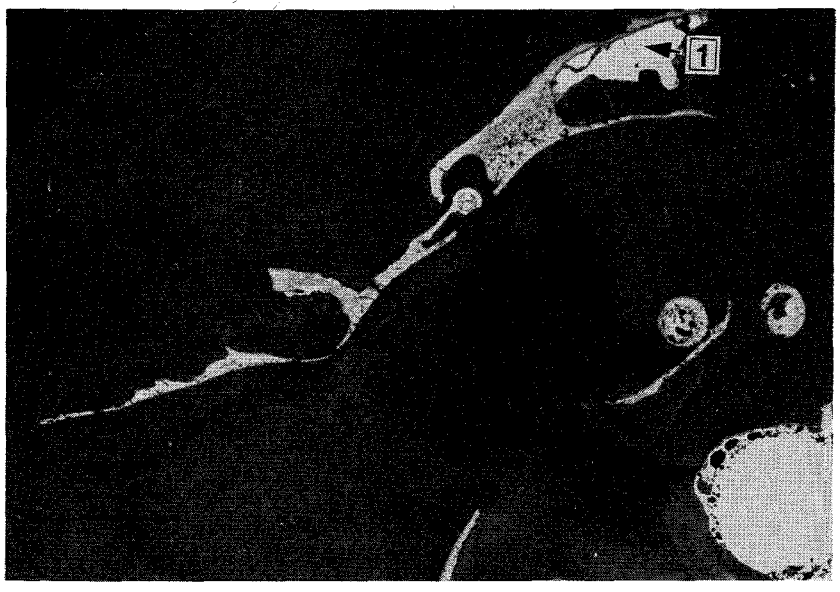

Position 1

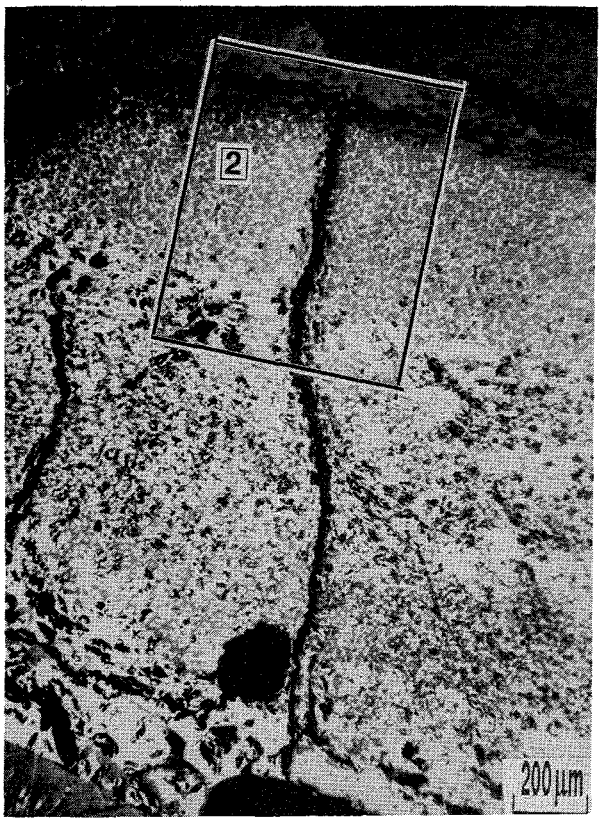

Position 2

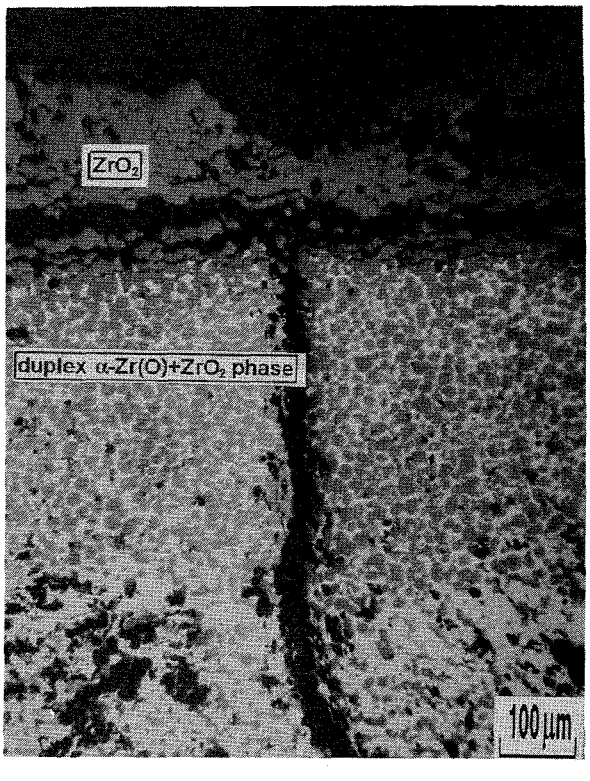

Fig.25. Microstructure of the shroud remnant. Dissolution of the initially formed ZrO_2 layer in the α-Zr(O) melt.

Post-test-Investigation at Elevations 141,498, and 964 mm (Draft contribution to joint post-test examination report on VVER-1000 fuel rod bundle CORA-W2)

Sokolov N.B., Karpov V.M., Salatov A.V., Nechaeva O.A.,
Andreeva-Andrievskaya L.N., Vlasov F.Yu.

All-Russian Scientific and Research Institute of Inorganic Materials named after Academician A.A.Bochvar

Moscow, 1995

2.1. Bundle Elevation 141 mm (bottom)
(CORA-W2-01)

At this elevation the bundle is devoid of any visible damages (fig.2.1). However, some specificity is to be noted. The fuel simulator bundle is displaced relative to the assembly shroud. This is likely to reflect the bundle status prior to the experiment, but it is more probable that this displacement is due to bundle damages in the top sections during the experiment. There are three parts of the total area of 51 mm^2 filled with molten metal. There is no boron carbide in the absorber rod. This is likely to be explained by boron carbide powder tipping out during the cutting of the bundle into specimens. No traces of interaction between boron carbide and stainless steel or oxidation of fuel simulator claddings and bundle shroud were found out.

Cracks were available in some UO_2 pellets. Some pellets have no fuel fragments. However, this crumbling is not related to the fuel damage during the experiment, it is most probable to occur during bundle cutting or preparation of section.

The microstructures of fuel simulator claddings, shroud, absorber rod claddings, guide tube and fuel pellets do not essentially differ from the structures of the materials prior to the experiment.

2.2. Bundle Elevation 498 mm (bottom)
(CORA-W2-04)

At this elevation the bundle is strongly damaged (fig 2.2). However, the fuel pellets of all 18 rods are available and their damage can be characterized as insignificant. The absorber rod and its guide tube are missing. There are three boron carbide fragments of the total area of 60 mm^2. Boron carbide is impregnated with a metallic melt containing iron, zirconium, uranium and other elements. These fragments are likely to have been relocated from the top sections and they cannot be identified as B_4C that belongs to this section.

The fuel simulator claddings have been badly damaged. In

some rods they are essentially missing. The characteristic cross-sections of the rods are illustrated in fig.2.2. The outer layer of the rod consists seemingly of two layers. The outer layer is zirconium dioxide that resulted from the interaction between the cladding material in the solid state and steam. The second layer is a phase containing in the main zirconium, oxygen, uranium and insignificant amounts of iron and chromium. Within a single rod cladding over the azimuth the thickness of ZrO_2 varies in a wide range (the maximum thickness of ZrO_2 reaches 0.6 mm). The causes of this can be different. First, non-uniform temperature field of cladding; second, cladding deformation; third, possible separation of oxide films. To estimate the zirconium thickness needed to form zirconium dioxide ($\delta_{Zr(ZrO2)}$) the following relations were used:

$$\delta_{Zr(ZrO2)} = \frac{\max \delta_{ZrO2}}{k} , \qquad (2.1)$$

$$\delta_{Zr(ZrO2)} = \frac{\sum_{i}^{N} \max \delta_{ZrO2i}}{k\ N} , \qquad (2.2)$$

$$\delta_{Zr(ZrO2)} = \frac{\sum_{i}^{N} \frac{F_{ZrO2i}}{P_i}}{k\ N} , \qquad (2.3)$$

were max δ_{ZrO2} is a maximum thickness of ZrO_2 layer in fuel simulators of the section, k = 1,54 is Pilling-Bedworth coefficient, N is the number of rods having claddings in the section, F_{ZrO2} is ZrO_2 area of the rod, P_i is ZrO_2 layer length of the rod, i is the rod number. The quantitative results of $\delta_{Zr(ZrO2)}$ calculation are given in section 2.4.

The bundle shroud in the section has significant damages. The thickness sometimes reaches 3 mm. As it has been shown by the X-ray spectral microanalysis (CAMECA) there appeared uranium and iron over the whole shroud thickness for the exception of the outer and inner layers of ZrO_2. In some points the mass content of uranium attains 20-50 %. It is likely that formation of low melting eutectics (U-Zr), (Fe-Zr), (U-Fe) is a cause of some parts of shroud melting down and separation of a thin internal part of ZrO_2. At the sites where the inner and outer layers of ZrO_2 are retained, one can observe a two phase region between them, that contains particles having different contents of Zr, U and O. Visually the specimen plane has a mettallic lustre of various intensity therefore it cannot be attributed to a ceramic phase.

2.3. Bundle Elevation 964 mm (bottom) (CORA-W2-08)

At this elevation the bundle is badly damaged (fig.2.3). Essentially there is no bundle shroud. There is but a thin layer of ZrO_2 6 mm long. The fuel pellets are significantly displaced relative to their initial position. However, changes in the area occupied by UO_2 are small. The quantitative results are given in section 2.4.

Five rods have essentially no claddings. The absorber rod array is completely missing. The section contains an insignificant amount of molten metal and rather a small amount of ceramic materials.

2.4. Some Quantitative Data

The results on the amount (thickness) of Zr needed to form ZrO_2 as calculated by formulae (2.1 - 2.3) are tabulated in table 2.1 and are shown in fig.2.4. The initial thickness of cladding was assumed equal to 0.705 mm.

Table 2.1

Fraction of Reacted Zirconium to Form ZrO_2 in Claddings of Fuel Simulators and Bundle Shroud, %

Section				
		W2-01	W2-04	W2-08
Section Height from Bundle Bottom, mm		141	498	964
Simulator Claddings	Formula (2.1)	0	55.26	46.05
	Formula (2.2)	0	43.17	21.29
	Formula (2.3)	0	35.13	16.88
Bundle Shroud	Formula (2.1)	0	25.97	2.92*

* - quantity was calculated on very small fragment of shroud remained in this section.

It is evident from the table that the fractions of reacted zirconium as calculated with different formulae differ to a significant extent. The causes of this are: first, the non-uniform degree of oxidation of the bundle rods which is likely to be due to the non-uniform temperature field in section; second, the error in the measurement of ZrO_2 area is higher than that in the measurement of ZrO_2 thickness. When interpreting these results one should keep in mind that the table shows the fraction of zirconium in the initial position that formed ZrO_2 through the interaction with steam. The indicated Zr was solid in the process of oxidation.

The fragments identified as a solidified melt are located both outside the simulators and between UO_2 of fuel and ZrO_2 of cladding. These are oxygen saturated phases containing mainly zirconium and uranium. The materials of these phases either initially belonged to this section or were relocated from the top sections. They were assumed to be unindentifiable products of interaction. It does not seem feasible to estimate the fraction of oxidized zirconium in those materials.

Table 2.2 and fig 2.5 give the results of measurements of characteristic areas.

Table 2.2

Characteristic Areas in Bundle Sections and Blockage

Parameter		Section		
		W2-01	W2-04	W2-08
Section Height from Bundle Bottom, mm		141	498	964
Pellet Area (UO_2), mm^2		606.6	595.2	582.6
ZrO_2 Area of Claddings, mm^2		0	110.0	65.5
ZrO_2 Area of shroud, mm^2		0	293.0	-
Area of Undefined Materials, mm^2		51	381 650*	274
Blockage of Cross Section,%	Formula (2.4)	3.7	-0.1	-10.6
	Formula (2.5)	2.1	-0.1	- 5.9

* - taking account of bundle shroud materials.

The blocage of the cross section of bundle was determined as follows:

$$B = \frac{F_{mat} - F^{0}_{mat}}{F^{0}} \cdot 100\% , \qquad (2.4)$$

where $F^{0} = 19F_{6} - F^{0}_{mat}$;

$F^{0}_{mat} = 18\pi R_{g}^{2} + \pi R_{a}^{2}$;

$F_{6} = \sqrt{3}/2\, L_{g}^{2}$;

L_{g} is traingular grid pitch, 12,75 mm;
R_{g} is outer radius of simulator cladding, 9,13 mm;
R_{a} is outer radius of absorber rod guide tube, 12,6 mm;
F_{mat} is determined as the total area of materials in section including the area of closed porosity and excluding the area of materials that belong to shroud.

Besides, to calculate the blockage the use was made of the formula:

$$B = \frac{(F_{r} - F^{0}_{мат}) - (F_{r} - F_{мат})}{F_{r} - F^{0}_{мат}} , \qquad (2.5)$$

where F_{r} is initiated area inside bundle shroud, F^{0}_{mat} and F_{mat} are respectively initial and final areas of materials in section.

2.5. Conclusion

The fact that there are no changes in the structure of fuel simulator claddings and bundle shroud materials at elevation of 141 mm (no oxide film or α-Zr(O) layer) indicates that the temperature in the section was not above 610°C (start of α → α+β transformation of Zr1%Nb alloy).

Fe, Cr identified in the material adjacent to UO_2 pellet as well as U, Fe, Cr in the shroud material (section W2-04) point to the feasible mass relocation not only in the vertical direction.

Metallic melts are essentially missing from sections W2-04 and W2-08.

Damage of UO_2 pellets (dissolution, flowing down) in section W2-04 and W2-08 is relative low.

List of Figures

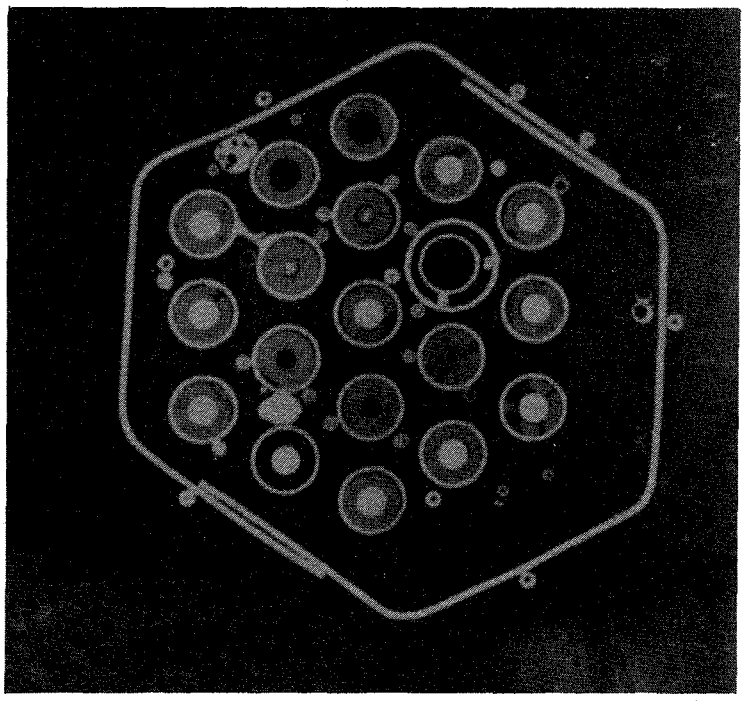

Fig.2.1. General View of Section W2-01.

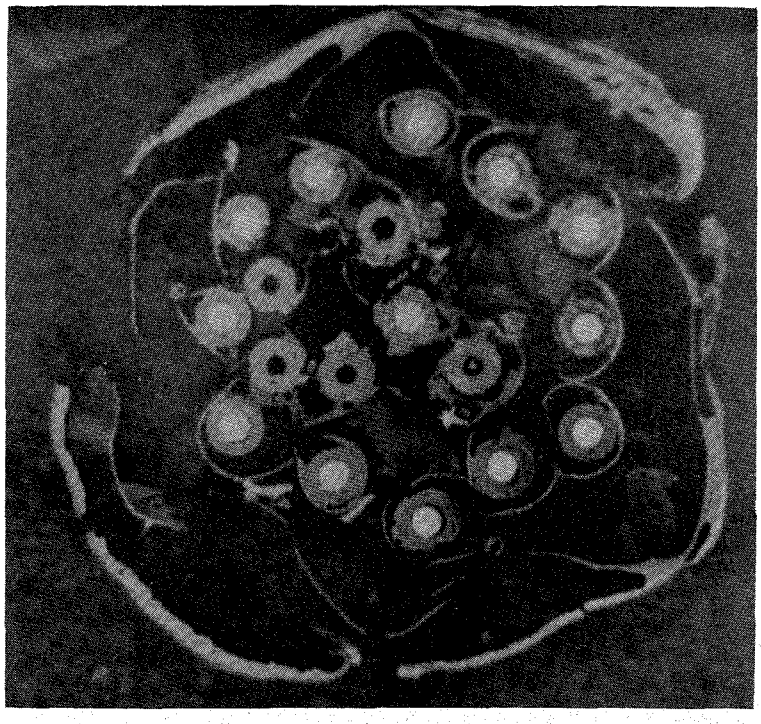

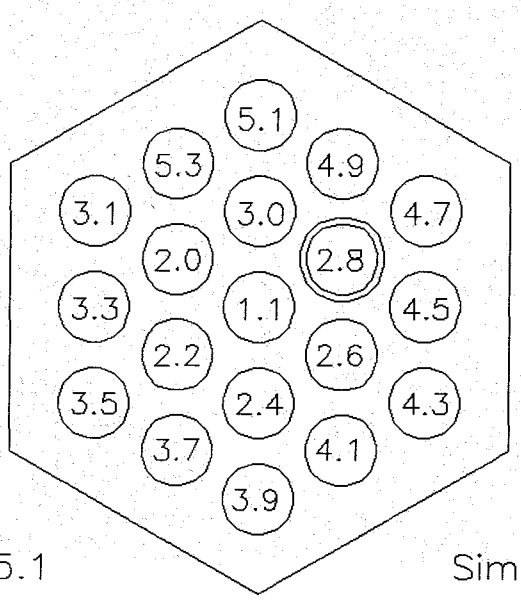

Simulator 5.1 Simulator 3.7

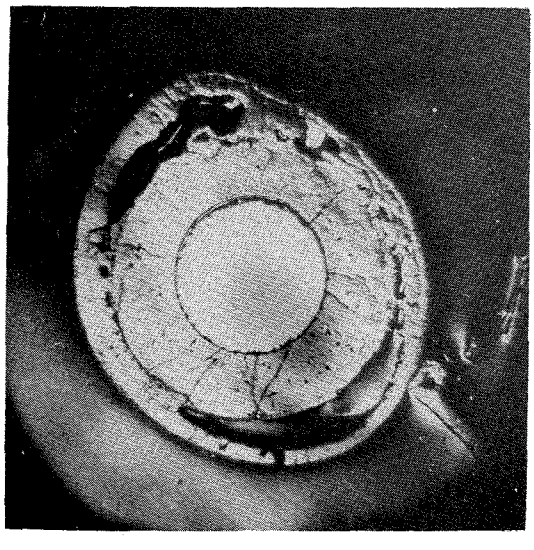

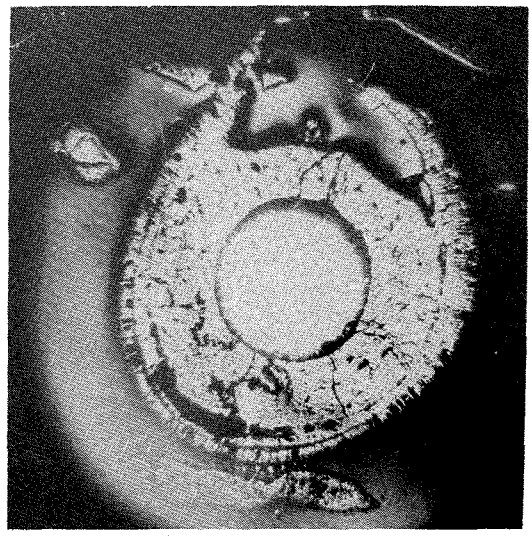

Fig.2.2. Section W2—04. General view and sections of two simulators

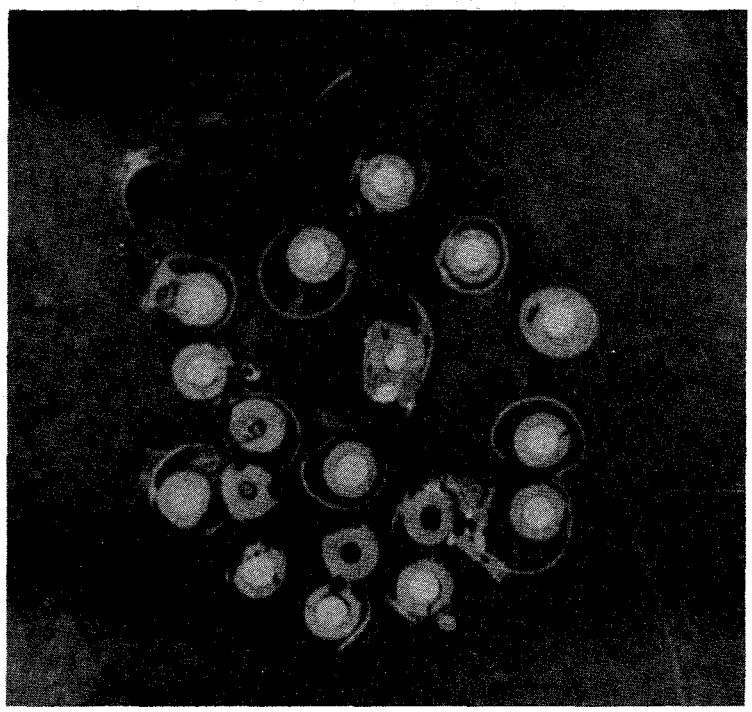

Fig.2.3. General View of Section W2-08.

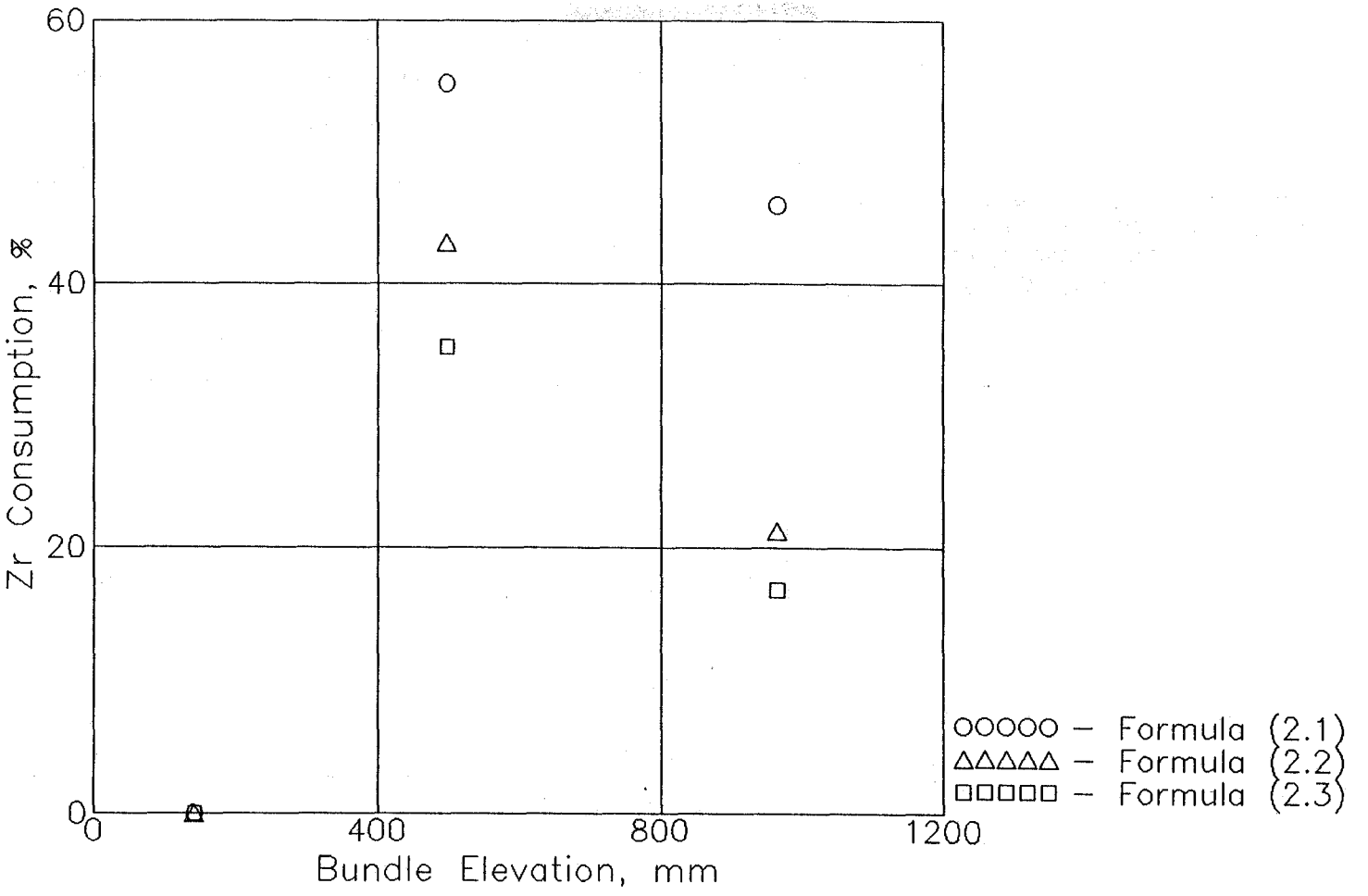

Fig.2.4. Cladding Oxidation at the Elevations 141, 498 and 964 mm of the Bundle CORA–W2 (at original position)

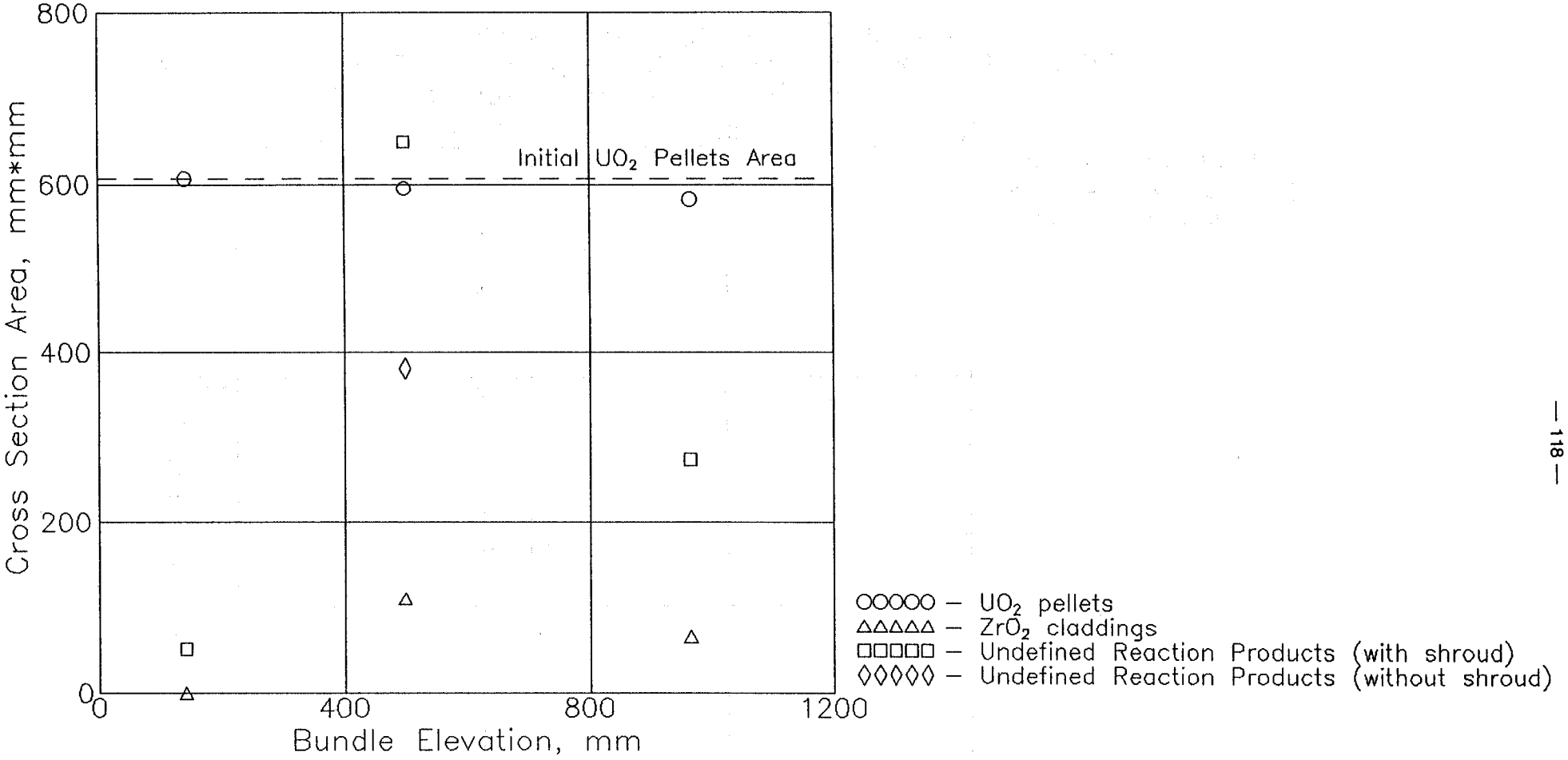

Fig.2.5. UO_2 Pellets, ZrO_2 Claddings and Undefined Reaction Products Cross Section Areas at the Elevations 141, 498 and 964 mm of the Bundle CORA–W2

Microstructural Post-test-Investigation at the Elevations 206, 392, 605 und 910 mm

G. Schanz, P. Hofmann, H. Metzger, J. Burbach

Aug. 1994

Kernforschungszentrum Karlsruhe
Institut für Materialforschung

Microstructural Post-test Investigation at the Elevations 206, 392, 605 and 910 mm

1. Introduction

In this chapter the final status of the bundle is described on the basis of the metallographic investigation of four cross sections, beginning with the lowest elevation. Next, the series of oxide scale thickness measurements, performed on fuel rod cladding across the bundle and at the external and internal surface around the shroud, are presented separately, in order to facilitate the comparison of different elevations. All the information is interpreted in the effort, to reconstruct the bundle degradation mechanisms and sequences.

This approach requires sufficiently detailed and comprehensive analytical information. Analytical results as gained in a systematic SEM/EDX analysis of the bundle, which are reported in a separate chapter, have been used. Some additional element analysis has been especially performed in support of this microstructural investigation.

2. Bundle Elevation 206 mm (CORA-W2-d, top)

At this elevation the bundle is characterized by its still retained configuration (Fig. 1). Relative to spacer grid, fuel rods and absorber rod, the shroud is found excentric and slightly tilted. Considerable proportions of the free volume are blocked by melt, mostly of metallic nature. The annulus between absorber cladding and guide tube is completely filled.

Uniform layers of ZrO_2 scale followed by an α-Zr(O) sublayer, the β -Zr cladding matrix, and finally an interaction zone in contact with the fuel, here denoted as uranium-modified α-Zr(O), are observed (Fig. 2 , Pos. 1). At other positions, lenticular scale growth and spalling of partial layers have occurred (Pos. 2). Often, a layer of externally adhering melt, which has oxidized and is locally lifted off the scale, cannot be clearly distinguished from the usually formed thin external subscale of Zr1Nb cladding, for which similar morphologies are known from HT oxidation studies (Pos. 3, 4).

Embedded into relocated metallic melt, in this case stainless steel melt with molybdenum content (Mo originating from dissolved TC cladding), the fuel rod

cladding got isolated from further steam oxidation (Fig. 3). At Pos. 1 the temperature was sufficiently high to dissolve the scale and to partially melt the cladding. At Pos. 3 a delicate sequence of thin, spalled sublayers have been preserved below the melt, an interesting example of the breakaway oxidation phenomenon /1/.

The oxidation of the shroud has resulted in scales with considerable azimuthal thickness variation and, unexpectedly, the external scales are in general thicker than the internal ones (Fig. 4). This will be discussed later.

The absorber rod arrangement is partly in external contact with molybdenum containing steel melt, probably originating from higher elevations of the absorber itself (Fig. 5). The former guide tube annulus is also filled by steel melt, whereas the absorber cladding is going to be transformed by reaction with the boron carbide into absorber melt. It is mentioned here, that this melt is formed according to an SEM/EDX analysis under dissolution of boron from decomposed B_4C /2/. After solidification a multiphase microstructure with characteristically shaped angular or acicular boride phase primary crystals is observed. The reaction zone around dissolving B_4C particles, enriched in the residual carbon, is clearly visible.

The spacer grid has remained in its original structural geometry (Fig. 6). At most positions the grid did not melt in contact to metallic or oxidized molten masses: At Pos. 2 of Fig. 6 two of the three branches of a junction position are unmolten, whereas the third got partially molten from one side. Besides the predominant metallic stainless steel melt, some unimportant amount of ceramic melt between spacer parts and absorber guide tube are shown in Fig. 6. This multicomponent melt (containing Si, Cr, Fe, Mg, Zr, Ti, Al and O) with respectively low melting temperature must have been formed at higher elevation by interaction of steel with destroyed thermocouples. Details of the oxidation condition of the spacer, the ongoing scale dissolution in contact with metallic melt and the presence of oxidized spacer elements could be used as indications for the locally reached temperature level and the meltdown sequence.

The morphology of the spacer grid oxidation is illustrated in Fig. 7 . The complete scale (Pos. 3) consists of an external and an internal sublayer. The external layer is often missing, either as a result of spalling (Pos. 1), or possibly because it was not formed within narrow gaps under reduced oxidation potential

(Pos. 2). The identification of the layers can be based on the identical morphologies obtained in oxidation studies on the austenitic 15Cr15Ni steel DIN W.Nr. 1.4970 /3/: Accordingly, the external layer consists of coarse-grained wustite and magnetite, the inner layer of iron-nickel-chromium spinel with residual nickel-enriched metallic zones.

The different types of thermocouples shown in Fig. 8 , two of them surrounded by melt, are preserved in still intact condition at the given elevation.

The spectrum of observed melt distributions and morphologies, as illustrated by Fig. 9 to 11 , often allows an identification of the melt type. The melt in Fig. 9 can be summarized roughly as steel melt, contributing elements from cladding, fuel or absorber cannot be directly identified. The originally molten fragment at Pos. 2 in Fig. 10 is interpreted to result from the cladding itself or the fuel dissolution process (ZrO_2 or (Zr, U)O_2 phase plus (Zr,O) phase). At Pos. 4 (and 3) steel melt is indicated by the typical scale morphology. In Fig. 11 the seriously and non-protectively oxidizing metallic melt of Pos. 2 is of the (Zr,U,O) type, at Pos. 3 in contact with another, less oxidized metallic melt.

3. Bundle Elevation 392 mm (CORA-W2-g, top)

According to Fig. 12 the bundle is characterized by strong degradation of absorber rod, spacer grid, and fuel rod cladding compared to relatively intact fuel, and relatively small fractions of retained melt.

The cladding oxidation is almost complete, even for fuel rods of the second ring, which show complete conversion of the cladding to Zirconia (Fig. 13). The morphologies allow to distinguish the already discussed bulged surface layer, at Pos. 2 analyzed as oxidized (Zr,U,O) melt, the bulk scale, which was formed by solid state oxidation, and the inner oxidized part, which was formed after the melting of the cladding (Pos. 4). At Pos. 3 external melt has formed a porous, ceramic structure and modified the substrate scale morphology.

The corner rod of Fig. 14 shows isolated metallic or partly metallic residues, either identified as fuel rod melt with duplex structure of (Zr,O) phase and (Zr,U)O_2 phase (Pos. 2 and 5) or an unidentified alloy of the most oxidation resistent bundle materials (Pos. 3). The also observed local pellet attack is treated below in more detail.

The shroud oxidation is much advanced, but not complete (Fig. 15). The wall thickness is larger than the original 1 mm plus the expected increment related with oxide formation. The thickness increase can only be explained by the assumption, that melt, most probably from the molten shroud matrix above, has accumulated between the stabilizing external and internal scale. The shroud microstructures confirm this interpretation in so far, as shroud melting is indicated by duplex α-Zr(O) + ZrO_2 phase distribution with obviously flat oxygen concentration profiles. In addition, also interference with other melt, originating from steel structures is identified, according to the special microstructures, Fe-modified ZrO_2 in Fig. 15, Pos. 2 and Fe-modified ZrO_2+(Zr,O) at Pos. 4. This contamination might have penetrated from the internal side into the shroud wall. This would also explain the observation, that the internal scale is generally thinner than the external scale: Eutectic melt formation by interaction between the steel-rich melt and the shroud could have protected the internal shroud surface from extensive oxidation.

The absorber rod arragement has not survived at this elevation, but most of the boron carbide absorber material itself, which is infiltrated and thus mechanically stabilized by absorber melt, is still present (Fig. 16). The surrounding melt with variable microstructures can be interpreted as "fuel rod melt" ((Zr,U)O_2 at Pos. 2 and (Zr,U)O_2 + (Zr,O) at Pos. 3, both Fe-contamined) or "absorber melt" with (Zr,O) matrix at Pos. 4 and (Zr,U)O_2 matrix and boride phases at Pos. 5 to 7.

The spacer grid, mostly destroyed as already mentioned, has been completely oxidized in the remaining parts (Fig. 17 , Pos. 1 und 3), or had been in contact with melt, subsequently oxidized (Pos. 2, probably a partly molten junction in Pos. 4).

Fig. 18 is depicting a grid spacer thermocouple embedded by melt and a fuel centerline thermocouple, both in the status of proceeding destruction. The latter, with its cladding on molybdenum basis and its beryllium oxide insulation has melted and reacted with the pellet. Beryllium oxide is found precipitated from the metallic thermocouple melt and in form of eutectic UO_2/BeO microstructure within the pellet.

Examples for fuel rod melt and fuel rod infiltration by melt are shown in Fig. 19 , Pos. 3 and 1, respectively, in the latter case with metallic residues in the oxidized

melt. The aspects of fuel pellet dissolution and cladding attack after penetration of melt into the fuel rod are illustrated in Fig. 20 . Cavities help to quantity the extent of the dissolution, since most of the product melt has relocated later on. The pellet was influenced in the bulk (Pos. 4) and completely transformed within an originally liquefied, reaction layer (Pos. 5).

Fig. 21 combines some observations on varieties of pellet destruction, the desintegration (Pos. 1), the formation of a reaction layer (Pos. 2) and the homogeneous reaction within the bulk (in Pos. 3 with metallic particle and growth of UO_2/BeO eutectic, in Pos. 4 with unidentified metallic precipitates, probably of (U,Zr) phase).

4. Bundle Elevation 605 mm (CORA-W2-k, top)

At this elevation the bundle is characterized by accumulation of melt, resulting mainly from fuel dissolution into molten cladding, which has occurred here and above (Fig. 22). The absorber rod arrangement has completely disappeared, the spacer grid is almost destroyed, ca. one third of the shroud is missing.

The cladding oxidation, as illustrated in Fig. 23 for corner rods of the second ring, was almost complete. Obviously, simultaneous reactions, competing with the external cladding oxidation by steam, have been the internal clad melting and fuel dissolution (Pos. 1), the axial splitting of the cladding, its opening under oxide growth stresses (the so-called flowering), the penetration of melt into the rod (Pos. 3) and the melt relocation downwards and outwards. At another corner rod (Fig. 24, Pos. 2) such a melt has developed considerable porosity and has oxidized completely at place within the rod. This figure shows in addition the complete oxidative conversion of various rubble fragments and of a residual spacer grid segment.

The shroud oxidation is not yet complete at all circumferential positions, according to duplex matrix microstructures of some remaining metallic α-Zr(O) together with ZrO_2 (Fig. 25), Pos. 2 to 4). With the increased total wall thickness and the relatively thin or even missing internal scale the shroud oxidation corresponds to that of the already discussed elevation 392 mm.

Figures 26 to 33 have been composed to illustrate the variability of melts and their interaction with remaining bundle structures. Fig. 26 combines duplex

metallic/ceramic melts, which can be attributed to the fuel/cladding interaction. For Pos. 1 the obvious oxygen concentration gradients are mentioned, for Pos. 4 and 5 the contamination of the melt, originating from steel, according to the complex microstructures. Without the attempt of interpreting the various metallic and ceramic melt constituents, Fig. 27 gives examples of their distribution and their decomposition into different phases during cooldown and solidifaction. In a schematic way Fig. 28 compares a multicomponent metallic melt and a mostly oxidized melt, in contact with a pellet and, observed elsewhere, far off, in their ability to dissolve a pellet. Strong dissolution by the metallic melt is going on at Pos. 1. In contrast, only some oxygen transport from the fuel across a contact layer is visualized by the absence of the metallic residues of the oxidized melt (Pos. 3). Accordingly, the fuel in contact with the oxidized melt in Fig. 29 is no longer attacked, finally. The melt is most probably of the "fuel rod type" (Zr,U,O), as identified with the typical eutectic $(Zr,U)O_2$ / $(U,Zr)O_2$ microstructure at Pos. 2. In contrast, the void of Fig. 30, Pos. 1, which is very close to the steel-containing (Zr,U,O) melts of Fig. 26 must have been filled by metallic melt of strong fuel dissolution potential, before it has relocated and the reaction layers have oxidized. Considerable dissolution is also seen in the macrograph for the pellet of another fuel rod, which will be shown in the next two figures: Fig. 31 shows the attack of metallic melt on oxidized cladding (Pos. 1) together with complex microstructures of resolidified melt (Pos. 2, 3). According to an SEM/EDX analysis, in which the elements Zr,U,Fe,O, at some positions also Cr or Ni have been identified, a multicomponent melt from cladding, fuel and absorber rod or spacer grid interaction has dissolved and re-precipitated ZrO_2 or $(Zr,U)O_2$, respectively, and formed a metallic residual melt, in the figure denoted as (Zr,U,Fe,O). The surrounded pellet, as illustrated by Fig. 32 is attacked and deeply infiltrated by the melt described above, as confirmed by detection of Zr,Fe,Cr in addition to U and O. Similar metallic melt containing Zr,U,Fe,Cr,Ni and O from complex cladding/fuel/absorber rod or spacer grid interaction is found to have attacked fuel rod cladding as well as pellets at various positions (Fig. 33).

5. Bundle Elevation 910 mm (CORA-W2-p, top)

At this elevation the bundle is characterized by completely oxidized (and "flowered") cladding residues, oxidized fuel interaction melt, in contrast to a pool of other retained, still metallic melt (Fig. 34). A wide spectrum of pellet conditions and the absence of absorber rod and shroud are mentioned.

The oxidation status of the cladding, as shown in Fig. 35, is that of complete conversion of the total wall (Pos. 1) or the residual wall fraction (Pos. 3) to oxide. Melt in external or internal contact is remaining in oxidized form.

The metallic melt in contact with three of the six rods, adjacent to the missing absorber rod, has been analyzed as melt from the absorber rod degradation (Fig. 36, Pos. 3 and 5). It is characterized by complex microstructure (Pos. 3) and considerable pellet attack (Pos. 5). This melt is found to interfere with melt from fuel/cladding interaction (Pos. 2 and 4), which is identified in the oxidized final form as $(Zr,U)O_2$ / $(U,Zr)O_2$ eutectic (Pos. 1).

A closer inspection of other fuel rods (Fig. 37) shows oxidized melt residues between cladding and fuel (Pos. 1), a melt-modified cladding microstructure (Pos. 3, 4) and a deeply dissolved pellet. In Fig. 38, Pos. 3 metallic melt, assumed to correspond to the complex composition as discussed with Fig. 31 to 33 (cladding/absorber rod/fuel interaction melt) is depicted and compared to simple fuel rod melt (Pos. 1). Finally, in Fig. 39 microstructures of two pellets are shown, the one after complete infiltration by melt but without loss of integrity (Pos. 1, 2), the other after loss of volume and form by intense reaction, partial melting, relocation or solidification as complex reaction product.

6. Quantitative Results on Fuel Rod Cladding and Shroud Oxidation

In order to quantify the extent of oxidation of the fuel rod cladding and the shroud, series of ZrO_2 scale thickness measurements have been performed at the already discussed bundle elevations 206, 392, 605 and 910 mm.

The minimum / average / maximum values for the individual fuel rods are based on typical local values obtained at several circumferential positions with free steam exposed scale surface. They include not only the internal partial scale, grown after clad melting, but also the oxidized originally molten reaction zone with the pellet, since these zones cannot be easily distinguished in the oxidized condition. In order to draw oxidation profiles across the bundle, pairs of measurements at opposite sides in the 90°/270° direction were included for the two lowest elevations. The shroud oxidation was determined on both sides every 20° around the circumference.

Cladding oxidation profiles across the bundle in the 90° to 270° direction along the central row of five rods and the parallel rows of four or three rods are drawn for the 206 mm elevation in Fig. 40. The central profile is rather flat and decreases sharply towards the small internal shroud scale values. The parallel profiles, as far as measurable, are comparatively low. The respective values at the 392 mm level are more than an order of magnitude higher (Fig. 41). Compared to the central profile, by chance rather regular, the parallel side profiles are very unsystematic. Low values are the consequence of partial cladding meltdown before complete oxidation. Temporal contact with relocated melt could also have delayed the cladding oxidation locally. The high scale thickness values always include the contribution of agglomerated and subsequently oxidized melt. In total the observed disturbances of the oxidation profiles are explained.

The plot of the shroud oxidation around its circumference at the 206 mm level is rather complex (Fig. 42): Some high external side values are comparable to the cladding oxidation at this elevation. A certain correlation between the both sides is obvious, the internal oxidation is generally less advanced or even negligible at a few position. The corresponding plot at the 392 mm elevation (Fig. 43) combines the smooth external scale curve with the fluctuating internal scale curve. Similar results are drawn for the 605 mm elevation in Fig. 44. Here the smooth additional curve for total oxidation, the percentage of cladding conversion to oxide, was defined as the fractional thickness of both scales plus the estimated volume fraction of ZrO_2 in the ceramic/metallic matrix. The discrepancy between thin scales, as measured, and the high oxygen content of the wall matrix, as deduced from the microstructure, are the typical result of fast, equilibrating oxygen diffusion in the liquid state, in which a strong dissolution tendency was moderating the scale growth. This interpretation alone does not explain the smaller scale thickness at the inner side. Here the already mentioned interaction with other metallic melt has occurred, deduced from the iron contamination of the shroud. A further, most probable explanation is, that spalling of scale has occurred during the transient or in the cooldown phase. Consequently, the measured thickness values of the internal side of the shroud would not be adequate for a comparison with oxidation calculations.

The axial oxidation profile along the bundle, drawn in Fig. 45, shows unimportant differences between the average values for central rod, first and second ring, broad scatter bands and the steep axial increase to the plateau of complete oxidation.

7. Summary

- Morphologies of oxidized cladding and shroud indicate the formation of regular sublayers or, locally observed, forms of lenticular scale growth or spalling of scale sublayers. This must have influenced the oxidation kinetics.

- Towards complete external steam oxidation the fuel rod cladding is also degraded by melting and fuel dissolution together with deformation ("flowering") and embrittlement.

- Lateral cladding oxidation profiles across the bundle are rather flat, but disturbed and therefore irregular, at the lowest elevation due to resolidified metallic melt, at the higher elevations due to partial meltdown before oxidation or melt agglomeration and continuing oxidation.

- According to the axial cladding oxidation profile more than half of the bundle length is completely oxidized.

- The shroud oxidation profiles around the circumference confirm the pronounced axial gradient and indicate considerable azimuthal variations and disturbances in relation with shroud melting and contamination by melt, wall thickening and local scale spalling.

- The lower half of the bundle has retained relatively intact fuel pellets compared to the advanced degradation of other components and the relocation of metallic melt.

- Stainless steel melt, formed by melting of spacer grid and absorber arrangements is accumulating as a partial bundle blockage.

- Compared to a western-type BWR with Zircaloy absorber channel box and consequently Zr/SS eutectic melt formation, the absorber arragement meltdown seems to be less dramatic. This could be an advantage with respect to potential recriticality.

- the upper half of the bundle has experienced strong melt formation and relocation due to fuel dissolution as well as strong degradation of all components by chemical interactions and fragmentation.

- Multicomponent melt, formed by interaction of cladding, fuel and stainless steel from spacer grid and absorber rod, is able to penetrate through the cladding and to dissolve fuel pellets severely by infiltration and liquefaction.

Literature

/1/ G. Schanz, S. Leistikow
Microstructural Reasons for Mechanical Oxide Degradation (Breakaway Effect) and Resulting Kinetic Anomalies of Zircaloy-4/Steam-HT-Oxidation
Proc. 8th Intern. Congress Metallic Corrosion, Mainz 6. - 11.9.81, Vol. II, p. 1712-1717

/2/ P. Hofmann, M. Markiewicz, J. Spino:
Reaction Behavior of B_4C Absorber Material with Stainless Steel and Zircaloy in Severe LWR Accidents, Nuclear Technology, Vol. 90 (1990) 226-244

/3/ S. Leistikow, G. Schanz, Z. Zurek:
Comparison of High Temperature Steam Oxidation Behaviour of Zircaloy-4 Versus Austenitic and Ferritic Steels under Water Reactor Safety Aspects.
First Polish-German Seminar on Properties of High Temperature Alloys, 3-6 July 1985. Proc. in Chemistry Bulletin 5, Cracow 1987, 123 - 154

List of figures

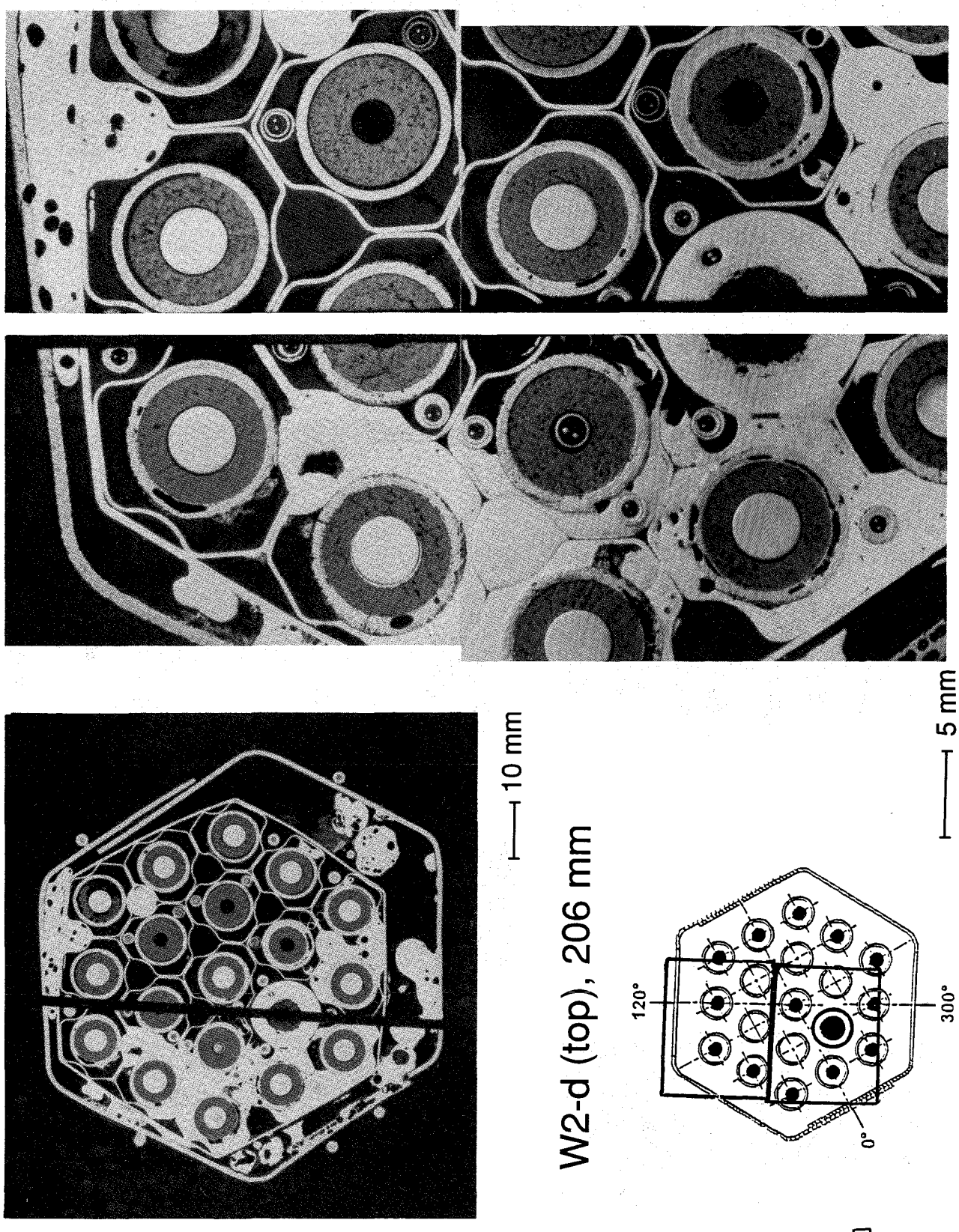

KfK IMF

Fig. 1:

Cross Section CORA-W2-d (top), Elevation 206 mm
Overview

W2-d (top), 206 mm

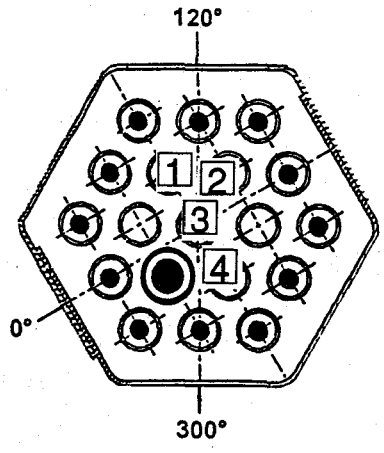

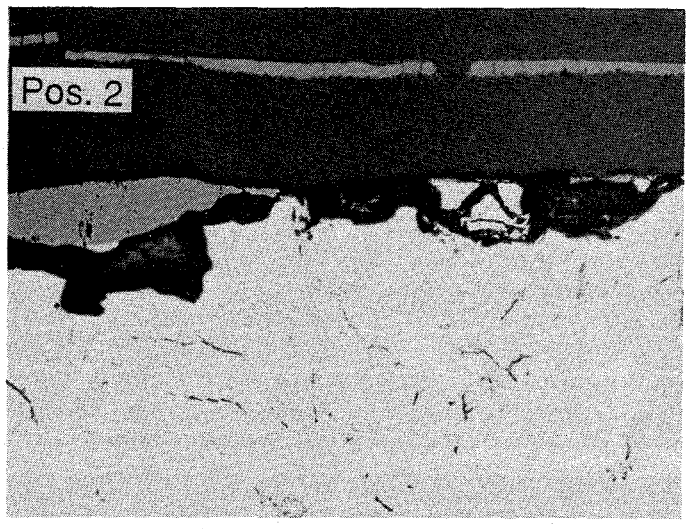

50 µm

Pos. 3

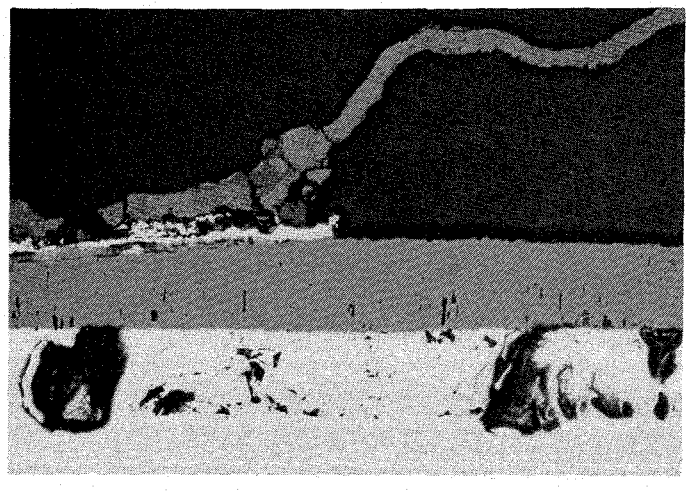

50 µm

Pos. 1 Unheated fuel rod

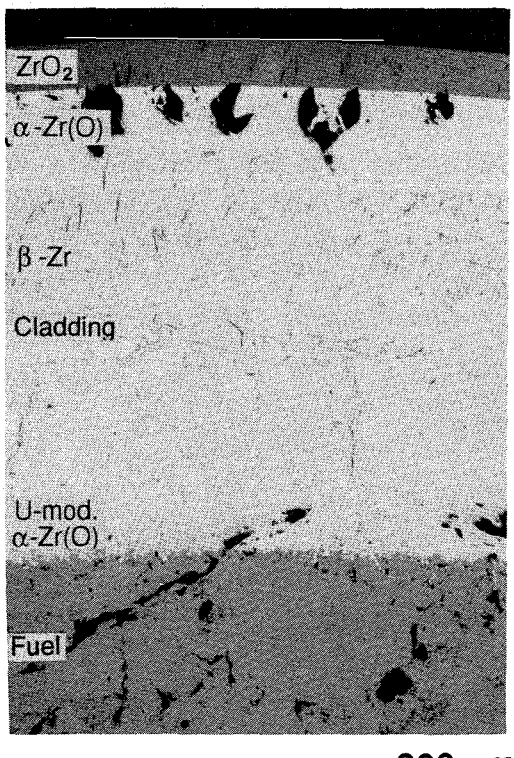

200 µm

Pos. 4

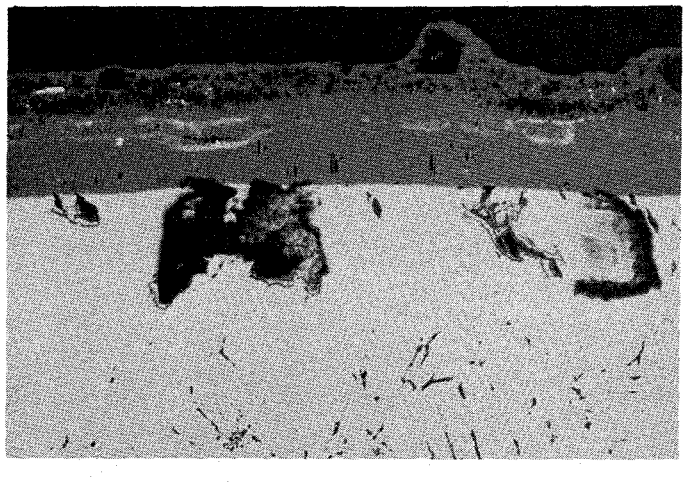

50 µm

KfK IMF

Fig. 2:

Cross Section CORA-W2-d (top), Elevation 206 mm
Cladding Oxidation

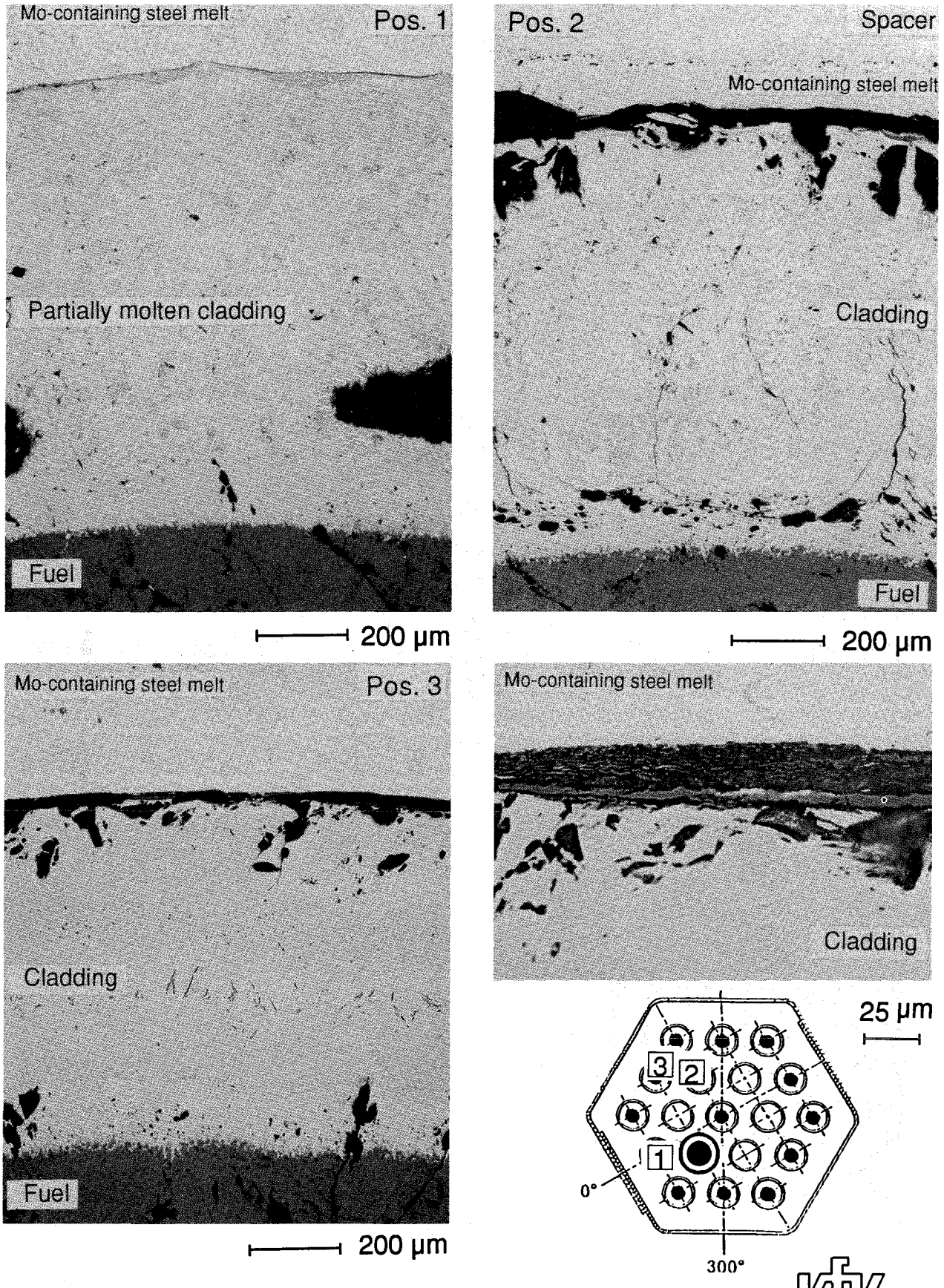

Fig. 3:

Cross Section CORA-W2-d (top), Elevation 206 mm Cladding in Contact with Metallic Melt

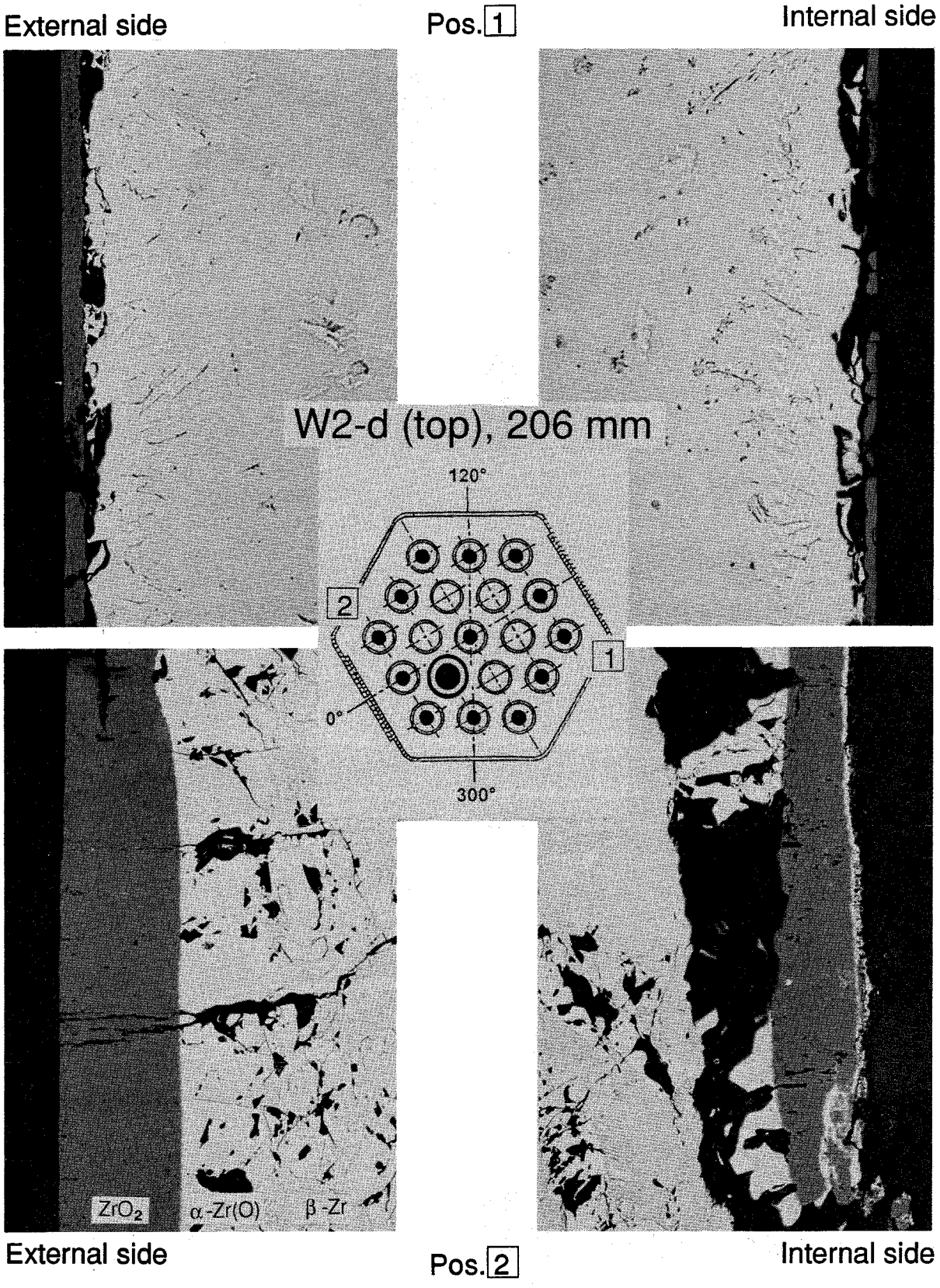

Fig. 4:

Cross Section CORA-W2-d (top), Elevation 206 mm Shroud Oxidation

W2-d (top), 206 mm

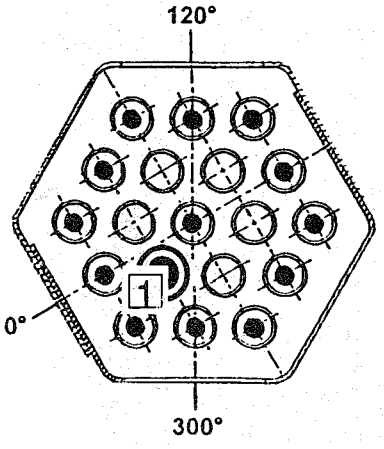

Pos. 1

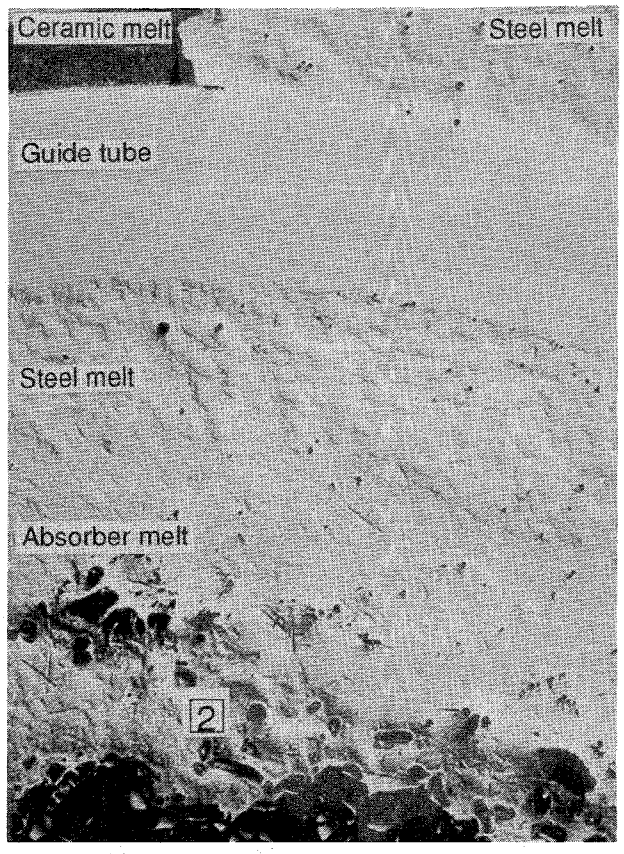

500 µm

Absorber melt, embedding B_4C particles

Pos. 2

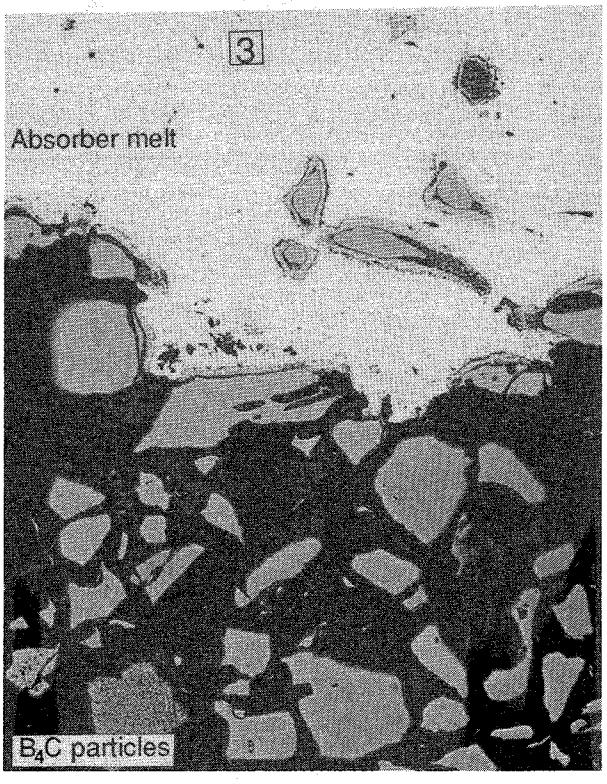

100 µm

Pos. 3

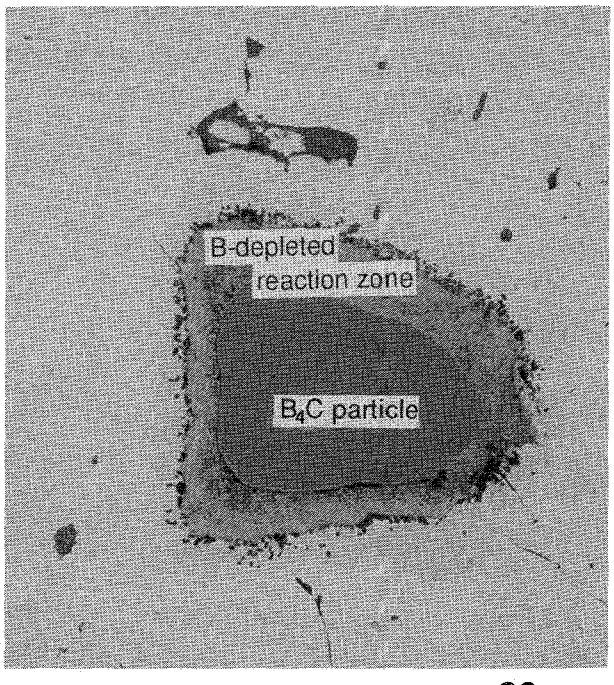

20 µm

IMF

Fig. 5:

Cross Section CORA-W2-d (top), Elevation 206 mm
Absorber Rod

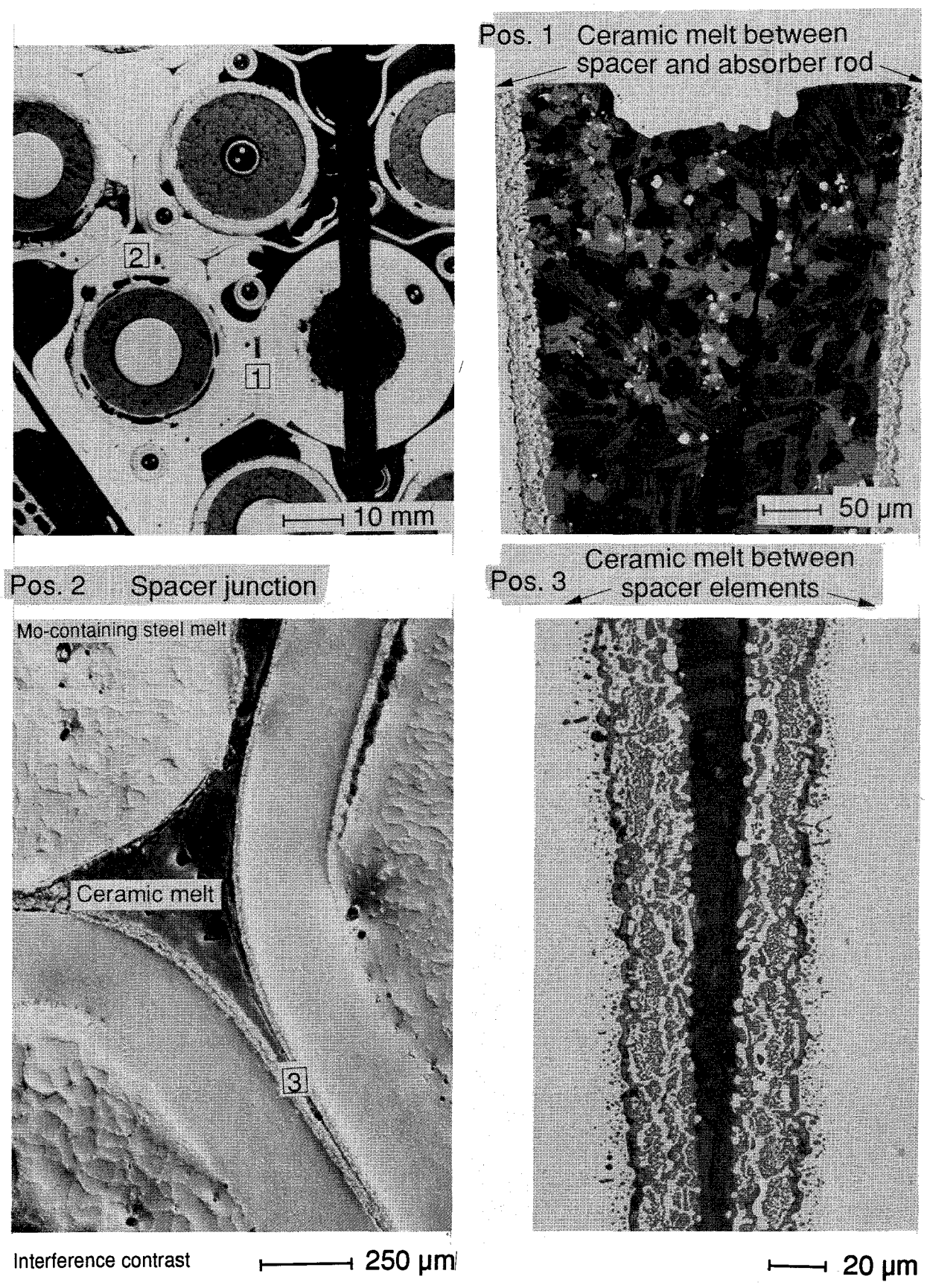

Fig. 6:

Cross Section CORA-W2-d (top), Elevation 206 mm
Spacer Grid, Ceramic and Metallic Melt

Pos. 1

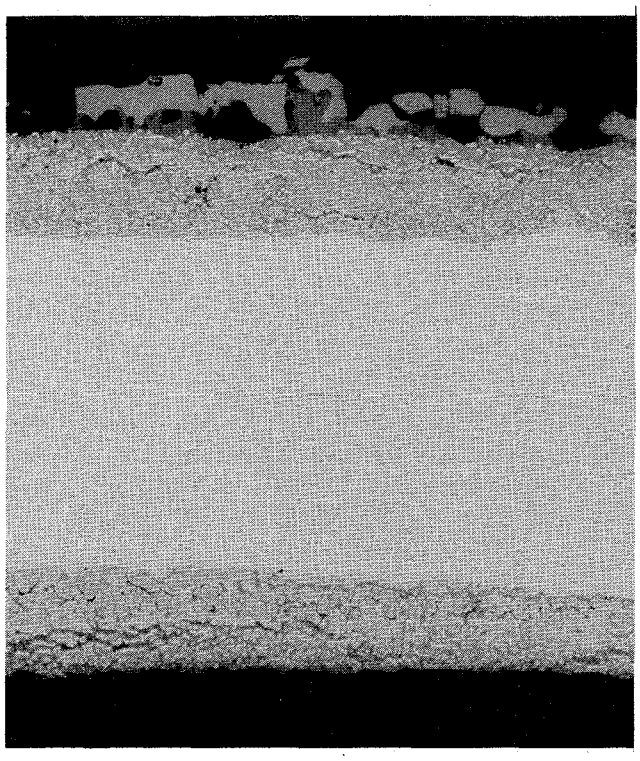

50 µm

Pos. 2

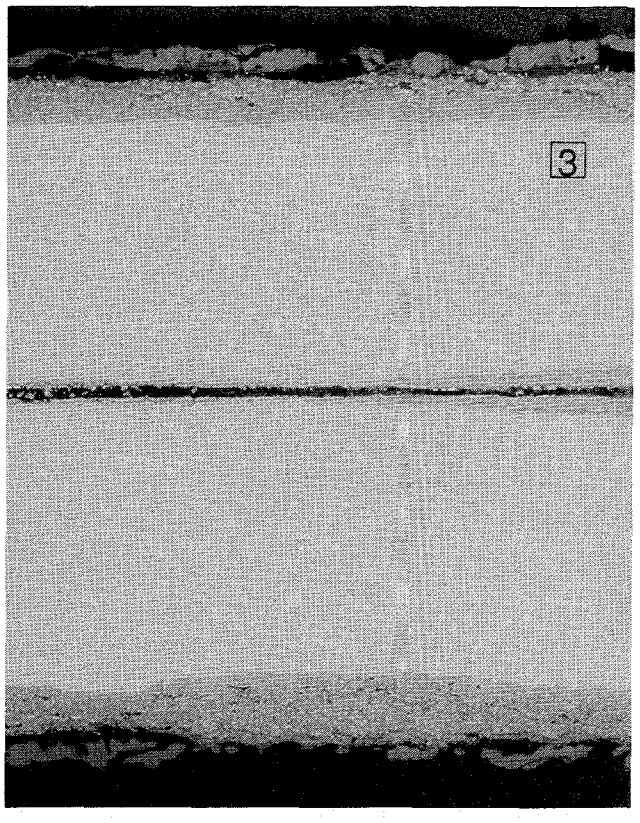

100 µm

W2-d (top), 206 mm

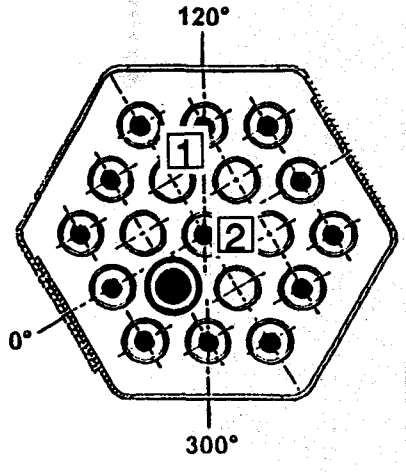

Pos. 3

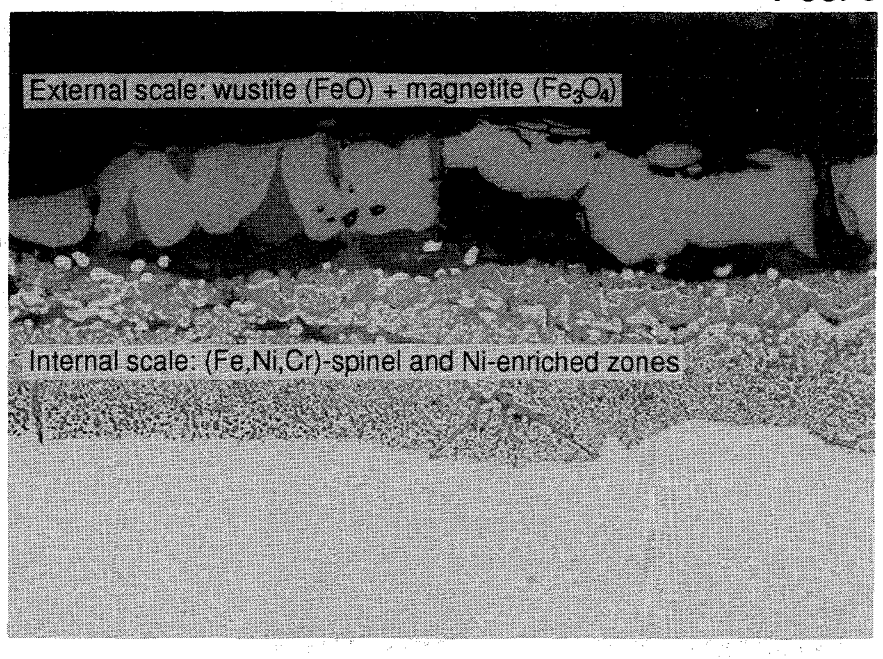

20 µm

Fig. 7:

Cross Section CORA-W2-d (top), Elevation 206 mm
Spacer Grid Oxidation

Spacer grid TC

Pos. 1

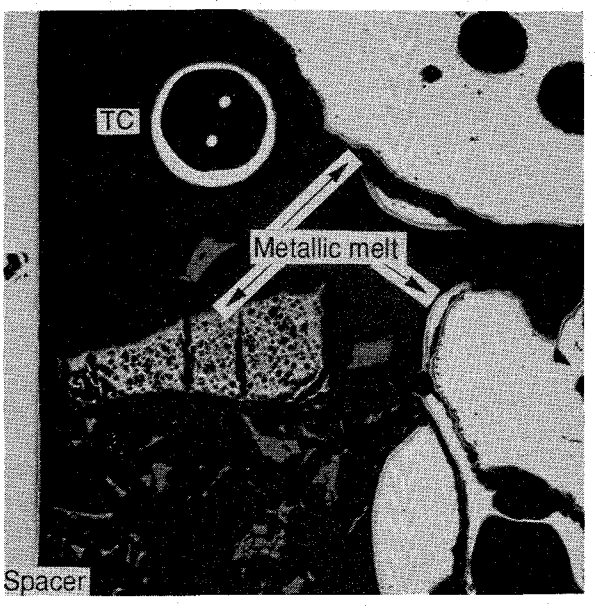

1 mm

W2-d (top), 206 mm

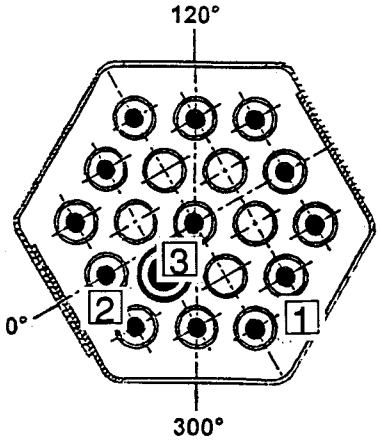

Pos. 2 Heated rod TC

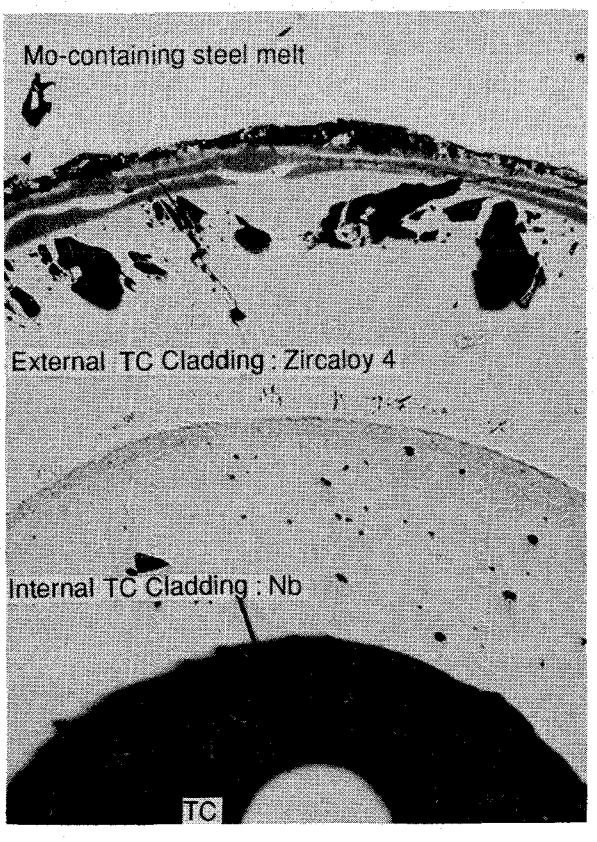

200 µm

Pos. 3 Absorber rod TC

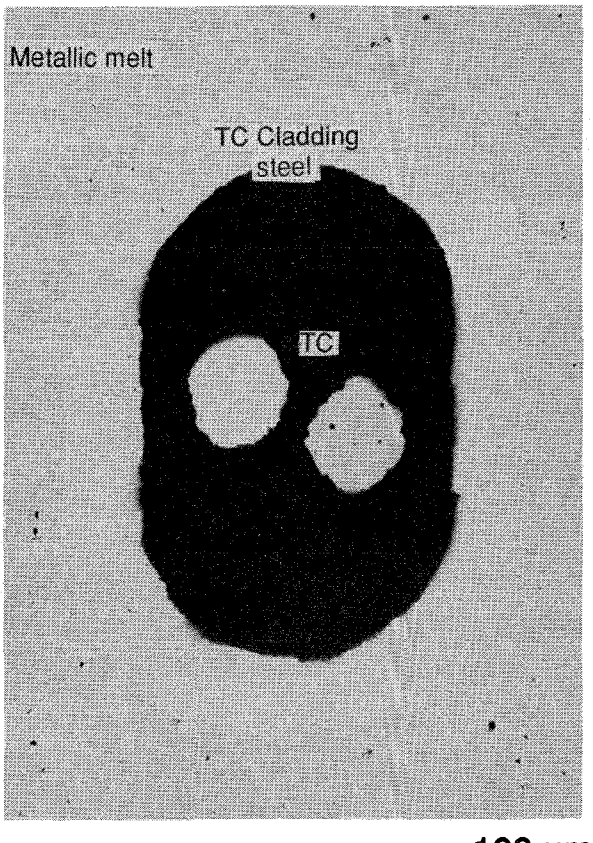

100 µm

KfK IMF

Fig. 8:

Cross Section CORA-W2-d (top), Elevation 206 mm
Thermocouples

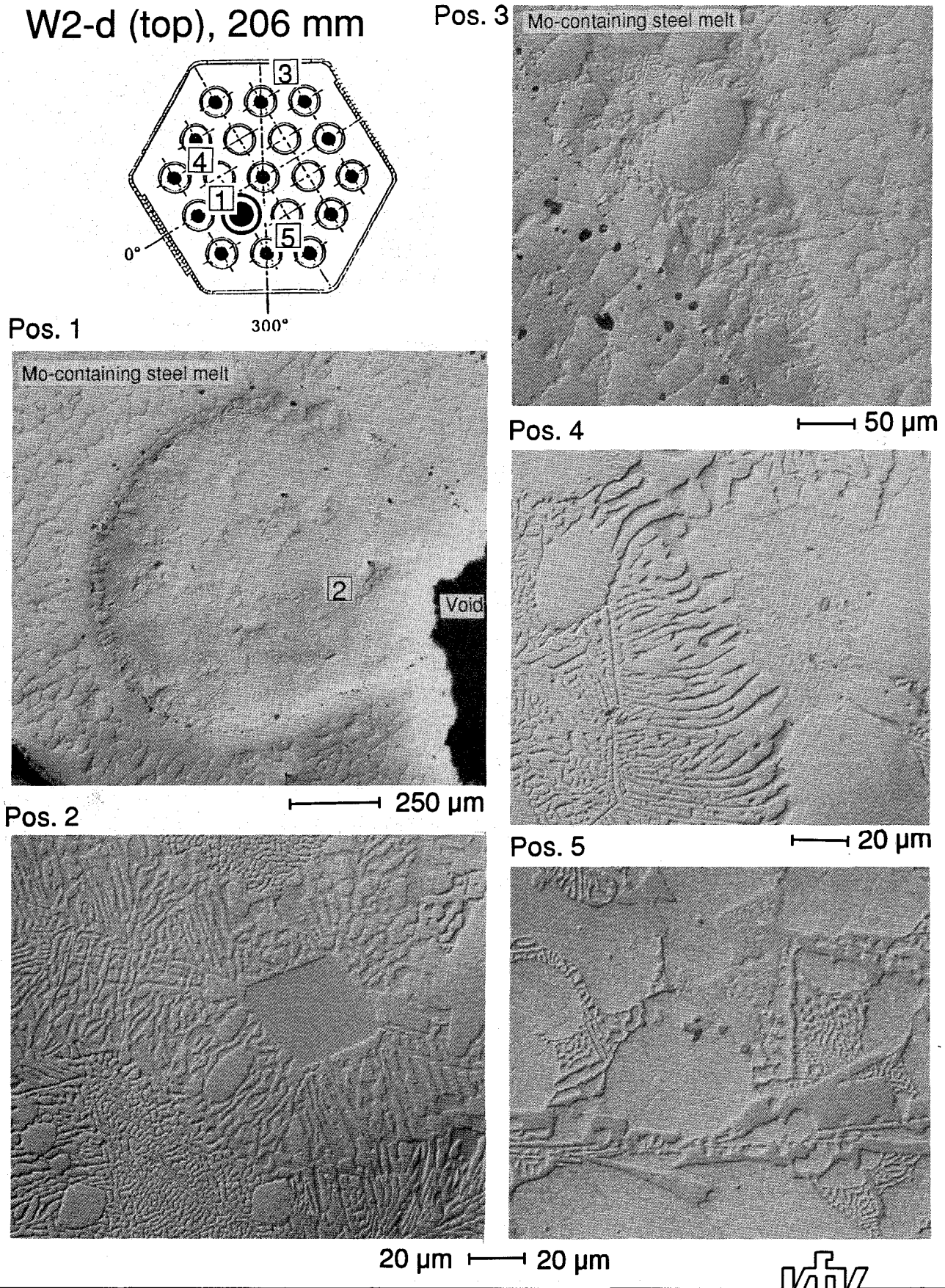

Fig. 9:

Cross Section CORA-W2-d (top), Elevation 206 mm
Morphology of Metallic Melt (Interference Contrast)

W2-d (top), 206 mm

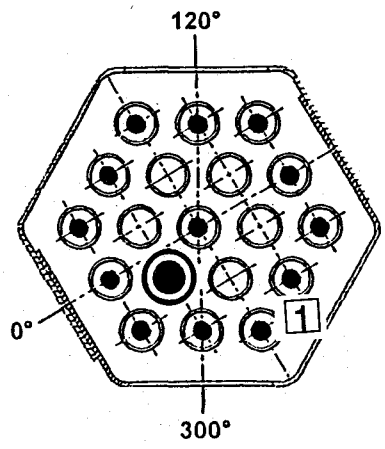

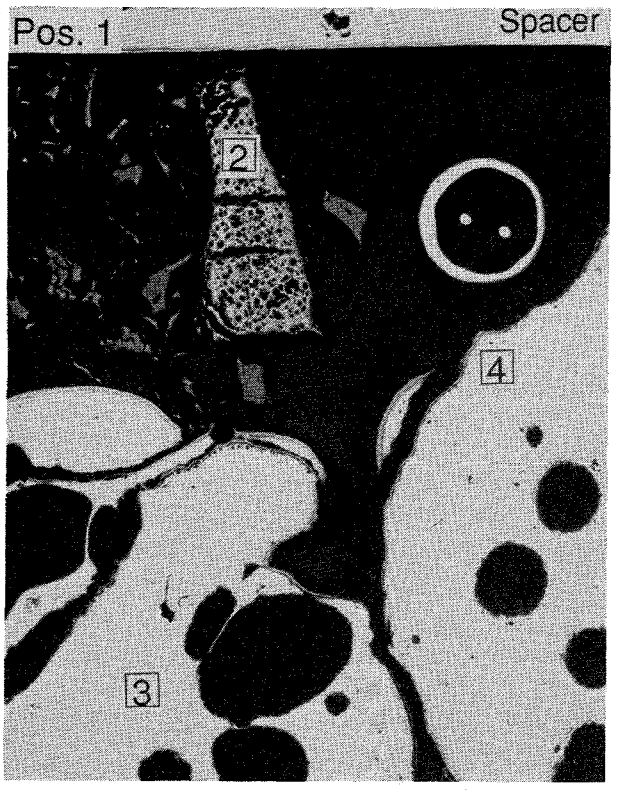

1 mm

Pos. 2

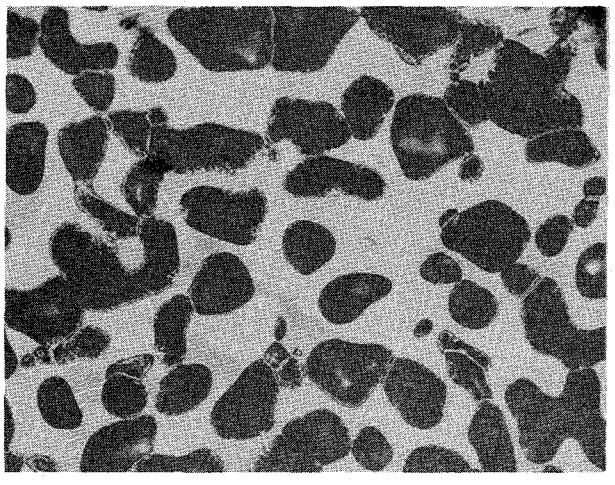

20 µm

Pos. 3

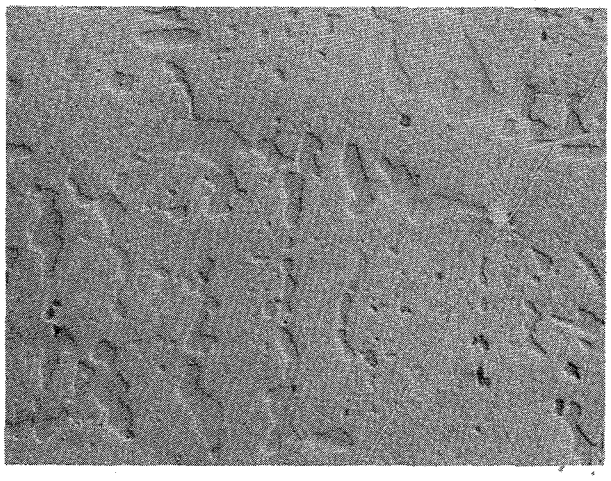

Pos. 4

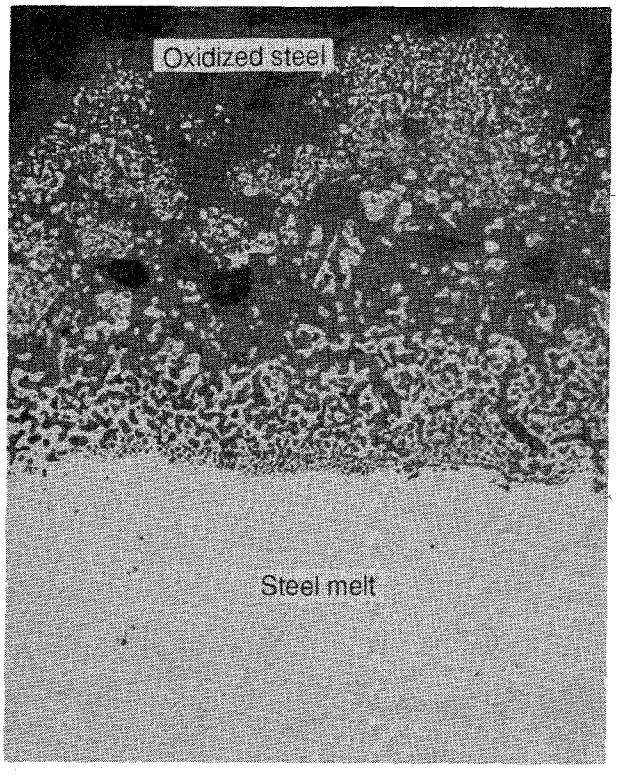

Interference contrast

20 µm 20 µm

KfK IMF

Fig. 10:

Cross Section CORA-W2-d (top), Elevation 206 mm
Relocated Melts between Spacer Grid and Shroud

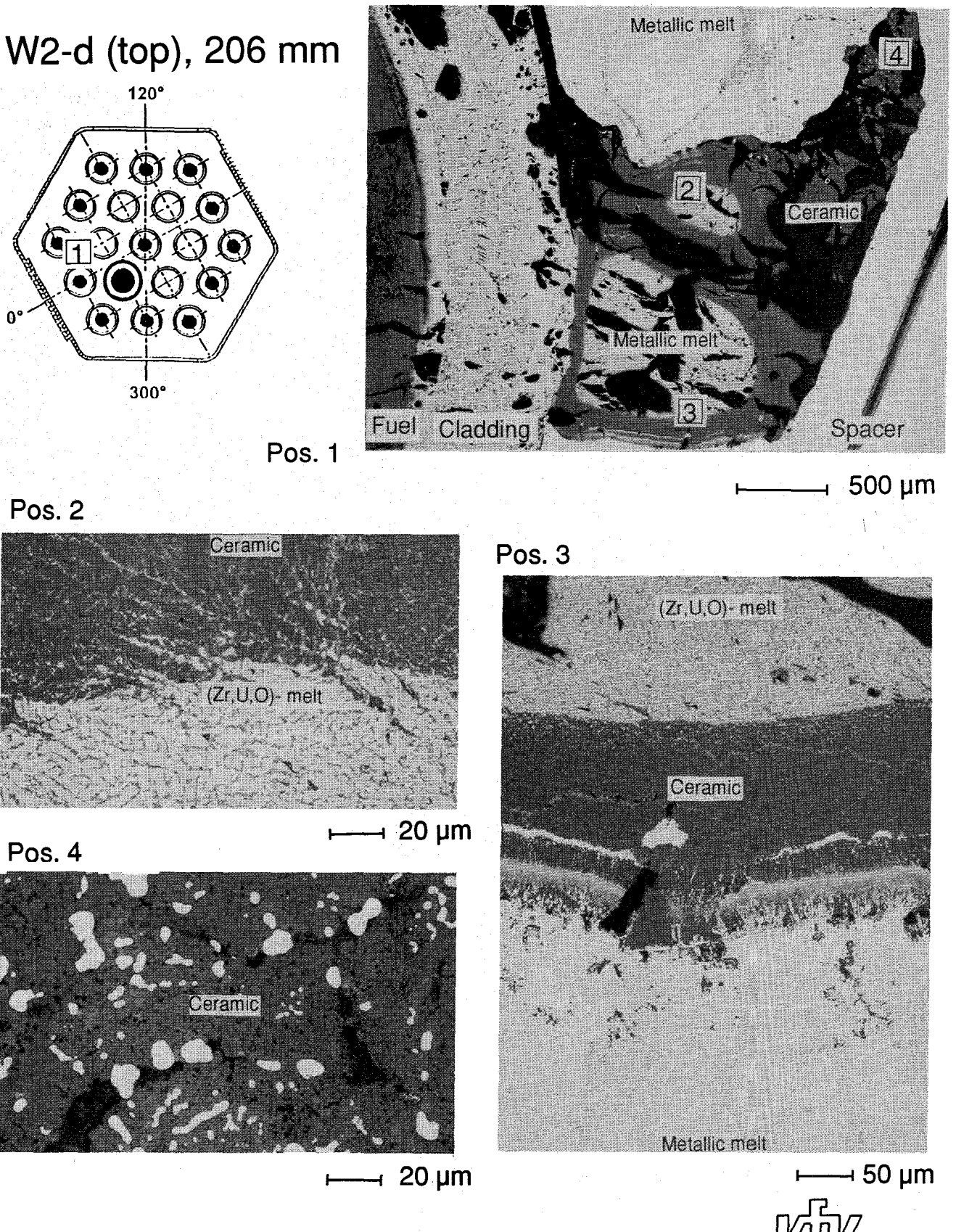

KfK IMF

Fig. 11:

Cross Section CORA-W2-d (top), Elevation 206 mm
Distribution of Relocated Melts

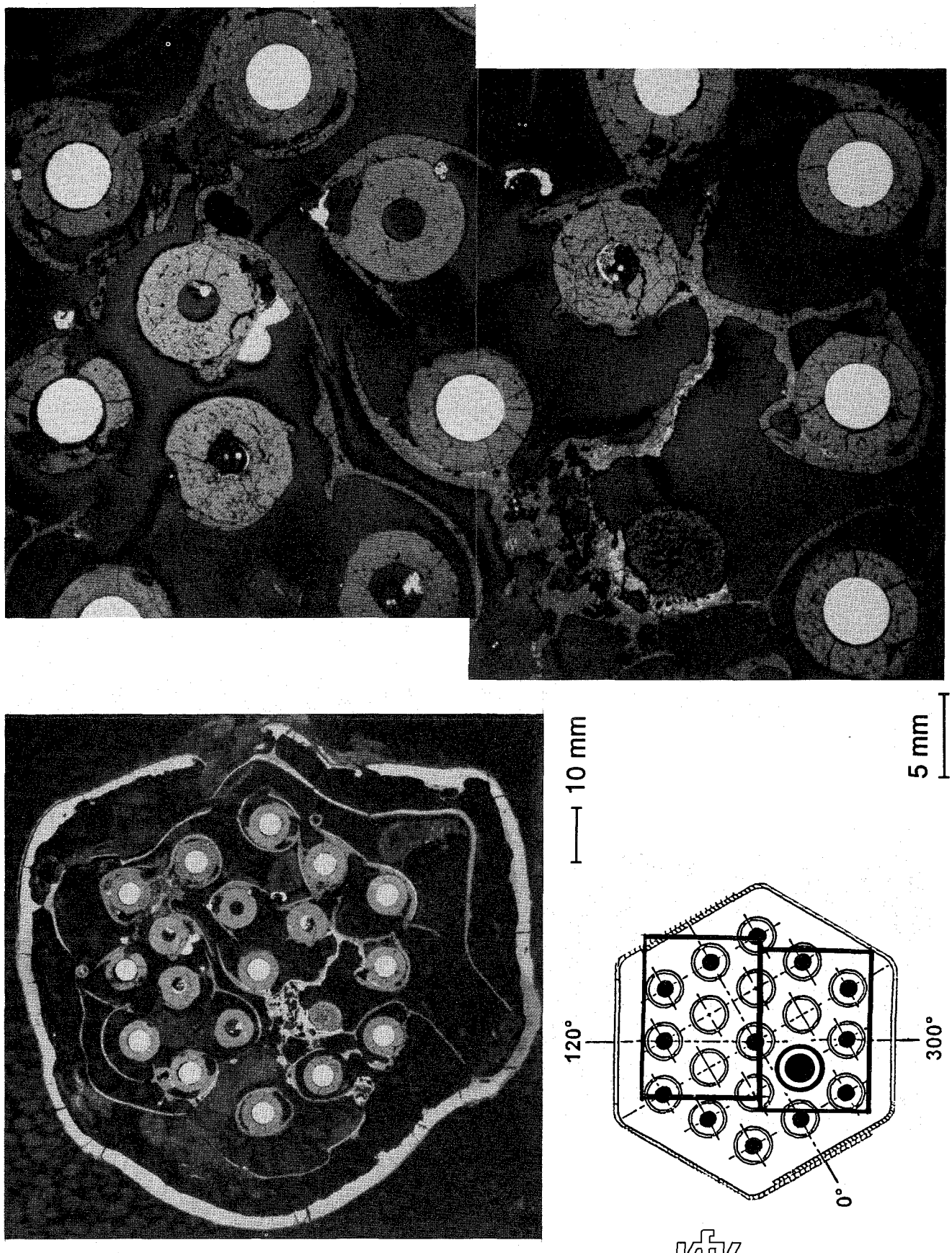

KfK IMF

Fig. 12:
Cross Section CORA-W2-g (top), Elevation 392 mm
Overview

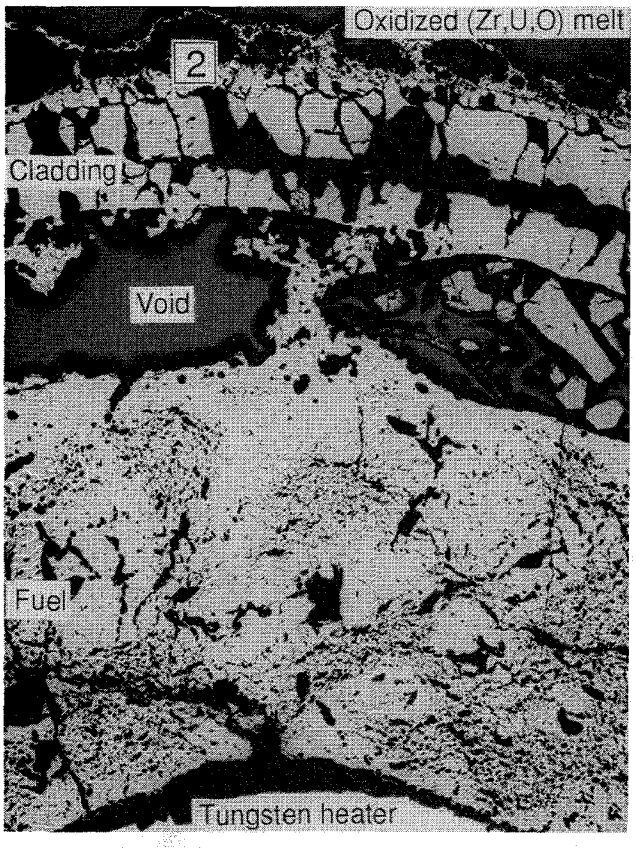

Pos. 1 ⟷ 500 µm

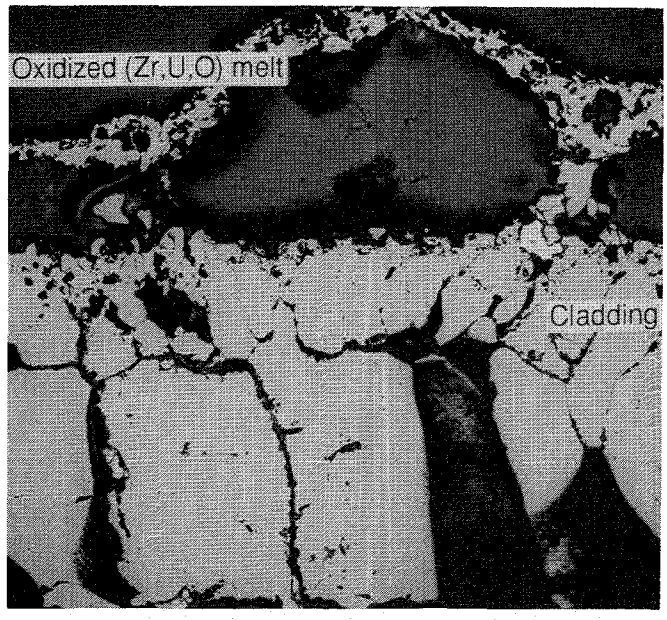

Pos. 2 ⟷ 100 µm

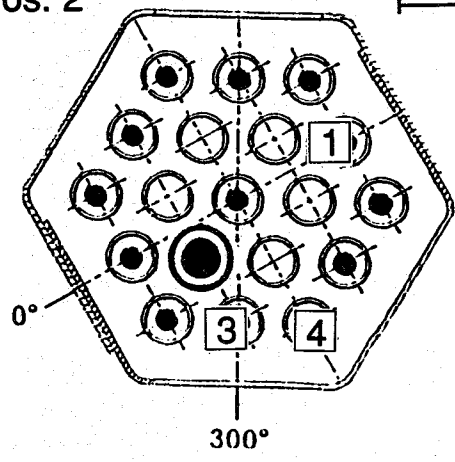

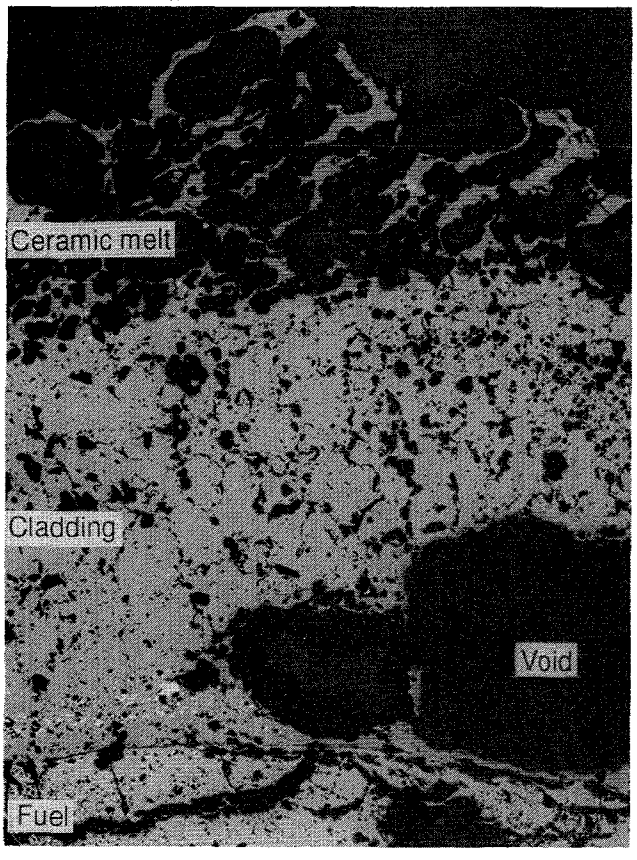

Pos. 3 ⟷ 200 µm

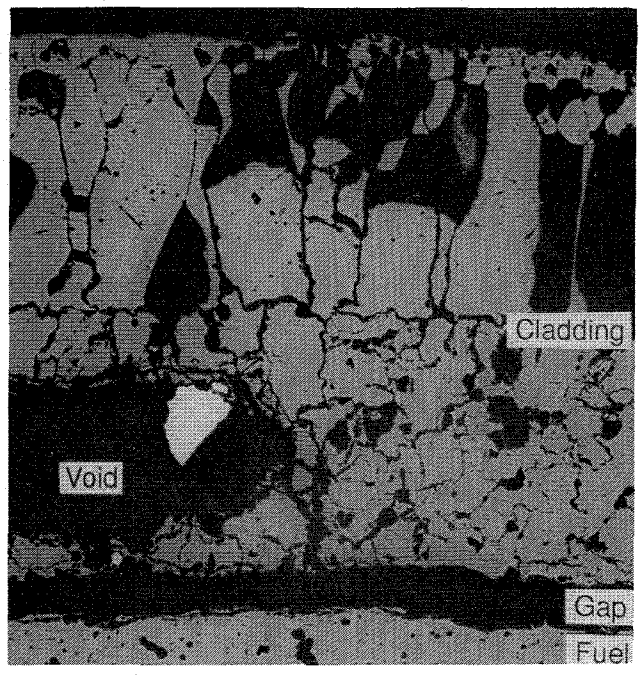

Pos. 4 ⟷ 200 µm

KfK IMF

Fig. 13:
Cross Section CORA-W2-g (top), Elevation 392 mm
Cladding Oxidation

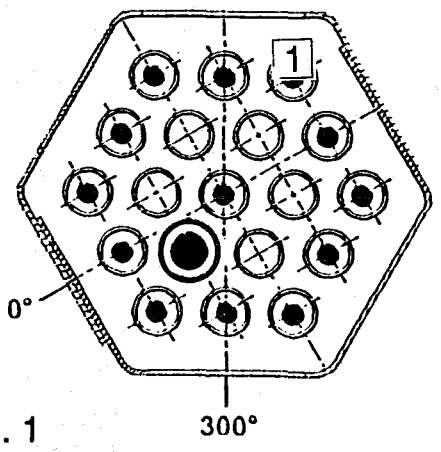

Pos. 1

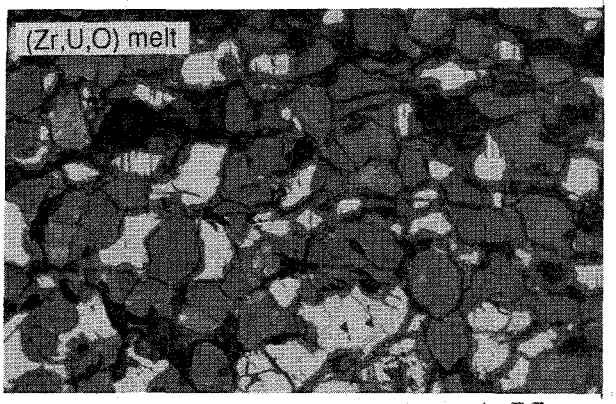

Pos. 2 ⟷ 20 µm

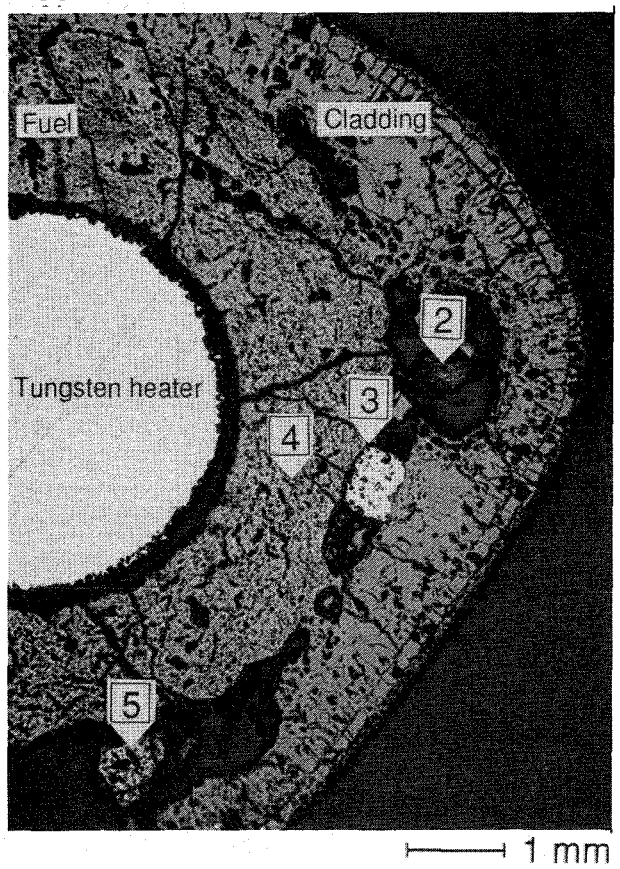

⟷ 1 mm

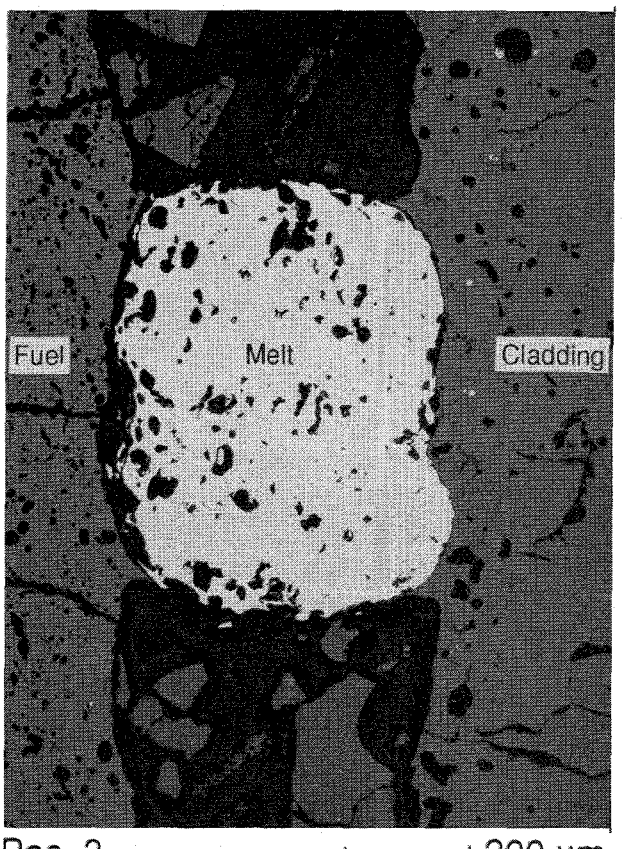

Pos. 3 ⟷ 200 µm

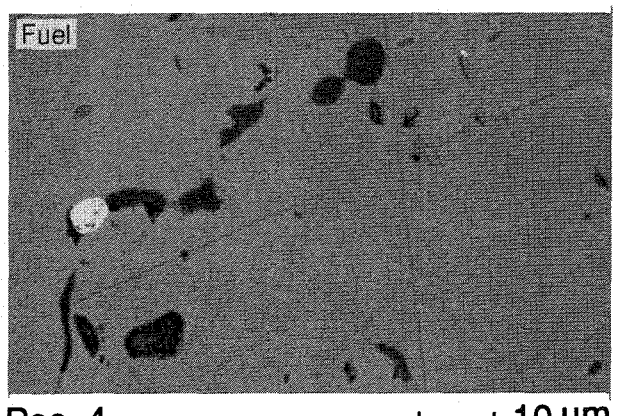

Pos. 4 ⟷ 10 µm

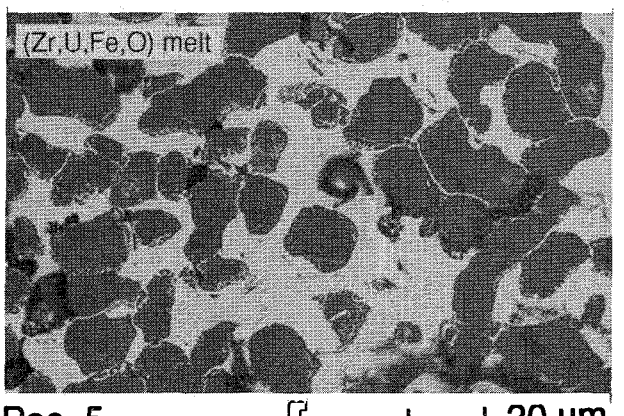

Pos. 5 ⟷ 20 µm

KfK IMF

Fig. 14:

Cross Section CORA-W2-g (top), Elevation 392 mm
Melt Between Fuel and Cladding

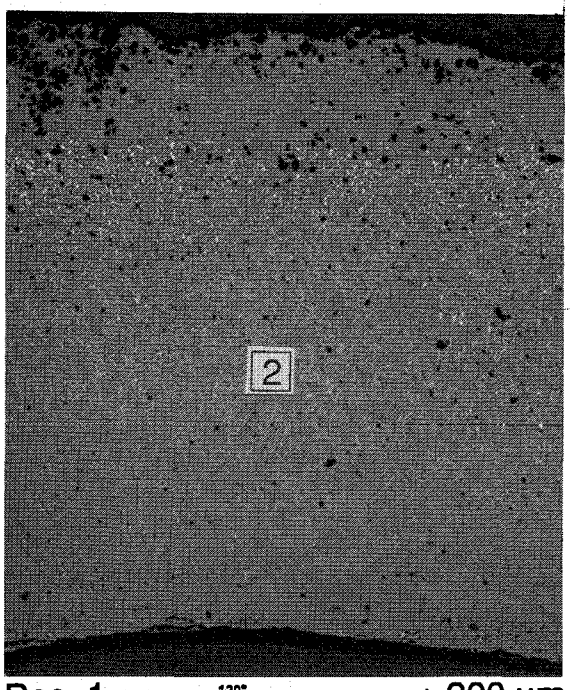

Pos. 1 200 µm

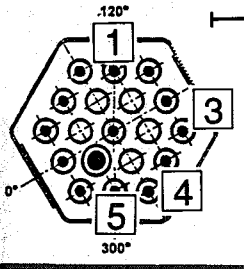

Internal side

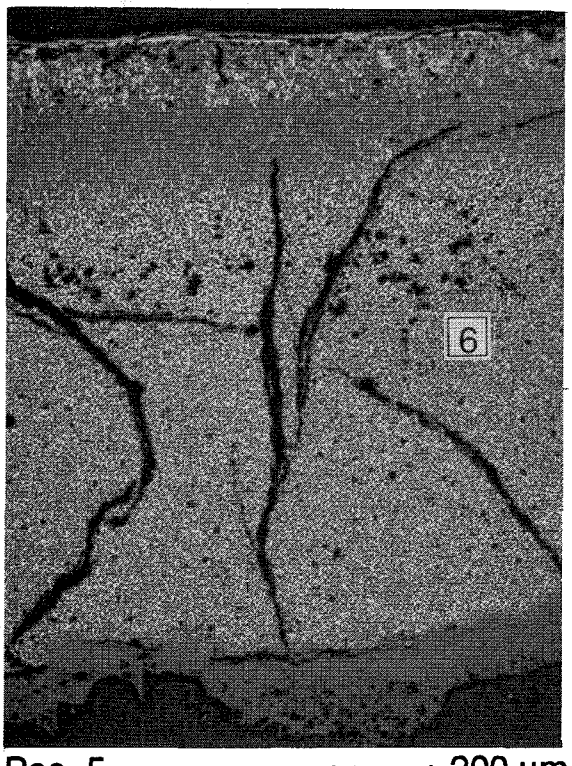

Pos. 5 200 µm

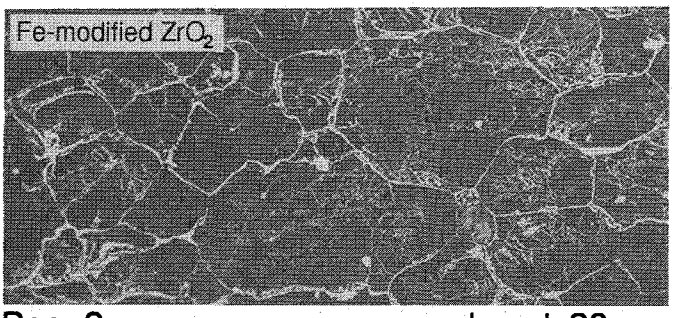

Pos. 2 20 µm

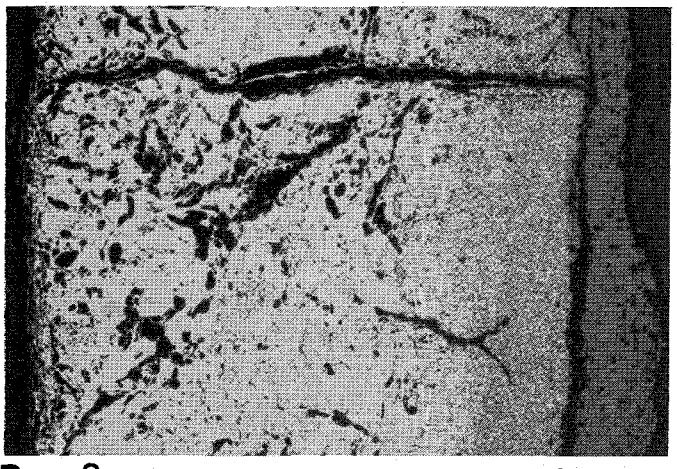

Pos. 3 200 µm

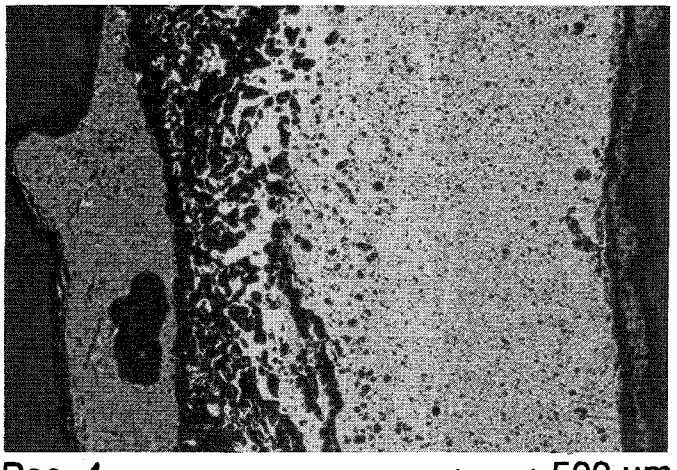

Pos. 4 500 µm

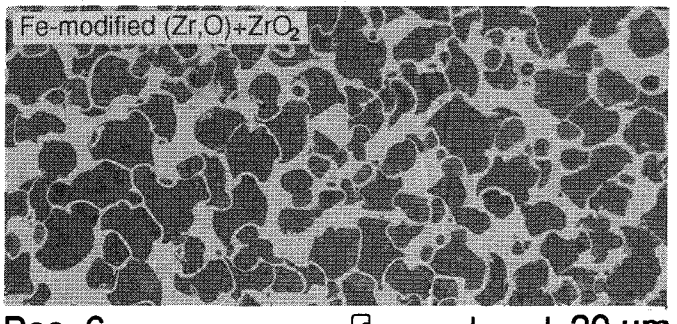

Pos. 6 20 µm

KfK IMF

Fig. 15:

Cross Section CORA-W2-g (top), Elevation 392 mm Shroud Oxidation

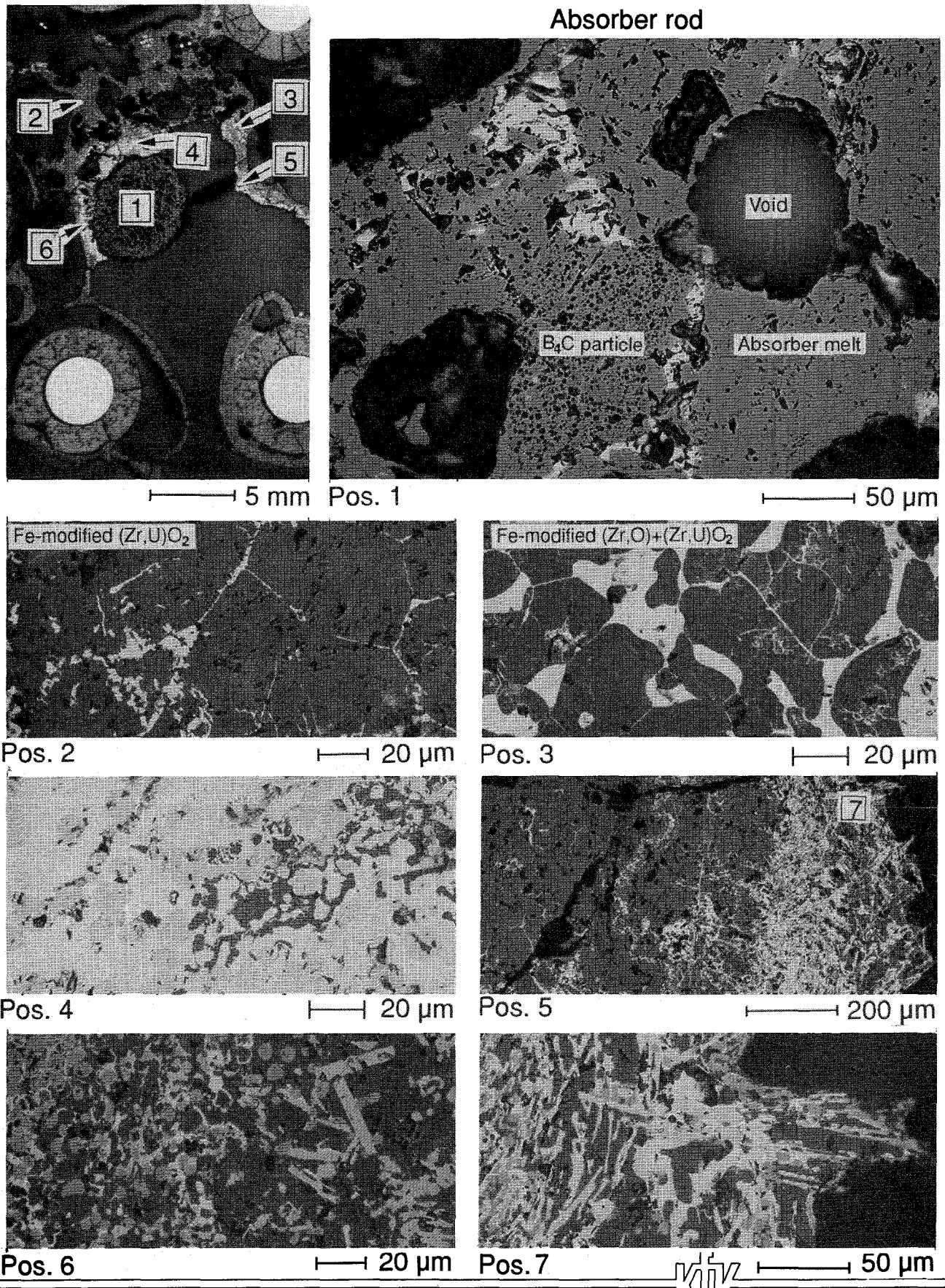

Fig. 16:

Cross Section CORA-W2-g (top), Elevation 392 mm
Melt Microstructures Around Absorber Rod

Pos. 1 100 µm

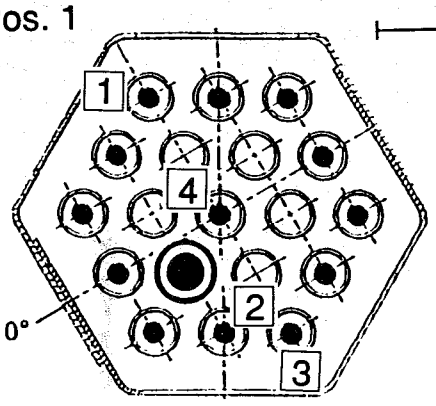

Spacer, penetrated by melt

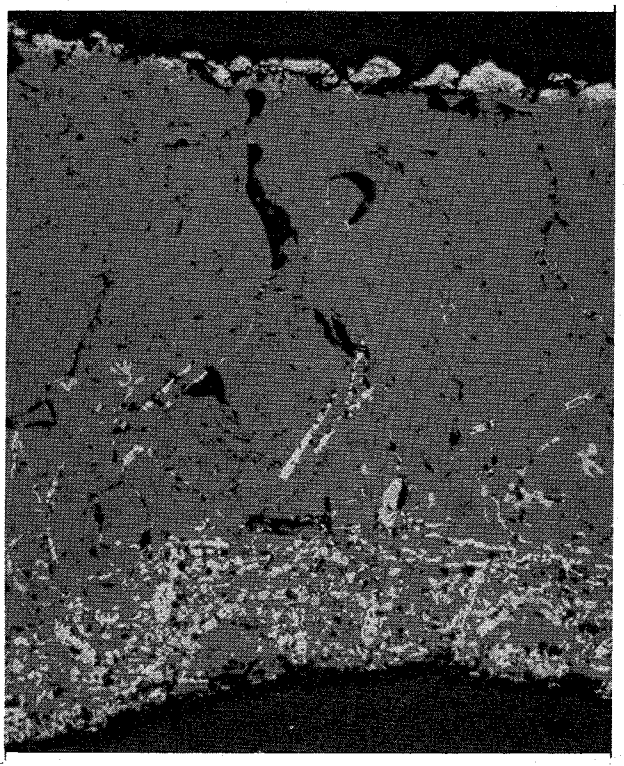

Pos. 2 100 µm

Spacer in contact with oxidized melt

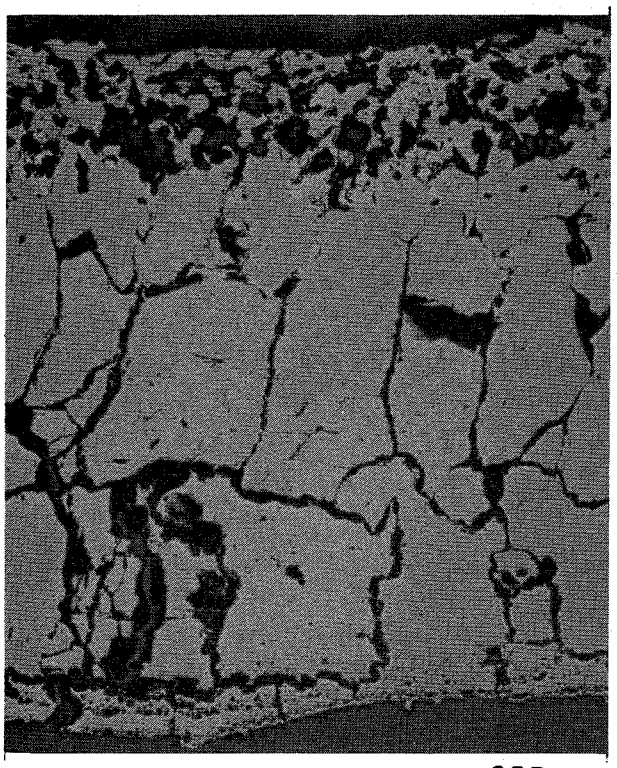

Pos. 3 200 µm

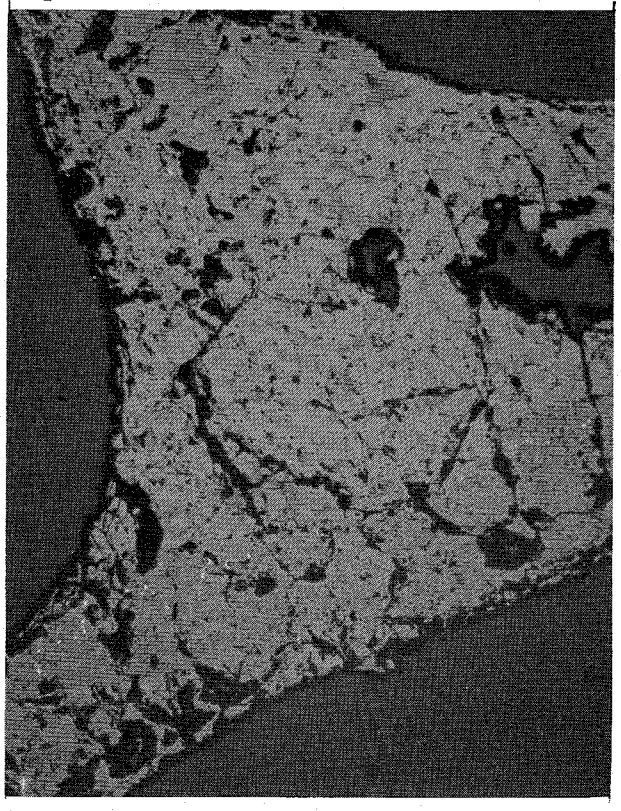

Pos. 4 200 µm

KfK IMF

Fig. 17:

Cross Section CORA-W2-g (top), Elevation 392 mm
Spacer Grid

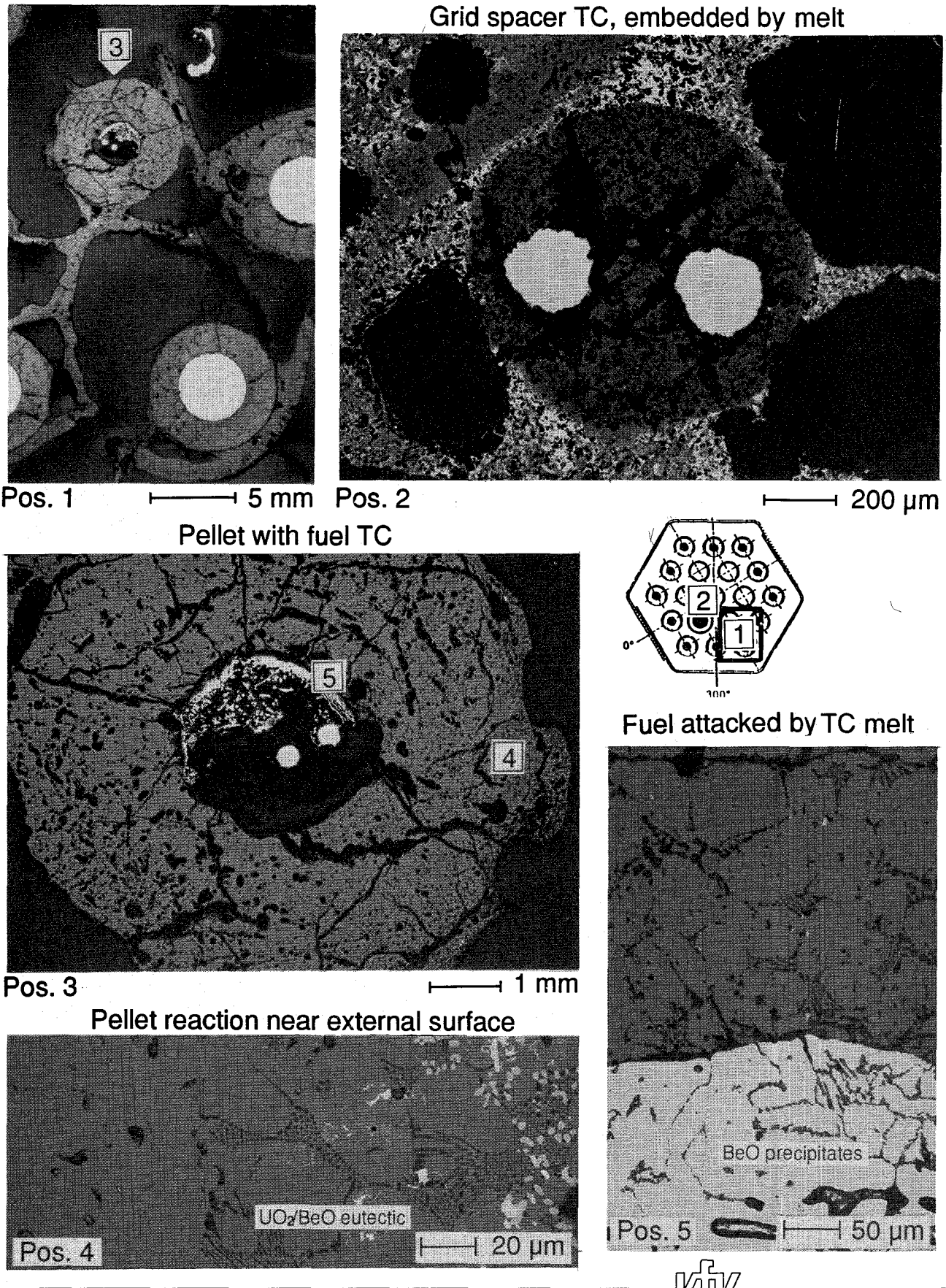

Fig. 18:

Cross Section CORA-W2-g (top), Elevation 392 mm Thermocouples

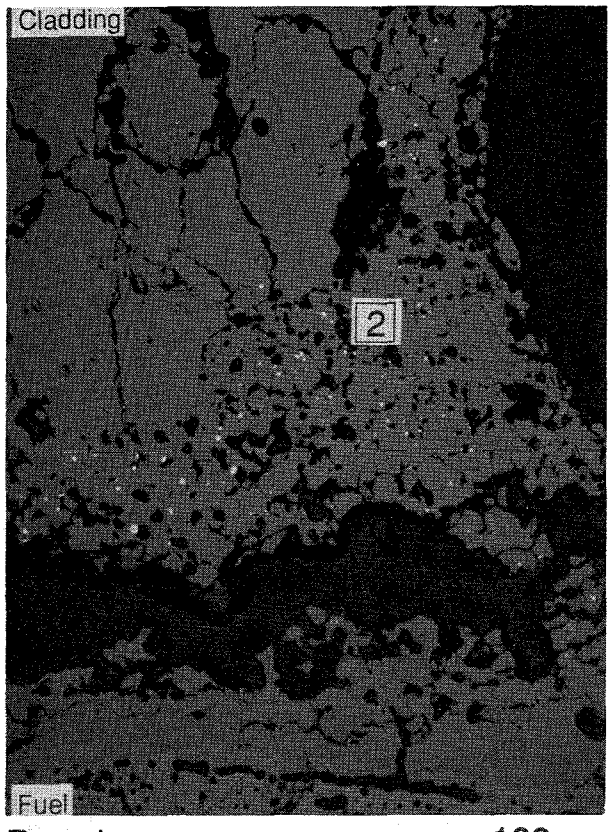

Pos. 1 100 µm

Pos. 3

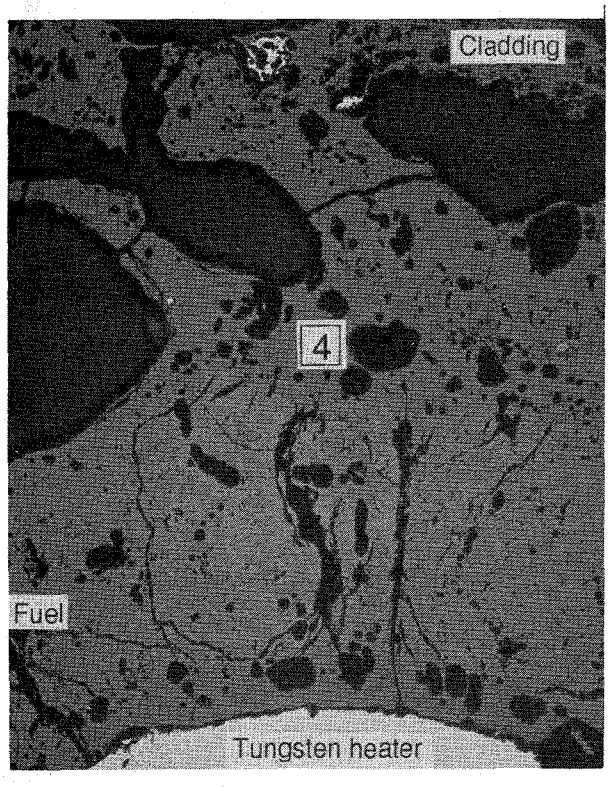

500 µm

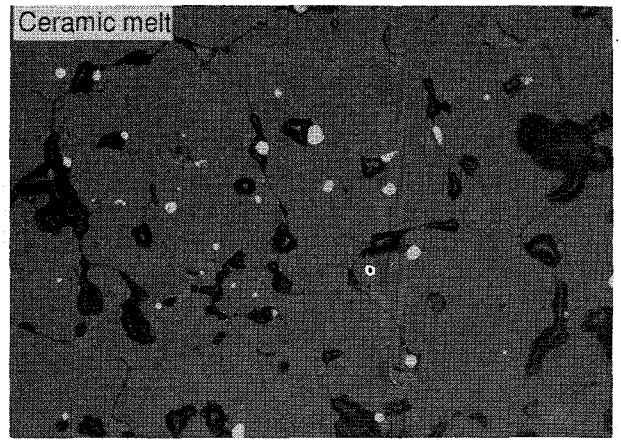

Pos. 2 20 µm

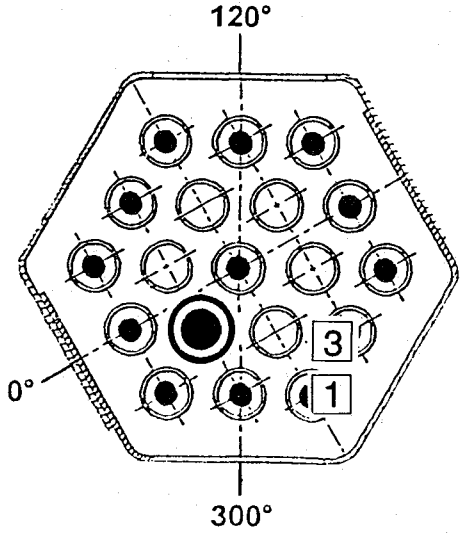

Pos. 4

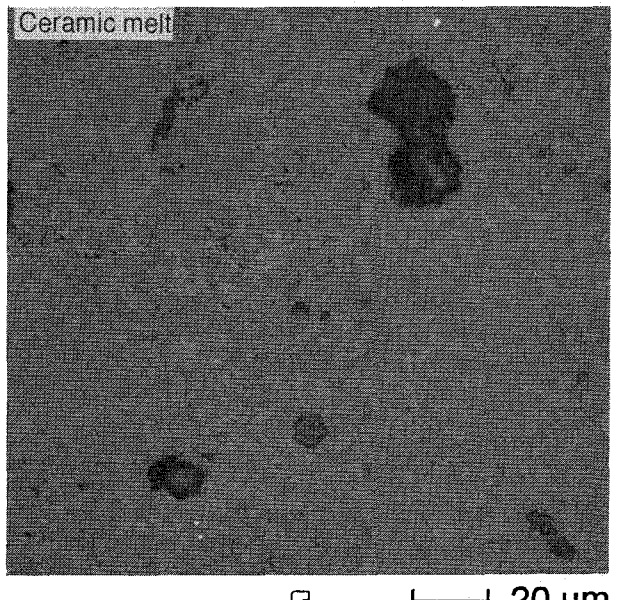

20 µm

KfK IMF

Fig. 19:
Cross Section CORA-W2-g (top), Elevation 392 mm
Melt Between Fuel and Cladding

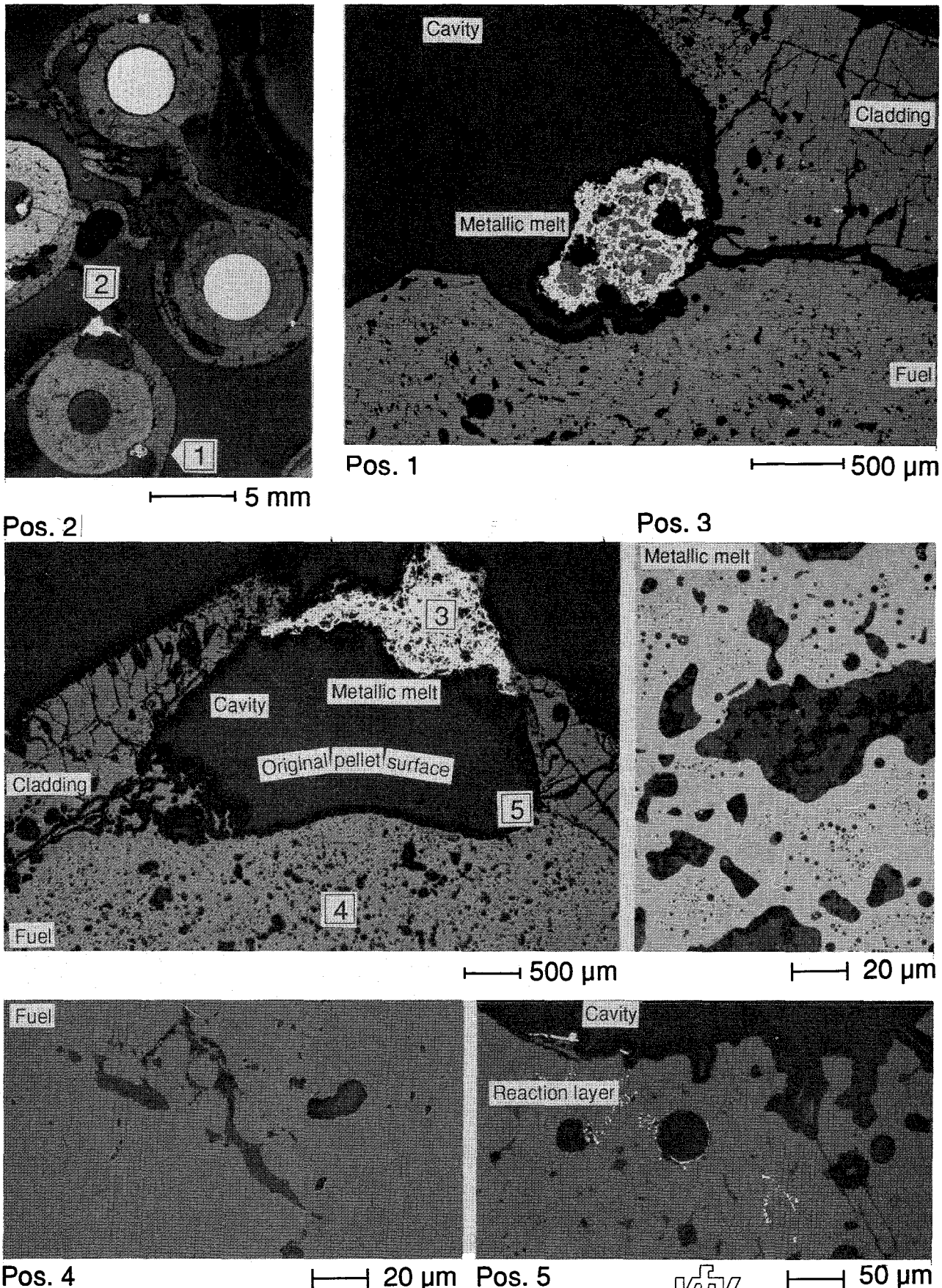

Fig. 20:

Cross Section CORA-W2-g (top), Elevation 392 mm
Fuel Dissolution by Metallic Melt

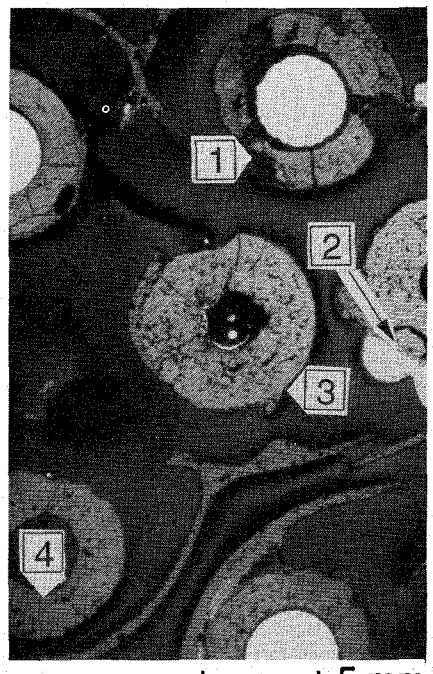

5 mm

Pellet desintegration

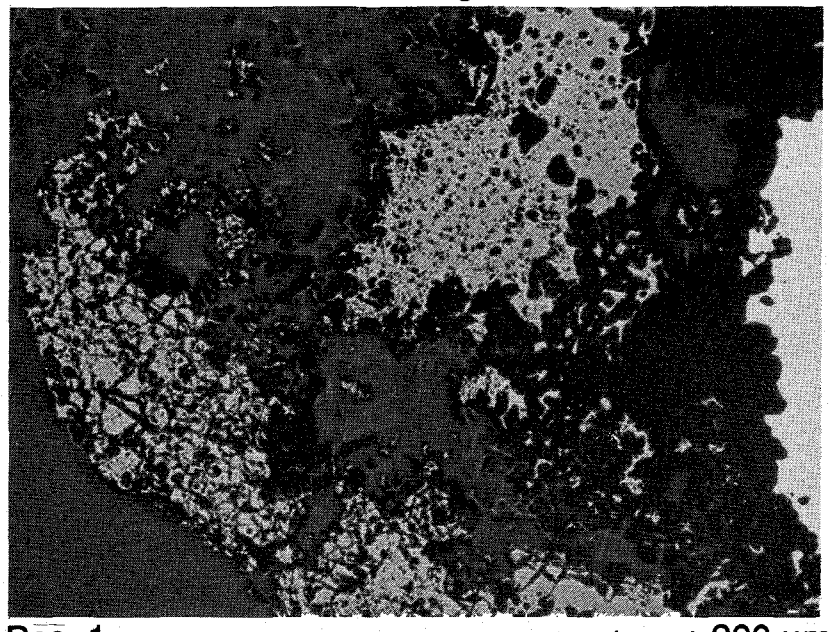

Pos. 1

200 µm

Reaction zone in contact with metallic melt

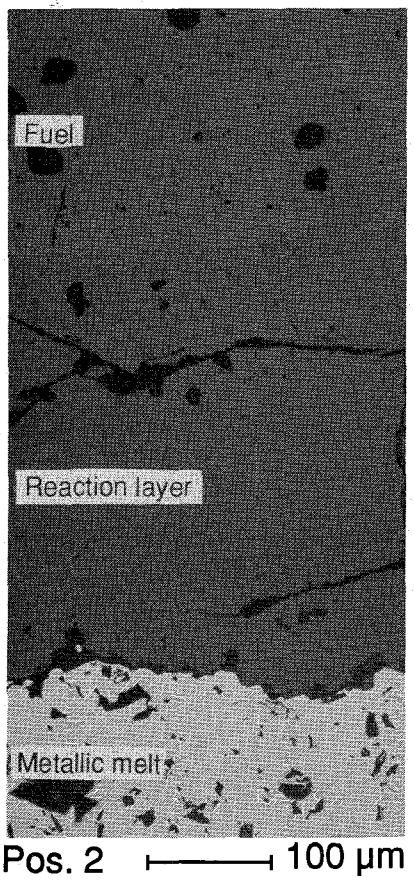

Pos. 2

100 µm

Pellets after bulk infiltration and decomposition

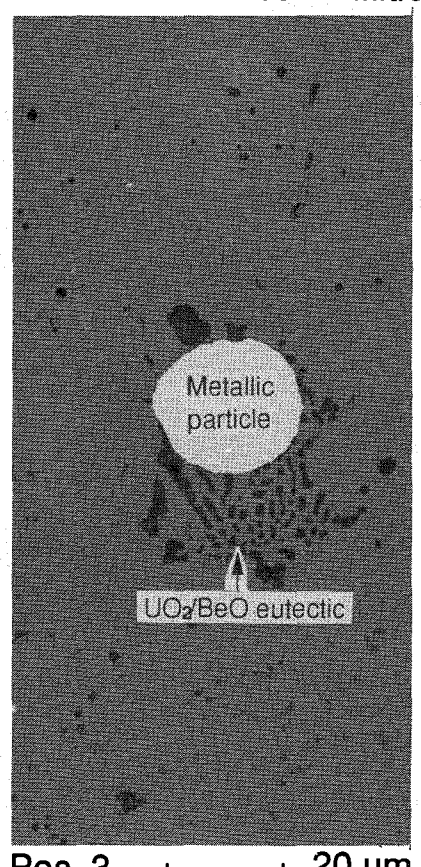

Pos. 3

20 µm

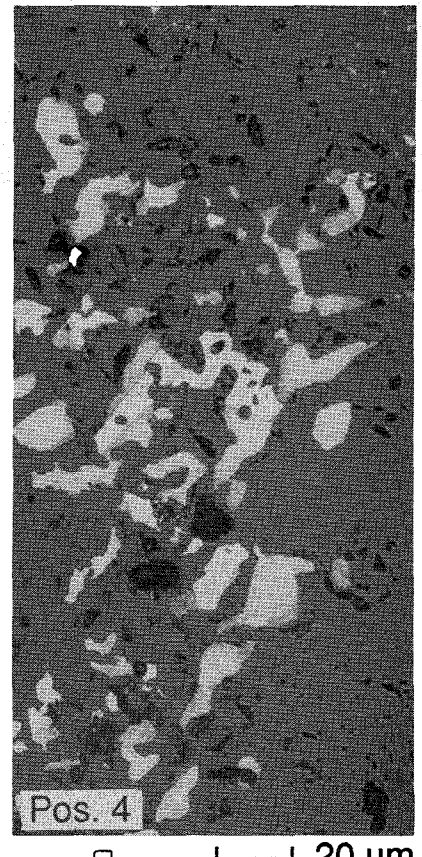

20 µm

KfK IMF

Fig. 21:

Cross Section CORA-W2-g (top), Elevation 392 mm
Fuel Dissolution

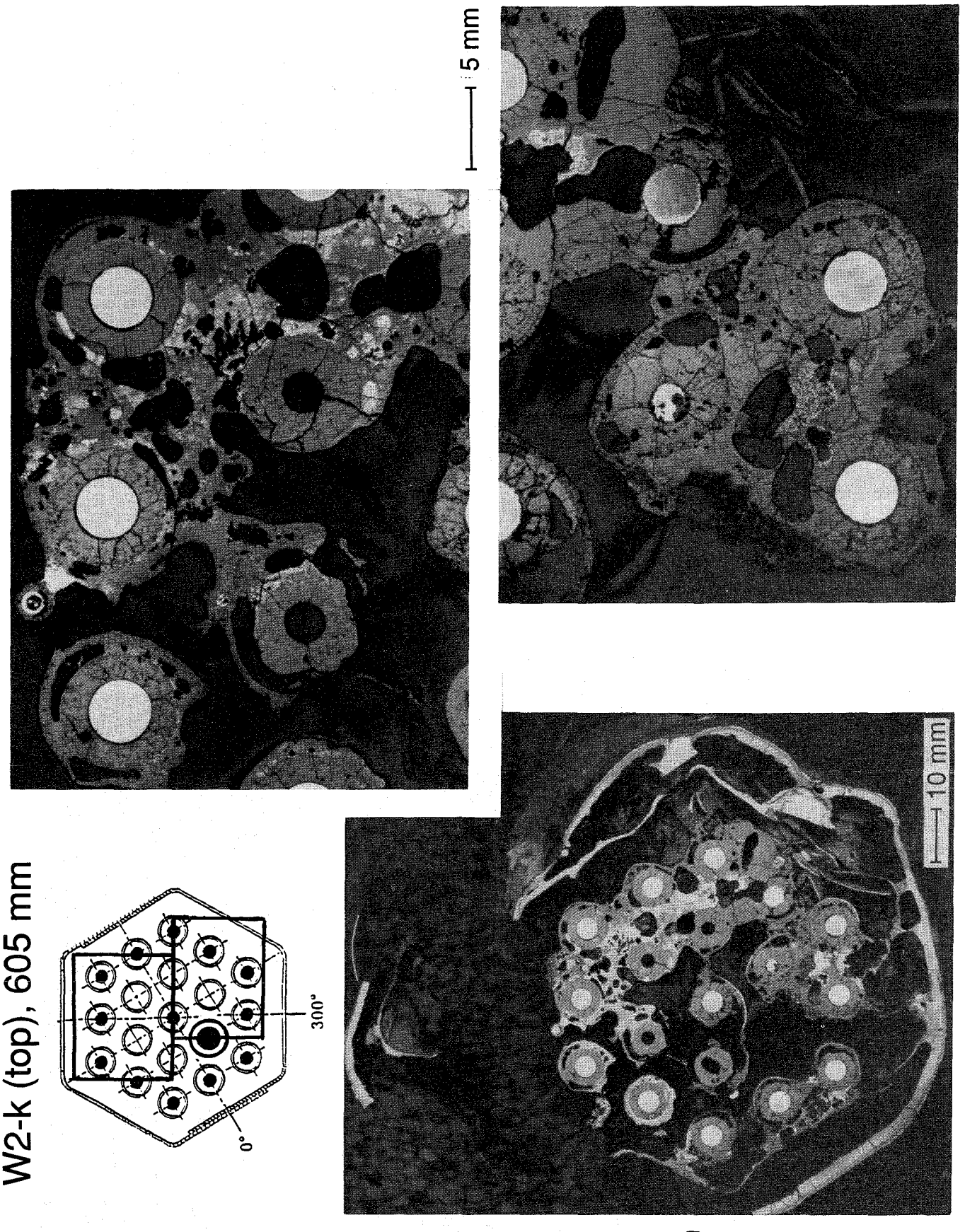

Fig. 22:

Cross Section CORA-W2-k (top), Elevation 605 mm

Overview

Pos. 1

W2-k (top), 605 mm

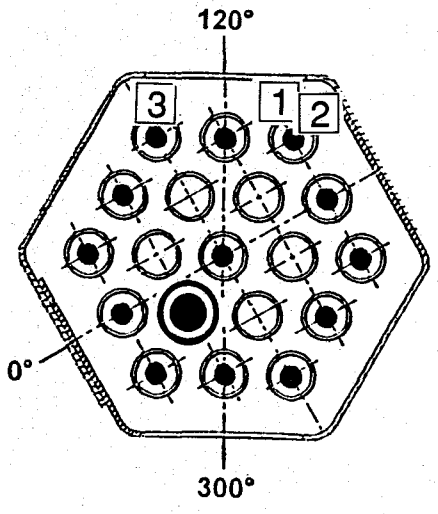

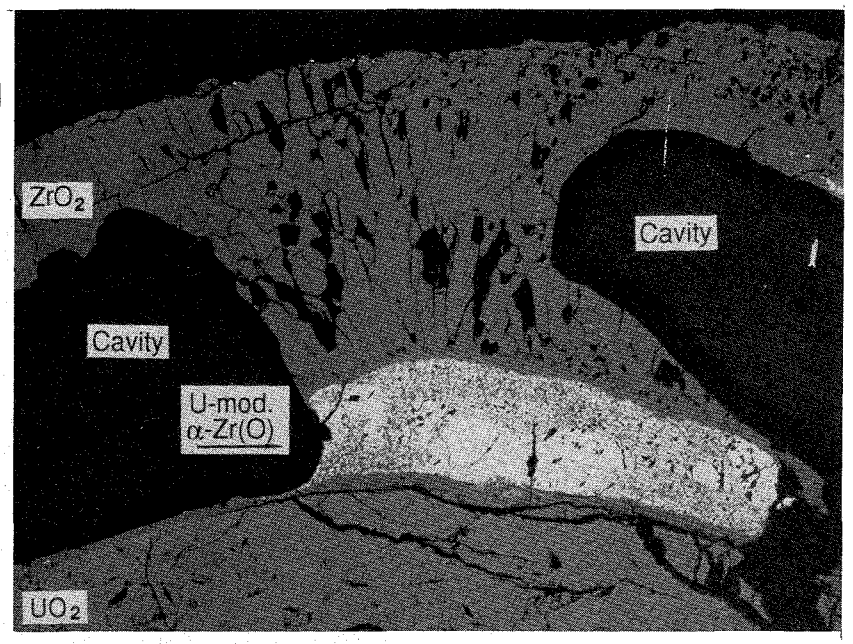

Pos. 2

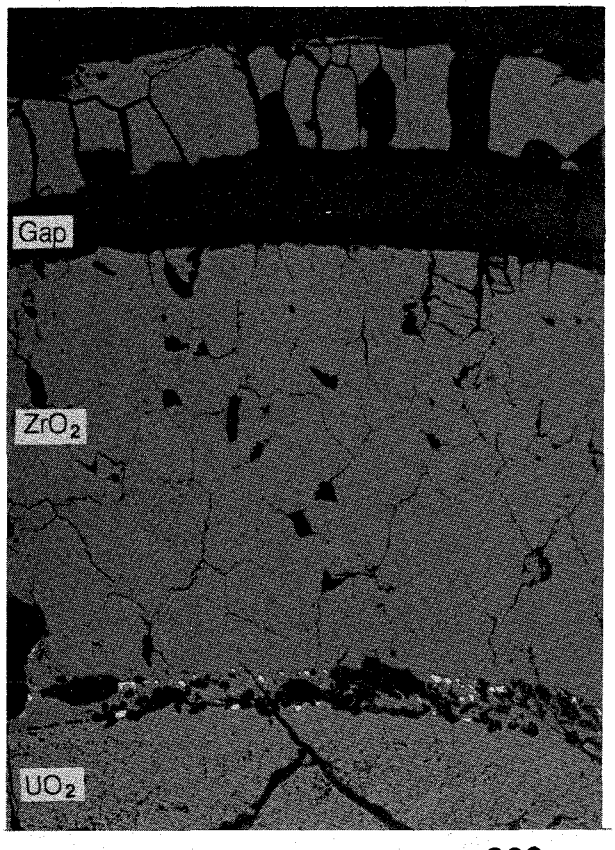

Pos. 3

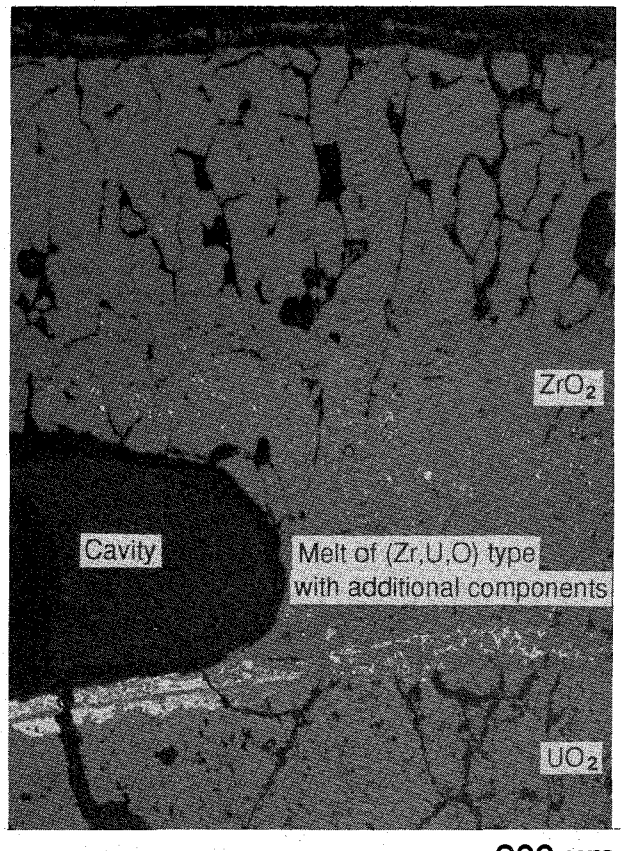

Fig. 23:

Cross Section CORA-W2-k (top), Elevation 605 mm
Cladding Oxidation

W2-k (top),
605 mm

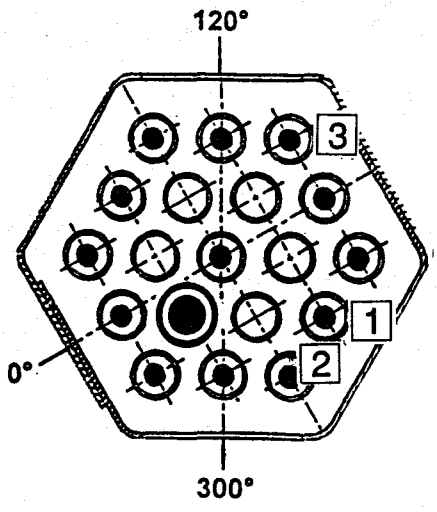

Pos. 1 Fragments

500 µm

Pos. 2 Fuel rod, infiltrated by subsequently oxidized melt

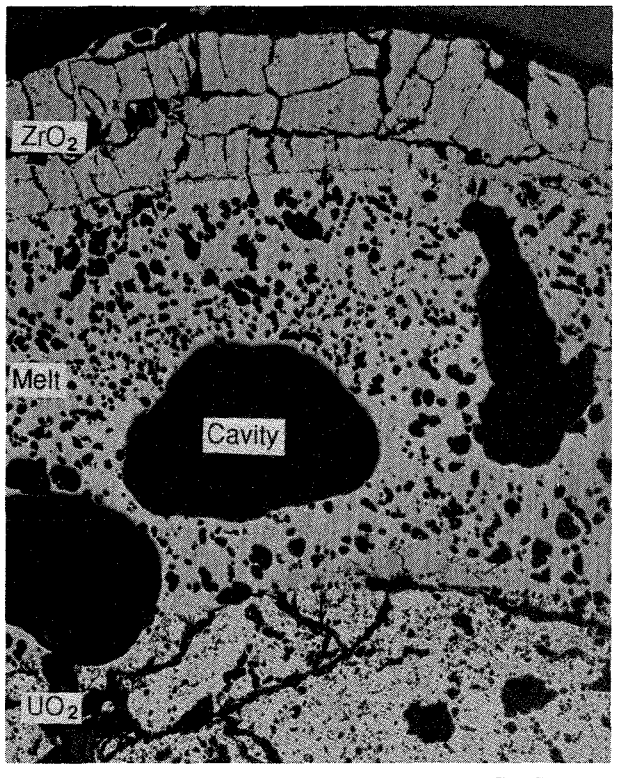

250 µm

Pos. 3 Spacer

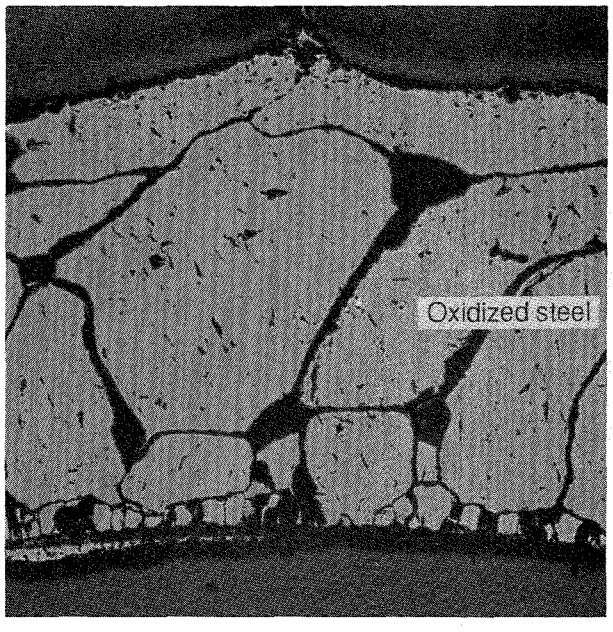

200 µm

KfK IMF

Fig. 24:

Cross Section CORA-W2-k (top), Elevation 605 mm
Completely Oxidized Components

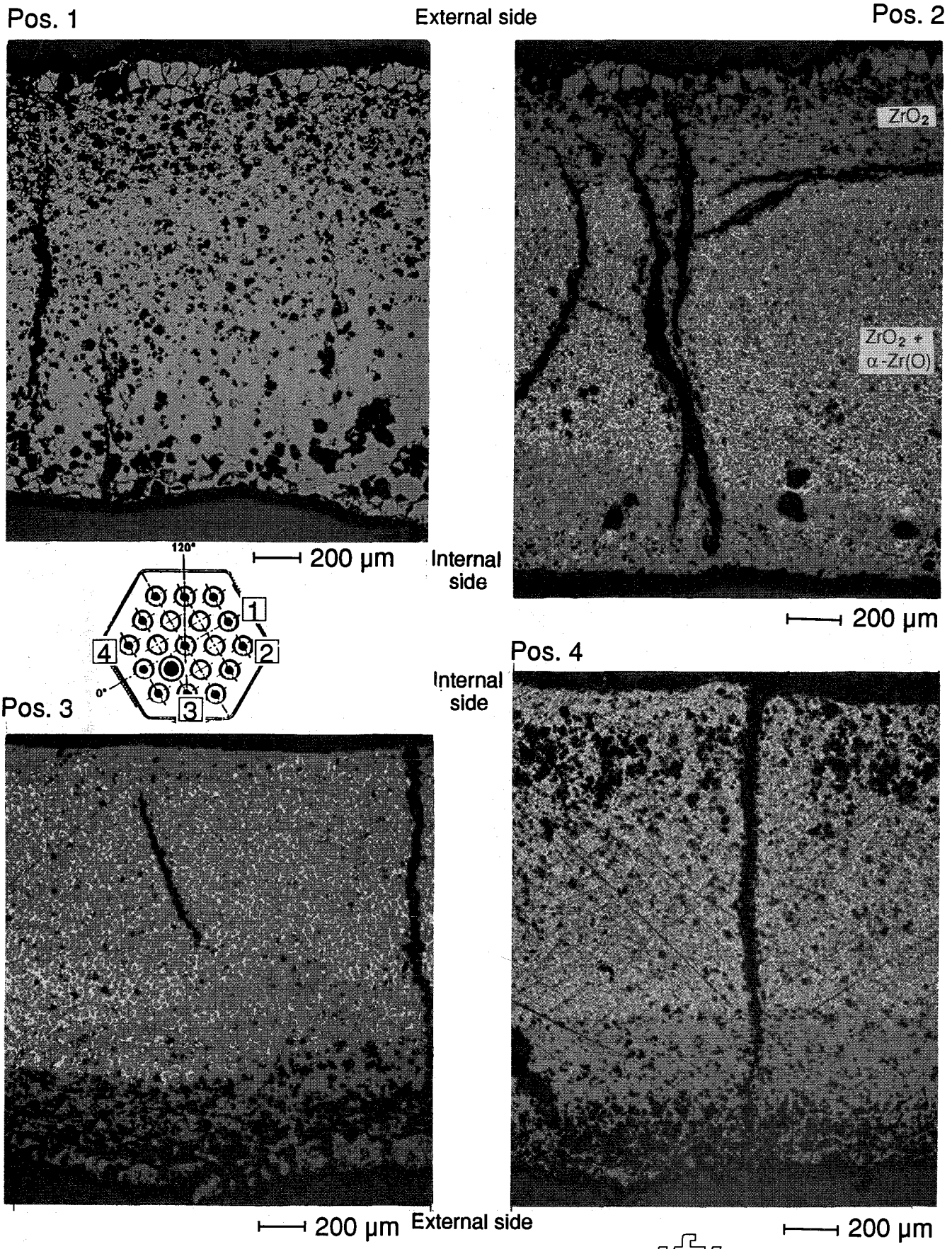

Fig. 25:

Cross Section CORA-W2-k (top), Elevation 605 mm Shroud Oxidation

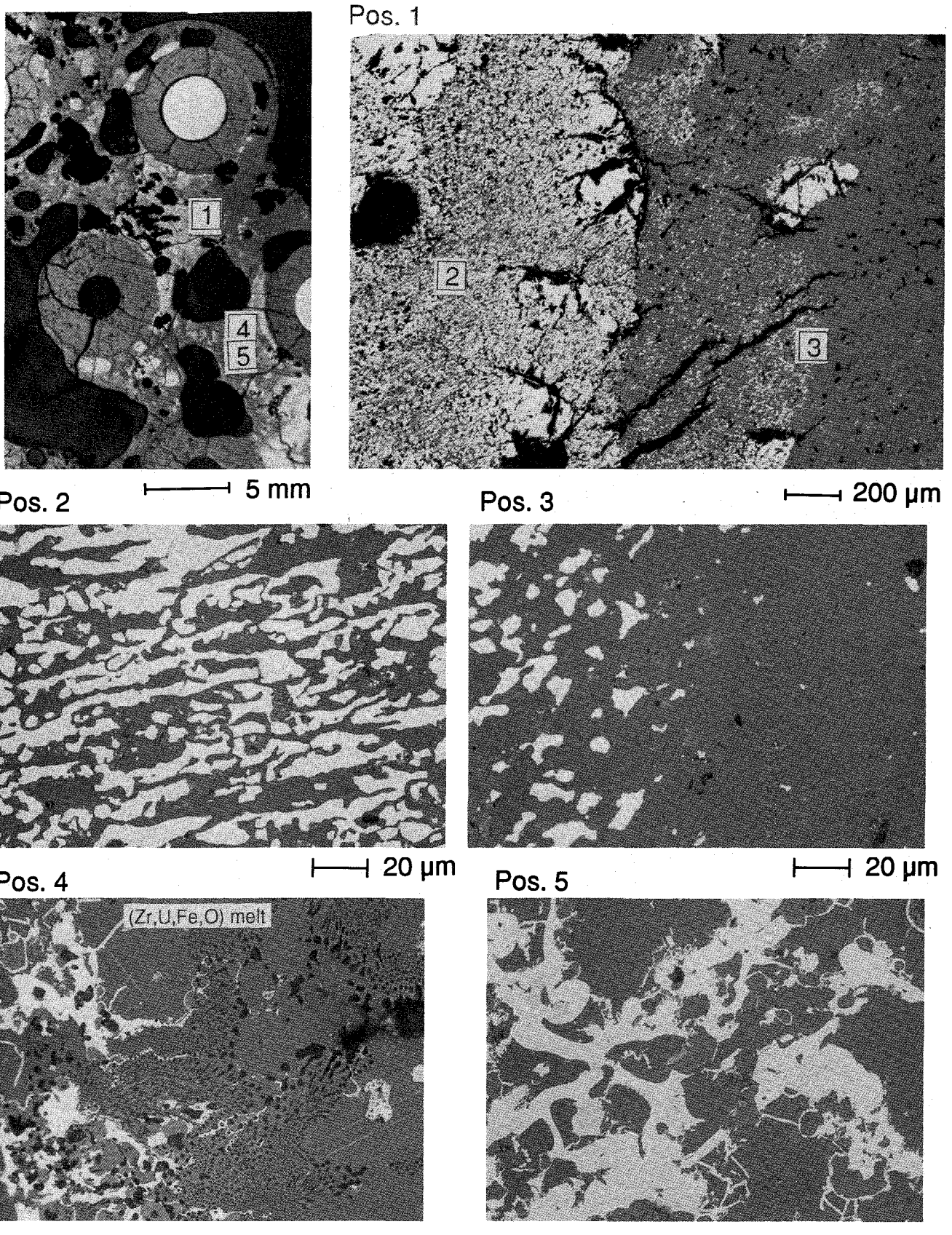

Fig. 26:

Cross Section CORA-W2-k (top), Elevation 605 mm

Melt Microstructures

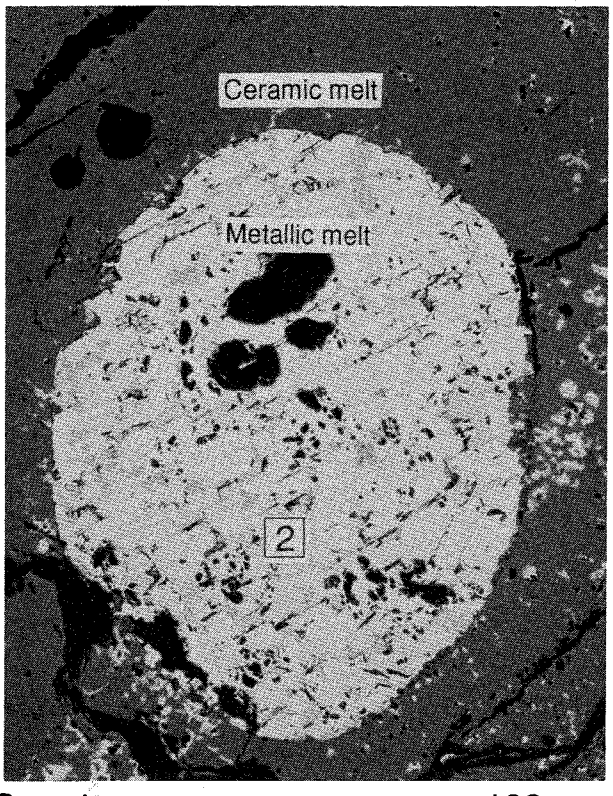

Pos. 1 100 µm

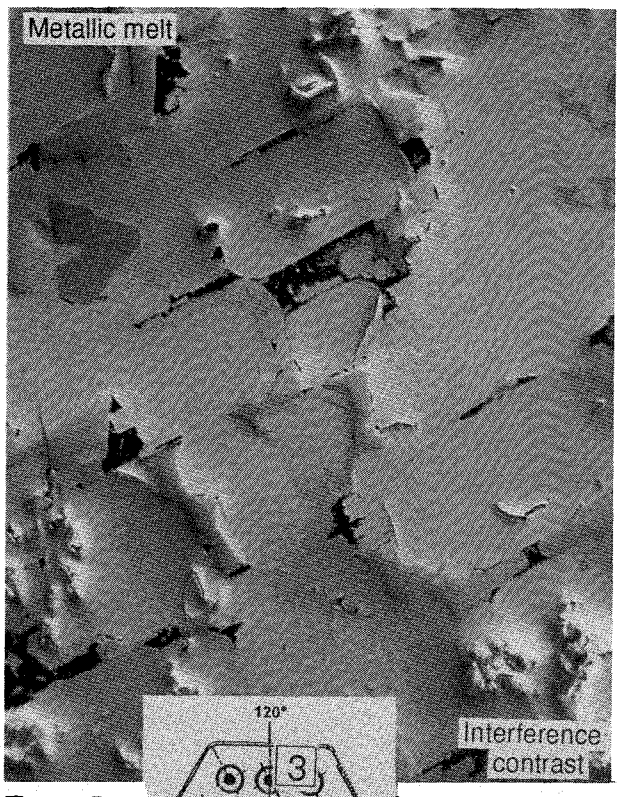

Pos. 2 20 µm

Pos. 3

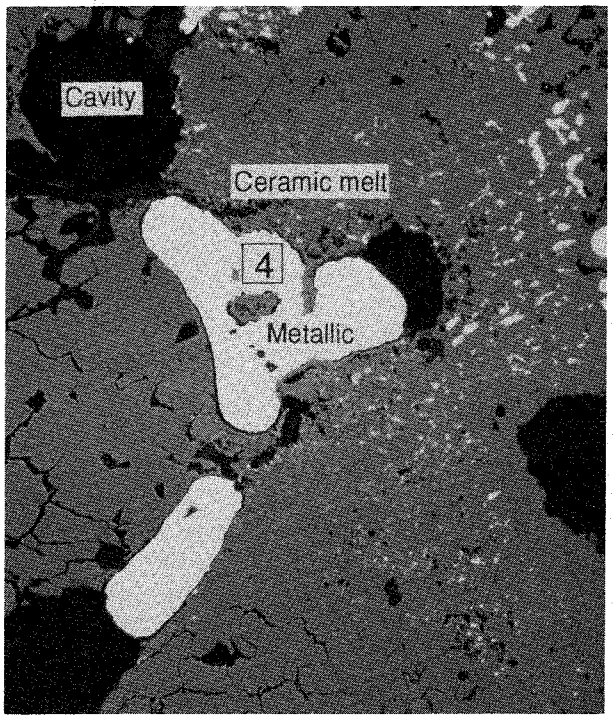

100 µm

Pos. 4

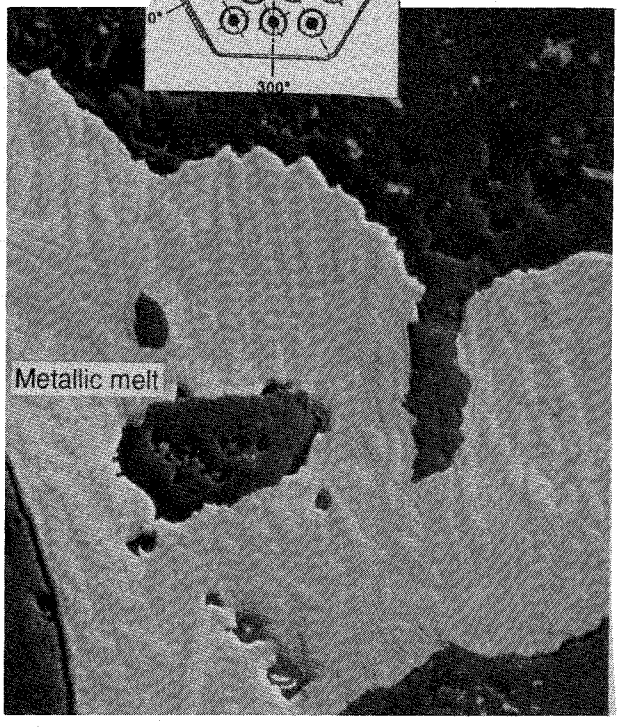

Interference contrast 20 µm

KfK IMF

Fig. 27:

Cross Section CORA-W2-k (top), Elevation 605 mm Melt Distribution and Morphology

Pos. 1 Pellet dissolution by metallic melt Pos. 2

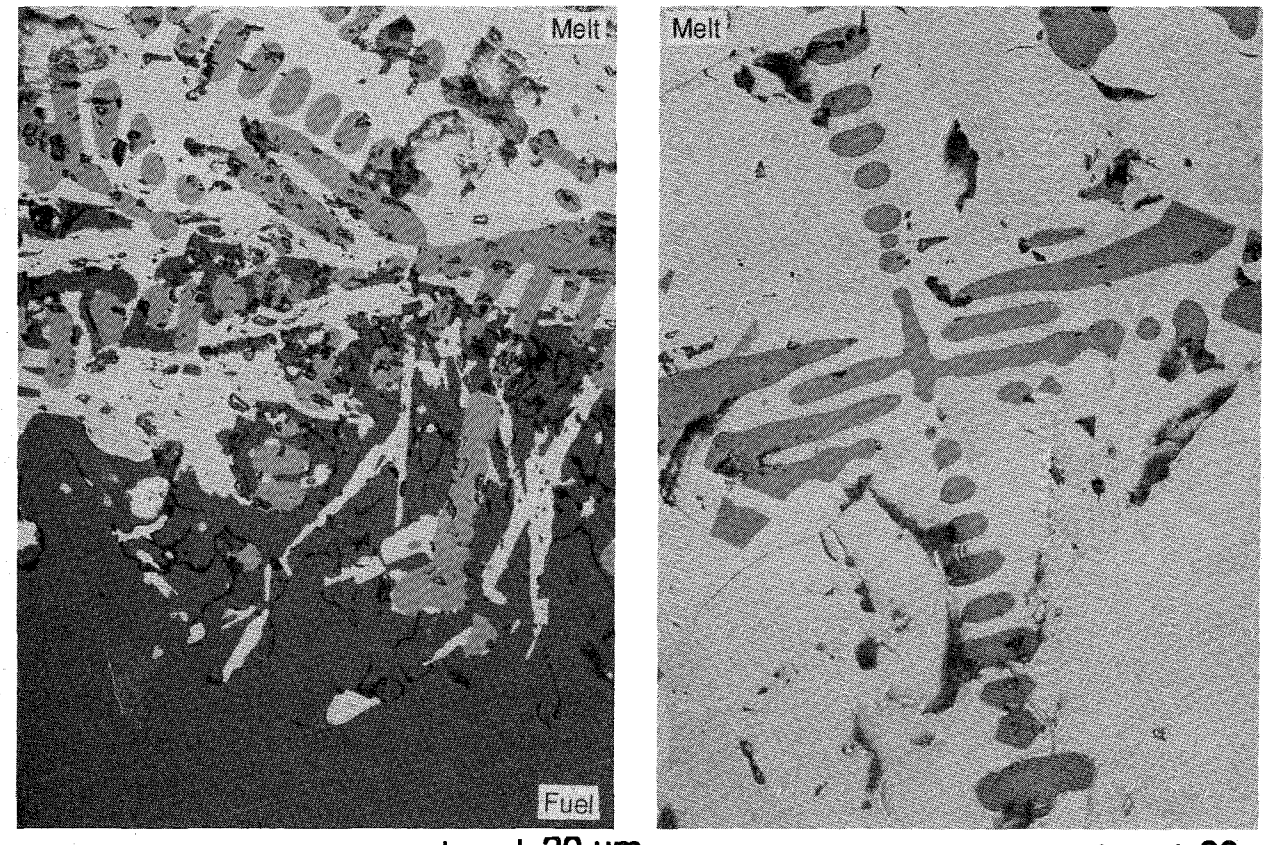

Pos. 3 Pellet, resistent against oxidized melt Pos. 4

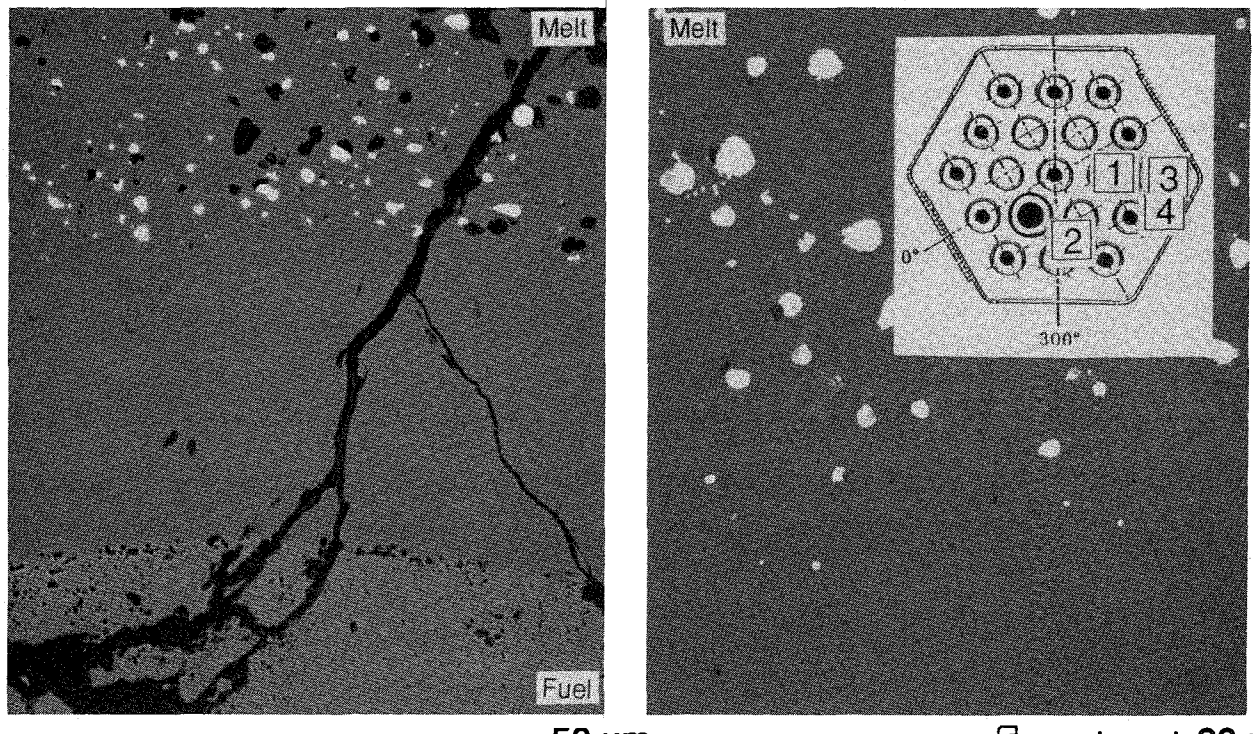

KfK IMF

Fig. 28

Cross Section CORA-W2-k (top), Elevation 605 mm
Fuel Pellet in Contact with Melt

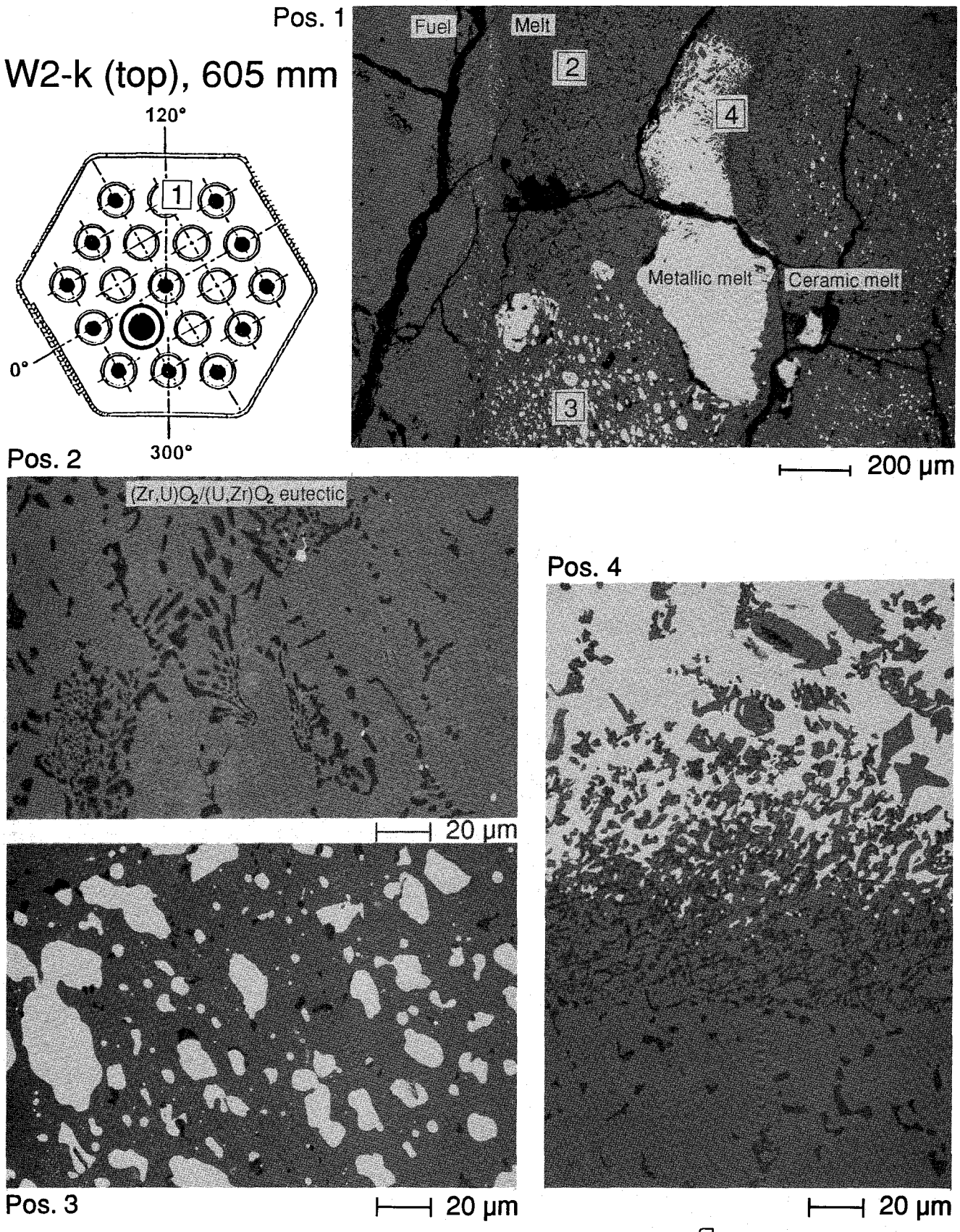

Fig. 29:

Cross Section CORA-W2-k (top), Elevation 605 mm
Melt in Contact with Fuel Pellet

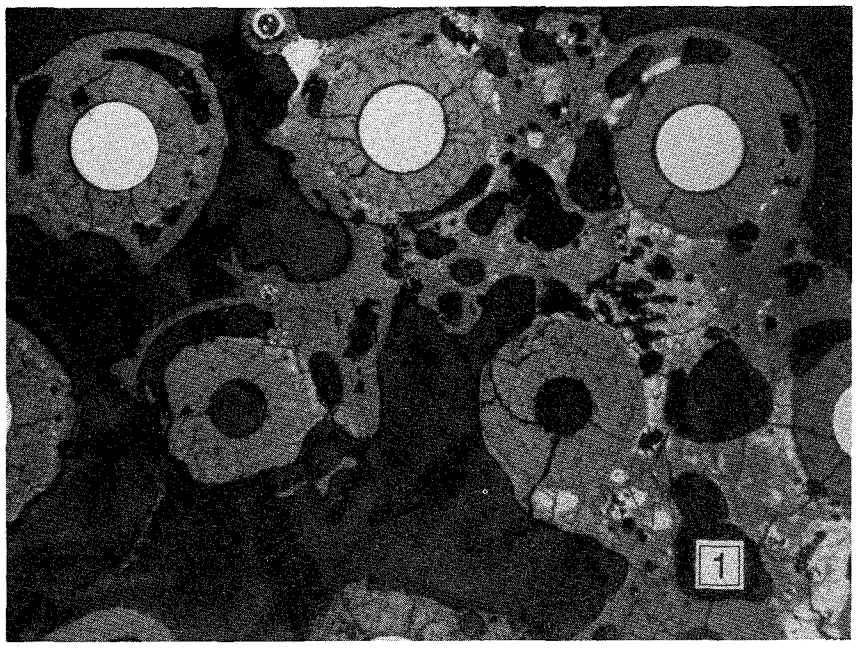

W2-k (top), 605 mm

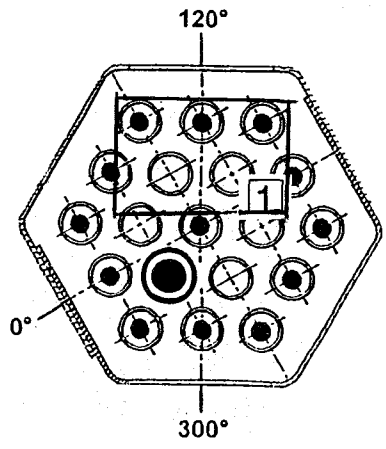

5 mm

Pos. 1

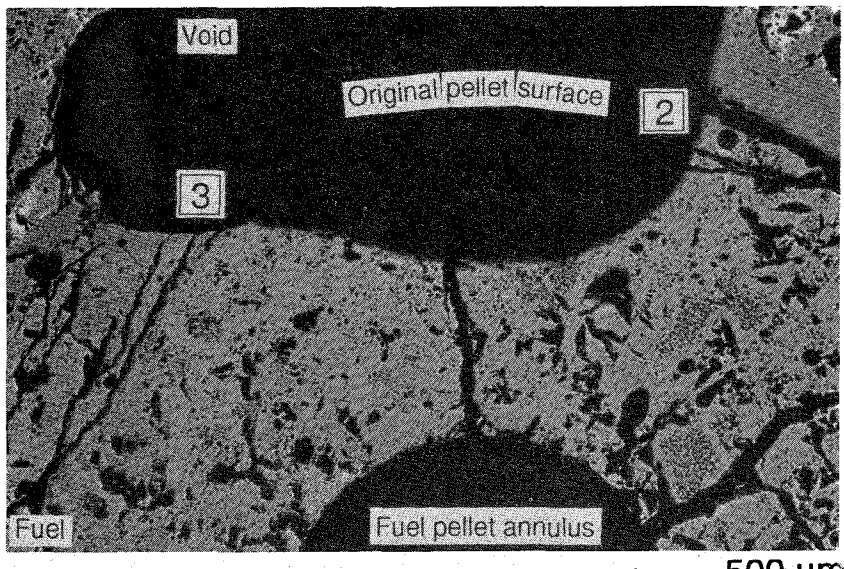

500 µm

Pos. 2

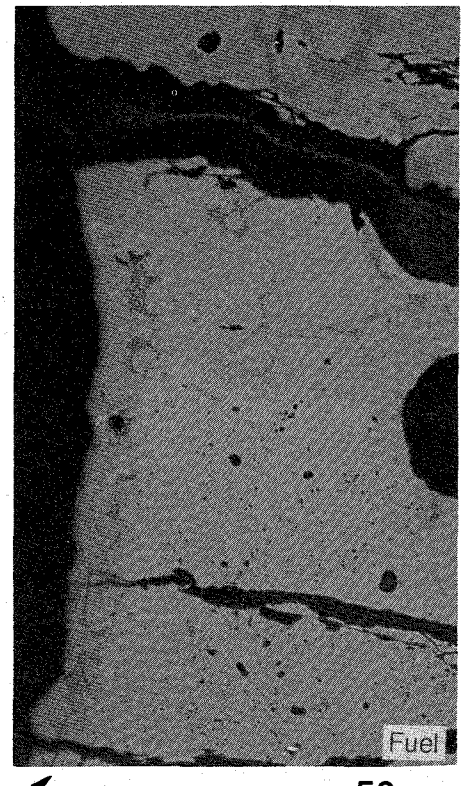

50 µm

Pos. 3

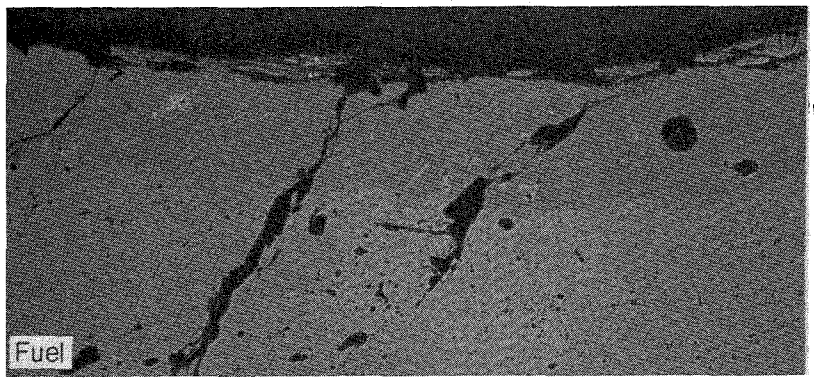

Reaction layer

50 µm

KfK IMF

Fig. 30:

Cross Section CORA-W2-k (top), Elevation 605 mm Fuel Pellet Dissolution

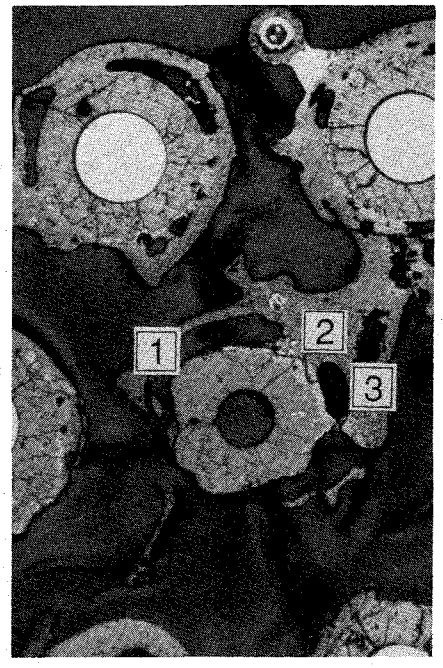

Pos. 1 Cladding dissolution

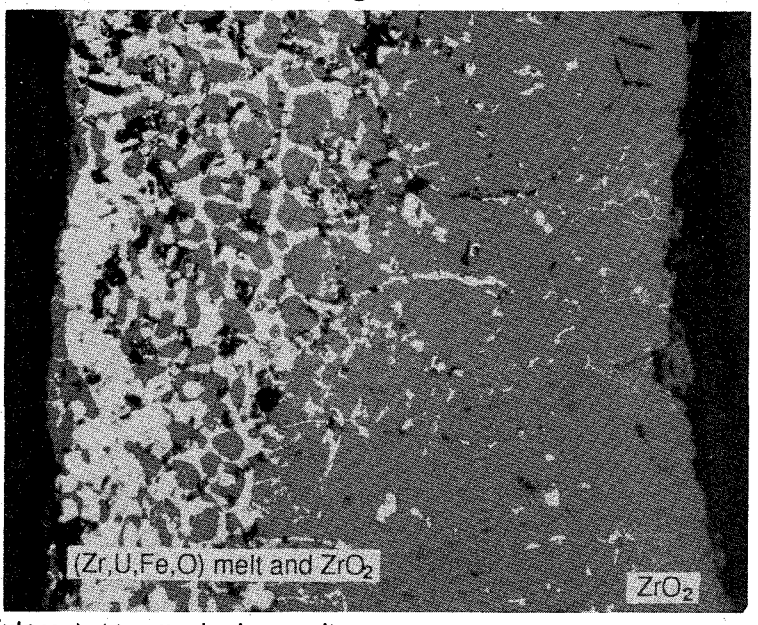

External side attacked by melt

50 µm

Pos. 2 Microstructures of resolidified melt Pos. 3

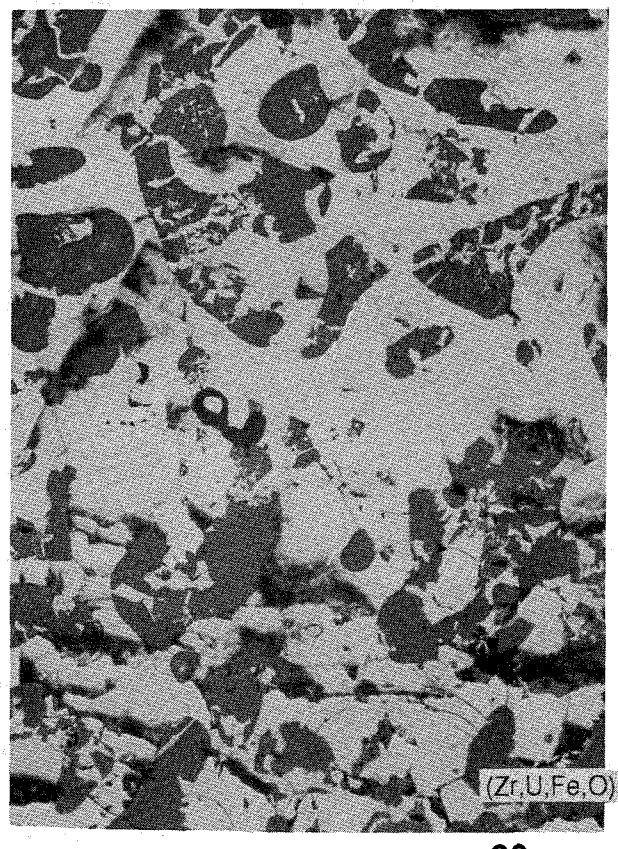

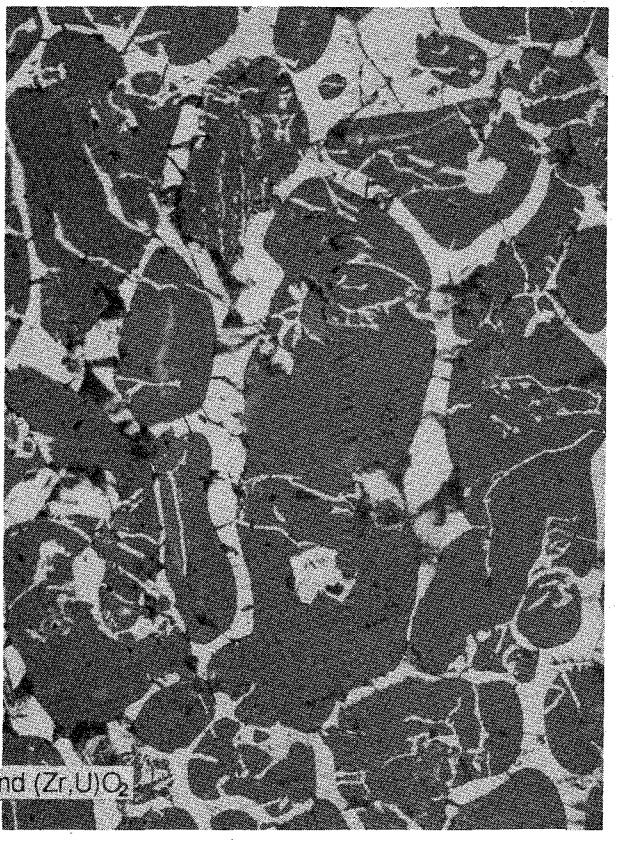

20 µm 20 µm

KfK IMF

Fig. 31:

Cross Section CORA-W2-k (top), Elevation 605 mm
Cladding Dissolution, Reaction Product Microstructure

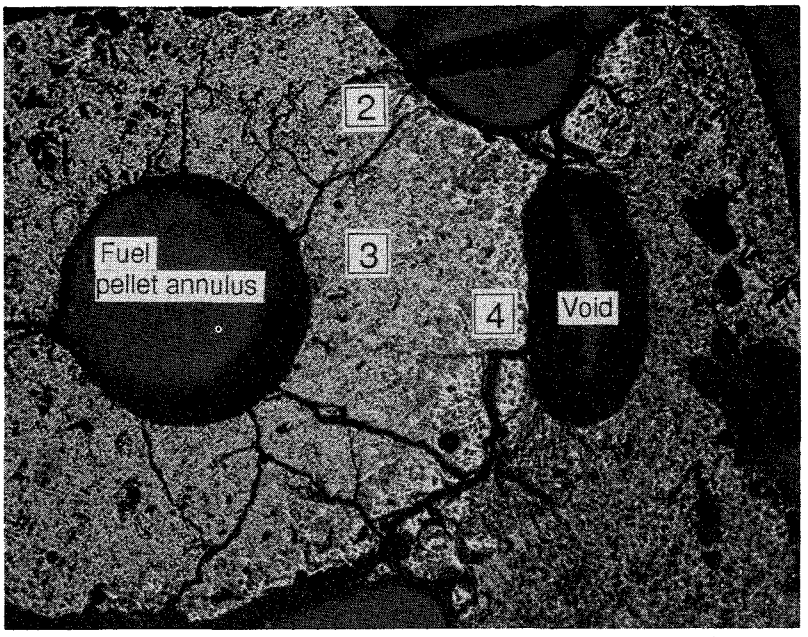

Pos. 1 — 1 mm

Pellet infiltration

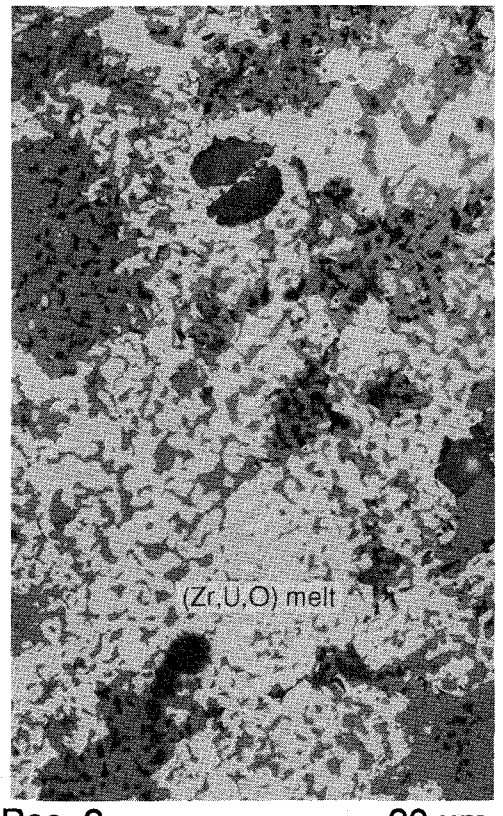

Pos. 2 — 20 µm

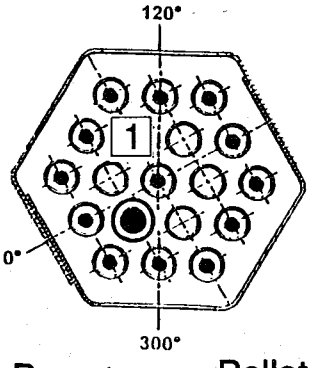

Pos. 3 Pellet infiltration

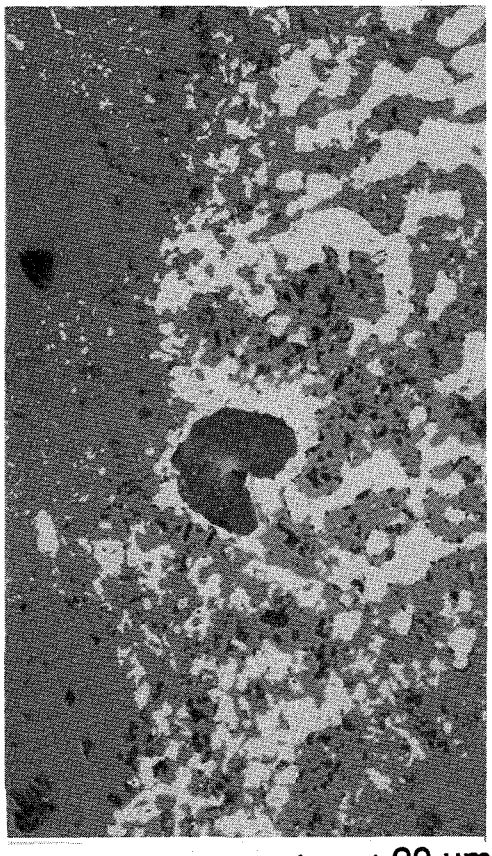

20 µm

Pos. 4 Pellet surface dissolution

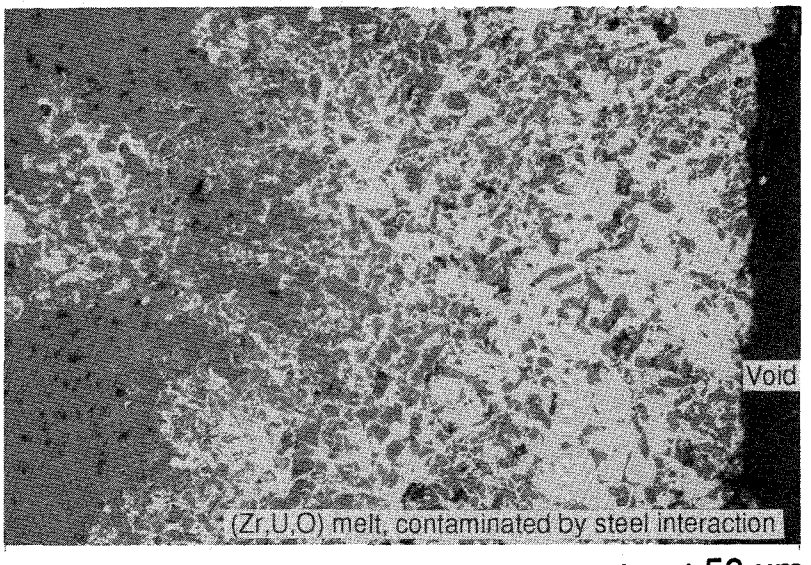

50 µm

KfK IMF

Fig. 32:

Cross Section CORA-W2-k (top), Elevation 605 mm
Fuel Pellet Infiltration and Dissolution

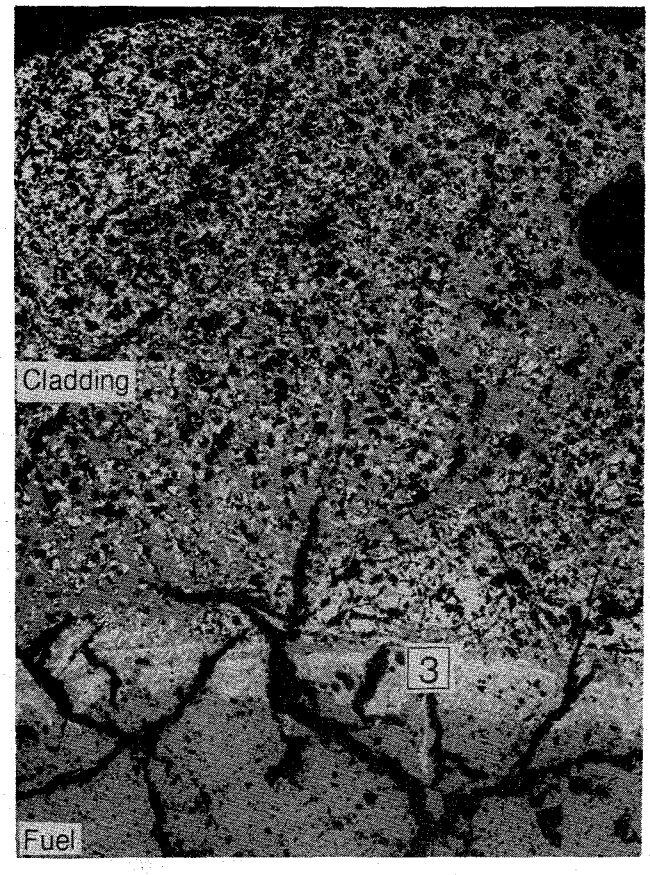

Pos. 1

200 µm

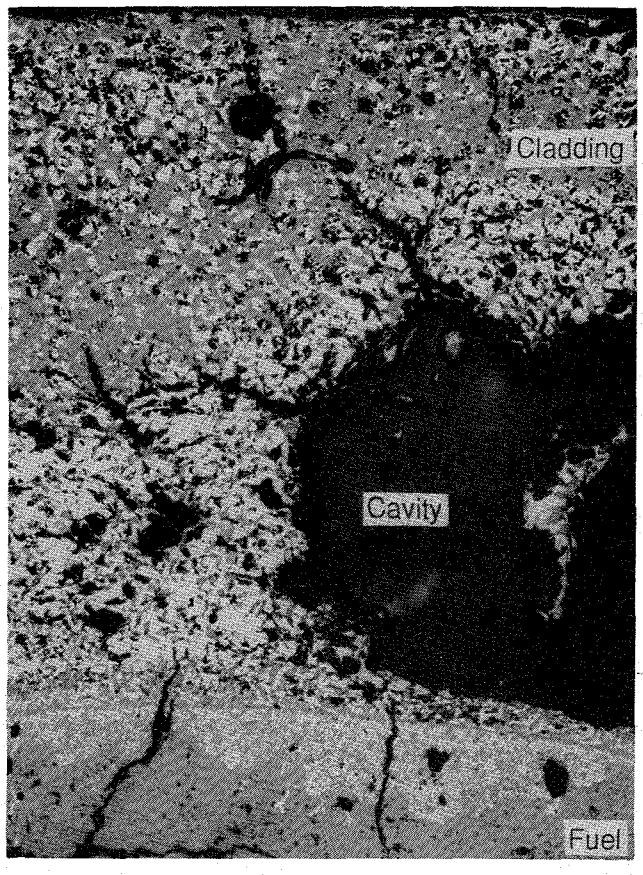

200 µm Pos. 2

Pos. 3

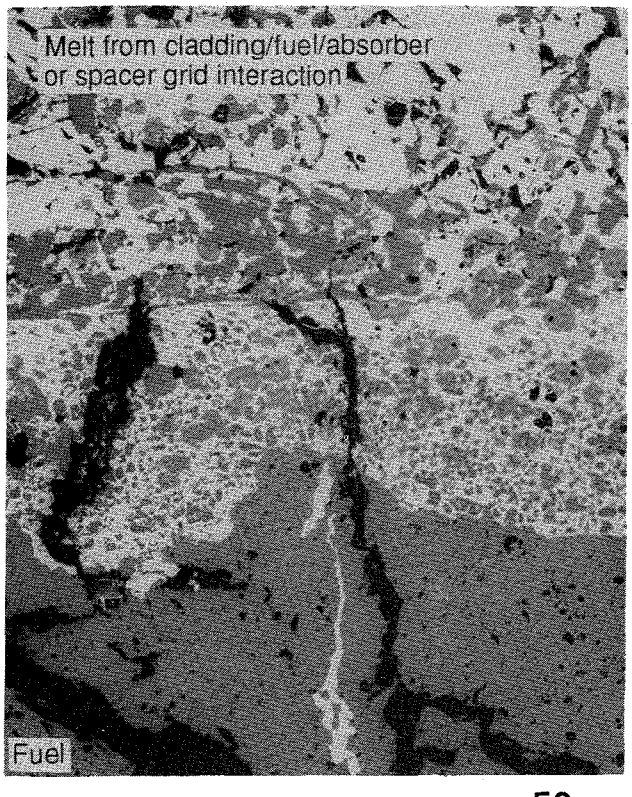

50 µm

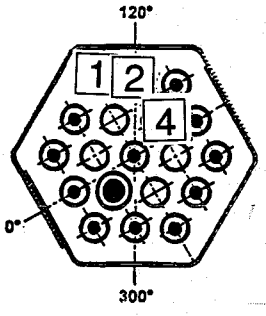

Pos. 4

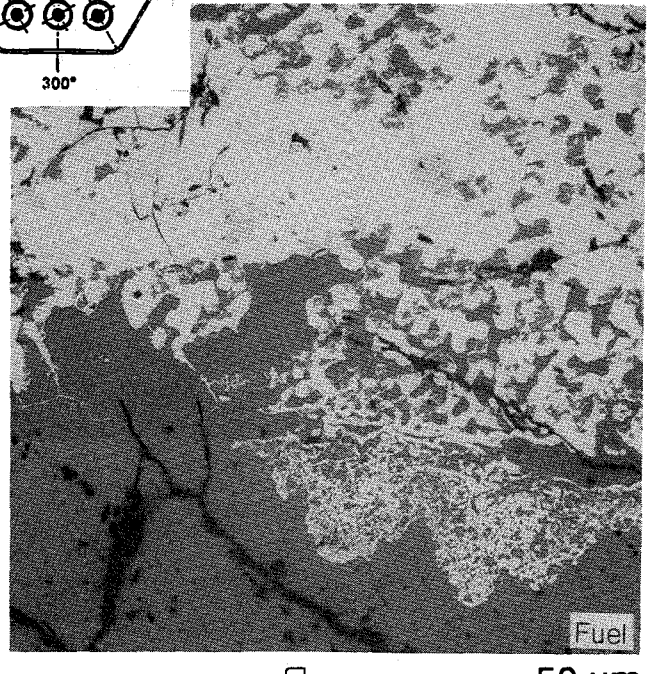

50 µm

KfK IMF

Fig. 33

Cross Section CORA-W2-k (top), Elevation 605 mm Fuel Rod Dissolution by Metallic Melt

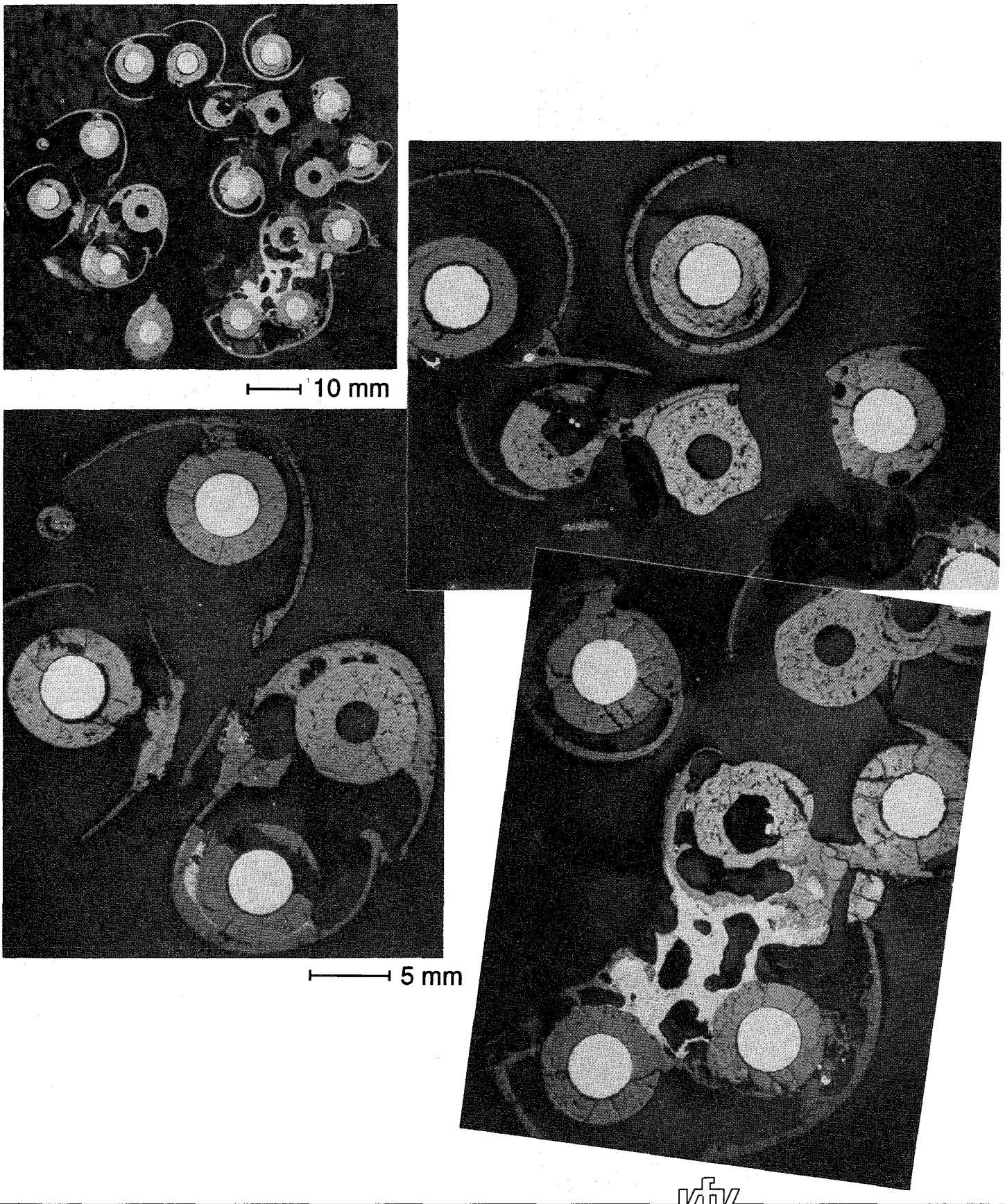

Fig. 34

Cross Section CORA-W2-p (top), Elevation 910 mm
Overview

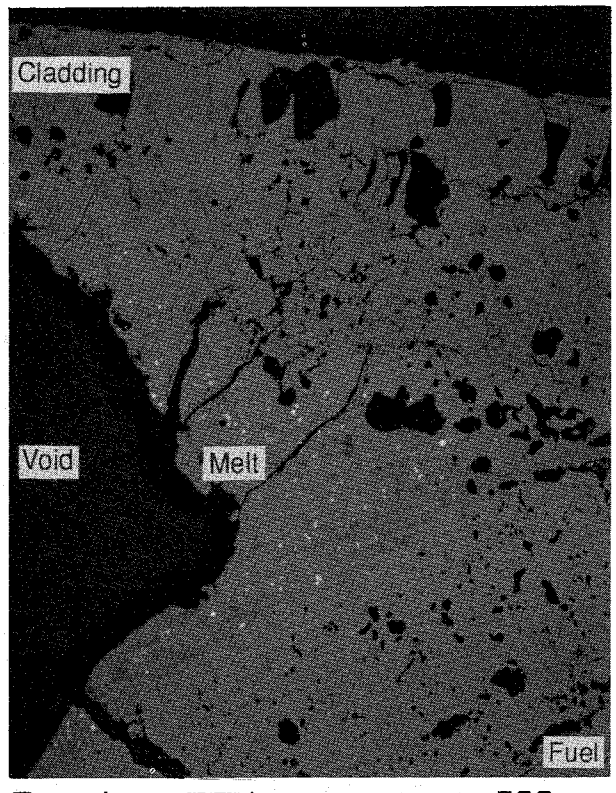

Pos. 1 ⟵⟶ 500 µm

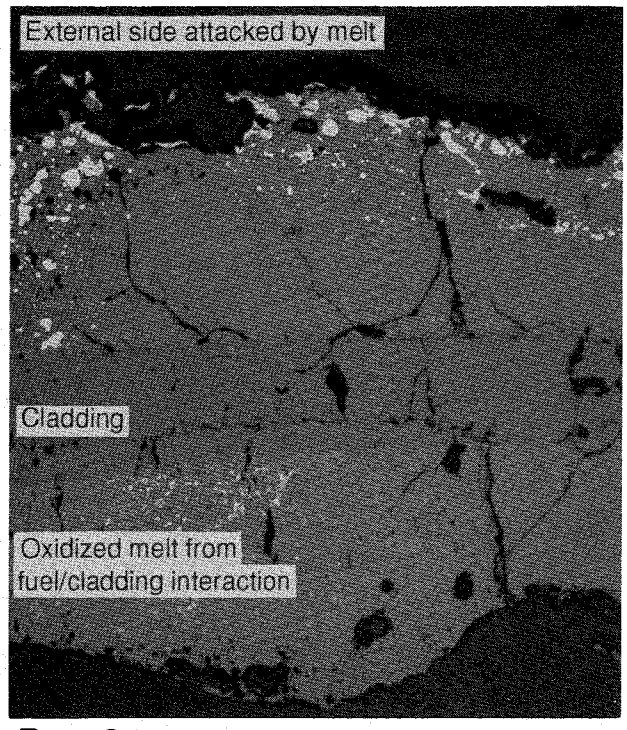

Pos. 2 ⟵⟶ 250 µm

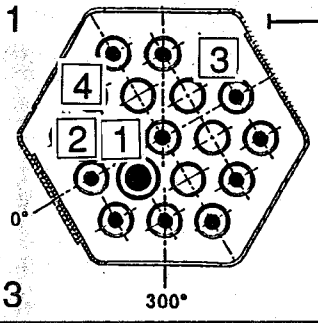

Pos. 3

⟵⟶ 100 µm

Pos. 4

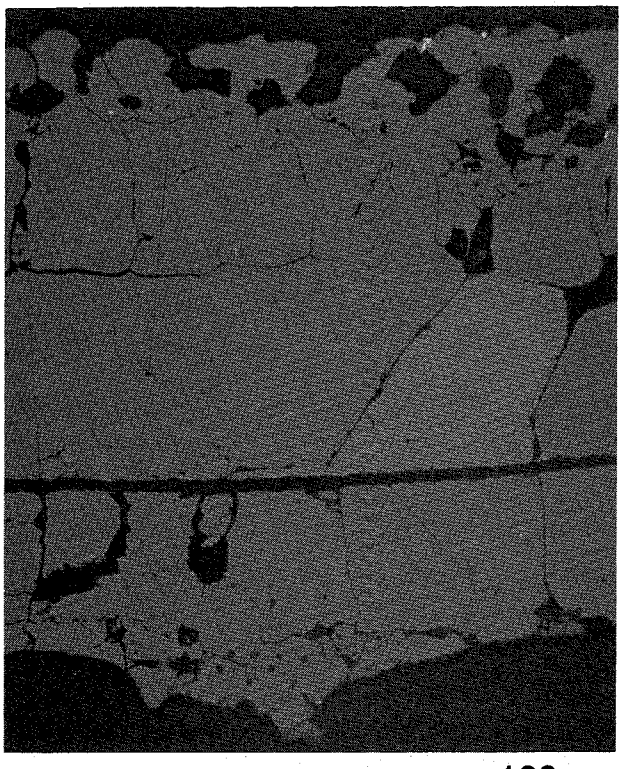

⟵⟶ 100 µm

KfK IMF

Fig. 35:

Cross Section CORA-W2-p (top), Elevation 910 mm Cladding Oxidation

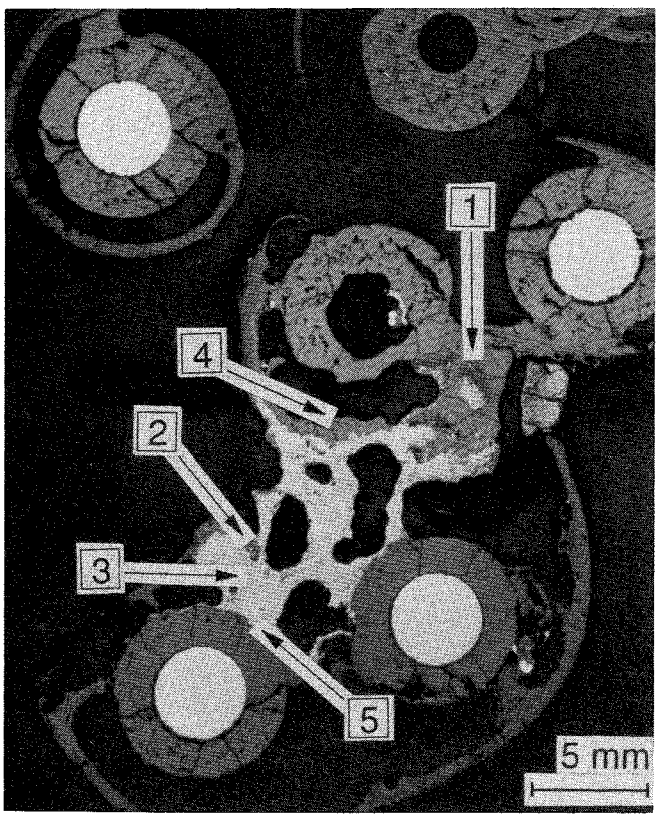

Melt from fuel/cladding interaction

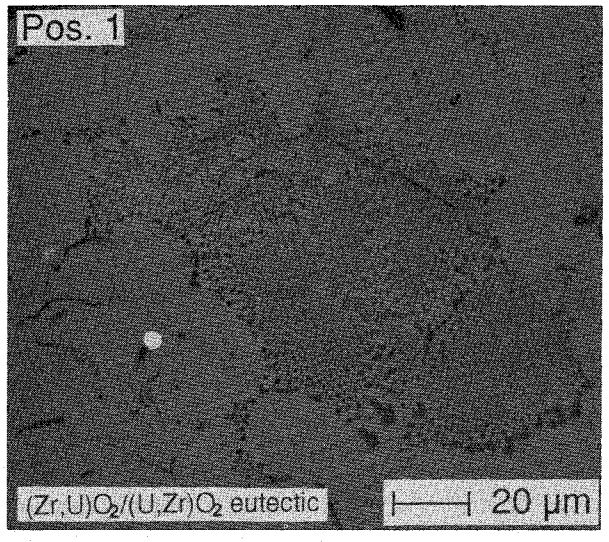

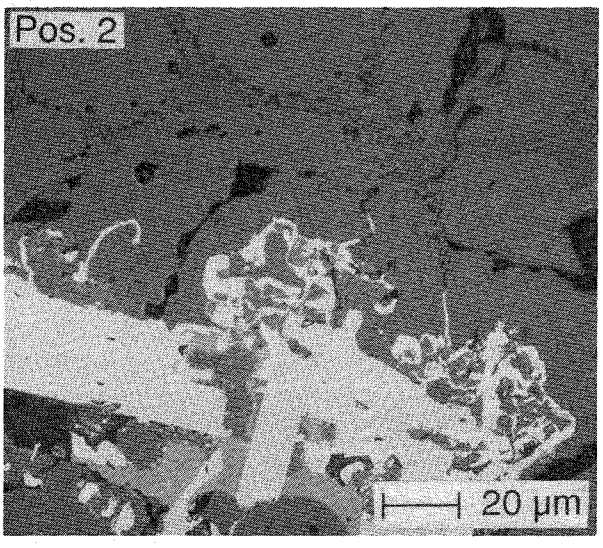

Melt from absorber degradation

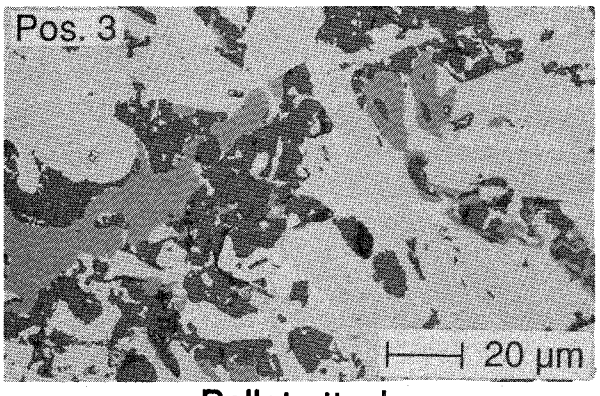

Pellet attack

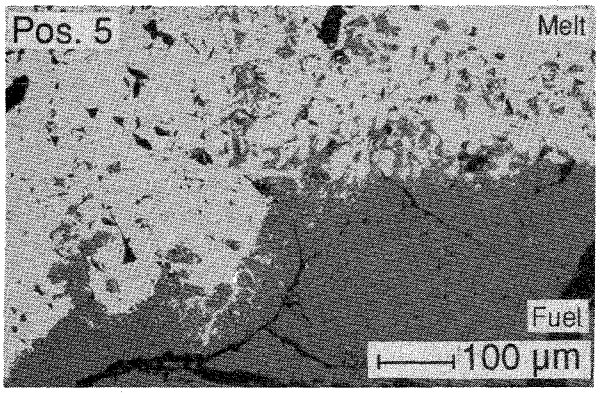

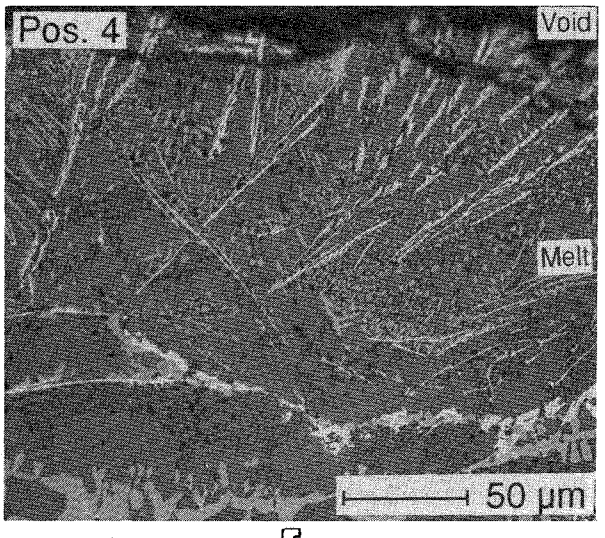

Fig. 36:

Cross Section CORA-W2-p (top), Elevation 910 mm
Melt Distribution and Morphology

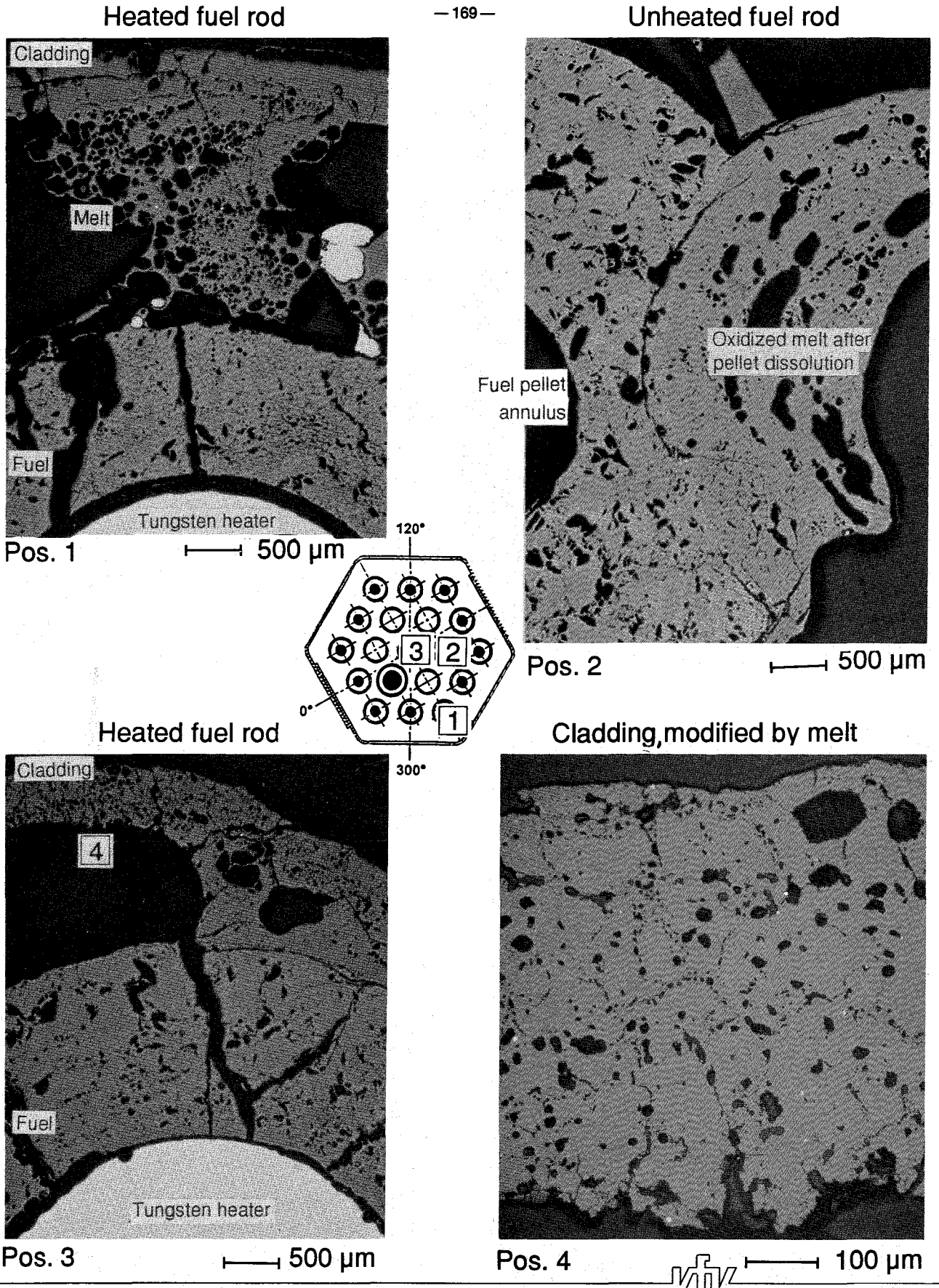

Fig. 37:

Cross Section CORA-W2-p (top), Elevation 910 mm Fuel Rods

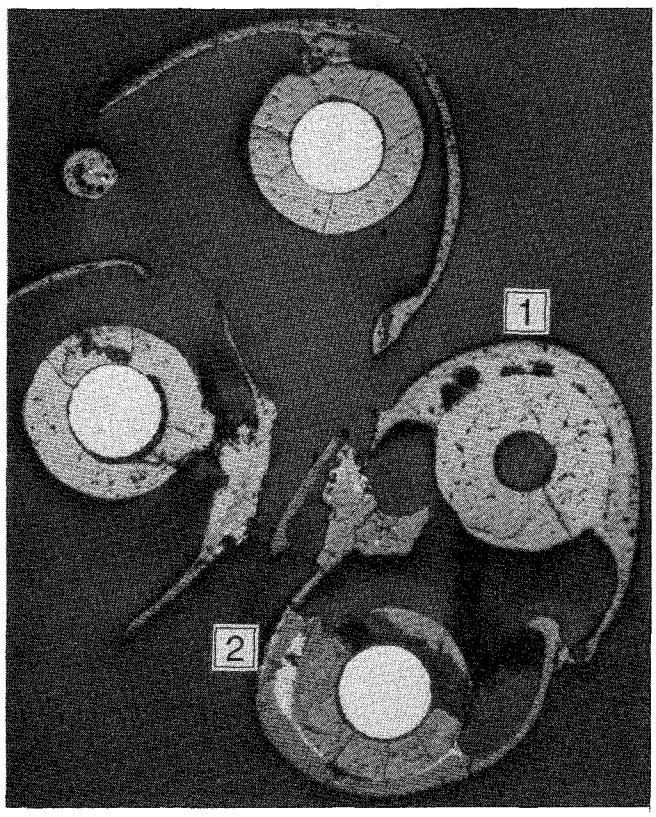

5 mm

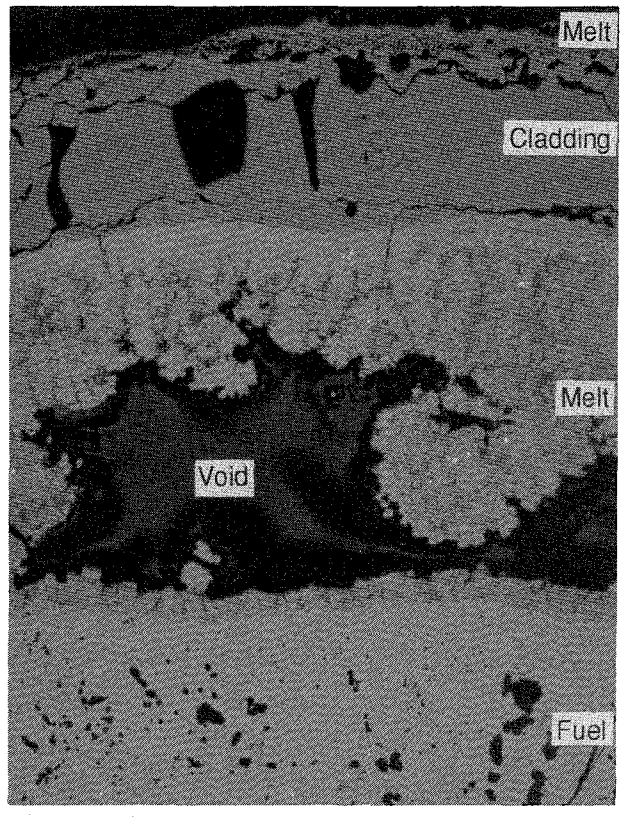

Pos. 1

200 µm

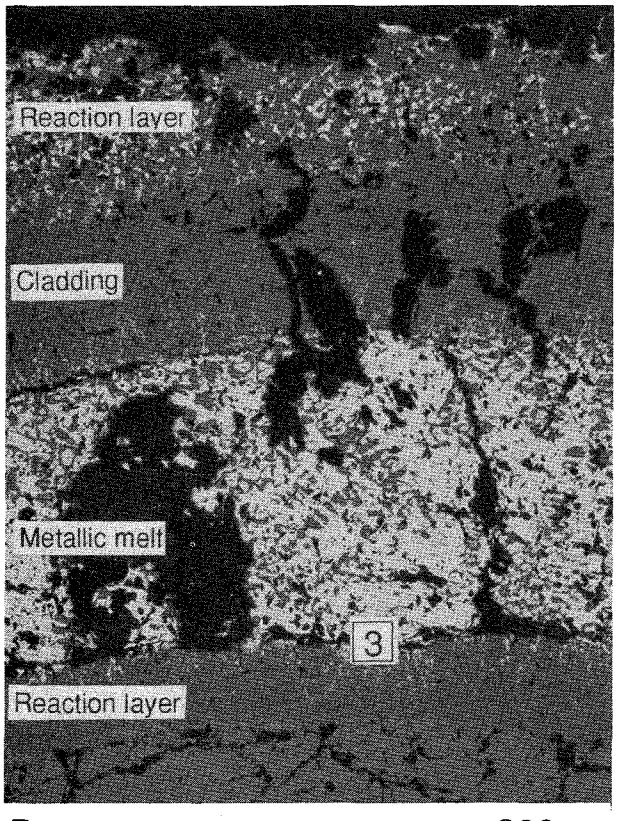

Pos. 2

200 µm

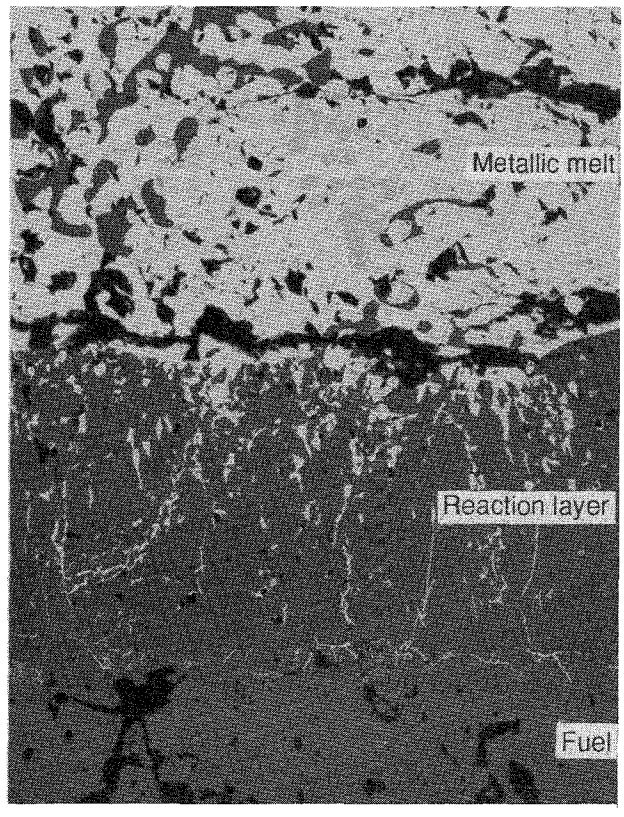

Pos. 3

50 µm

KfK IMF

Fig. 38:

Cross Section CORA-W2-p (top), Elevation 910 mm Fuel Rod Dissolution

Fuel pellet infiltration

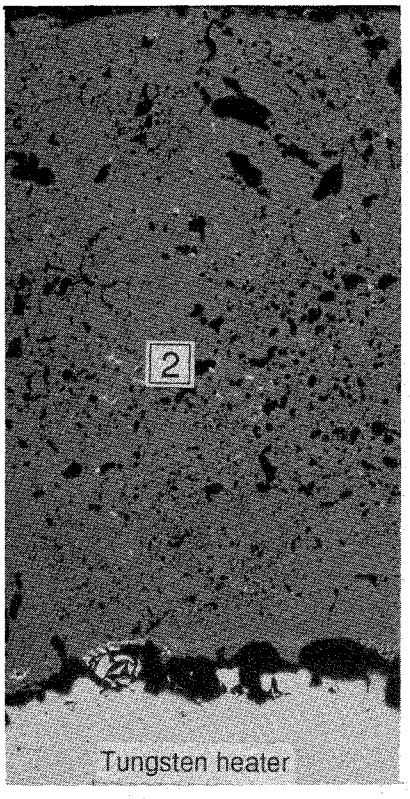

Pos. 1 ⟷ 200 µm

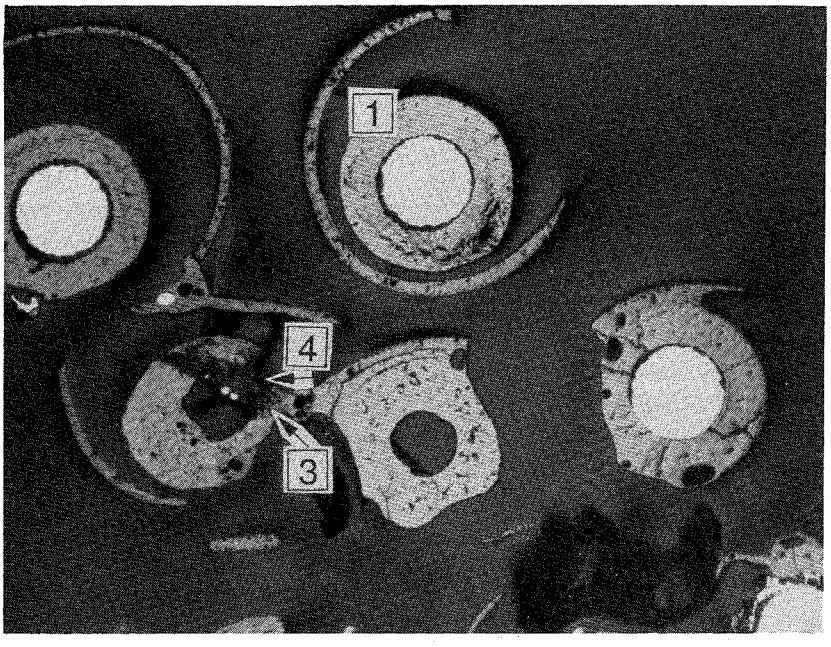

⟷ 5 mm

Pos. 2

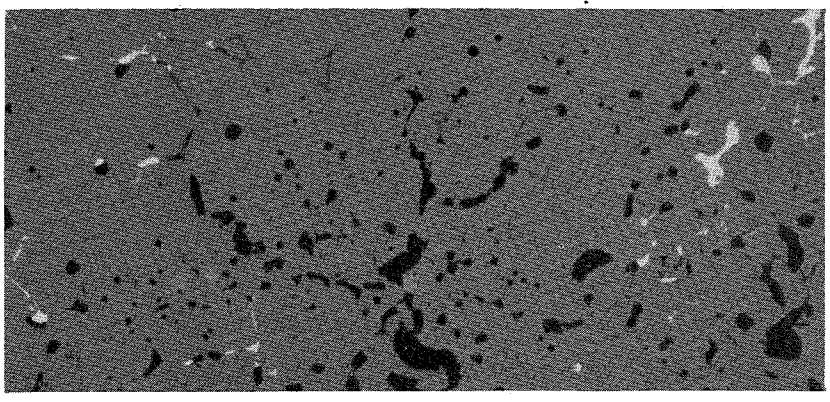

⟷ 20 µm

Pos. 3

Fuel pellet reaction product

Pos. 4

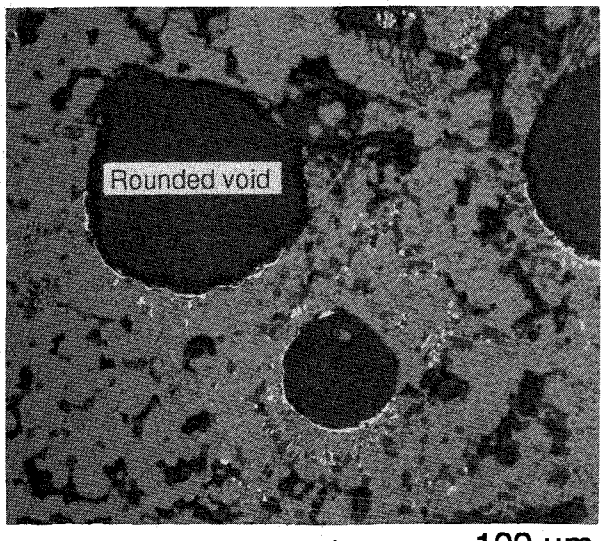

⟷ 100 µm

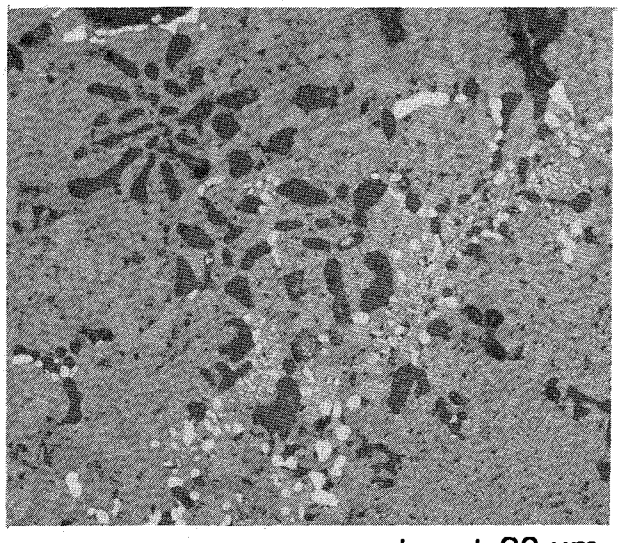

⟷ 20 µm

KfK IMF

Fig. 39:

Cross Section CORA-W2-p (top), Elevation 910 mm Fuel Pellet Destruction

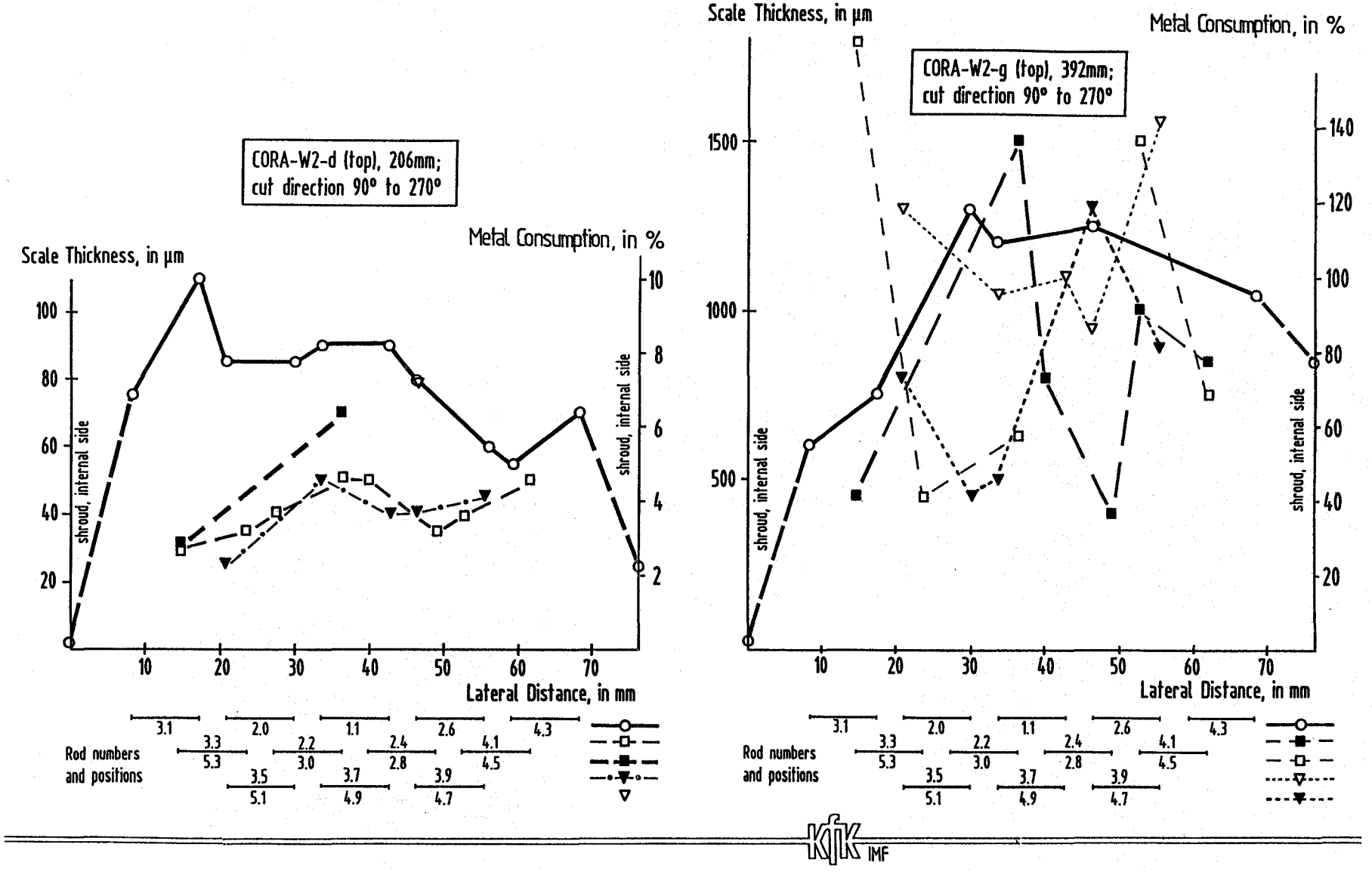

Fig. 40: Cladding Oxidation Profiles Across the Bundle CORA-W2 from 90° to 270° at the Elevations 206mm and 392mm

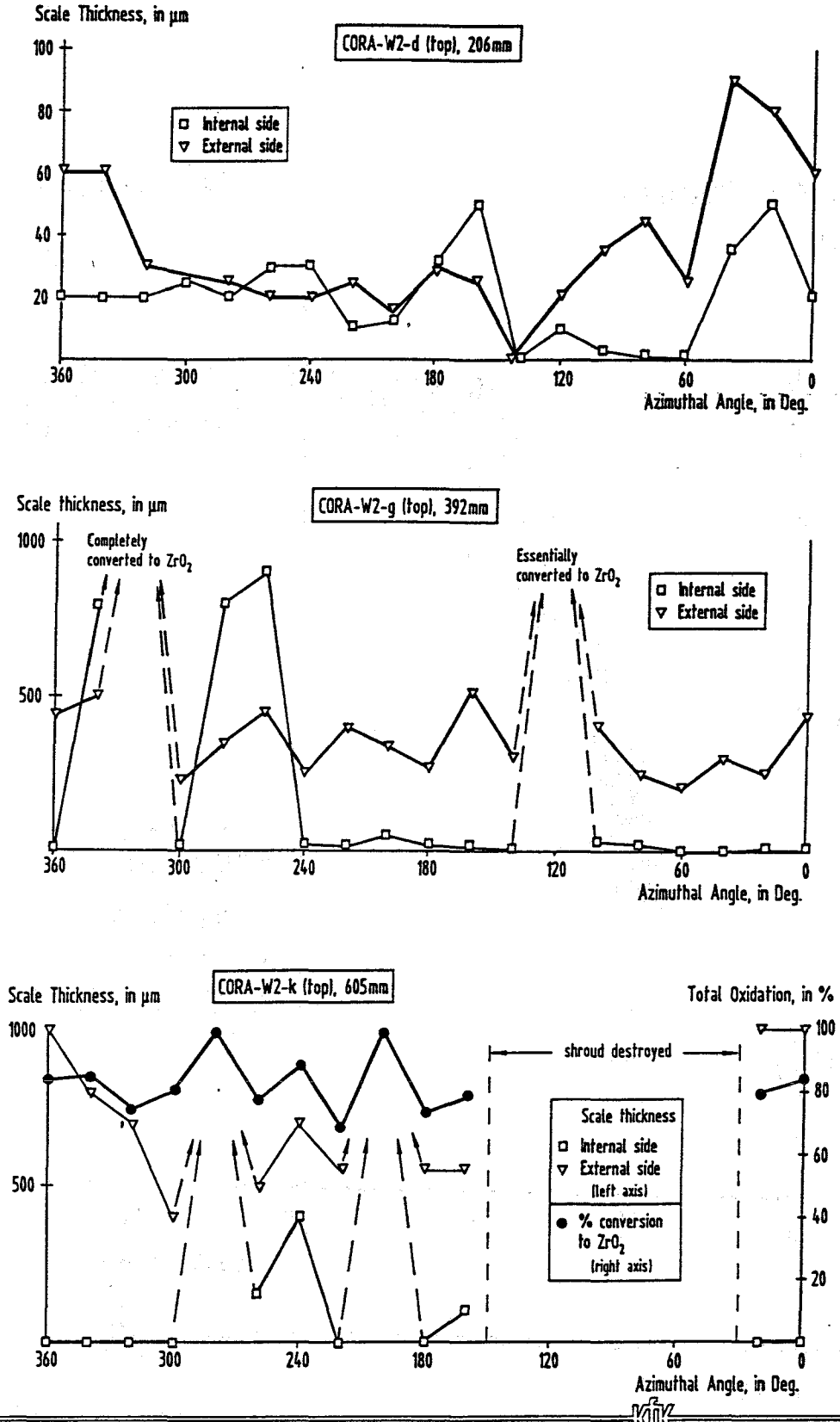

Fig. 41:

Shroud Oxidation Profiles Around the Bundle CORA-W2 at the Elevations 206mm, 392mm and 605mm

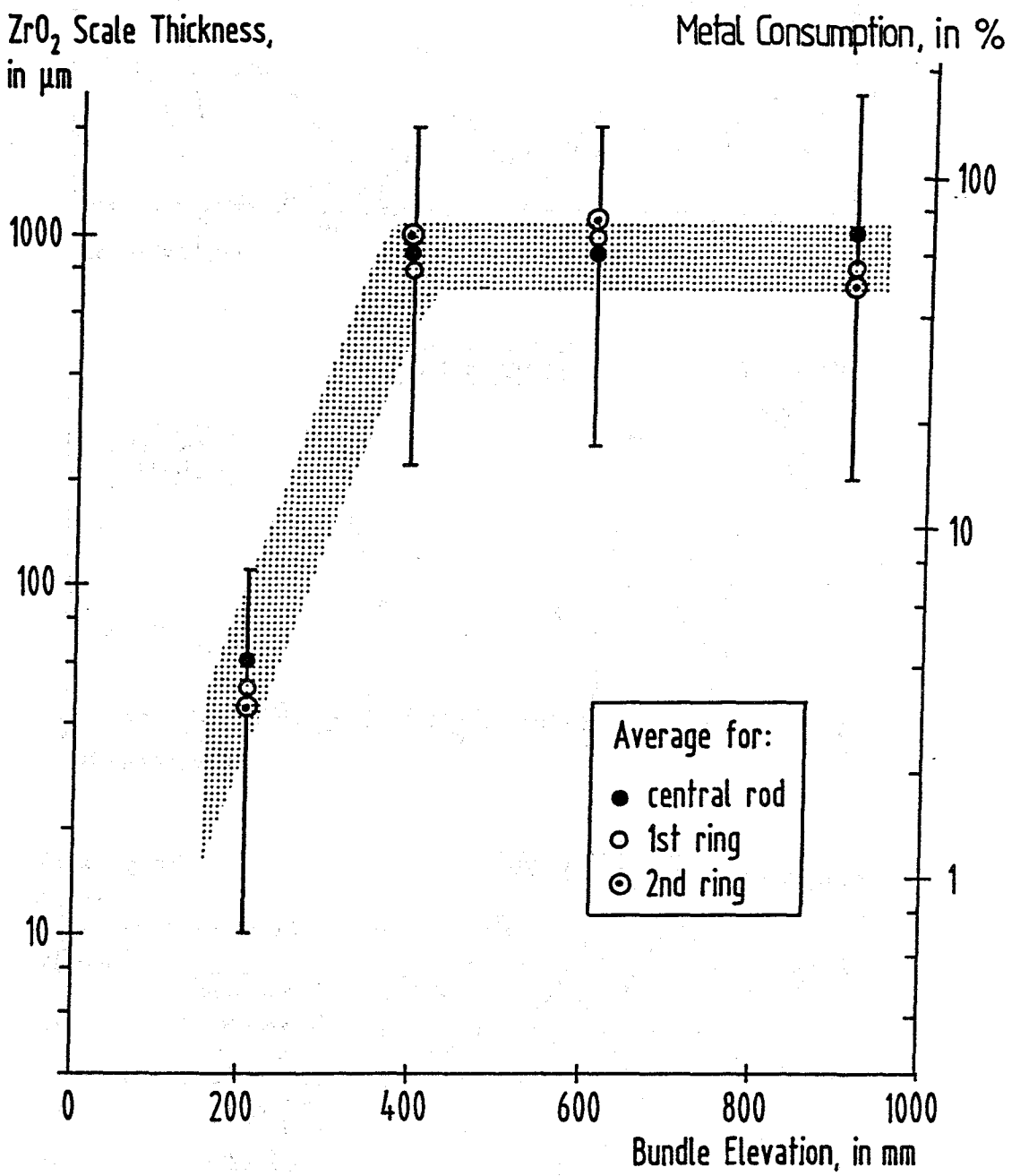

Fig. 42:

Axial Profile of Cladding Oxidation Along the Bundle CORA-W2

Post-Test SEM/EDX Examination Results of the VVER-1000 Fuel Rod Bundle CORA-W2

P. Hofmann
G. Schanz
J. Burbach
H. Metzger

August 1994

Kernforschungszentrum Karlsruhe
Institut für Materialforschung I

Post-Test SEM/EDX Examination Results of the VVER-1000 Fuel Rod Bundle CORA-W2

Introduction

Four cross sections of the fuel rod bundle CORA-W2 were chemically analyzed by SEM/EDX (scanning electron microscope, energy dispersive X-ray) examinations to

- describe the high-temperature reaction behavior among the bundle components, and to
- provide reference chemical compositions of typical phases (reaction products, solidified melts).

The measurements were performed with a SEM type JEOL 6100. For the EDX examination a newly developed light element (B, C, N, O) detector was used (Quantum 3600 - 19, Kevex).

Altogether 13 cross sections of the bundle CORA-W2 were metallographically prepared and chemically analyzed by MPA or SEM examinations in Germany and Russia. In the following chapter only the examination results of four cross sections are described which were examined in Germany (Figure 1); the other nine cross sections were analyzed in Russia. Therefore, the description of the chemical behavior of the bundle CORA-W2 in this report has to be considered as preliminary.

The objective of the SEM/EDX examiantions has been to describe at each examined cross-section elevation

- the fuel/cladding chemical interactions,
- the chemical behavior of th B_4C absorber assembly,
- the chemical behavior of the shroud, and
- the chemical composition and homogeneity of the solidified melts.

At the examined lowest cross-section elevation CORA-W2-d (206 mm) the majority of the reaction products and relocated and solidified melts are metallic in nature. The B_4C absorber assembly is still present. At all the other examined

cross-section elevations CORA-W2-g (392 mm), W2-k (605 mm), and W2-p (910 mm) the reaction products and a great part of the once molten material are oxidized. The absorber assembly has dissappeared at these elevations (Figure 1).

Cross-section elevation CORA-W2-d (206 mm)

The cross section W2-d is shown in Figure 2. The original arrangement of the heated and unheated rods, the B_4C absorber assembly, the stainless steel spacer grid, and the shroud can still be recognized. Various metallic melts relocated to this elevation and solidified. The heat content of the melts resulted in localized onset of melting of the ZrNb1 shroud and cladding and caused intensified chemical interactions with the UO_2 fuel. The B_4C absorber assembly is still present at this bundle elevation; the gap between the stainless steel guide tube and stainless steel clad B_4C absorber rod is filled with once molten material. The B_4C was chemically attacked by the stainless steel. The cross section also exhibits the great number of thermocouples which were used for temperature measurements. Especially at higher cross-section elevations, which reached higher temperatures, the thermocouples participated in the chemical interactions.

The examined locations of the cross section are indicated by numbers. Melts were analyzed with respect to their homogeneity at different spots indicated by letters.

The cross-section location #1 shows a heated fuel rod simulator with the central tungsten heater, the annular UO_2 pellet und the ZrNb1 cladding tube (Figure 3). As a result of the low temperatures only slight fuel/cladding interactions took place (Figure 4). At the adjacent fuel rod the temperature was higher which resulted in localized melting and relocation of the cladding under formation of a void (Figure 5). In Figure 6 the examined locations are indicated and the chemical compositons are given in the table. The chemical composition of the once molten material indicates eutectic chemical interactions between the ZrNb1 cladding and stainless steel at some other location. Besides Zr and U also the stainless steel components Fe, Cr, and Ni could be detected. The melt was kept in between the inner α-Zr(O) layer, which formed as result of chemical interactions with the fuel, and the α-Zr(O)/ZrO_2 layers on the outer cladding surface. The melting temperature of the once molten material can be much below of that for stainless steel ($<1450°C$).

At the cross-section location #3 (Figure 7) the fuel rod temperatures were even higher. At the fuel/cladding interface strong chemical interactions occurred. A great part of the cladding was liquefied and relocated partially under the formation of voids (Figure 7). The results of the chemical examinations show that not only chemical interactions of the cladding with the fuel and stainless steel took place but also with B_4C (Figure 8). The B_4C absorber assembly was adjacent to that fuel rod which was completely liquefied above the cross-section elevation CORA-W2-d. The resulting B_4C/stainless steel melt attacked and liquefied the ZrNb1 cladding.

The cross-section location #4 shows the partially degraded B_4C absorber assembly (Figure 2); Figure 9 shows details. Due to the chemical interactions between B_4C and stainless steel both components can be liquefied at temperatures as low as 1250°C. The B_4C/stainless steel melt penetrates into the B_4C pellet and is fixed by the outer stainless steel guide tube (Figure 9). Figure 10 shows details of the B_4C dissolution and of the outer surface of the guide tube. The results of the analytical examination are presented in Figures 11 and 12. Figures 11 and 12 show the chemical process of B_4C dissolution by the stainless steel melt; the resulting reaction products are indicated. The reason for the Mo content of the reaction products may be the thermocouple material which was located at the absorber assembly. One sould keep in mind that the various phases formed on cooldown of the melt and that the average Mo content in the melt was below 1 at %.

At the cross-section location # 5 a relocated metallic melt solidified in the open space of the stainless grid spacer between the fuel rods. The chemical composition corresponds to stainless steel with some dissolved Zr and Mo (Figure 13). Figure 14 through Figure 16 show some details of the phase analysis at or around the location #5.

The cross-section location # 6 shows a solidified melt between the shroud and the grid spacer (Figure 17). The chemical composition corresponds to that of the melt at the location # 5 (about 69 wt. % Fe, 16 wt. % Cr, 11 wt. % Ni, 5 wt. % Mo, and 1 wt. % Zr).

The average chemical compositon of the various metallic melts solidified at the cross-section location # 7 is given in Figure 18. The individual measurements of the melts at this location and of melts at all the other examined locations exhibit a very great similarity in their chemical compositon. This means, the origin of the molten material is probably the same. Since it is maily stainless steel with small

quantities of dissolved Zr and Mo the material is part of the molten absorber assembly which relocated from higher bundle elevations.

Cross-Section Elevation CORA-W2-g (392 mm)

The cross section W2-g is shown in Figure 19. The cladding of the fuel rods has partially melted and relocated to lower bundle elevations; the remaining part has been oxidized. The molten part of the cladding has been oxidized later in the course of the test. The molten cladding dissolved a part of the UO_2 fuel. The B_4C absorber assembly has been destroyed; some of the B_4C absorber material remained at this elevation. The shroud was partially molten and the post-test wall thickness is much thicker than the original one before the test.

The cross-section location # 1 shows a heated fuel rod simulator. The cladding was partially molten and relocated to some extent under formation of voids at the bundle elevation of 392 mm (Figure 20). At the position "a" analytical examinations of the various phases were performed; the results are given in Figures 21 through 23. One can recognize the formation of various (U, Zr, O) phases of different U concentration which were oxidized in solid or liquid state to $(U, Zr)O_2$ during the high-temperature transient. (Figure 21). One of the phases contains beside U, Zr, and O larger quantities of Mo, Fe, Ni, Cr, and Nb reflecting eutectic chemical interacions with stainless steel and probably some thermocouple material. A detailed analysis of the phases formed at the fuel/cladding interface is given in Figure 22. The UO_2 fuel dissolution process by the molten cladding is clearly visible. The phases which formed at the cladding tube surface are described in Figure 23. There is one location with high oxygen concentration but no other elements (point analysis # 4, Figure 23). It is probably BeO which was used in some thermocouples; Be can not be detected by the EDX system. The results of the analytical examinations at the position "b" (Figure 20) of the same fuel rod as above are given in Figure 24.

At the cross-section location # 2 the remaining B_4C/stainless steel melt was analysed at different positions ("a" through "g"); the results of the integral measurements are shown in Figures 25 through 31. A detailed examination of the phases at the position "a" is given in Figure 32. The chemical compositions of the melts at location #2 are very inhomogeneous; some contain a higher oxygen content and no boron, others contain boron. In all cases Fe, Zr, and U are components of the solidified melts; the Mo concentration varies between 0 and

23 wt. %. The detailed analysis of the various phases at position "a" shows that the main phase at this location is (U, Zr)O_2; Figure 32.

At the cross-section location # 3 the remaining B_4C is in contact with some liquefied material of different chemical composition described above. Details are shown in Figure 33: The corresponding composition of the various phases at the positions "a" and "b" are given in Figures 34 through 36. The chemical composition of the remaining "B_4C" pellet is given in Figure 37; the B_4C is depleted in B.

The shroud became thicker at this bundle elevation and was partially molten. The chemical composition of the once molten material is rather inhomogeneous; it contains besides Zr and O some Fe and U. This is a hint that relocating melts interacted with the shroud forming this post-test configuration (Figures 38 and 39).

Cross-Section Elevation CORA-W2-k (605 mm)

The cross section is shown in Figure 40. The destruction of the individul fuel rods is stronger and the fuel dissolution is more intensive than at the lower cross-section elevations. A great part of the molten material remained at this elevation. The absorber assembly has completely melted and relocated. The cladding has partially dissappeared and the remaining part is fully oxidized. The shroud has a similar appearance as that of the cross-section elevation CORA-W2-g (392 mm); it became thicker due to interactions with relocating melts and failed locally.

The cross-section location # 1 shows a heated fuel rod simulator; its cladding has partially molten and relocated forming large voids (Figure 41). The detailed analytical examinations of the various phases in the once molten cladding tube and its oxidized surface indicate mainly a (U, Zr)O_2 solid solution and a type of metallic α-Zr(O) which contains different amounts of U, Fe, Cr, and Ni (Figures 42 through 45). This is a clear indication that also at higher bundle elevations the early failure or liquefaction of the cladding below its melting point was caused by eutectic chemical interaction with stainless steel. The initially metallic α-Zr(O, U, Fe, Cr, Ni) was completely oxidized during the high-temperature transient at some positions (Figure 45).

At the cross-section location # 2 different melts accumulated; the positions of the analytical examinations are indicated by letters (a - e), the results are given in Figures 46 through 50. Beside the cladding and fuel components the melts

contain stainless steel and different quantities of Mo and W. The origin of the W are the tungsten heaters which were used in the heated fuel rod simulators; its concentration in the melts varies between 5 an 18 wt. %.

At the cross-section location # 3 different positions were analyzed (see Figue 40); the integral examination results are given in Figures 51 to 55. Figures 51, 52 and 55 indicate (U, Zr)O_2 phases. The materials of the positions "c" and "d" contain in addition to U, Zr, O also Fe, Cr, Ni and partially Mo and W. The majority of phases at the position "c" seem to be metallic (Figure 53).

At the cross-section location # 4 the chemical composition of the "melt bridge" between two fuel rods was determined at some positons (a - f). Figure 56 shows the various melts between the UO_2 pellets; the cladding was molten. At the positon "a" the material consists mainly of an (U, Zr)O_2 solid solution containing small concentrations of stainless steel and Mo (Figures 57 and 58). The material at position "b" is nearly pure (U, Zr)O_2 (Figure 59). At position "c" some stainless steel components are dissolved in the (U, Zr)O_2 (Figure 60). The solidified melt at positon "d" is metallic in nature and contains all elements of the fuel rod bundle including Mo and W (Figures 61 and 62). The position "e" shows some oxidic melts (formerly metallic) which penetrated into the gap between the tungsten heater and the fuel pellet (Figure 63); The melt corresponds to (U, Zr)O_2. Most probably it penetrated into the gap as an (U, Zr, O) alloy which was oxidized to (U, Zr)O_2 later in the test. The position"f" shows as matrix material (U, Zr)O_2 with an eutectic phase mixture at the grain boundaries (Figures 64 and 65). The eutectic is probably caused by BeO (thermocouple material)/(U, Zr)O_2 chemical interactions (Figure 65).

The analytical examinations of the shroud at the cross-section elevation # 5 shows a once molten mixture of α-Zr(O) and ZrO_2 which is kept at place by the ZrO_2 layers on the surface of the shroud (Figures 66 through 70). Neither stainless steel nor U could be detected at this position.

Cross-Section Elevation CORA-W2-p (910 mm)

The cross-section is shown in Figure 70. One can recognize the strong destruction of the bundle arrangement at this elevation. The B_4C absorber assembly has completely disappeared. The molten part of the cladding relocated and dissolved some UO_2 fuel; the remaining part of the cladding is completely oxidized. Some

once molten material remained at this elevation. The shroud is completely missing (either destroyed during the test or during dismantling of the bundle).

The cross-section location # 1 shows a heated fuel rod simulator; the once molten metallic part of the cladding was kept at place by the ZrO_2 layer on the tube surface (Figure 71). The results of the analytical examinations at the positions "a" through "d" are given in Figures 72 through 75. The molten (U, Zr, O) alloy was oxidized to (U, Zr)O_2 of different chemical composition, that means of different U and Zr content.

The cross-section location # 2 shows an accumulation of once molten material (Figure 70). The detailed chemical examinations of their chemical compositon is given in Figures 76 through 84.

Chemical Composition of the Melts

The chemical composition of the various melts at different cross-section elevations is listed in Tables 1 and 2 and plotted in Figure 85 as a function of the axial bundle elevation. The results indicate that at the lowest examined cross-section elevation of 206 mm all melts are metallic in nature. The melts consist mainly of stainless steel components with very small amounts of Zr (1 - 2 wt. %) and some Mo (3 - 7 wt. %), which is coming from the thermocouple material; and no U, B, C or O. This is an indication that the melts formed rather early during the high-temperature transient by liquefaction of the absorber assembly and relocation to this bundle elevation. At this early stage of bundle degradation the chemical interactions of the stainless steel melts with other bundle components or the steam environment are very small.

At the higher cross-section elevations, besides the metallic melts, also ceramic (U, Zr)O_2 melts of different chemical composition can be recognized. The average Zr content of the mixed oxide decreases from about 55 to 38 wt. % with increasing bundle elevation; the average U concentration increases simultaneously from about 14 to 41 wt. % (Figure 85). The concentration of the stainless steel components in the (U, Zr)O_2 mixed oxide varies between 0 and 10 wt %. In some cases also some Mo, W and Nb can be detected (Tables 1, 2). The metallic melts at the higher cross-section elevations 392, 605 and 910 mm are rich in Zr, Mo, U and B and contain various concentrations of stainless steel components and some oxygen. In some metallic melts also W and Nb is present.

It is interesting to note the behavior of C of the B_4C absorber material; it could neither be detected in any once liquid nor in any solid phase. B is concentrated in the metallic melts.

Summary and Conclusions

The post-test examination results show the strong impact of the B_4C absorber assembly and stainless steel grid spacer on the early damage progression of the VVER-1000 fuel rod bundle simulator. The stainless steel of the absorber assembly and/or grid spacer interacts eutectically with the ZrNb1 cladding tubes. This results in liquid phase formation below the melting point of the cladding. In many fuel rods, which showed still an intact cladding tube, a solidified (Zr, Fe, Cr, Ni, O) melt could be detected inbetween the UO_2 pellet and the ZrO_2 layer on the cladding outer surface. This indicates a liquefaction process of the "oxygen-poor" cladding by stainless steel in axial direction over long distances.

During the high-temperature transient the ZrNb1 cladding interacts with the UO_2 forming the typical solid state interaction layers [α-Zr(O,U), (U, Zr) alloy, α-Zr(O)]. At temperatures above the melting point of the cladding extensive fuel dissolution occurred forming larger quantities of α-Zr(O, U) and $(U, Zr)O_2$ reaction products at higher bundle elevations.

The impact of the thermocouple materials and the tungsten heaters on the melt-down behavior of the fuel rod simulator is probably negligible. Damage initiation and damage progression is caused exclusively by the bundle components.

Whereas in other CORA tests with B_4C absorber rods the absorber material relocated completely to the lower bundle elevations in the test CORA-W2 some B remained within the bundle (fixed in metallic melts). This observation may be important with respect to accident management considerations.

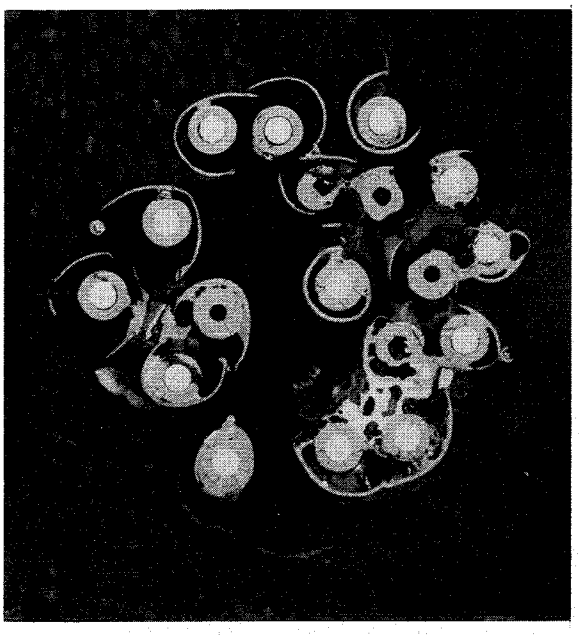

cross section W2-p (top)
910mm

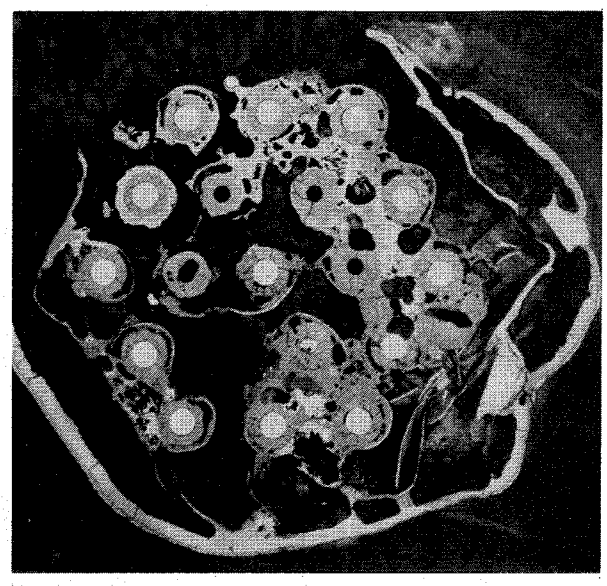

cross section W2-k (top)
605mm

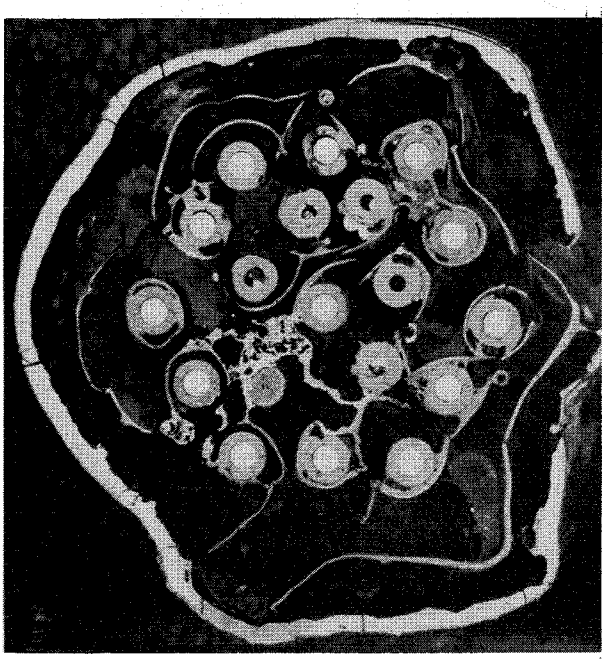

cross section W2-g (top)
392mm

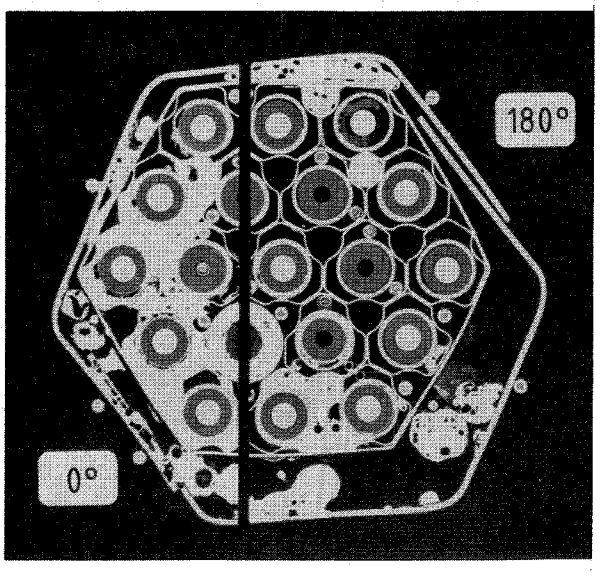

cross section W2-d (top)
206mm

10mm

Fig. 1: Cross sections of the bundle VVER-1000/CORA-W2 which were analysed at KfK (206, 392, 605 and 910 mm bundle elevation)

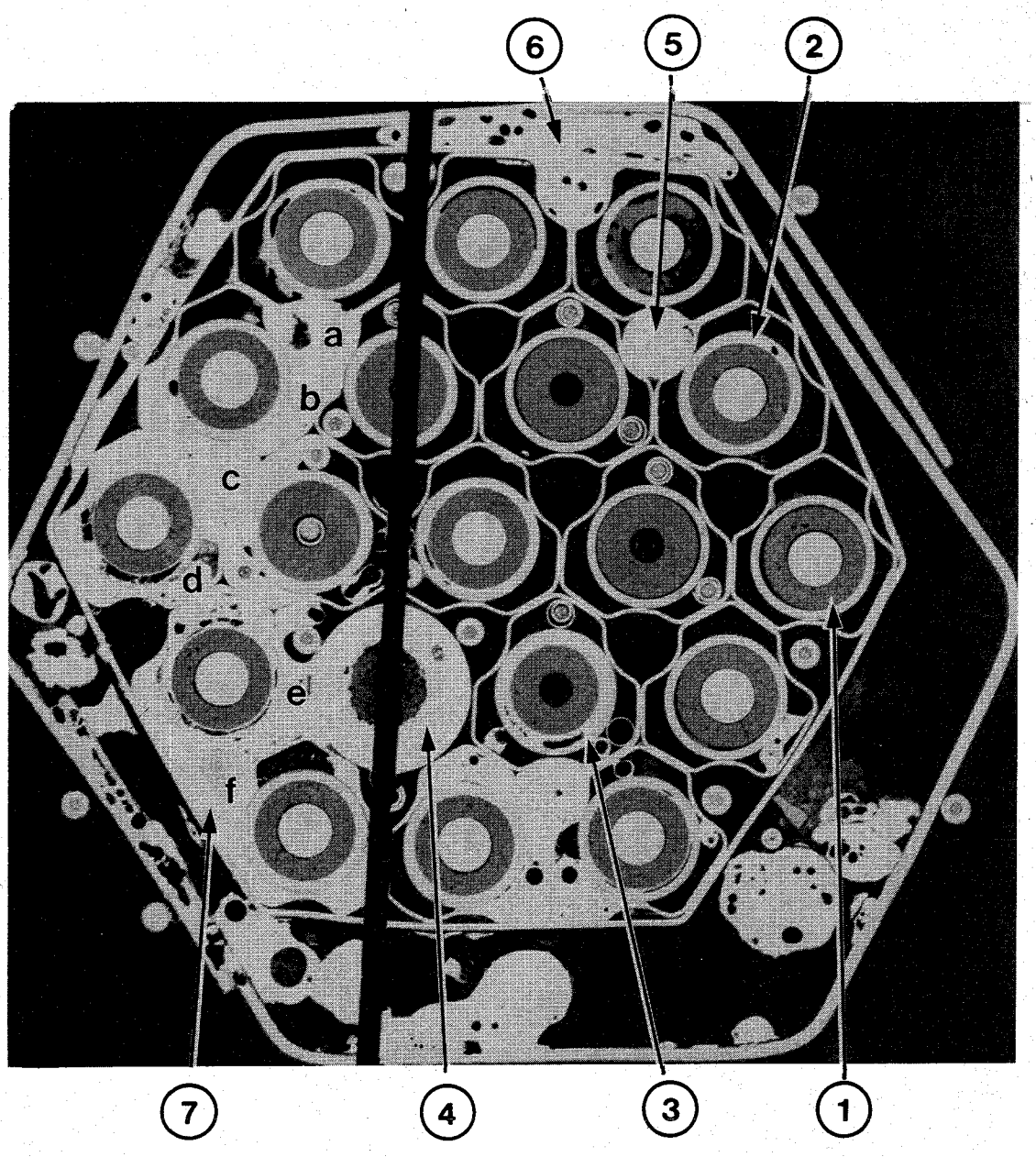

Maßstab 2 : 1

Fig. 2: Fuel rod bundle CORA-W2, cross section # d (206 mm); Positions of SEM/EDX analysis

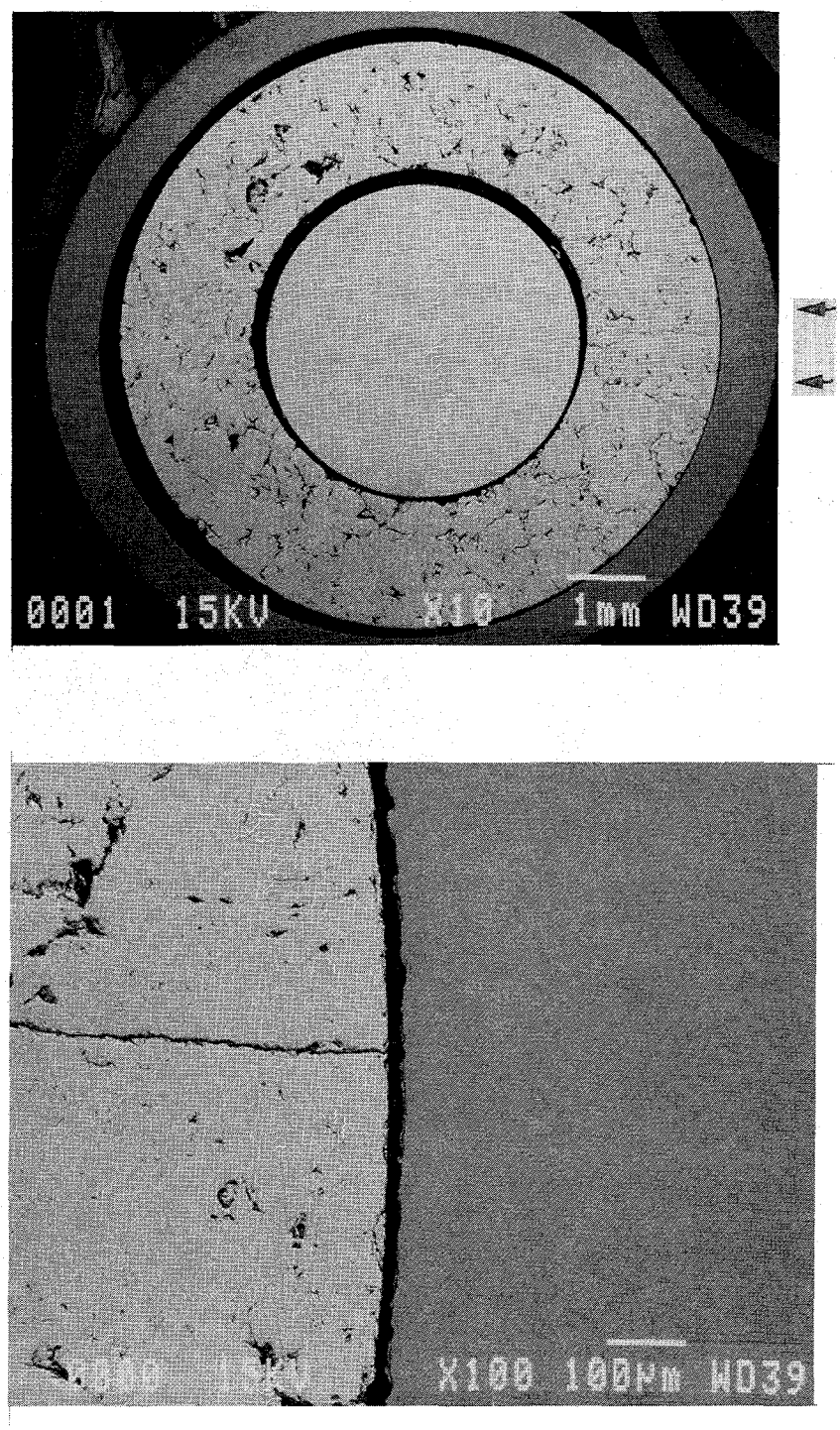

Fig. 3: Fuel rod bundle CORA-W2, cross section # d (206 mm); General view of position # 1 (fuel/cladding contact)

Punktanalyse Nr. Nr.	Element	Gew.-%	Atom %*
1	O U	11.5 88.5	66 34
2	Zr U	98.7 1.3	99.5 0.5
3	Zr	100	100
4	O U	12 88	67 33

* auf 100 % normalisiert

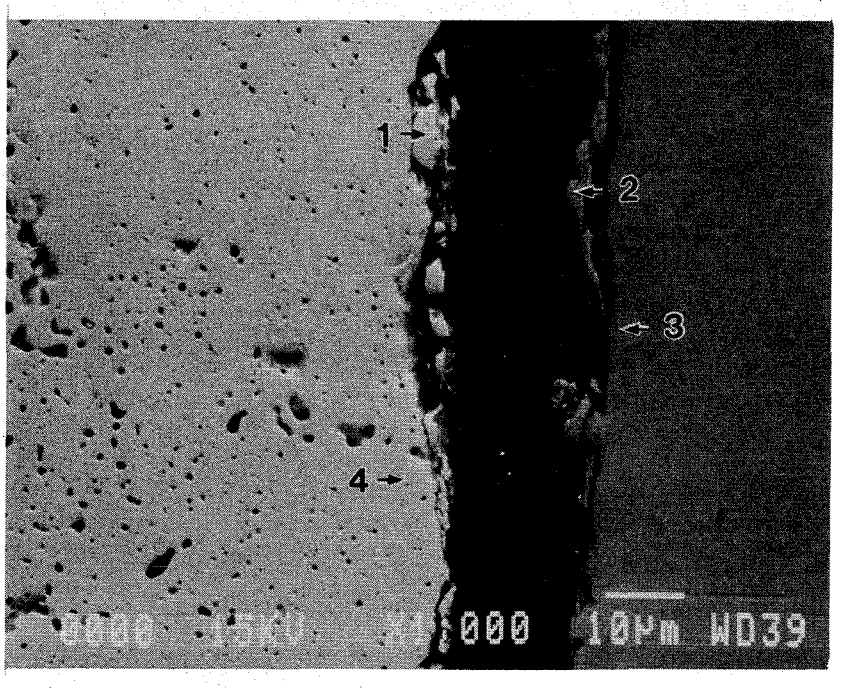

Fig. 4: Fuel rod bundle CORA-W2, cross section # d (206 mm); SEM/EDX analysis at position # 1 (fuel/cladding interface)

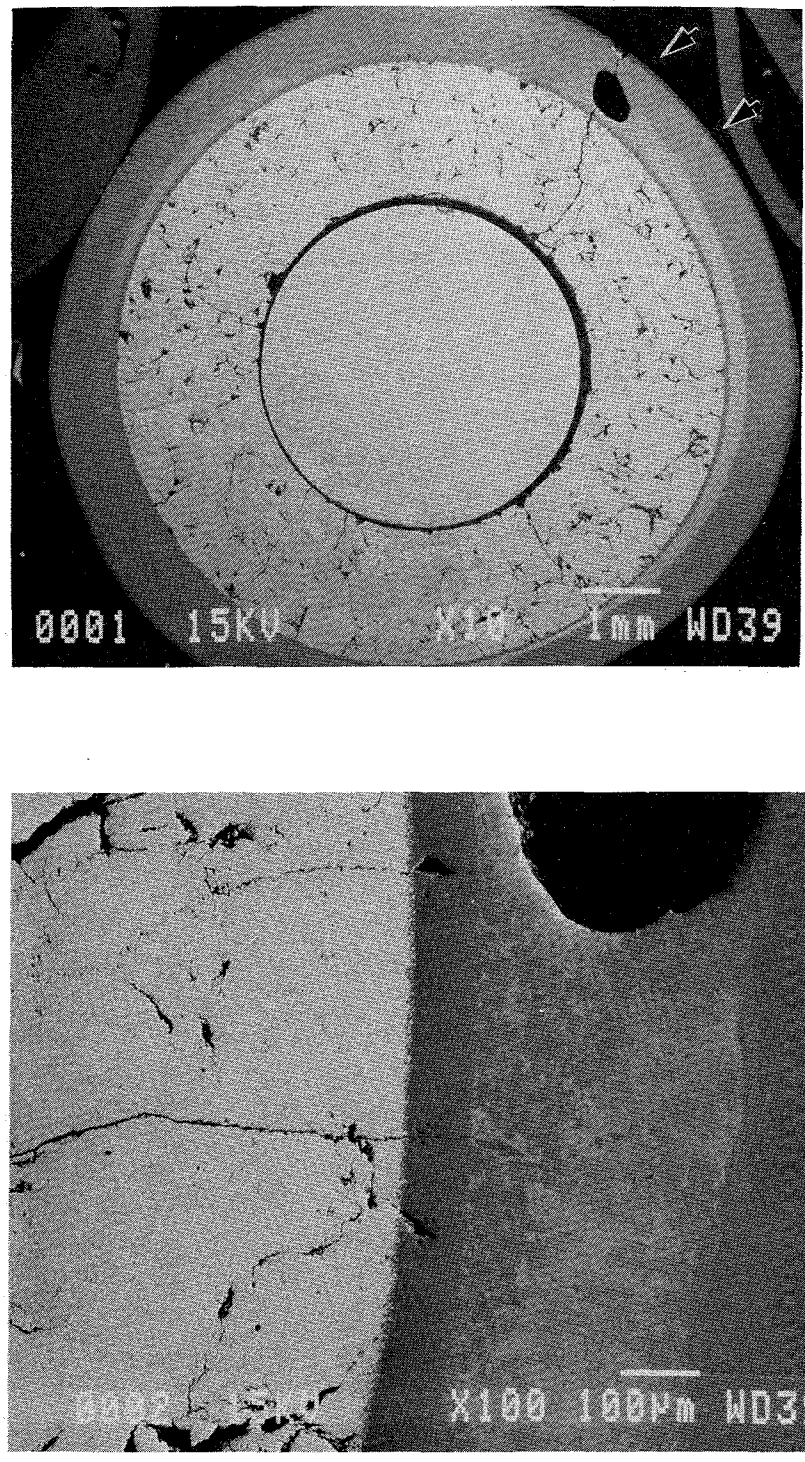

Fig. 5: Fuel rod bundle CORA-W2, cross section # d (206 mm); General view of position #2 (fuel rod)

Punktanalyse Nr.	Element	Gew.-%	Atom %*
1	Cr	1.4	2.4
	Fe	7.1	11.9
	Ni	1.3	2.1
	Zr	76.5	78.2
	U	13.8	5.4
2	O	2.7	13.5
	Zr	97.3	86.5
3	Cr	1.3	2.4
	Fe	6.1	10.4
	Ni	1.3	2.1
	Zr	75.2	78.6
	U	16.1	6.4

* auf 100 % normalisiert

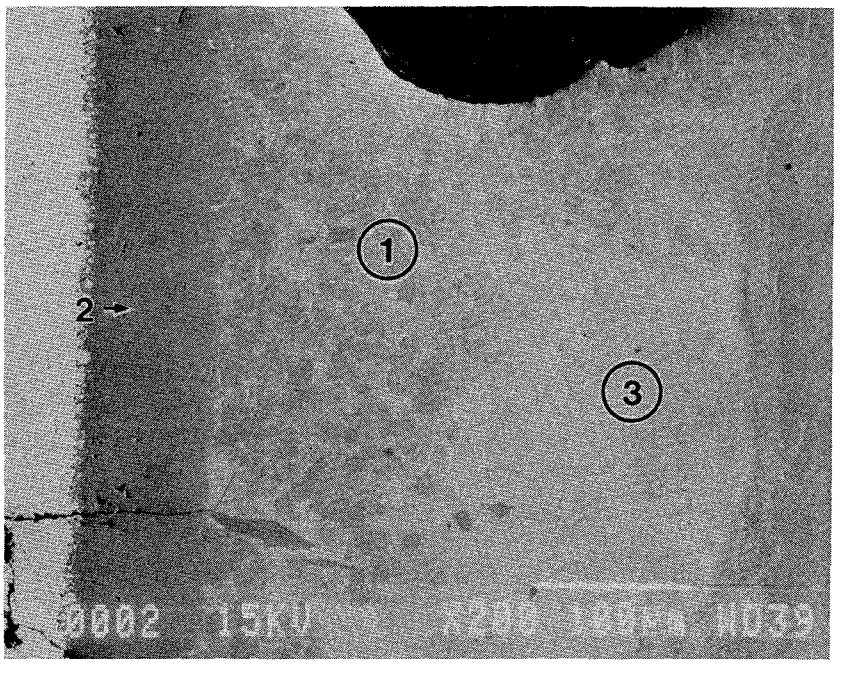

Fig. 6: Fuel rod bundle CORA-W2, cross section # d (206 mm); SEM/EDX analysis at position # 2 (fuel/cladding interface)

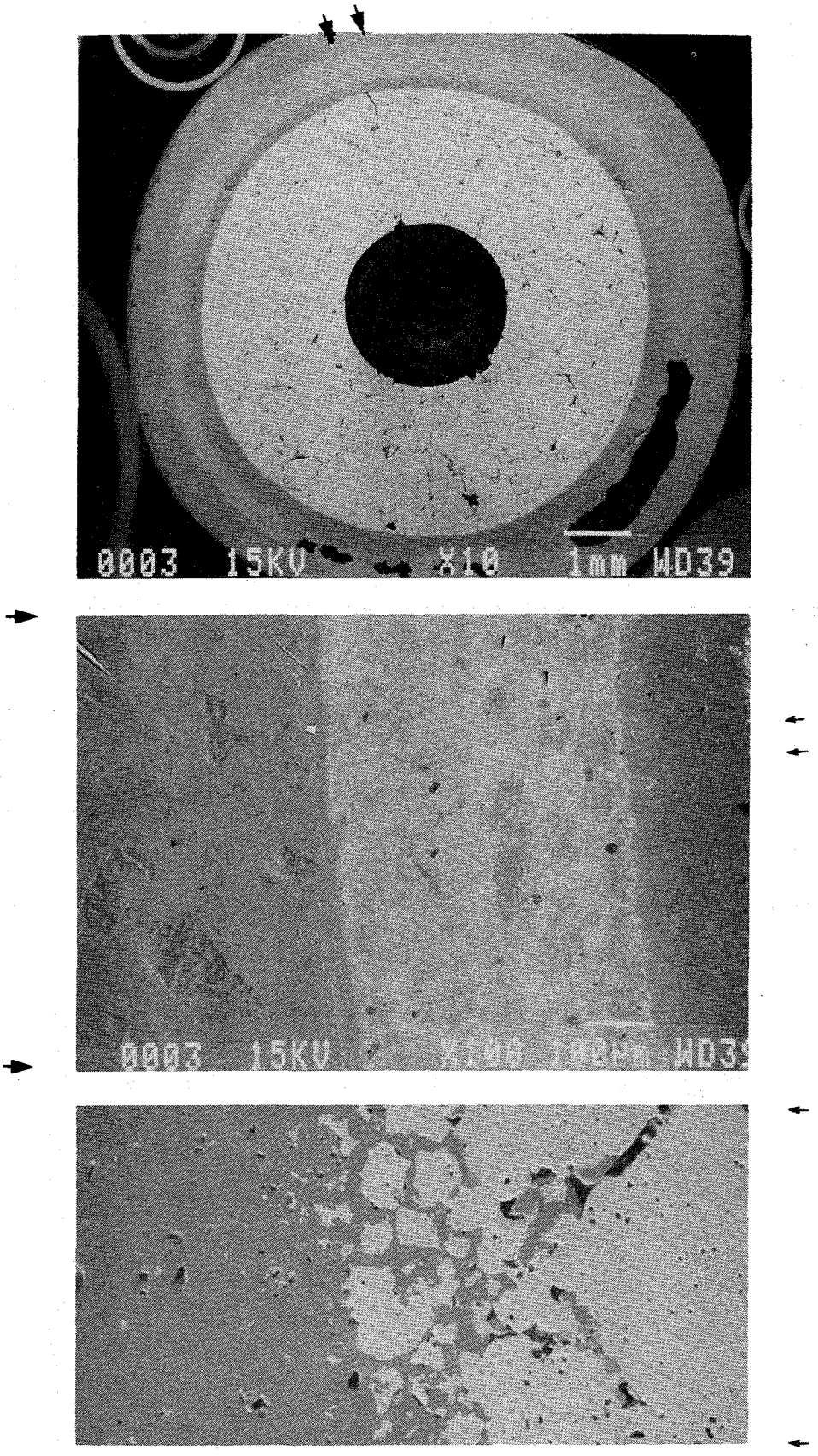

Fig. 7: Fuel rod bundle CORA-W2, cross section # d (206 mm); General view of position # 3 (fuel rod)

Punktanalyse Nr.	Element	Gew. %	Atom %*
1	Zr	93.2	97.3
	U	6.8	2.7
2	Cr	4.1	7.1
	Fe	14.6	23.3
	Ni	2.1	3.2
	Zr	61.6	59.9
	U	17.5	6.5
3	Cr	8.9	14.7
	Fe	8.3	12.9
	Ni	0.3	0.5
	Zr	72.0	68.1
	U	10.4	3.8
4	Zr	85.8	94.1
	U	14.2	5.9
5	B	15	60
	Zr	85	40
6	B	5	29
	Zr	95	71

* auf 100 % normalisiert

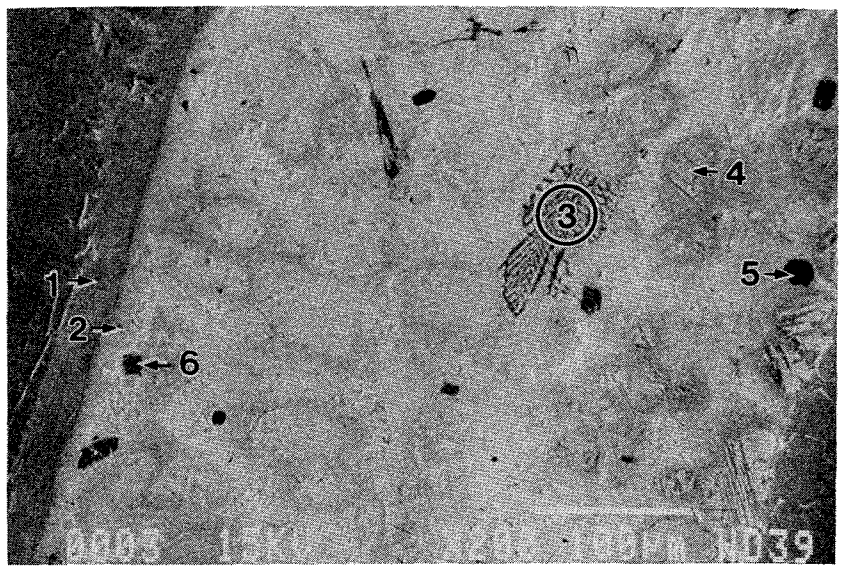

Fig. 8: Fuel rod bundle CORA-W2, cross section # d (206 mm); SEM/EDX analysis at position # 3 (fuel rod cladding)

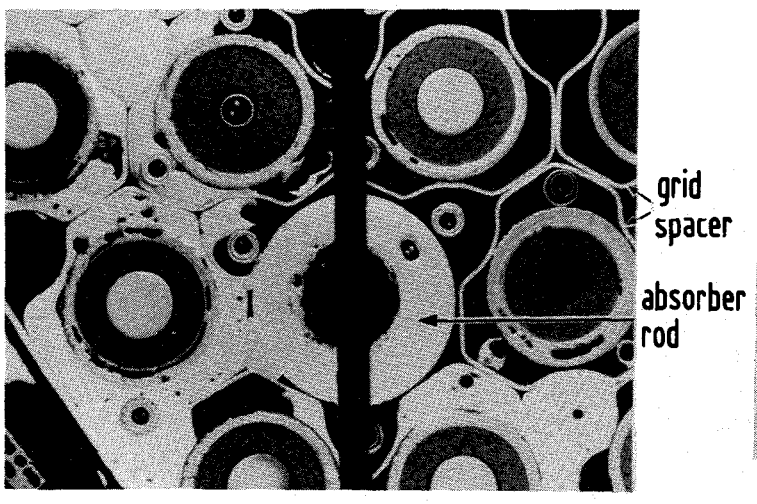

chemical behavior of B_4C absorber rod

500 µm

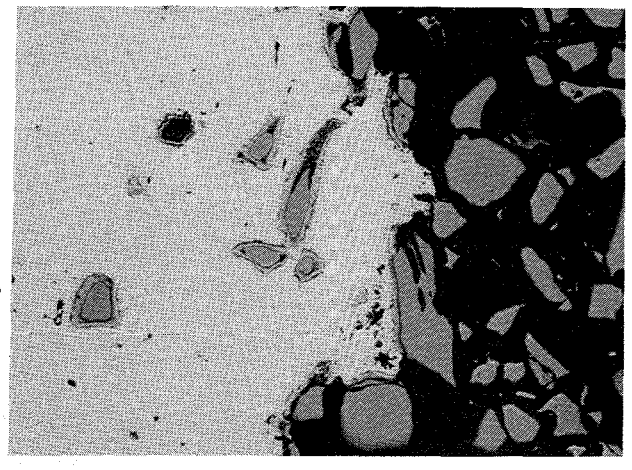

dissolution of B_4C by ss melt

100µm

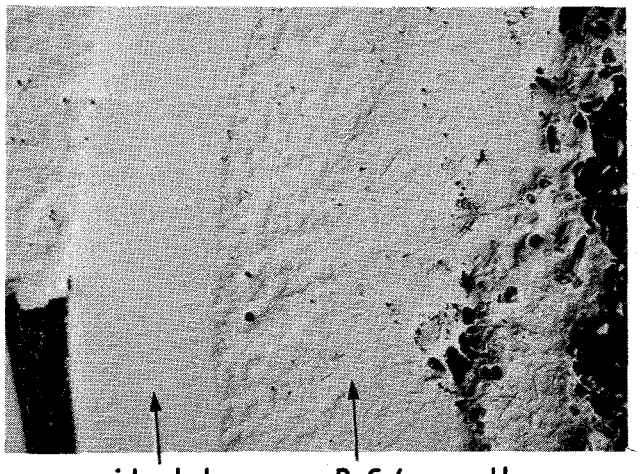

500 µm

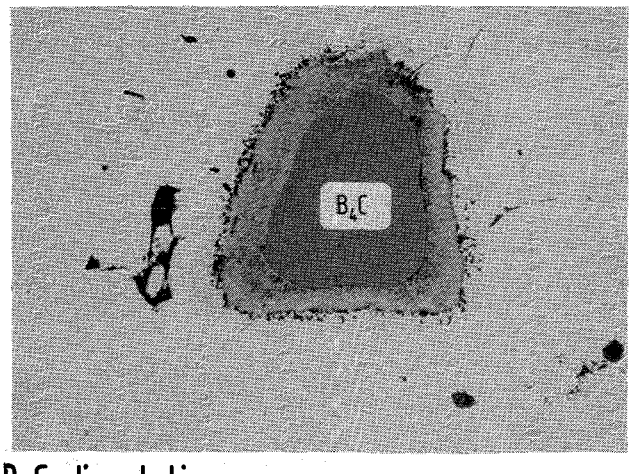

B_4C dissolution process

20µm

Fig. 9: Cross section W2-d (top) of the bundle VVER-1000/CORA-W2; 206 mm elevation (details of B_4C absorber rod)

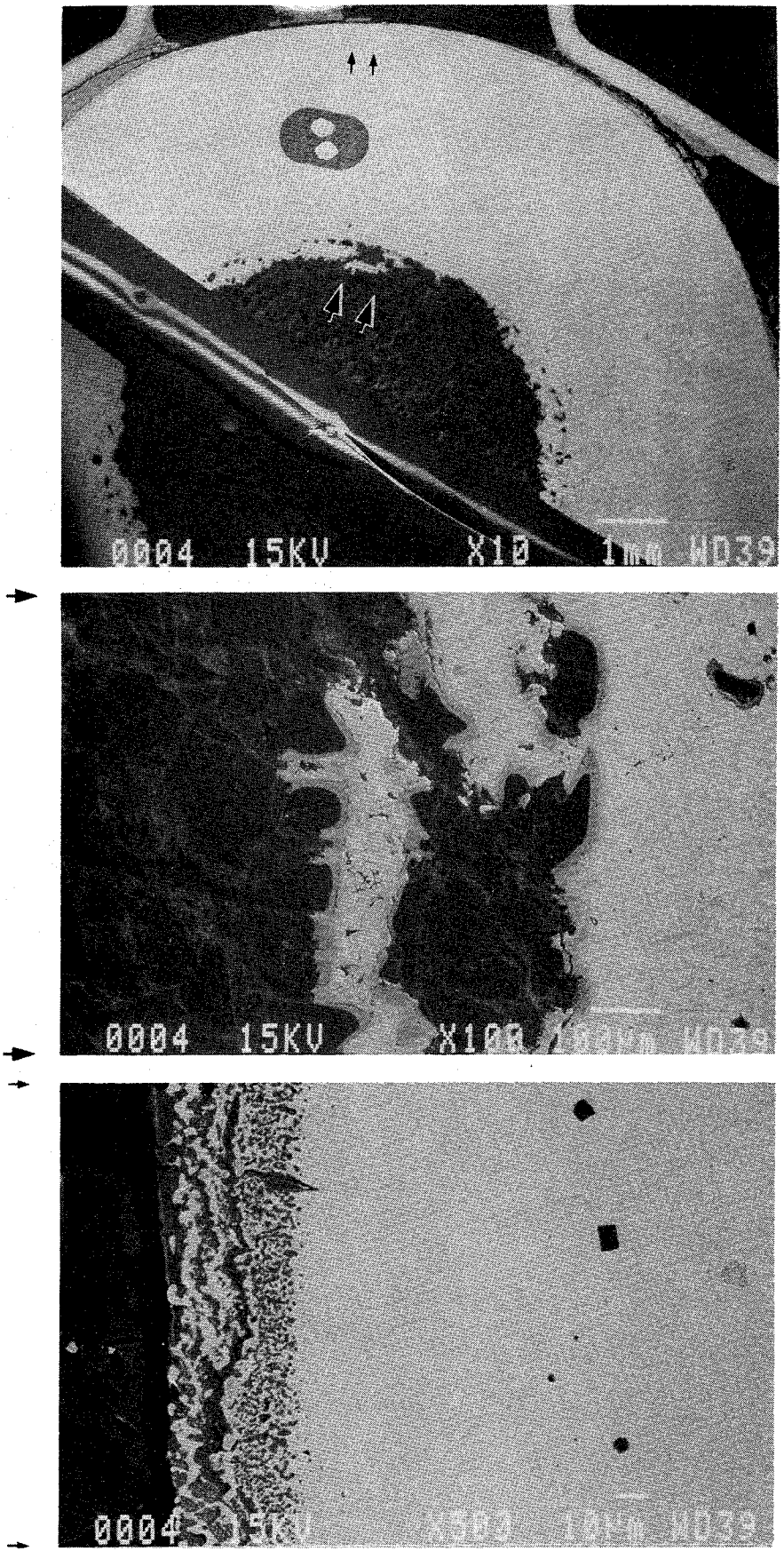

Fig. 10: Fuel rod bundle CORA-W2, cross section # d (206 mm); General view of position # 4 (B_4C absorber rod)

Punktanalyse Nr.	Element	Gew. %	Atom %*
1	N	26.9	55.8
	Ti	71.5	43.4
	Cr	0.8	0.4
	Fe	0.8	0.4
2	Si	0.4	0.7
	Cr	17.6	18.7
	Mn	1.7	1.7
	Fe	69.4	68.7
	Ni	10.9	10.2
3	Cr	1.0	1.0
	Fe	89.1	89.5
	Ni	9.9	9.5

* auf 100 % normalisiert

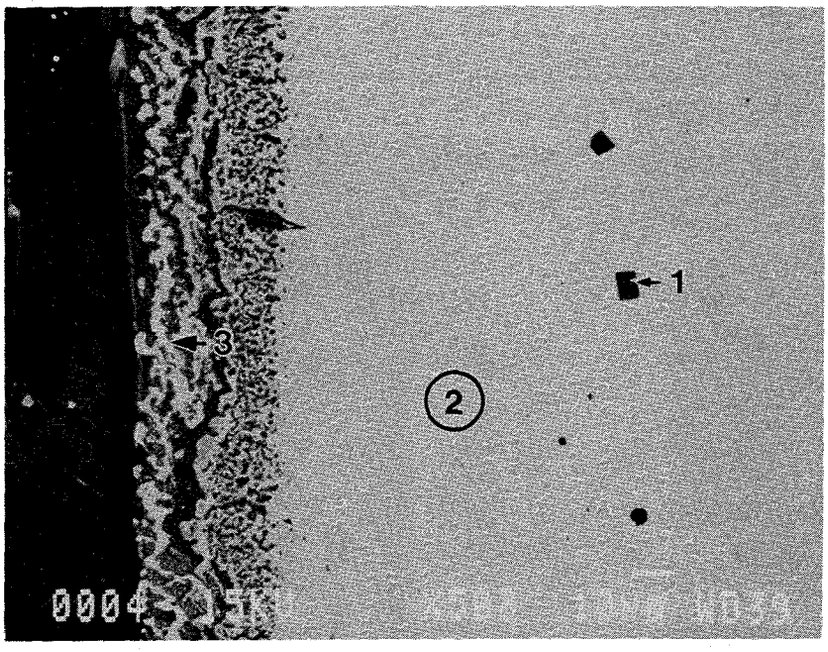

Fig. 11: Fuel rod bundle CORA-W2, cross section # d (206 mm); SEM/EDX analysis of position # 4 (absorber guide tube, OD)

Punktanalyse Nr.	Element	Gew. %	Atom %*
1	B	67.6	70.1
	C	31.9	29.7
	Si	0.1	0.1
	Fe	0.4	0.1
2	B	11.6	23.5
	C	29.6	53.7
	Cr	7.0	2.9
	Mn	1.8	0.7
	Fe	36.7	14.3
	Ni	12.7	4.7
	Mo	0.6	0.1
3	B	9.9	35.7
	Cr	34.6	26.0
	Fe	51.7	36.2
	Ni	1.7	1.2
	Mo	2.2	0.9
4	B	4.0	17.3
	Cr	40.8	36.9
	Fe	51.8	43.7
	Ni	1.4	1.2
	Mo	1.9	1.0
5	C	2.1	8.9
	Si	0.7	1.2
	Cr	8.2	8.2
	Mn	0.9	0.8
	Fe	72.0	66.9
	Ni	15.2	13.4
	Mo	1.0	0.5
6	B	7.9	34.4
	Cr	18.5	16.7
	Fe	32.4	27.4
	Ni	3.8	3.1
	Mo	37.4	18.4

* auf 100 % normalisiert

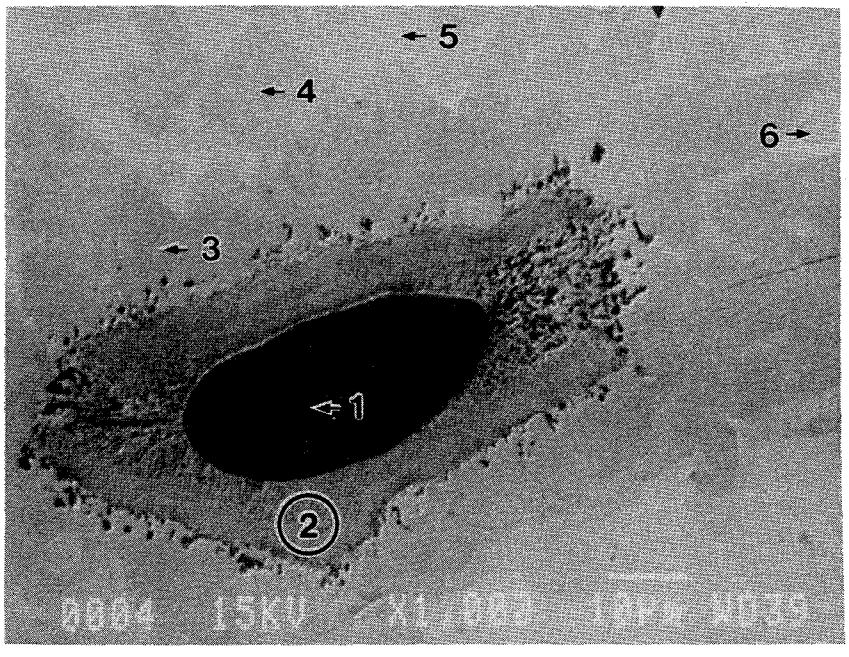

Fig. 12: Fuel rod bundle CORA-W2, cross section # d (206 mm); SEM/EDX analysis at position #4 (dissolution of B_4C by molten stainless steel)

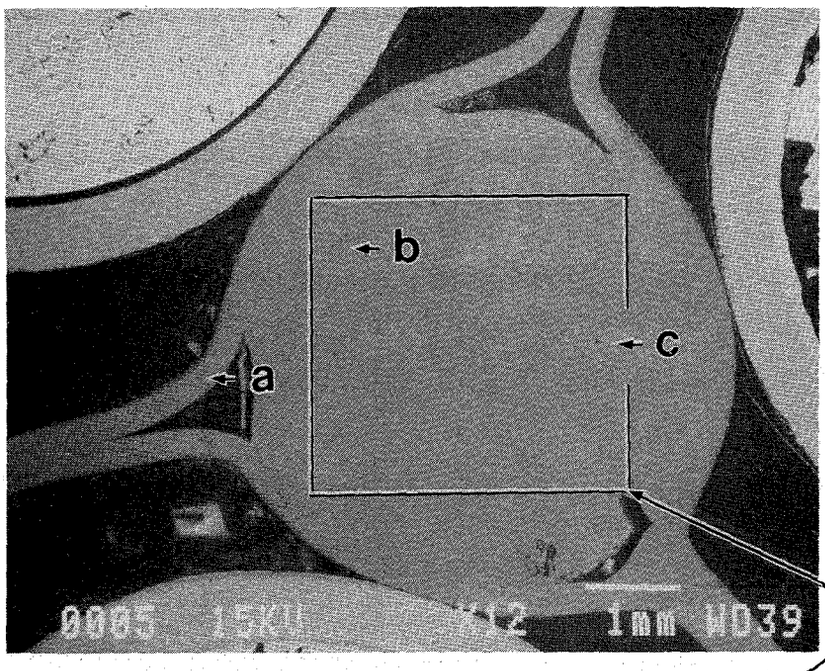

16-Mar-1994 09:15:38
CORA-W2 / Probe d / REM 5 / Integralanalyse Nr.1

Vert= 1964 counts Disp= 1 Comp= 3 Preset= 100 secs Elapsed= 100 secs

Element & Linie	Gew.-Prozent	Atom-Prozent*	Präzision 3 Sigma	k-Verh.**	Iter.
Si KA	0.21	0.43	0.04	0.0014	
Cr KA	16.46	17.85	0.49	0.1754	
Fe KA	68.20	68.86	1.27	0.6387	
Ni KA	10.51	10.10	0.63	0.0944	
Zr LA	1.57	0.97	0.15	0.0109	
Mo LA	3.05	1.79	0.22	0.0226	2
Gesamt	100.00				

*Hinweis: Atom-Prozente sind auf 100 normalisiert
**Hinweis: k-Verhältnis = k.-Verh. x R
Quantex+>mit R = Referenzwert(Std.)/Referenzwert(Probe)

1 2 3 4 5 6 7 8 9

0.000 Range= 10.230 keV 10.110

Integral 8 = 74940

Fig. 13: Fuel rod bundle CORA-W2, cross section # d (206 mm); General view of position # 5 (stainless steel spacer grid)

Punktanalyse Nr. im Bereich "a" Nr.	Element	Gew. %	Atom %*
1	Si	0.3	0.7
	Ti	0.5	0.6
	Cr	17.9	19.0
	Mn	1.9	1.9
	Fe	68.0	67.1
	Ni	11.4	10.7
2	N	26.5	55.2
	Ti	72.1	44.0
	Fe	1.4	0.8
3	O	6.7	20.0
	Cr	7.2	6.6
	Mn	0.4	0.4
	Fe	65.8	56.6
	Ni	20.0	16.4
4	O	28.7	57.7
	Ti	0.8	0.5
	Cr	32.8	20.3
	Mn	2.2	1.3
	Fe	33.9	19.5
	Ni	0.5	0.3
	Zr	1.2	0.4

* auf 100 % normalisiert

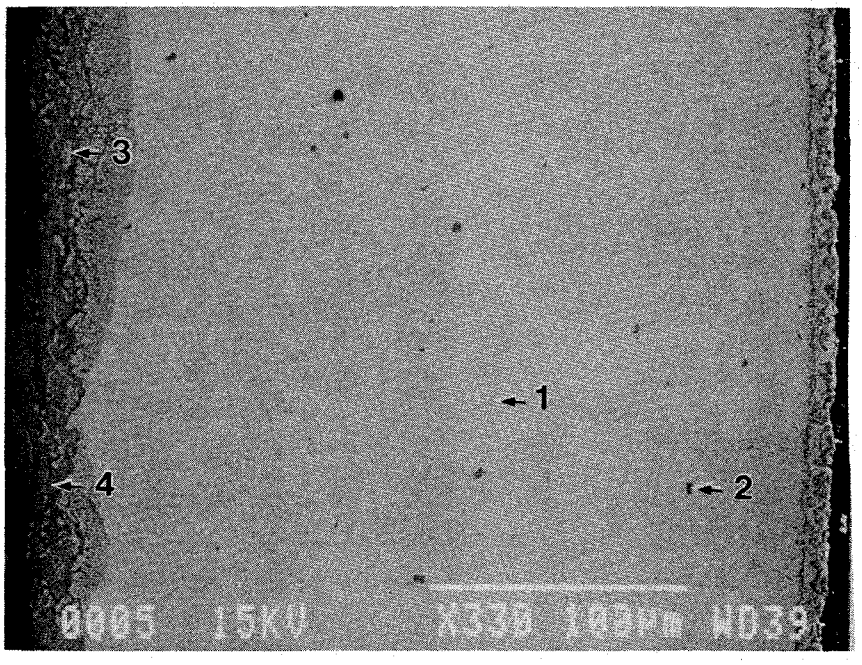

Fig. 14: Fuel rod bundle CORA-W2, cross section # d (206 mm); SEM/EDX analysis at position #5 (spacer grid)

Punktanalyse Nr. im Bereich "b" Nr.	Element	Gew. %	Atom %*
1	Si Cr Fe Ni Mo	0.3 12.6 73.6 12.5 1.0	0.6 13.5 73.4 11.9 0.6
2	O Cr Fe Mo	5.6 47.6 44.1 2.6	16.9 43.9 37.9 1.3
3	Cr Fe Mo	27.9 23.0 49.1	36.7 28.2 35.0
4	C	100	100
5	Si Cr Mn Fe Ni Mo	0.4 12.2 0.7 73.2 13.2 1.3	0.8 13.1 0.7 72.1 12.6 0.8

* auf 100 % normalisiert

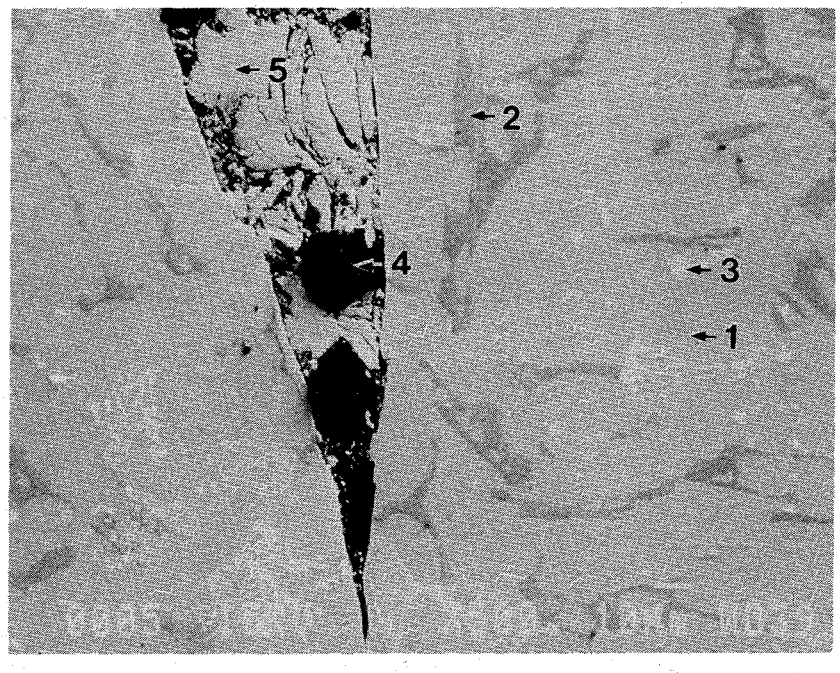

Fig. 15: Fuel rod bundle CORA-W2, cross section # d (206 mm); SEM/EDX analysis at position #5 (spacer grid)

Punktanalyse Nr. im Bereich "c" Nr.	Element	Gew. %	Atom %*
1	O	6.1	18.1
	Cr	45.7	41.9
	Fe	44.5	37.9
	Ni	0.9	0.7
	Mo	2.8	1.8
2	Si	0.4	0.7
	Cr	12.2	13.1
	Fe	74.0	73.8
	Ni	12.4	11.7
	Mo	1.0	0.6
3	Cr	10.6	13.0
	Fe	50.0	56.9
	Ni	7.8	8.4
	Zr	21.6	15.1
	Mo	10.0	6.6
4	Ti	0.9	1.5
	Cr	10.5	16.0
	Fe	10.1	14.4
	Ni	1.1	1.5
	Zr	56.0	48.8
	Mo	21.4	17.8
5	Ti	0.4	0.5
	Cr	31.2	40.2
	Fe	21.9	26.3
	Ni	1.2	1.3
	Mo	45.3	31.6

* auf 100 % normalisiert

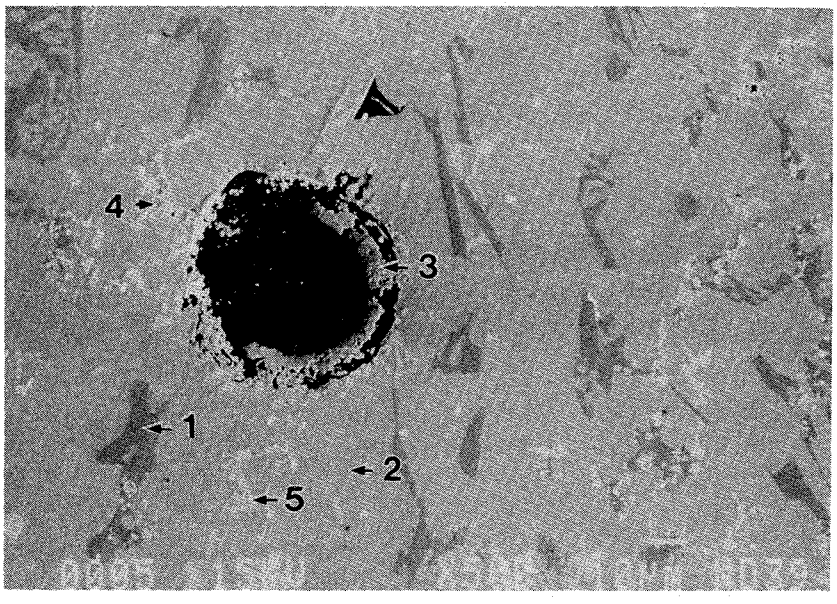

Fig. 16: Fuel rod bundle CORA-W2, cross section # d (206 mm); SEM/EDX analysis at position #5 (solidified melt at spacer grid)

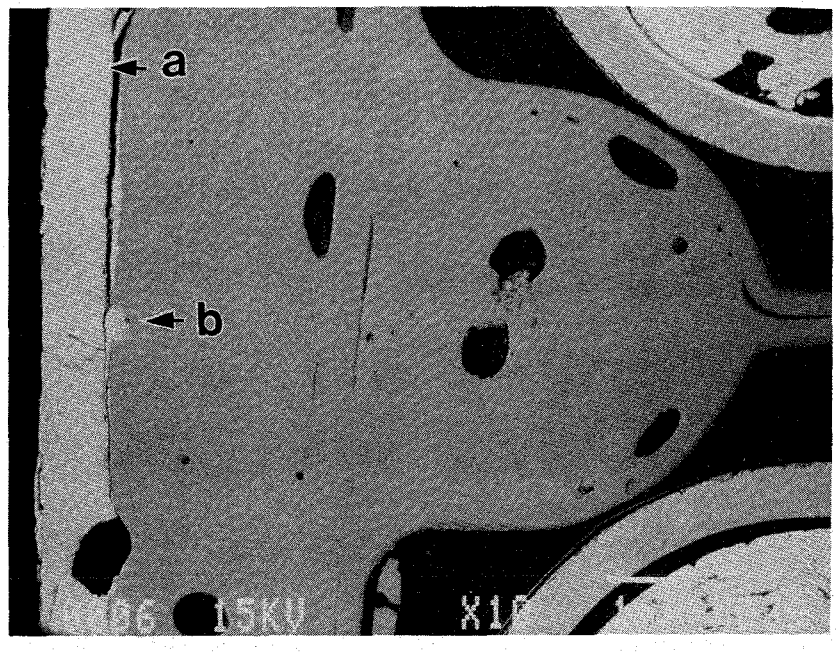

Fig. 17: Fuel rod bundle CORA-W2, cross section # d (206 mm); General view of position # 6 (solidified melt between spacer grid and shroud)

Element	Mittelwert (Gew.-%)	Standardabweichung (Gew.-%)
Si	0.32	± 0.12
Cr	14.10	± 1.06
Fe	66.71	± 1.94
Ni	10.81	± 0.55
Zr	0.41	± 0.28
Mo	7.59	± 3.74

Anzahl der Integralanalysen = 6
(bei 100-facher Vergrößerung)

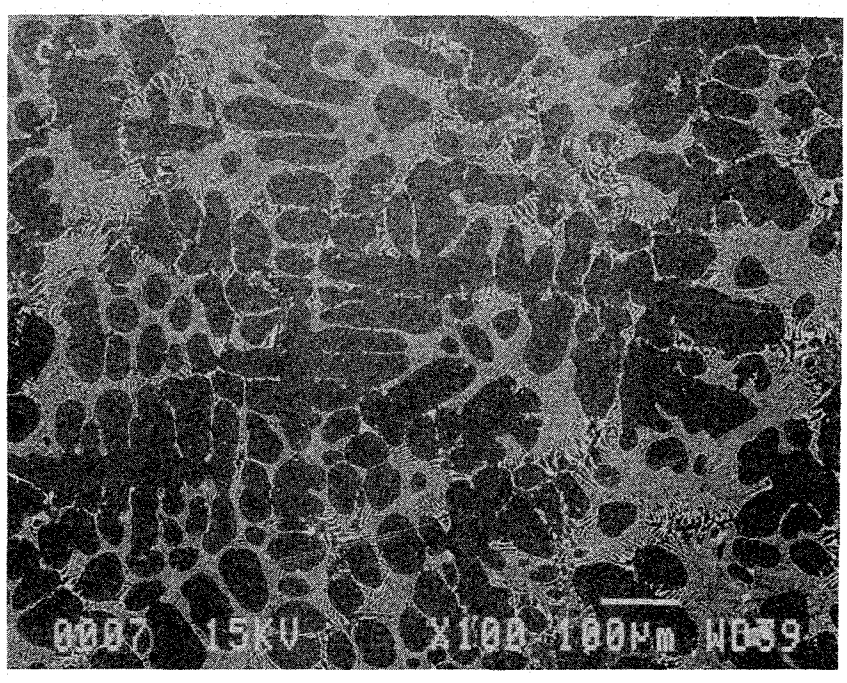

Fig. 18: Fuel rod bundle CORA-W2, cross section # d (206 mm); SEM/EDX analysis at position #7 (metallic melt)

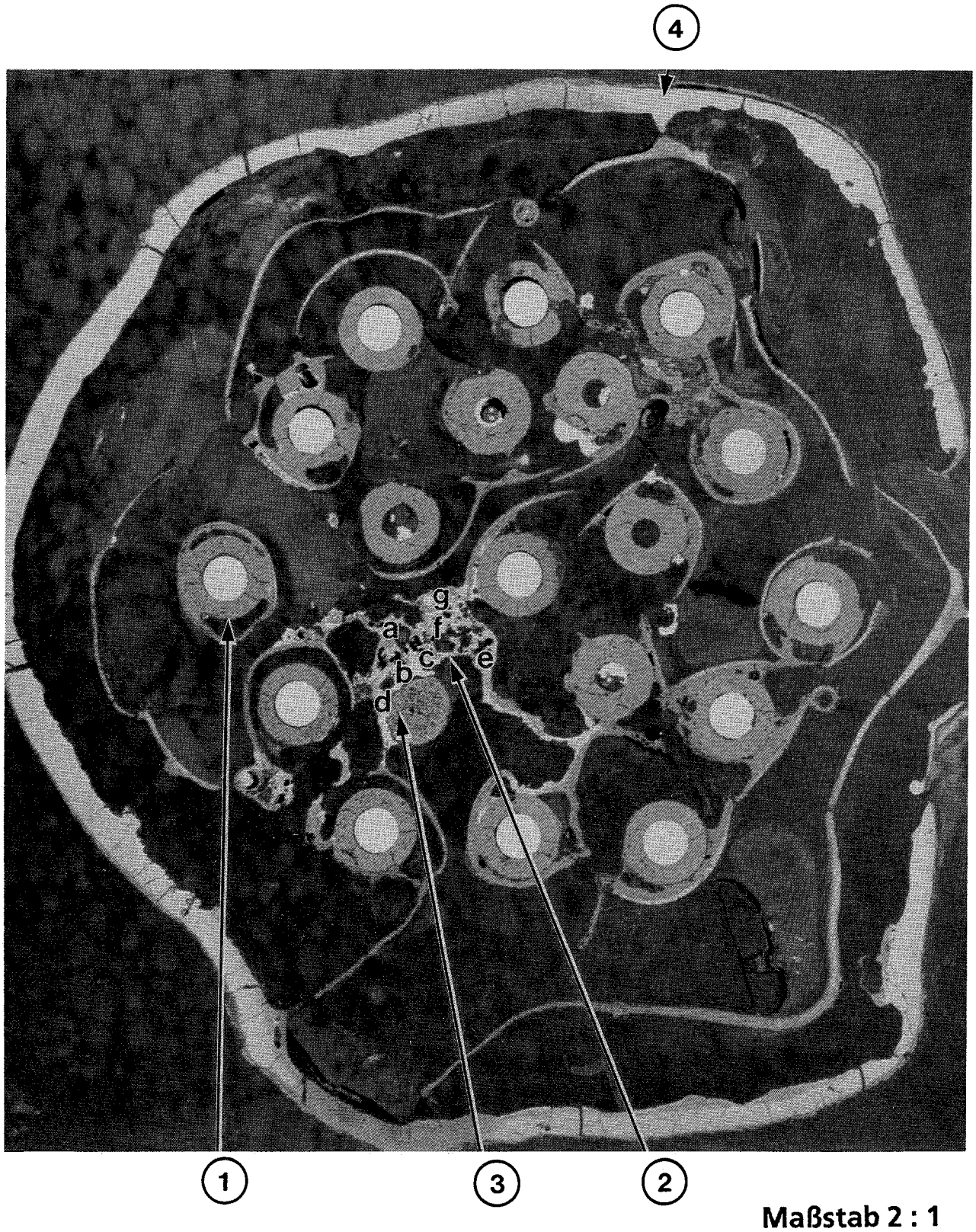

Fig. 19: Fuel rod bundle CORA-W2, cross section # g (392 mm); Positions of SEM/EDX analysis

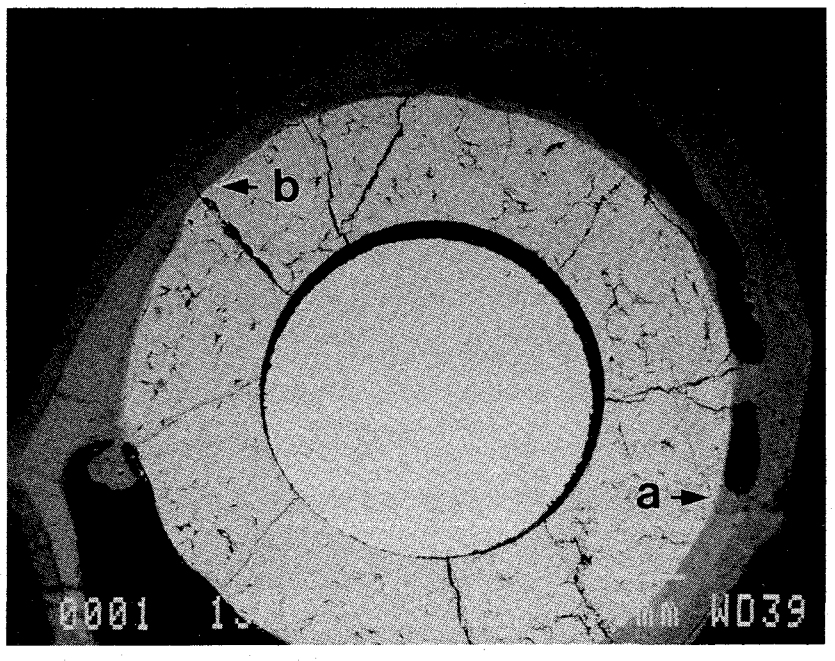

Fig. 20: Fuel rod bundle CORA-W2, cross section # g (392 mm);
General view of position # 1 (partially destroyed fuel rod)

Analyse Nr.	Element	Gew. %	Atom % *
1	Siehe Punktanalysen		
2	O Zr U	22.5 57.6 19.9	66.3 29.7 3.9
3	O Zr U	25.6 67.3 7.1	67.6 31.2 1.2
4	O Zr U	23.5 59.2 17.3	67.0 29.6 3.3
5	O Zr	26.4 73.6	67.1 32.9
6	Siehe Punktanalysen		
7	Si Cr Fe Ni Zr Nb Mo U	0.9 1.3 19.3 9.4 37.6 4.2 22.9 4.4	2.5 2.0 27.0 12.5 32.3 3.5 18.7 1.5

Integralanalyse bei 500-facher Vergrößerung

*auf 100 % normalisiert

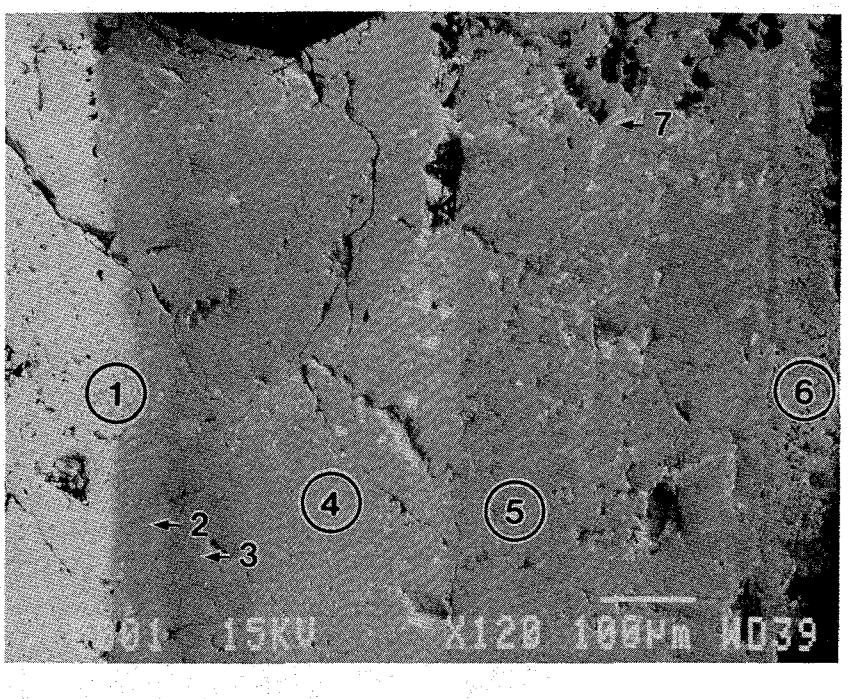

Fig. 21: Fuel rod bundle CORA-W2, cross section # g (392 mm); SEM/EDX analysis at position # 1 location a (fuel/cladding contact)

Punktanalyse Nr.	Element	Gew. %	Atom %*
1	O Zr U	16.3 26.0 57.7	65.9 18.4 15.7
2	O Zr U	15.0 16.4 68.6	66.7 12.8 20.5
3	O Fe Ni Zr Nb Mo W	5.1 8.3 8.7 59.6 9.5 3.9 4.9	22.3 10.4 10.3 45.6 7.1 2.9 1.4
4	O U	12.4 87.6	67.8 32.2
5	O Cr Fe Ni Zr Nb Mo U	5.1 0.5 7.7 8.0 59.6 5.2 8.9 4.9	22.4 0.7 9.7 9.6 45.8 3.9 6.5 1.4
6	O Zr U	14.7 11.8 73.5	67.7 9.6 22.7
7	O Zr U	22.5 60.9 16.6	65.6 31.1 3.3

* auf 100 % normalisiert

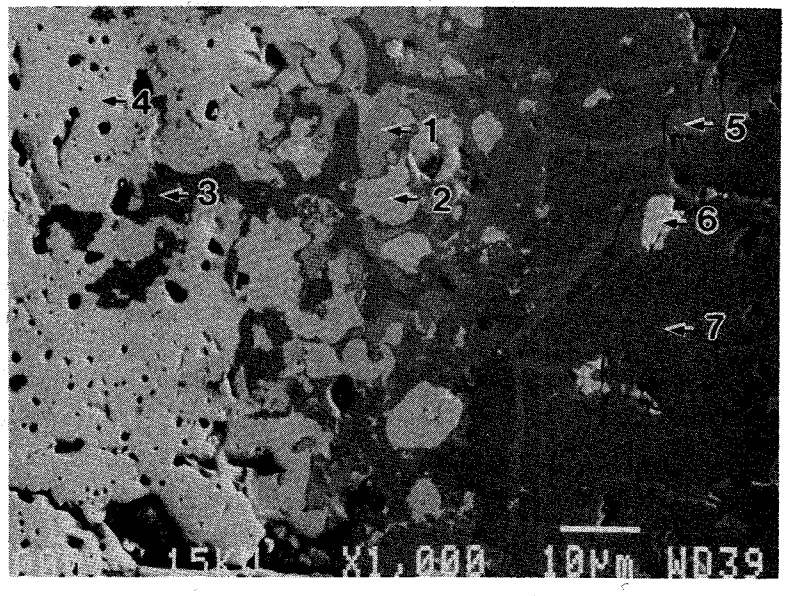

Fig. 22: Fuel rod bundle CORA-W2, cross section # g (392 mm); SEM/EDX analysis at position # 1 location a/1 (fuel/cladding contact)

Punktanalyse Nr. Nr.	Element	Gew. %	Atom % *
1	O Zr U	21.5 53.4 25.1	66.1 28.7 5.2
2	O Zr	5.9 94.1	26.5 73.5
3	O Zr	6.0 94.0	26.6 73.4
4	Be+ O Zr (gering)		
5	O Zr Mo U	15.05 16.1 0.7 67.7	67.5 12.3 0.5 19.8

*auf 100 % normalisiert.

+ Be kann mit dem EDX nicht erfaßt werden

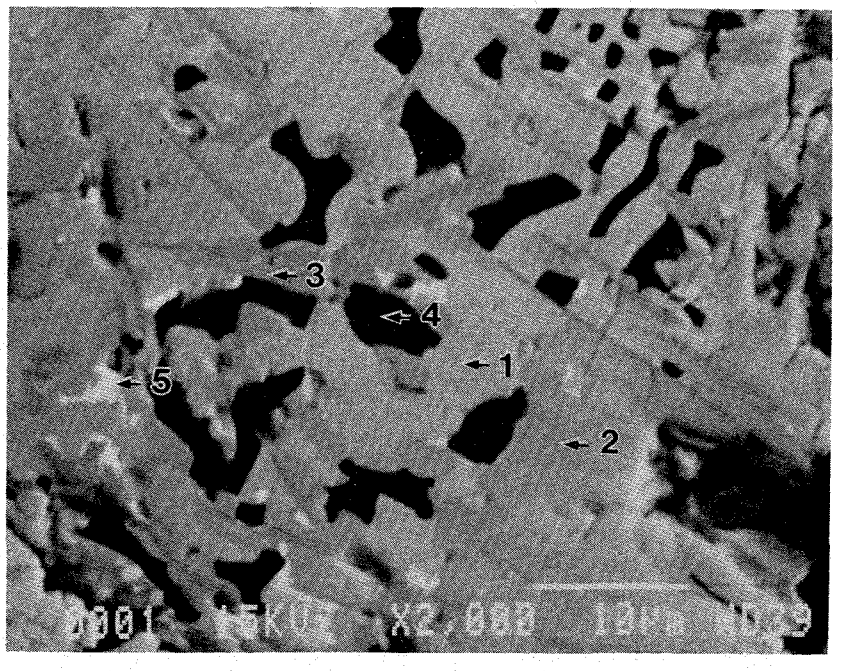

Fig. 23: Fuel rod bundle CORA-W2, cross section # g (392 mm); SEM/EDX analysis at position # 1location a/6 (location # 6; see Fig. 21)

Punktanalyse Nr. Nr.	Element	Gew. %	Atom % *
1	O Fe Zr Mo	20.2 1.4 72.0 6.4	58.9 1.2 36.8 3.1
2	O Zr	39.4 60.6	78.7 21.3
3	O Zr	8.5 91.5	34.6 65.4
4	O Zr U	22.3 58.0 19.7	65.9 30.1 3.9
5	O Zr U	9.5 67.4 23.1	41.5 51.7 6.8
6	O Fe Zr U	18.9 1.7 59.7 19.7	60.6 1.5 33.6 4.2
7	O U	11.8 88.1	66.7 33.3

*auf 100 % normalisiert

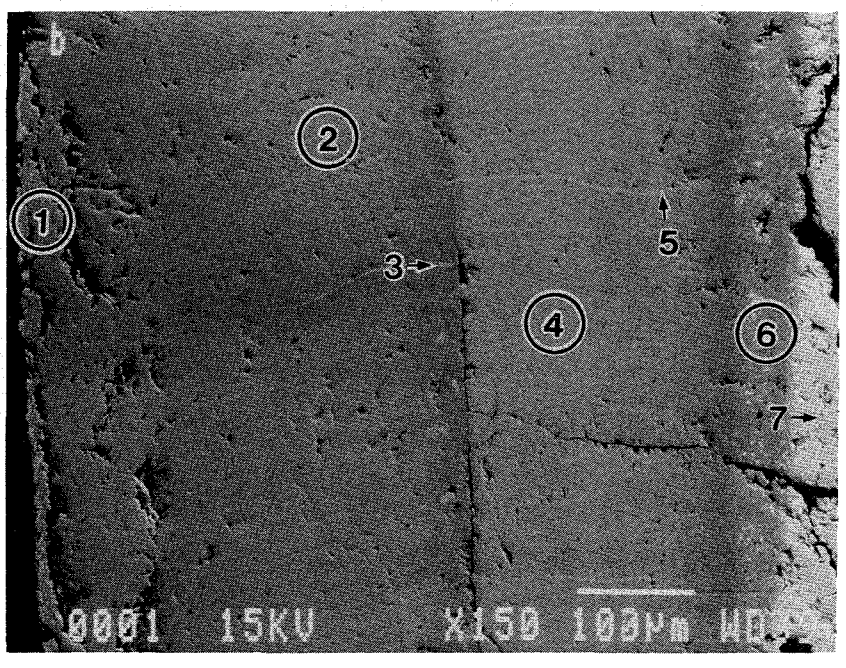

Fig. 24: Fuel rod bundle CORA-W2, cross section # g (392 mm); SEM/EDX analysis at position # 1 location b (fuel/cladding contact)

Integralanalyse Nr.	Element	Gew. %	Atom % *
a	O	19.3	59.5
	Cr	0.8	0.8
	Fe	2.7	2.4
	Zr	60.2	32.6
	Mo	4.1	2.1
	U	12.9	2.7

Integralanalyse bei 500-facher Vergrößerung
*auf 100 % normalisiert

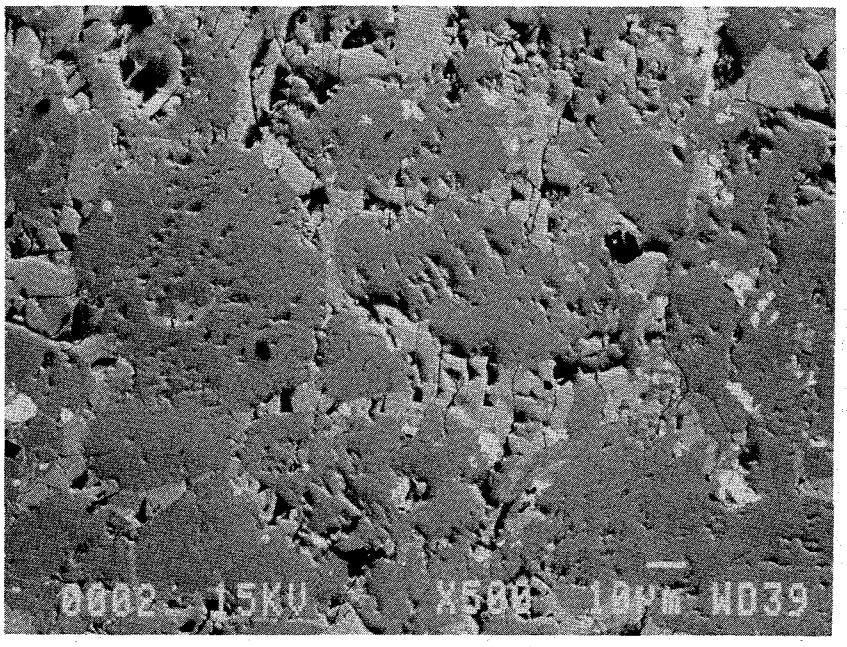

Fig. 25: Fuel rod bundle CORA-W2, cross section # g (392 mm); SEM/EDX analysis at position # 2 location a (see Fig. 19, relocated and solidified melts adjacent to B_4C absorber material)

Integralanalyse Nr.	Element	Gew. %	Atom % *
b	B	4.5	26.6
	O	1.9	7.7
	Cr	1.6	2.0
	Fe	6.1	7.0
	Zr	69.4	48.4
	Mo	9.6	6.4
	U	6.8	1.8

Integralanalyse bei 500-facher Vergrößerung
*auf 100 % normalisiert

Fig. 26: Fuel rod bundle CORA-W2, cross section # g (392 mm); SEM/EDX analysis at position # 2 location b (see Fig. 19, relocated and solidified melts adjacent to B_4C absorber material)

Integralanalyse Nr.	Element	Gew. %	Atom % *
c	B	11.4	49.4
	O	4.6	13.6
	Cr	1.6	1.5
	Fe	7.9	6.6
	Ni	1.6	1.3
	Zr	20.2	10.4
	Mo	23.2	11.4
	U	29.4	5.8

Integralanalyse bei 500-facher Vergrößerung
*auf 100 % normalisiert

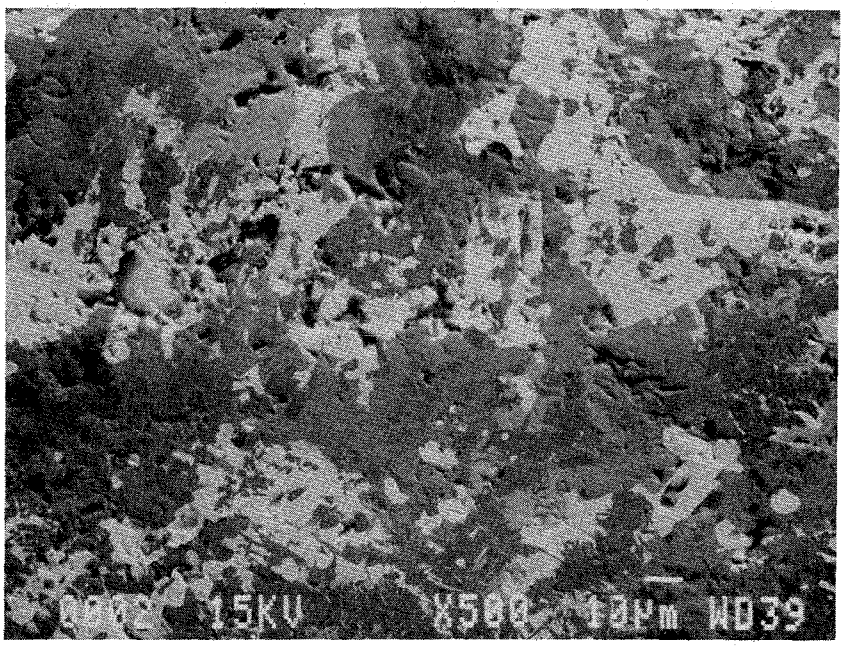

Fig. 27: Fuel rod bundle CORA-W2, cross section # g (392 mm); SEM/EDX analysis at position # 2 location c (see Fig. 19, relocated and solidified melts adjacent to B_4C absorber material)

Integralanalyse Nr.	Element	Gew. %	Atom % *
d	O	21.3	64.3
	Fe	2.0	1.7
	Zr	56.5	29.9
	U	20.3	4.1

Integralanalyse bei 500-facher Vergrößerung
*auf 100 % normalisiert

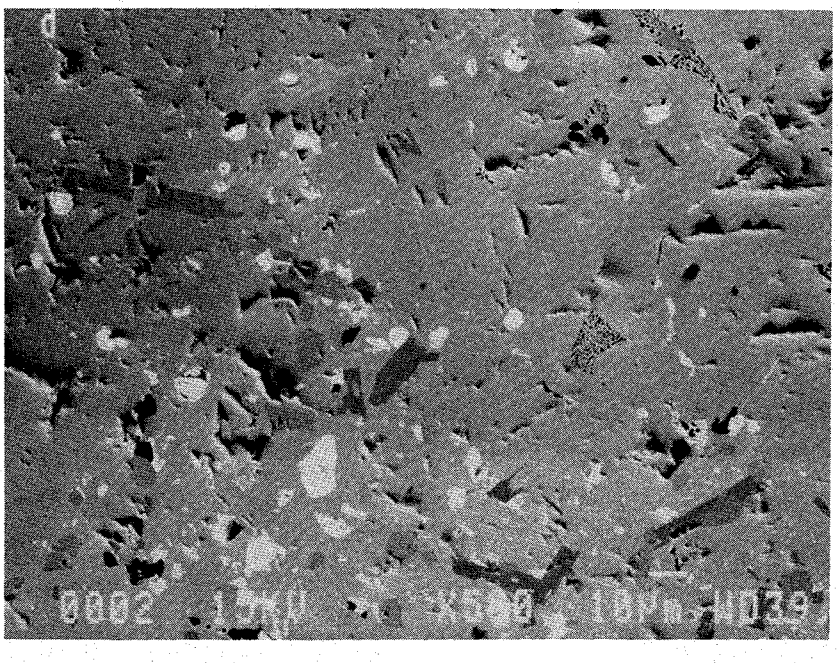

Fig. 28: Fuel rod bundle CORA-W2, cross section # g (392 mm); SEM/EDX analysis at position # 2 location d (see Fig. 19, relocated and solidified melts adjacent to B_4C absorber material)

Integralanalyse Nr.	Element	Gew. %	Atom % *
e	O	16.9	55.6
	Cr	0.8	0.8
	Fe	2.9	2.7
	Zr	58.0	33.6
	Nb	3.8	2.1
	Mo	3.7	2.1
	U	13.9	3.1

Integralanalyse bei 500-facher Vergrößerung
*auf 100 % normalisiert

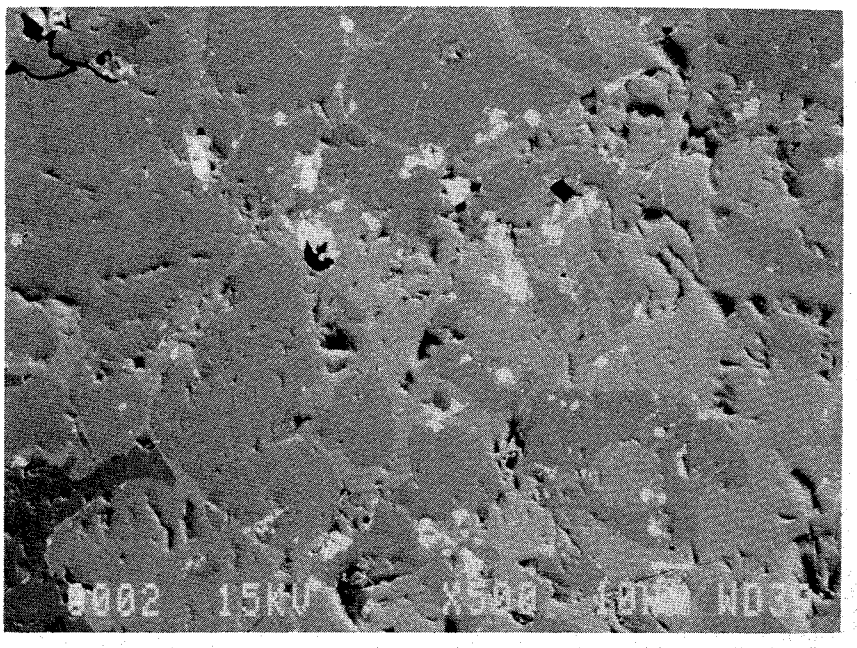

Fig. 29: Fuel rod bundle CORA-W2, cross section # g (392 mm); SEM/EDX analysis at position # 2 location e (see Fig. 19, relocated and solidified melts adjacent to B_4C absorber material)

Integralanalyse Nr.	Element	Gew. %	Atom % *
f	O	14.9	50.6
	Cr	1.9	2.0
	Fe	5.5	5.3
	Zr	49.5	29.4
	Nb	13.2	7.7
	Mo	4.7	2.7
	U	10.2	2.3

Integralanalyse bei 500-facher Vergrößerung
*auf 100 % normalisiert

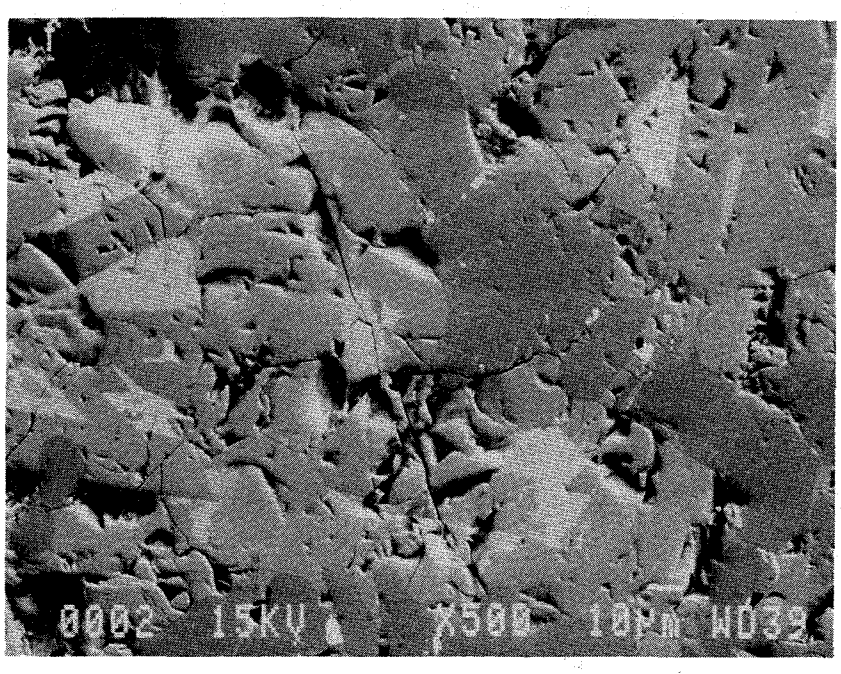

Fig. 30: Fuel rod bundle CORA-W2, cross section # g (392 mm); SEM/EDX analysis at position # 2 location f (see Fig. 19, relocated and solidified melts adjacent to B_4C absorber material)

Integralanalyse Nr.	Element	Gew. %	Atom % *
g	Be	+	+
	O	29	73
	Fe	1	1
	Zr	53	23
	Mo	3	1
	U	14	2

Integralanalyse bei 250-facher Vergrößerung
*auf 100 % normalisiert,
+ Ohne Be berechnet, da Be vom EDX nicht erfaßt wird!

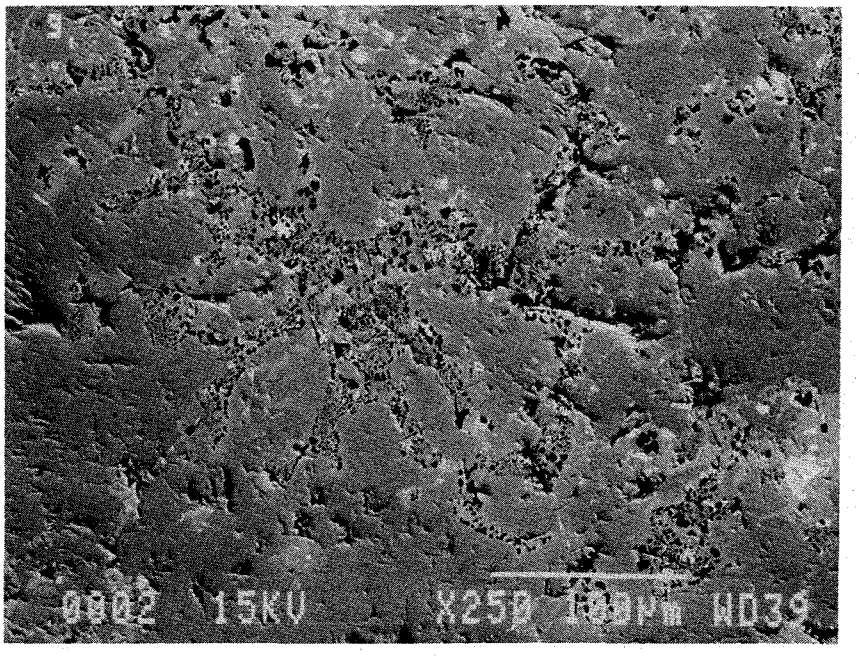

Fig. 31: Fuel rod bundle CORA-W2, cross section # g (392 mm); SEM/EDX analysis at position # 2 location g (see Fig. 19, relocated and solidified melts adjacent to B_4C absorber material)

Punktanalyse Nr. Nr.	Element	Gew. %	Atom % *
1	O Zr U	24.1 63.3 12.5	66.9 30.8 2.3
2	O Cr Fe Zr Nb Mo W	5.6 1.7 3.3 66.2 4.8 14.2 4.1	25.3 2.3 4.3 52.1 3.7 10.6 1.6
3	O Zr U	13.2 10.6 76.2	65.4 9.2 25.4
4	Be+ O		

*auf 100 % normalisiert.

+ Be kann mit dem EDX nicht erfaßt werden

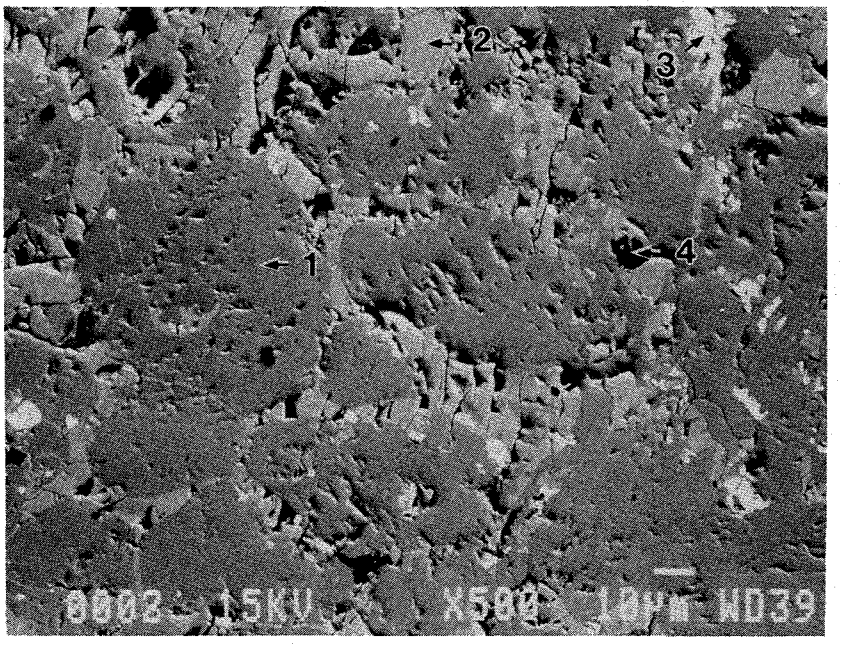

Fig. 32: Fuel rod bundle CORA-W2, cross section # g (392 mm); SEM/EDX analysis at position # 2 location a (detailed phase analysis of solidified melts; see Fig. 25)

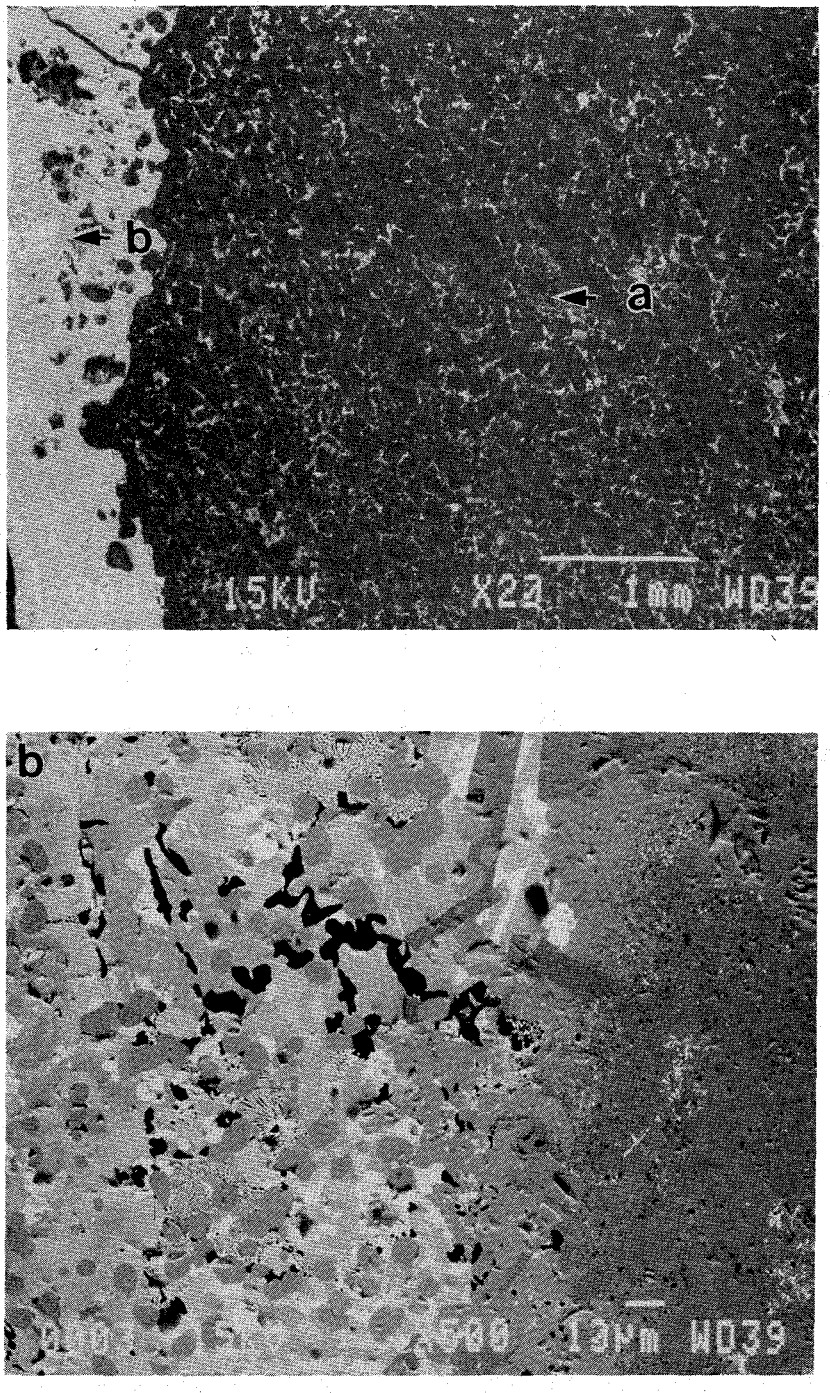

Fig. 33: Fuel rod bundle CORA-W2, cross section # g (392 mm); General view of position # 3 (B_4C/stainless steel melt interface)

Punktanalyse Nr. Nr.	Element	Gew. %	Atom % *
1	Si	0.2	0.1
	B	60.2	62.7
	C	39.7	37.2
2	B	56.3	58.8
	C	43.7	41.2
3	Präparationsmaterial		
4	Cr	4.2	4.5
	Mn	3.4	3.5
	Fe	81.4	81.5
	Ni	11.0	10.5

*auf 100 % normalisiert

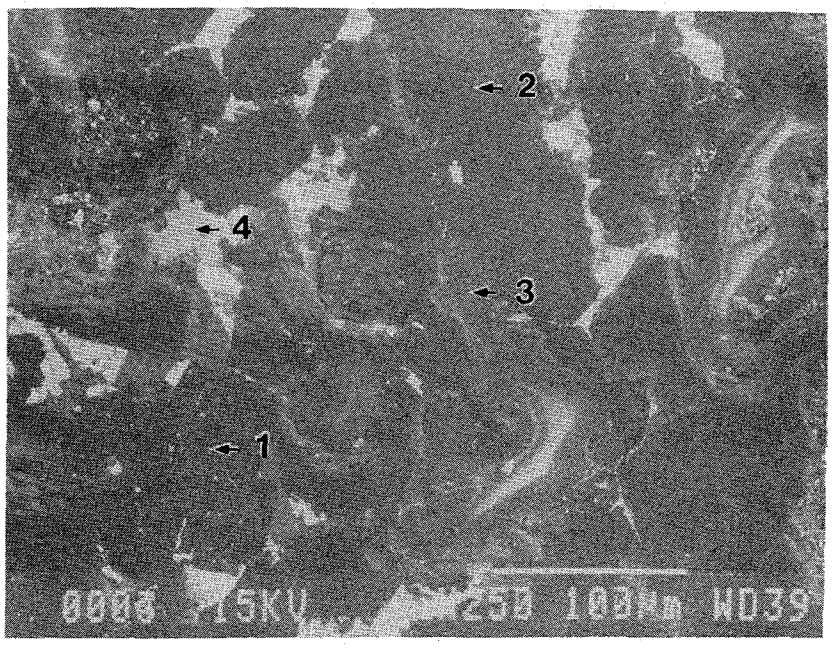

Fig. 34: Fuel rod bundle CORA-W2, cross section # g (392 mm); SEM/EDX analysis at position # 3 location a (detailed phase analysis of B_4C pellet, see Fig. 33)

Punktanalyse Nr. Nr.	Element	Gew. %	Atom % *
1	Zr	100	100
2	B Zr	12.6 87.4	55 45
3	Si Cr Mn Fe Ni Zr Nb Mo U	1.7 5.7 0.5 16.1 1.8 36.8 8.0 25.0 4.4	4.9 8.7 0.7 22.8 2.4 31.8 6.7 20.6 1.5
4	Fe Ni Zr Mo U	9.0 7.6 38.0 1.9 43.5	17.8 14.3 45.7 2.2 20.0
5	Be+ O		
6	Be+ O Zr U	 26 29 45	 76 15 9
7	Zr	100	100
8	B Zr	12.6 87.4	54.8 45.2
9	Cr Mn Fe Ni Zr Nb Mo W U	5.5 0.5 11.9 1.4 34.3 5.9 31.7 7.0 1.9	9.1 0.7 18.3 2.0 32.2 5.5 28.3 3.3 0.7

Fig. 35: Fuel rod bundle CORA-W2, cross section # g (392 mm); SEM/EDX analysis at position # 3 location b (detailed phase analysis of B_4C-stainless steel melt, see Fig. 33)

Punktanalyse Nr. Nr.	Element	Gew. %	Atom % *
10	Zr U	98.7 1.3	99.5 0.5
11	B Fe Ni Zr Mo U	12.2 2.2 2.1 74.0 4.5 5.0	54.3 1.9 1.7 38.9 2.2 1.0
12	B Fe Ni Zr Mo U	11.3 1.4 1.2 70.3 4.3 11.5	53.5 1.3 1.0 39.4 2.3 2.5

*auf 100 % normalisiert

+ Be kann vom EDX nicht erfaßt werden

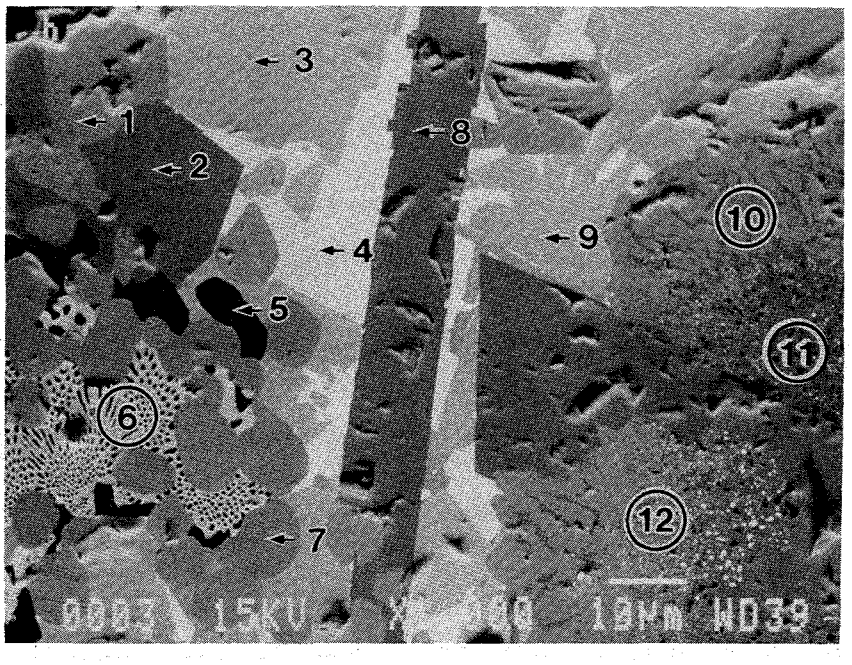

Fig. 36: Fuel rod bundle CORA-W2, cross section # g (392 mm); SEM/EDX analysis at position # 3 location b (detailed phase analysis of B_4C-stainless steel melt, see Fig. 33)

Integralanalyse	Element	Gew. %	Atom % *
Absorberzentrum	B	44.7	49.3
	C	46.9	46.5
	O	4.4	3.3
	Si	0.3	0.1
	Al	0.2	0.1
	Cr	0.4	0.1
	Fe	2.4	0.5
	Ni	0.4	0.1
	Zr	0.3	0.1

Integralanalyse bei 250-facher Vergrößerung
*auf 100 % normalisiert

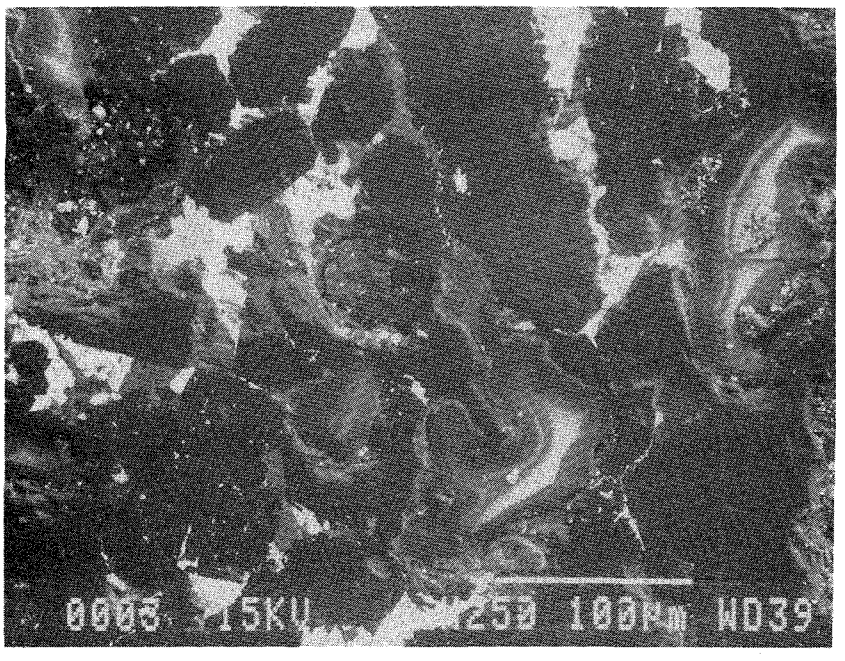

Fig. 37: Fuel rod bundle CORA-W2, cross section # g (392 mm); SEM/EDX analysis at position # 3 location a (B_4C pellet, see Figs. 33 and 34)

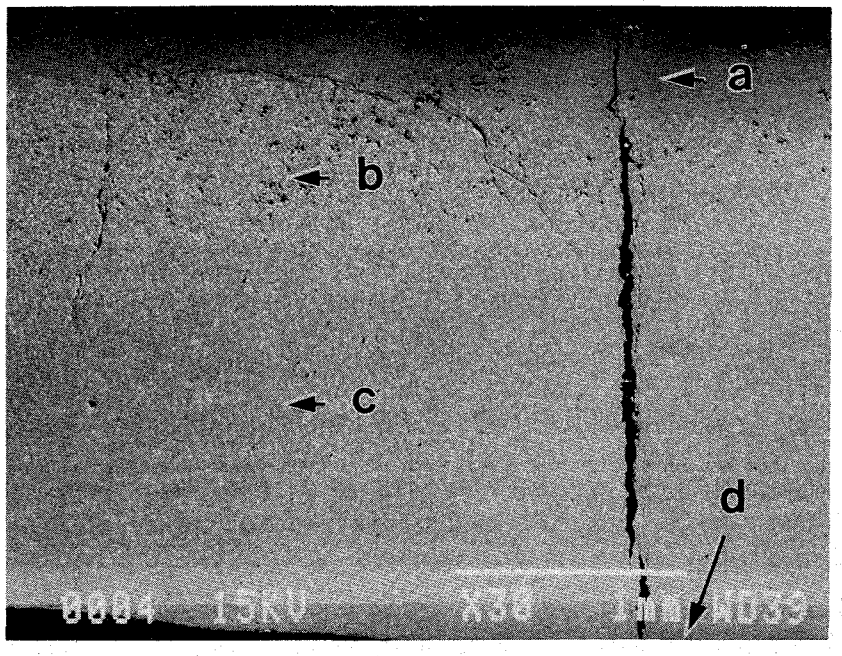

Fig. 38: Fuel rod bundle CORA-W2, cross section # g (392 mm); General view of position #4 (shroud)

Integralanalyse Nr.	Element	Gew. %	Atom % *
a	O Fe Zr	26.2 1.3 72.6	66.7 0.9 32.4
b	O Fe Zr	20.5 1.6 77.9	59.1 1.4 39.5
c	O Fe Zr	23.1 0.6 76.3	63.0 0.5 36.5
d	O Zr U	24.8 69.5 5.7	66.3 32.6 1.0

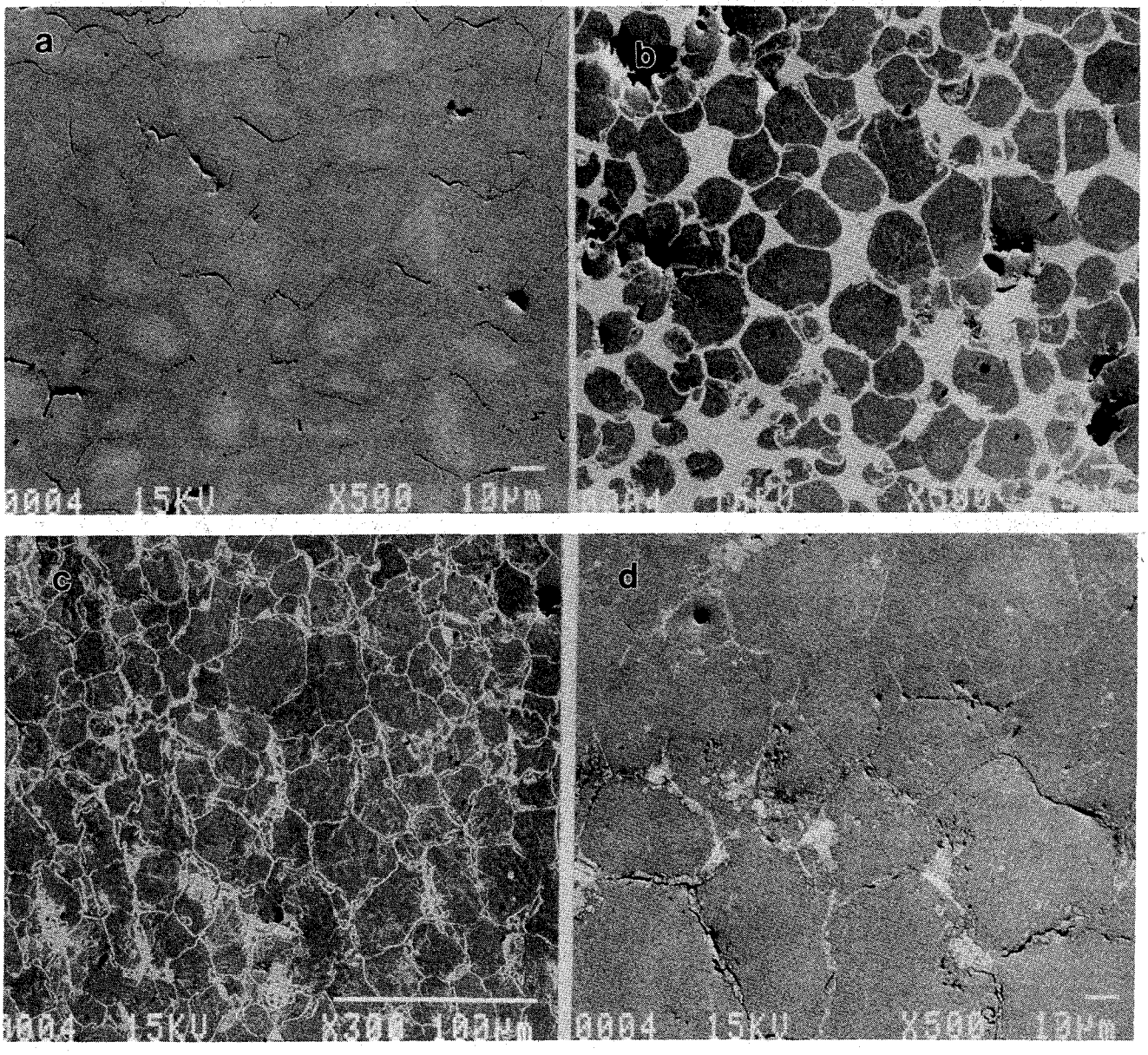

Fig. 39: Fuel rod bundle CORA-W2, cross section # g (392 mm); SEM/EDX analysis at position #4 (detailed phase analysis of shroud; locations see Fig. 38)

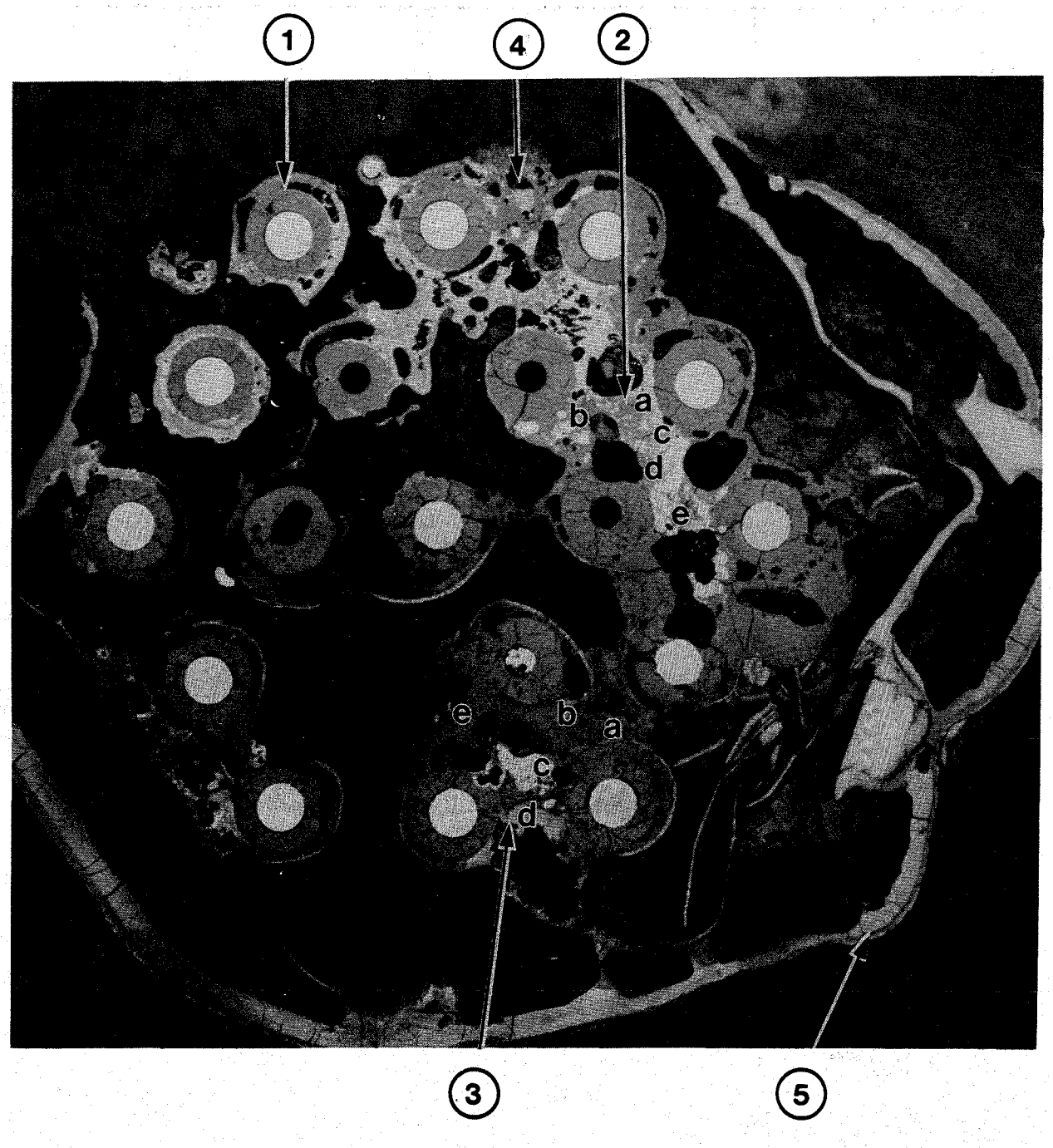

Maßstab 2 : 1

Fig. 40: Fuel rod bundle CORA-W2, cross section # k (605 mm); Positions of SEM/EDX analysis

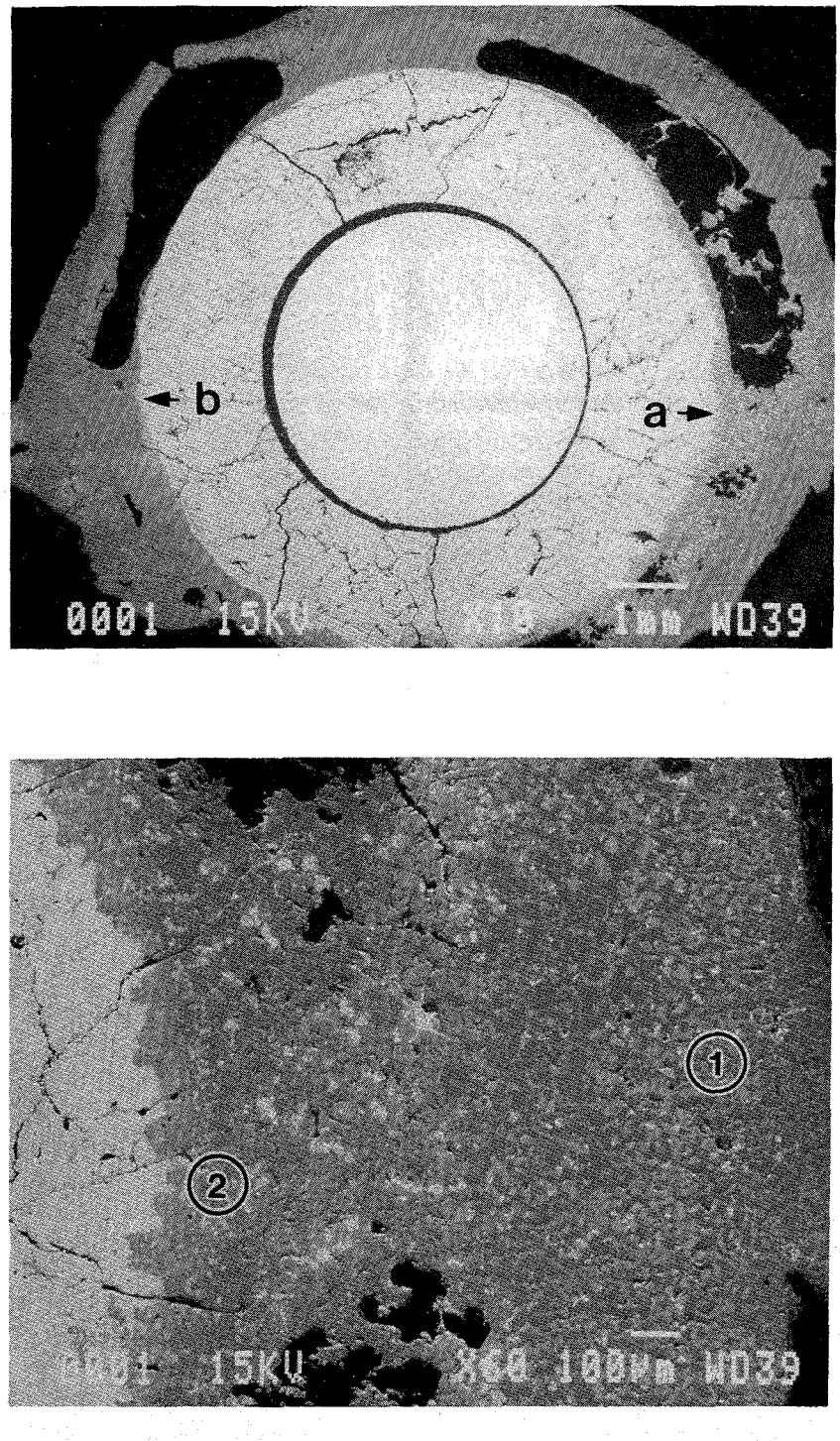

Fig. 41: Fuel rod bundle CORA-W2, cross section # k (605 mm); General view of position # 1 (destroyed fuel rod)

Punktanalyse Nr. Nr.	Element	Gew. %	Atom % *
1	Ti	0.5	0.8
	Cr	9.3	14.5
	Fe	13.9	20.1
	Ni	2.0	2.8
	Zr	66.8	59.7
	U	7.5	2.6
2	O	24.3	65.5
	Zr	71.2	33.7
	U	4.5	0.8
3	O	14.5	66.8
	Zr	13.4	10.8
	U	72.1	22.4

*auf 100 % normalisiert

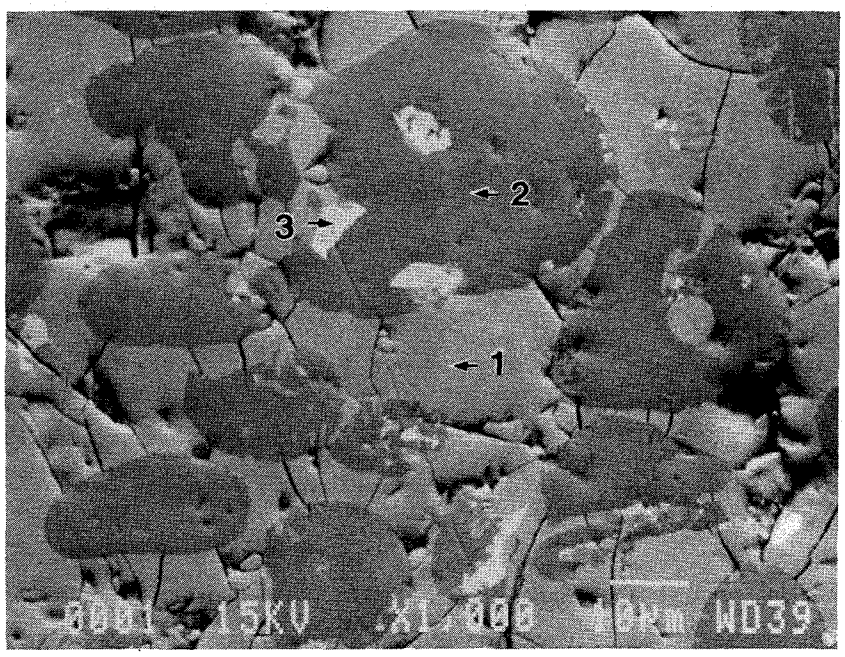

Fig. 42: Fuel rod bundle CORA-W2, cross section # k (605 mm); SEM/EDX analysis at positon # 1 location a (melt between UO_2 pellet and cladding material; see Fig. 41)

Punktanalyse Nr. Nr.	Element	Gew. %	Atom % *
1	O	11.9	66.7
	U	88.1	33.3
2	O	14.9	67.1
	Zr	14.8	11.7
	U	70.3	21.2
3	O	12.8	48.3
	Cr	3.0	3.4
	Fe	6.7	7.2
	Ni	1.0	1.1
	Zr	51.0	33.6
	U	25.4	6.4
4	O	4.6	20.5
	Cr	7.8	10.6
	Fe	12.1	15.3
	Ni	1.2	1.4
	Zr	62.5	48.6
	U	11.9	3.6
5	O	18.0	64.7
	Zr	39.8	25.1
	U	42.1	10.2
6	O	20.9	64.5
	Zr	57.3	31.0
	U	21.8	4.5
7	O	15.9	67.8
	Zr	17.6	13.2
	U	66.5	19.0
8	O	1.8	11.4
	Fe	11.4	20.9
	Ni	3.8	6.6
	Zr	36.3	40.9
	U	46.7	20.1
9	O	4.7	39.0
	Fe	3.9	9.2
	Zr	1.3	1.9
	U	90.1	49.9

*auf 100 % normalisiert

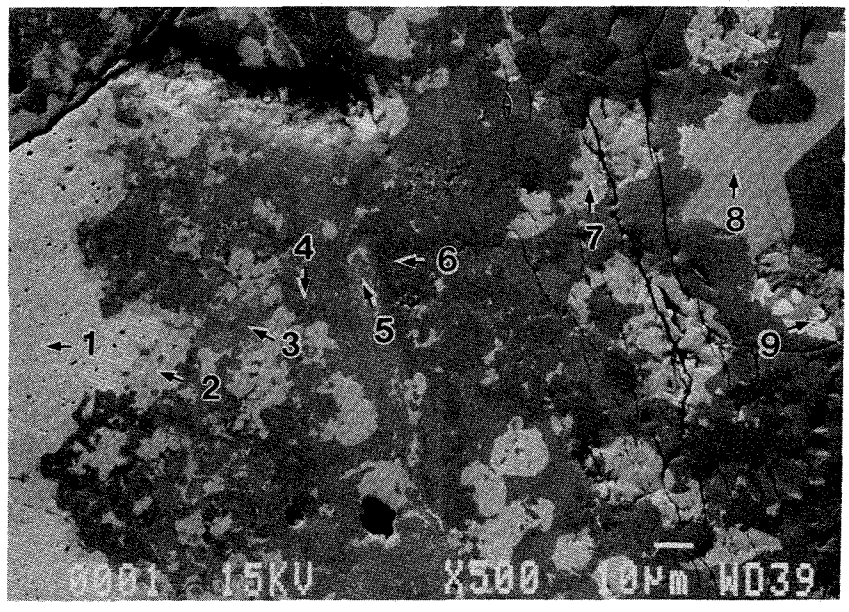

Fig. 43: Fuel rod bundle CORA-W2, cross section # k (605 mm); SEM/EDX analysis at position # 1location a (detailed phase analysis at UO_2/molten cladding interface; see Fig. 41)

Integralanalyse Nr.	Element	Gew. %	Atom % *
1	O	13.2	46.5
	Cr	4.9	5.3
	Fe	6.4	6.5
	Ni	1.0	1.0
	Zr	60.3	37.4
	U	14.2	3.4

Integralanalyse Nr. bei 150-facher Vergrößerung
*auf 100 % normalisiert

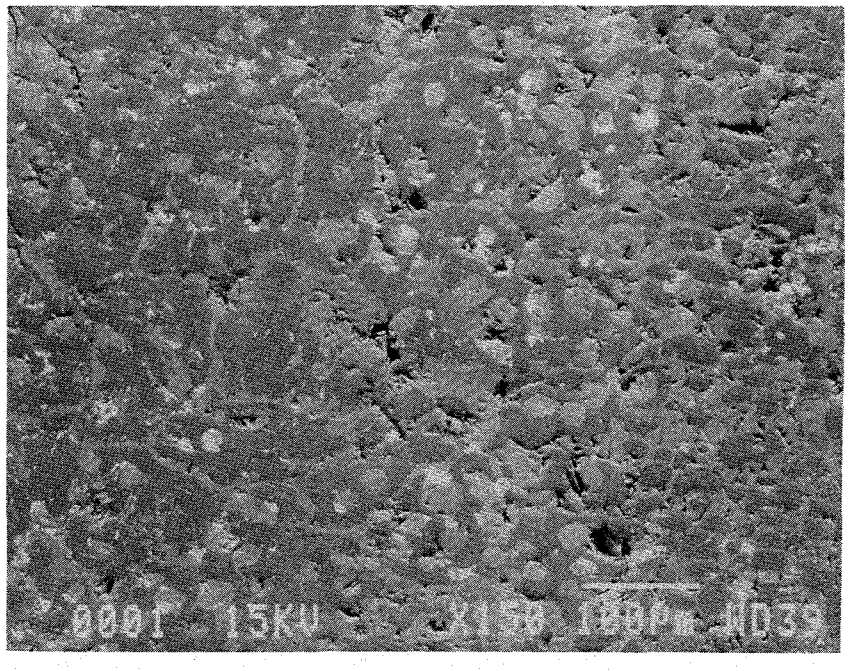

Fig. 44: Fuel rod bundle CORA-W2, cross section # k (605 mm); SEM/EDX analysis at position # 1 location a

Punktanalyse Nr. Nr.	Element	Gew. %	Atom % *
1	O Zr U	16.9 23.8 59.3	67.5 16.6 15.9
2	O Cr Zr U	23.2 1.6 65.0 10.2	64.8 1.4 31.9 1.9
3	O Cr Fe Zr U	20.0 1.9 3.7 62.8 11.6	59.8 1.8 3.2 32.9 2.3
4	O Cr Fe Zr U	17.1 2.1 4.5 58.9 17.4	56.0 2.1 4.2 33.9 3.8

*auf 100 % normalisiert

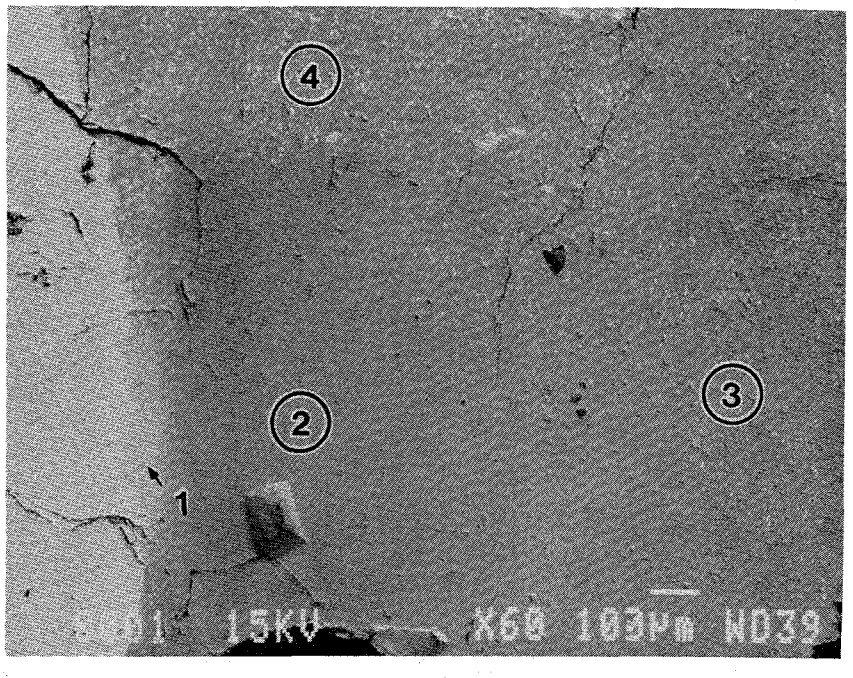

Fig. 45: Fuel rod bundle CORA-W2, cross section # k (605 mm); SEM/EDX analysis at position # location b (UO_2/molten cladding interface; see Fig. 41)

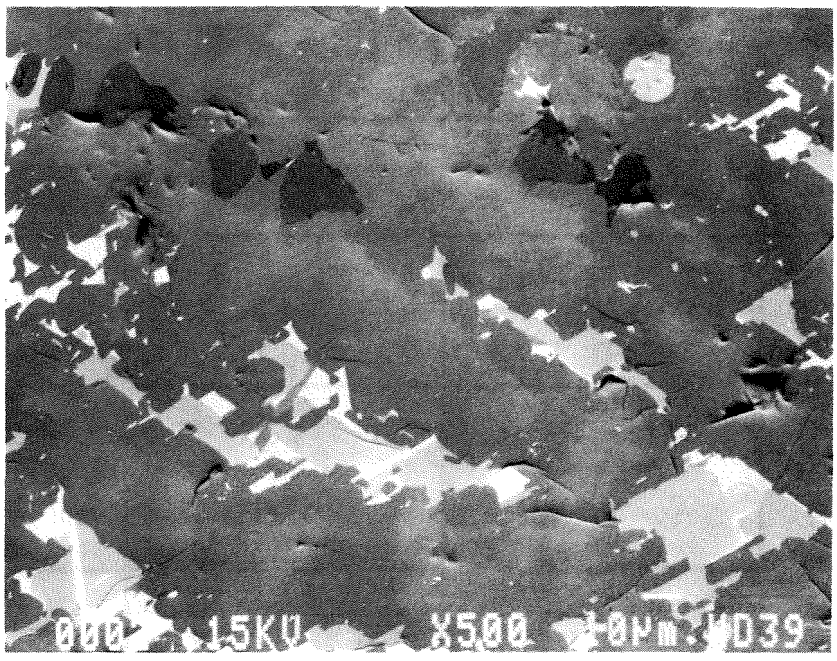

7-Apr-1994 11:23:19
CORA-W2 / Probe k / REM 2 / Integralanalyse Nr.a

Vert= 2643 counts Disp= 1 Comp= 3 Preset= 100 secs Elapsed= 100 secs

Element & Linie	Gew.-Prozent	Atom-Prozent*	Präzision 3 Sigma	k-Verh.**	Iter.
Cr KA	8.64	14.25	0.37	0.0867	
Fe KA	19.06	29.26	0.65	0.1936	
Ni KA	2.52	3.68	0.28	0.0264	
Zr LA	41.10	38.63	0.72	0.3227	
Mo LA	5.07	4.53	0.29	0.0351	
W MA	10.73	5.00	0.44	0.0795	
U MA	12.86	4.63	0.61	0.0899	3
Gesamt	99.98				

*Hinweis: Atom-Prozente sind auf 100 normalisiert
**Hinweis: k-Verhältnis = k.-Verh. x R
Quantex+>mit R = Referenzwert(Std.)/Referenzwert(Probe)

1 2 3 4 5 6 7 8 9
0.000 Range= 10.230 keV 10.110
Integral 8 = 88792

Fig. 46: Fuel rod bundle CORA-W2, cross section # k (605 mm); SEM/EDX analysis at positon # 2 (relocated and solidified melts, location a)

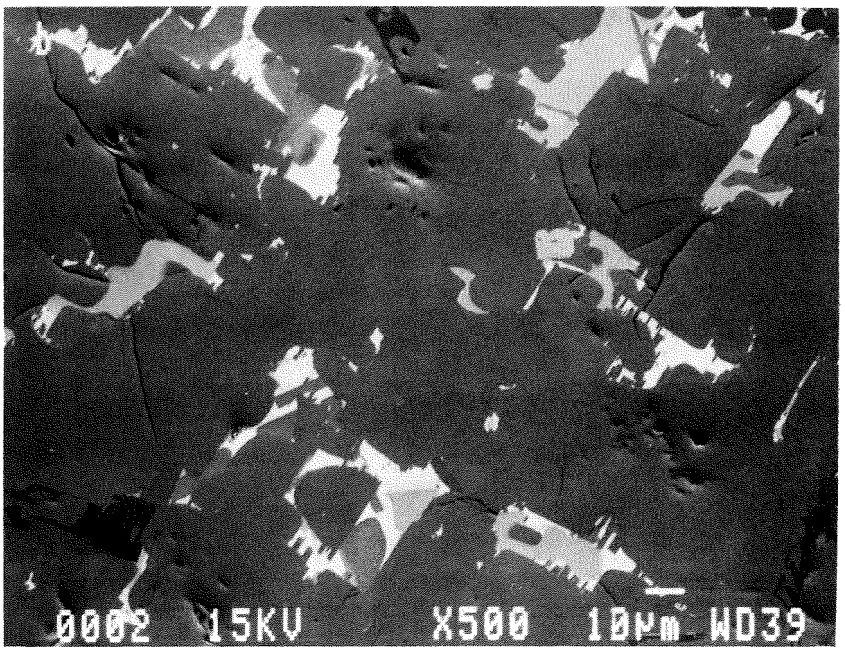

7-Apr-1994 11:33:47
CORA-W2 / Probe k / REM 2 / Integralanalyse Nr.b

Vert= 2694 counts Disp= 1 Comp= 3 Preset= 100 secs Elapsed= 100 secs

Element & Linie	Gew.-Prozent	Atom-Prozent*	Präzision 3 Sigma	k-Verh.**	Iter.
Ti KA	0.40	0.69	0.07	0.0038	
Cr KA	8.64	13.82	0.37	0.0869	
Fe KA	17.19	25.59	0.61	0.1750	
Ni KA	2.72	3.86	0.29	0.0285	
Zr LA	37.77	34.42	0.67	0.3136	
Nb LA	4.04	3.62	0.23	0.0347	
Mo LA	14.11	12.23	0.47	0.1036	
W MA	4.78	2.16	0.29	0.0360	
U MA	10.34	3.61	0.55	0.0719	3
Gesamt	99.99				

*Hinweis: Atom-Prozente sind auf 100 normalisiert
**Hinweis: k-Verhältnis = k.-Verh. x R
Quantex+>mit R = Referenzwert(Std.)/Referenzwert(Probe)

1 2 3 4 5 6 7 8 9
0.000 Range= 10.230 keV 10.110
Integral 8 = 93098

Fig. 47: Fuel rod bundle CORA-W2, cross section # k (605 mm); SEM/EDX analysis at positon # 2 (relocated and solidified melts; location b)

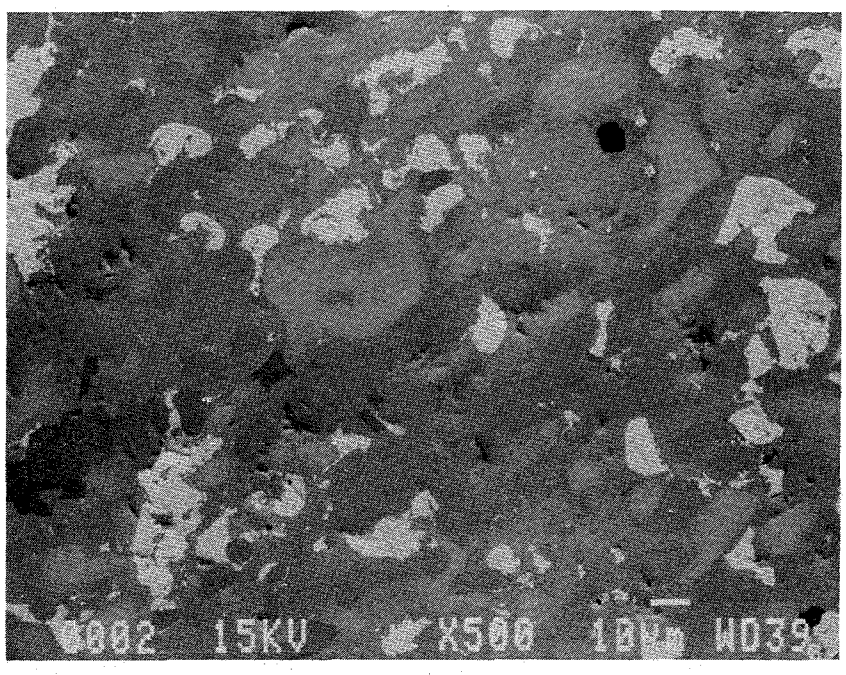

7-Apr-1994 11:40:56
CORA-W2 / Probe k / REM 2 / Integralanalyse Nr.c

Vert= 3161 counts Disp= 1 Comp= 3 Preset= 100 secs Elapsed= 100 secs

Element & Linie	Gew.-Prozent	Atom-Prozent*	Präzision 3 Sigma	k-Verh.**	Iter.
O KA	12.03	45.14	0.66	0.0335	
Cr KA	4.27	4.93	0.26	0.0423	
Fe KA	9.69	10.41	0.46	0.0984	
Ni KA	1.20	1.23	0.20	0.0127	
Zr LA	45.53	29.97	0.74	0.3797	
Mo LA	2.77	1.73	0.21	0.0198	
W MA	5.48	1.79	0.31	0.0419	
U MA	19.04	4.80	0.73	0.1367	3
Gesamt	100.01				

*Hinweis: Atom-Prozente sind auf 100 normalisiert
**Hinweis: k-Verhältnis = k.-Verh. x R
Quantex+>mit R = Referenzwert(Std.)/Referenzwert(Probe)

1 2 3 4 5 6 7 8 9
0.000 Range= 10.230 keV 10.110
Integral 8 = 82033

Fig. 48: Fuel rod bundle CORA-W2, cross section # k (605 mm); SEM/EDX analysis at positon # 2 (relocated and solidified melts; location c)

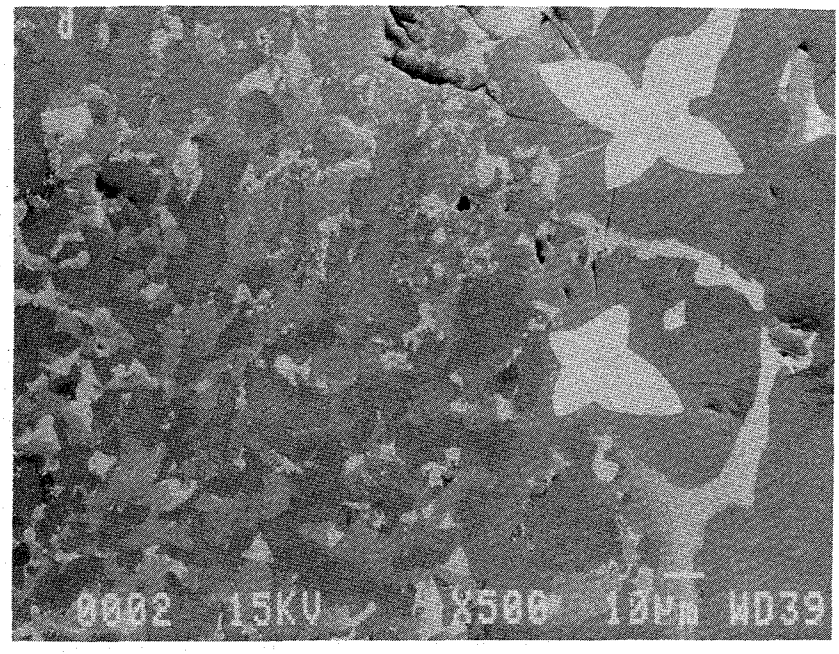

7-Apr-1994 11:46:41
CORA-W2 / Probe k / REM 2 / Integralanalyse Nr.d

Vert= 2378 counts Disp= 1 Comp= 3 Preset= 100 secs
Elapsed= 100 secs

Element & Linie	Gew.-Prozent	Atom-Prozent*	Präzision 3 Sigma	k-Verh.**	Iter.
O KA	8.87	36.96	0.53	0.0282	
Cr KA	5.80	7.44	0.29	0.0619	
Fe KA	13.22	15.78	0.52	0.1444	
Ni KA	2.19	2.49	0.25	0.0249	
Zr LA	34.22	25.01	0.63	0.2881	
Mo LA	3.30	2.29	0.22	0.0252	
W MA	11.42	4.14	0.43	0.0911	
U MA	20.99	5.88	0.74	0.1624	3
Gesamt	100.01				

*Hinweis: Atom-Prozente sind auf 100 normalisiert
**Hinweis: k-Verhältnis = k.-Verh. x R
Quantex+>mit R= Referenzwert(Std.)/Referenzwert(Probe)

1 2 3 4 5 6 7 8 9

0.000 Range= 10.230 keV 10.110

Integral 8 = 87610

Fig. 49: Fuel rod bundle CORA-W2, cross section # k (605 mm); SEM/EDX analysis at positon # 2 (relocated and solidified melts; location d)

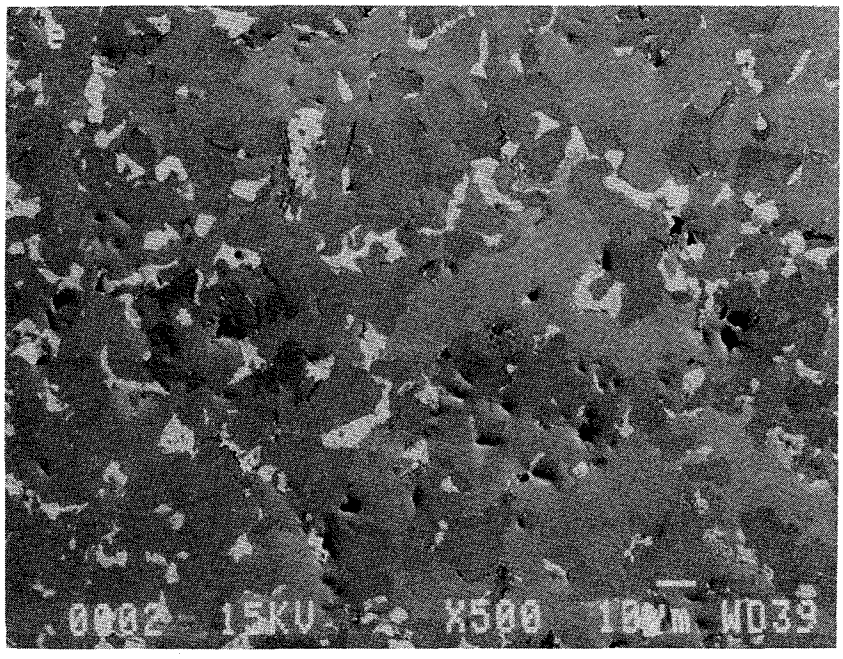

7-Apr-1994 11:55:03
CORA-W2 / Probe k / REM 2 / Integralanalyse Nr.e

Vert= 2424 counts Disp= 1 Comp= 3 Preset= 100 secs
Elapsed= 100 secs

Element & Linie	Gew.-Prozent	Atom-Prozent*	Präzision 3 Sigma	k-Verh.**	Iter.
O KA	12.78	48.06	0.67	0.0368	
Cr KA	4.23	4.89	0.26	0.0405	
Fe KA	10.34	11.14	0.48	0.1017	
Ni KA	1.32	1.35	0.21	0.0134	
Zr LA	37.75	24.89	0.69	0.2989	
Mo LA	2.04	1.28	0.18	0.0144	
W MA	5.68	1.86	0.32	0.0410	
U MA	25.86	6.53	0.86	0.1838	3
Gesamt	100.00				

*Hinweis: Atom-Prozente sind auf 100 normalisiert
**Hinweis: k-Verhältnis = k.-Verh. x R
Quantex+>mit R = Referenzwert(Std.)/Referenzwert(Probe)

1 2 3 4 5 6 7 8 9
0.000 Range= 10.230 keV 10.110
Integral 8 = 74924

Fig. 50: Fuel rod bundle CORA-W2, cross section # k (605 mm); SEM/EDX analysis at positon # 2 (relocated and solidified melts; location e)

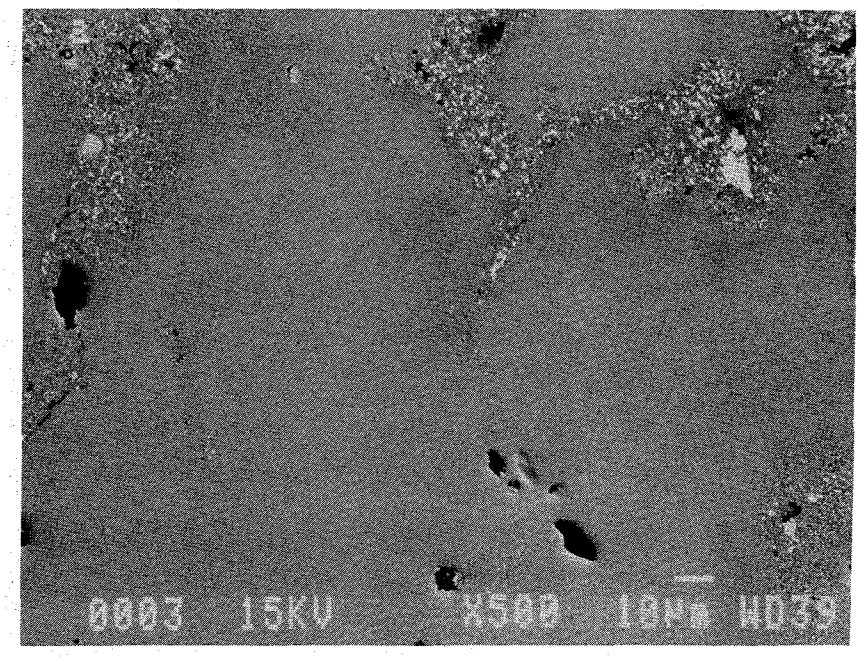

7-Apr-1994 14:42:02
CORA-W2 / Probe k / REM 3 / Integralanalyse Nr.a (500-fach)

Vert= 3122 counts Disp= 1 Comp= 3 Preset= 100 secs
Elapsed= 100 secs

Element & Linie	Gew.-Prozent	Atom-Prozent*	Präzision 3 Sigma	k-Verh.**	Iter.
O KA	20.81	66.67	0.88	0.0571	
Fe KA	0.89	0.81	0.14	0.0086	
Zr LA	45.19	25.39	0.74	0.3740	
U MA	33.12	7.13	0.97	0.2357	4
Gesamt	100.01				

*Hinweis: Atom-Prozente sind auf 100 normalisiert
**Hinweis: k-Verhältnis = k.-Verh. x R
Quantex+>mit R = Referenzwert(Std.)/Referenzwert(Probe)

1 2 3 4 5 6 7 8 9
0.000 Range= 10.230 keV 10.110
Integral 8 = 81287

Fig. 51: Fuel rod bundle CORA-W2, cross-section # k (605 mm); SEM/EDX analysis at position # 3 (relocated and solidified melts; location a)

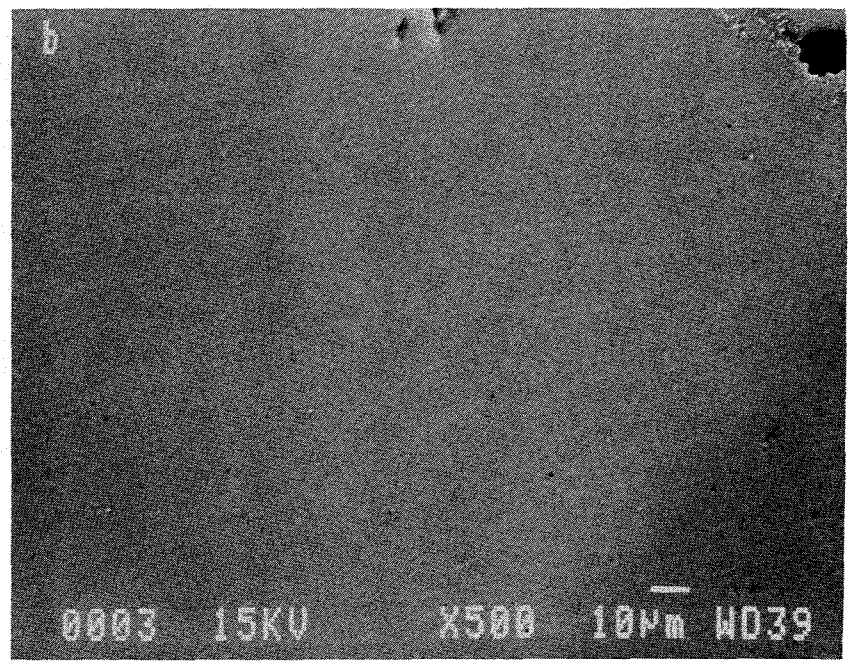

7-Apr-1994 14:48:05
CORA-W2 / Probe k / REM 3 / Integralanalyse Nr.b (500-fach)

Vert= 3114 counts Disp= 1 Comp= 3 Preset= 100 secs Elapsed= 100 secs

Element & Linie	Gew.-Prozent	Atom-Prozent*	Präzision 3 Sigma	k-Verh.**	Iter.
O KA	19.52	65.11	0.87	0.0508	
Fe KA	0.01	0.01	0.02	0.0001	
Zr LA	46.65	27.29	0.76	0.3760	
U MA	33.82	7.58	0.99	0.2333	4
Gesamt	100.00				

*Hinweis: Atom-Prozente sind auf 100 normalisiert
**Hinweis: k-Verhältnis = k.-Verh. x R
Quantex+>mit R = Referenzwert(Std.)/Referenzwert(Probe)

1 2 3 4 5 6 7 8 9
0.000 Range= 10.230 keV 10.110
Integral 8 = 73507

Fig. 52: Fuel rod bundle CORA-W2, cross-section # k (605 mm); SEM/EDX analysis at position # 3 (relocated and solidified melts; location b)

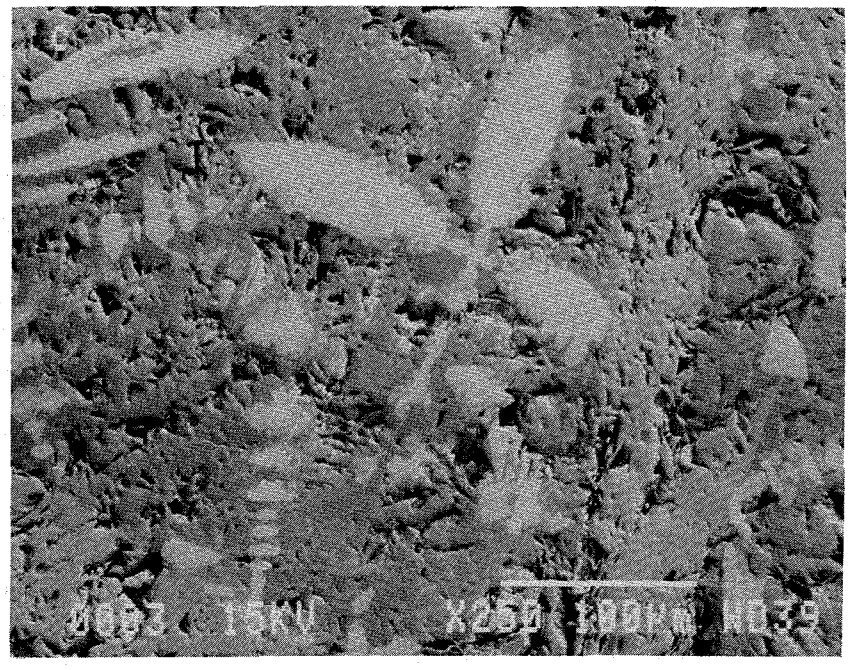

```
 7-Apr-1994 15:00:55
CORA-W2 / Probe k / REM 3 / Integralanalyse Nr.c (250-fach)
                                          Preset=        100 secs
Vert=     2389 counts   Disp= 1    Comp= 3   Elapsed=       100 secs

  Element     Gew.-      Atom-     Präzision
  & Linie   Prozent    Prozent*   3 Sigma  k-Verh.**  Iter.

   O  KA       6.93      29.60       0.54     0.0168
   Cr KA       6.32       8.30       0.31     0.0633
   Fe KA      11.06      13.53       0.49     0.1134
   Ni KA       1.74       2.02       0.23     0.0185
   Zr LA       9.68       7.25       0.35     0.0767
   Nb LA       6.17       4.53       0.29     0.0507
   Mo LA      39.14      27.87       0.76     0.3063
   W  MA      17.21       6.40       0.54     0.1357
   U  MA       1.75       0.50       0.23     0.0116       3
   Gesamt    100.00

 *Hinweis: Atom-Prozente sind auf  100 normalisiert
**Hinweis: k-Verhältnis = k.-Verh. x R
Quantex+>mit R = Referenzwert(Std.)/Referenzwert(Probe)
      |1      |2      |3      |4      |5      |6      |7      |8      |9      |
<-    0.000    Range=   10.230 keV                          10.110 ->
                                          Integral 8  =        85876
```

Fig. 53: Fuel rod bundle CORA-W2, cross-section # k (605 mm); SEM/EDX analysis at position # 3 (relocated and solidified melts; location c)

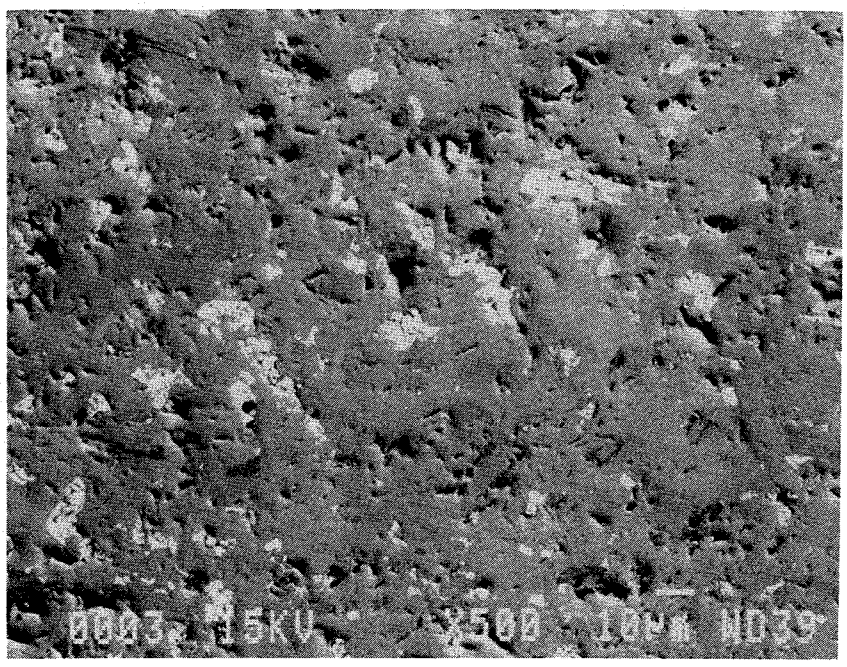

7-Apr-1994 15:06:09
CORA-W2 / Probe k / REM 3 / Integralanalyse Nr.d (500-fach)

Vert= 3601 counts Disp= 1 Comp= 3 Preset= 100 secs Elapsed= 100 secs

Element & Linie	Gew.-Prozent	Atom-Prozent*	Präzision 3 Sigma	k-Verh.**	Iter.
O KA	17.17	55.80	0.79	0.0481	
Cr KA	2.03	2.03	0.18	0.0199	
Fe KA	7.53	7.01	0.41	0.0756	
Ni KA	1.82	1.61	0.24	0.0188	
Zr LA	51.06	29.10	0.77	0.4404	
U MA	20.40	4.45	0.75	0.1472	4
Gesamt	100.01				

*Hinweis: Atom-Prozente sind auf 100 normalisiert
**Hinweis: k-Verhältnis = k.-Verh. x R
Quantex+>mit R = Referenzwert(Std.)/Referenzwert(Probe)

1 2 3 4 5 6 7 8 9

← 0.000 Range= 10.230 keV 10.110 →

Integral 8 = 88367

Fig. 54: Fuel rod bundle CORA-W2, cross section # k (605 mm); SEM/EDX analysis at position # 3 (relocated and solidified melts; location d)

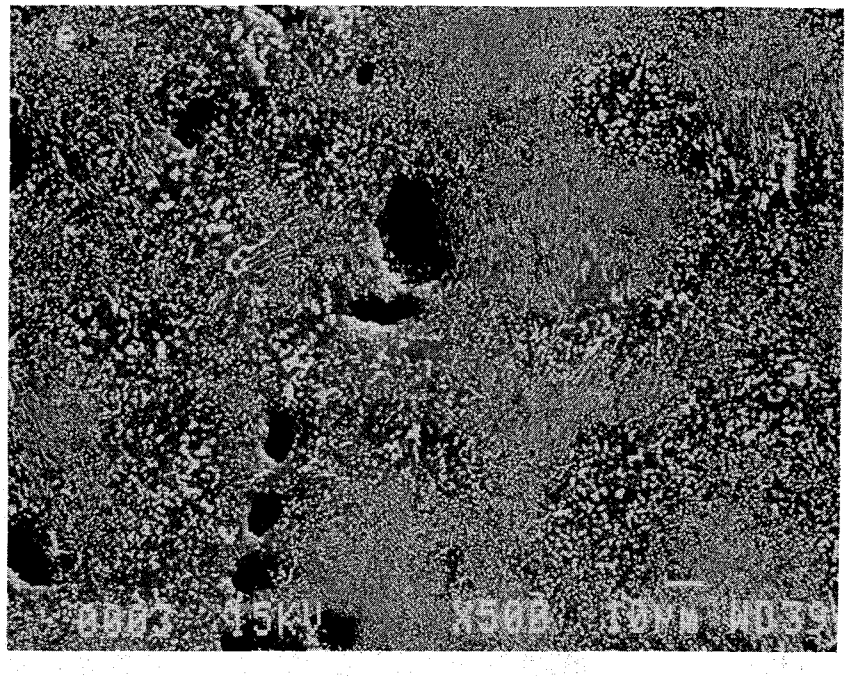

7-Apr-1994 15:10:46
CORA-W2 / Probe k / REM 3 / Integralanalyse Nr.e (500-fach)
Preset= 100 secs
Vert= 3042 counts Disp= 1 Comp= 3 Elapsed= 100 secs

Element & Linie	Gew.-Prozent	Atom-Prozent*	Präzision 3 Sigma	k-Verh.**	Iter.
O KA	19.80	66.33	0.84	0.0560	
Zr LA	43.06	25.30	0.71	0.3652	
U MA	37.14	8.36	1.01	0.2745	4
Gesamt	100.00				

*Hinweis: Atom-Prozente sind auf 100 normalisiert
**Hinweis: k-Verhältnis = k.-Verh. x R
Quantex+>mit R = Referenzwert(Std.)/Referenzwert(Probe)

1 2 3 4 5 6 7 8 9
0.000 Range= 10.230 keV 10.110
Integral 8 = 83165

Fig. 55: Fuel rod bundle CORA-W2, cross section # k (605 mm); SEM/EDX analysis at position # 3 (relocated and solidified melts; location e)

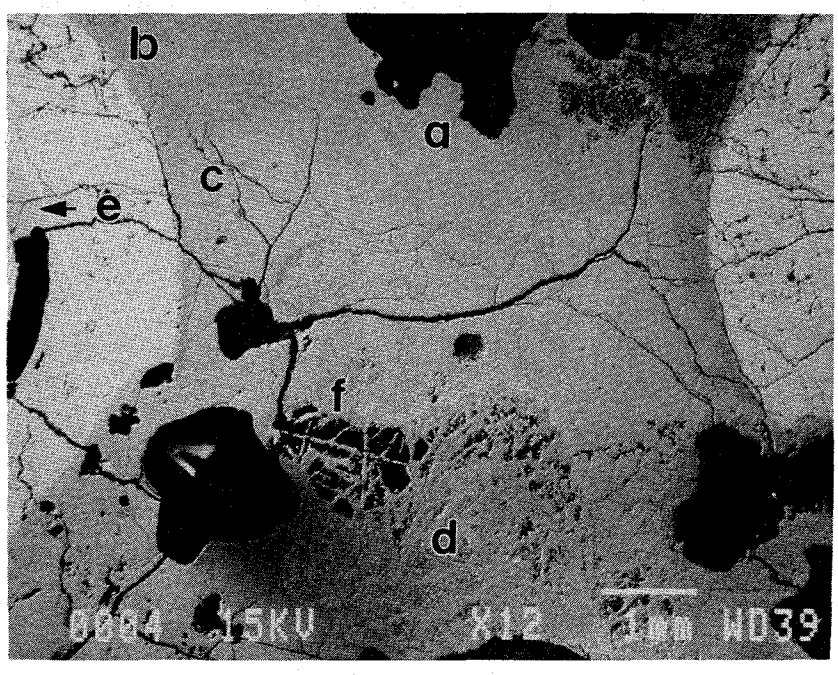

Fig. 56: Fuel rod bundle CORA-W2, cross section # k (605 mm); General view of positon # 4 (melt between two UO_2 fuel pellet columns; positons of SEM/EDX analysis)

Punktanalyse Nr.	Element	Gew. %	Atom %*
1	Si	0.8	2.0
	Ti	0.3	0.4
	Cr	9.7	12.6
	Fe	39.5	47.7
	Ni	5.7	6.5
	Zr	37.1	27.4
	Mo	3.6	2.5
	U	3.3	0.9
2	o	12.8	63.6
	Fe	0.7	1.0
	Zr	11.9	10.4
	U	74.6	25.0
3	O	17.8	55.6
	Cr	2.4	2.3
	Fe	6.7	6.0
	Ni	1.6	1.3
	Zr	58.4	32.0
	U	13.1	2.8
4	O	22.2	65.0
	Zr	62.1	31.9
	U	15.7	3.1

* auf 100 % normalisiert

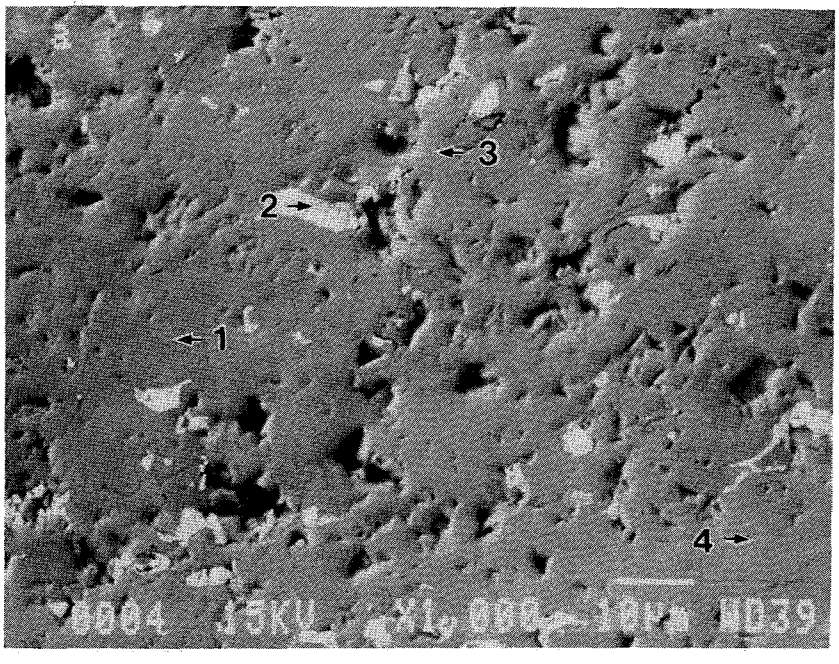

Fig. 57: Fuel rod bundle CORA-W2, cross section # k (605 mm); SEM/EDX analysis at position # 4 (melt at location a; see Fig. 56)

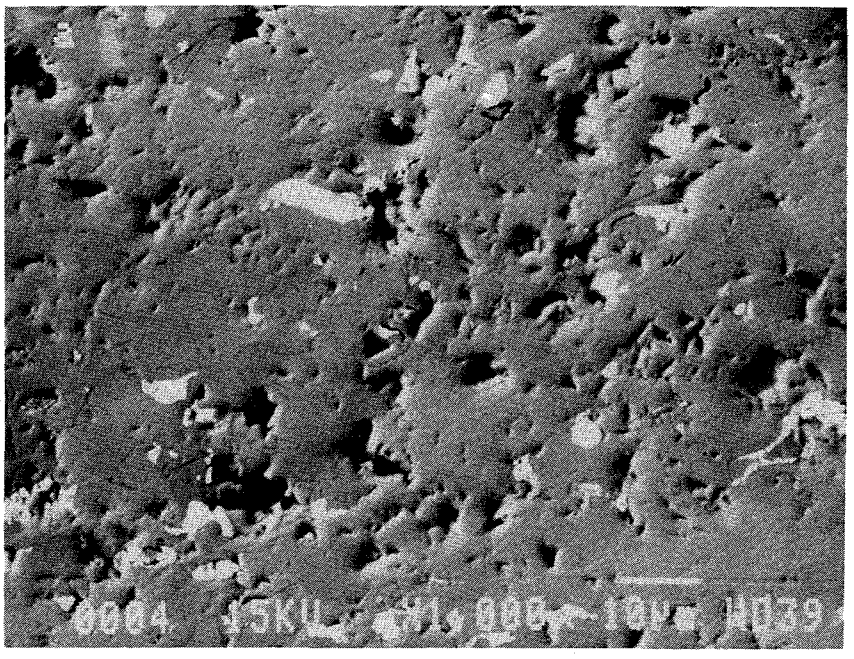

13-Apr-1994 14:01:24
CORA-W2 / Probe k / REM 4 / Ausschnitt a / Integralanalyse

Vert= 3579 counts Disp= 1 Comp= 3 Preset= 100 secs Elapsed= 100 secs

Element & Linie	Gew.-Prozent	Atom-Prozent*	Präzision 3 Sigma	k-Verh.**	Iter.
O KA	17.88	55.44	0.83	0.0468	
Cr KA	2.64	2.52	0.21	0.0241	
Fe KA	9.74	8.65	0.48	0.0907	
Ni KA	1.82	1.54	0.25	0.0174	
Zr LA	52.79	28.70	0.81	0.4250	
U MA	15.13	3.15	0.68	0.1007	4
Gesamt	100.00				

*Hinweis: Atom-Prozente sind auf 100 normalisiert
**Hinweis: k-Verhältnis = k.-Verh. x R
Quantex+>mit R = Referenzwert(Std.)/Referenzwert(Probe)

1 2 3 4 5 6 7 8 9
0.000 Range= 10.230 keV 10.110
Integral 8 = 83517

Fig. 58: Fuel rod bundle CORA-W2, cross section # k (605 mm); SEM/EDX analysis at position # 4 (melt at location a; integral analysis)

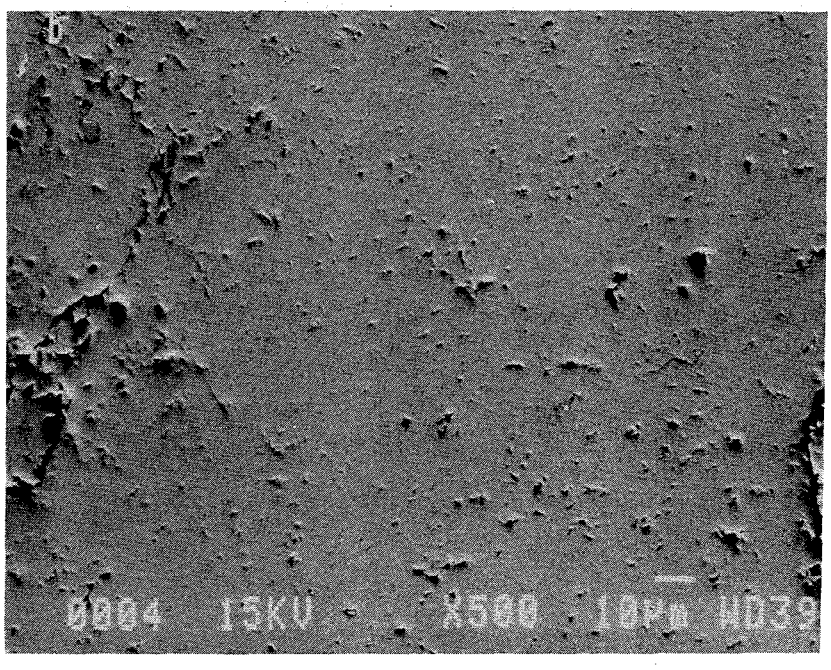

13-Apr-1994 13:49:10
CORA-W2 / Probe k / REM 4 / Ausschnitt b / Integralanalyse

Vert= 5000 counts Disp= 1 Comp= 3 Preset= 100 secs
Elapsed= 100 secs

Element & Linie	Gew.-Prozent	Atom-Prozent*	Präzision 3 Sigma	k-Verh.**	Iter.
O KA	23.97	66.72	1.01	0.0574	
Fe KA	0.49	0.39	0.11	0.0045	
Zr LA	62.28	30.41	0.86	0.5160	
U MA	13.26	2.48	0.64	0.0858	4
Gesamt	100.00				

*Hinweis: Atom-Prozente sind auf 100 normalisiert
**Hinweis: k-Verhältnis = k.-Verh. x R
Quantex+>mit R = Referenzwert(Std.)/Referenzwert(Probe)

1 2 3 4 5 6 7 8 9
0.000 Range= 10.230 keV 10.110
Integral 8 = 81305

Fig. 59: Fuel rod bundle CORA-W2, cross section # k (605 mm); SEM/EDX analysis at position # 4 (melts at location b; see Fig. 56)

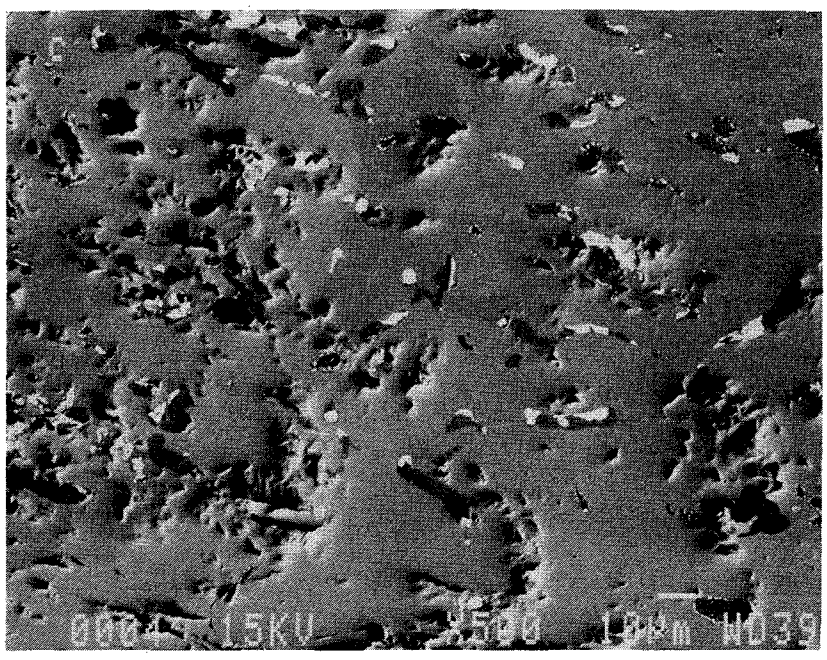

```
15-Apr-1994 10:31:18
CORA-W2 / Probe k / REM 4 / Ausschnitt c / Integralanalyse
                                          Preset=        100 secs
Vert=     2972 counts   Disp= 1    Comp= 3   Elapsed=       100 secs

  Element     Gew.-      Atom-     Präzision
  & Linie    Prozent    Prozent*   3 Sigma   k-Verh.**   Iter.

   O  KA      18.59      62.15       0.85      0.0491
   Cr KA       1.19       1.22       0.14      0.0107
   Fe KA       2.69       2.57       0.25      0.0250
   Ni KA       0.63       0.57       0.15      0.0061
   Zr LA      44.80      26.27       0.75      0.3544
   U  MA      32.12       7.22       0.97      0.2195       3
   Gesamt    100.02

 *Hinweis: Atom-Prozente sind auf  100 normalisiert
**Hinweis: k-Verhältnis = k.-Verh. x R
Quantex+>mit R = Referenzwert(Std.)/Referenzwert(Probe)
        |1       |2       |3       |4       |5       |6       |7       |8       |9       |
<-      0.000     Range=   10.230 keV                                    10.110 ->
                                                Integral 8  =          74719
```

Fig. 60: Fuel rod bundle CORA-W2, cross-section # k (605 mm); SEM/EDX analysis at position # 4 (melt at location c; see Fig. 56)

Ohne Abbildung

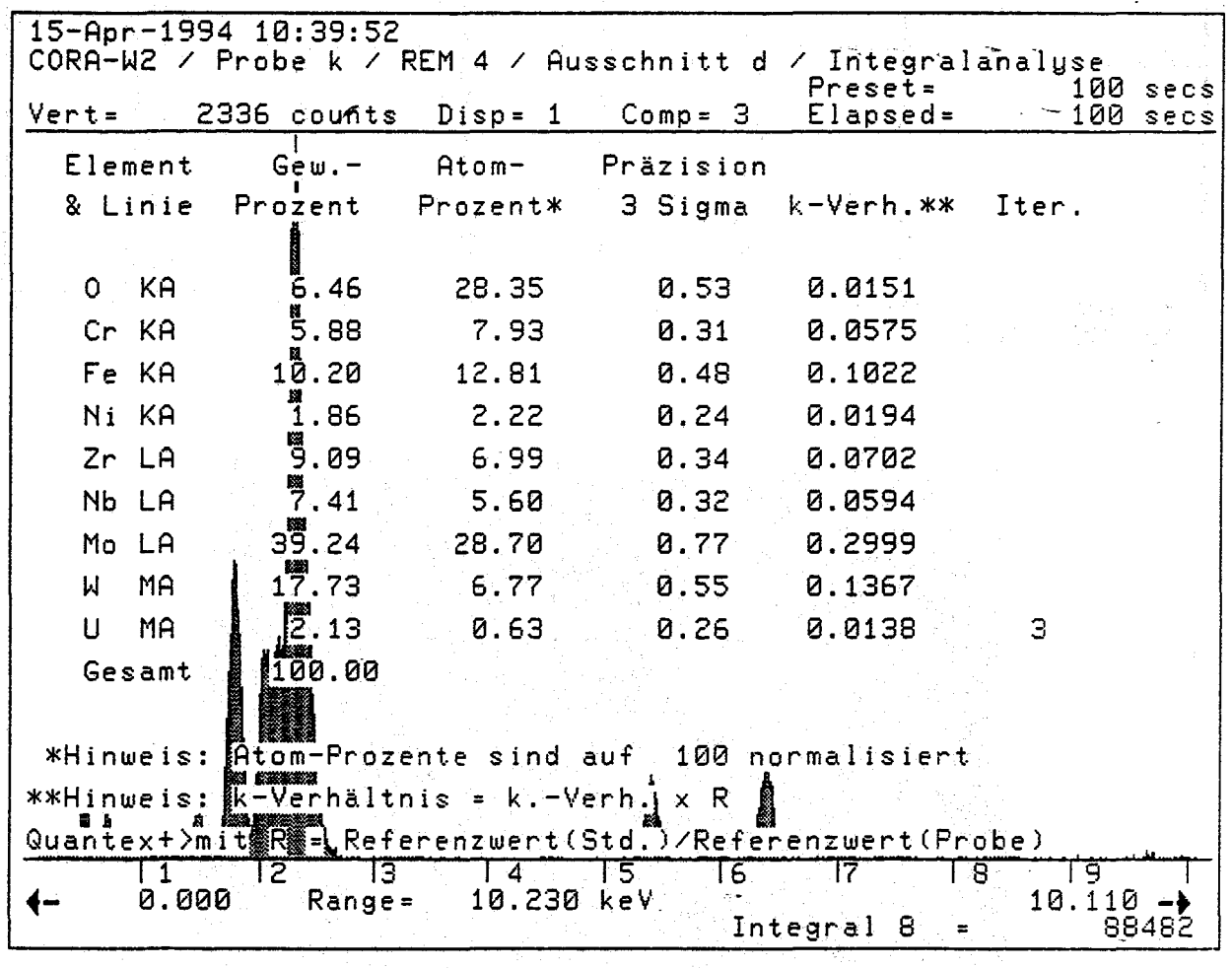

Fig. 61: Fuel rod bundle CORA-W2, cross-section # k (605 mm); SEM/EDX analysis at position # 4 (melt at location d)

Punktanalyse Nr.	Element	Gew. %	Atom %*
1	Cr	2.6	5.6
	Fe	1.2	2.4
	Mo	58.8	69.1
	W	37.4	22.9
2	Si	3.6	9.1
	Cr	10.2	13.8
	Fe	26.2	33.0
	Ni	4.2	5.0
	Zr	17.1	13.2
	Nb	4.4	3.4
	Mo	26.9	19.7
	W	6.2	2.4
	U	1.2	0.4
3	Ti	0.5	1.0
	Cr	3.7	7.3
	Fe	2.2	4.0
	Zr	3.7	4.1
	Nb	16.1	17.8
	Mo	48.0	51.4
	W	25.9	14.4

* auf 100 % normalisiert

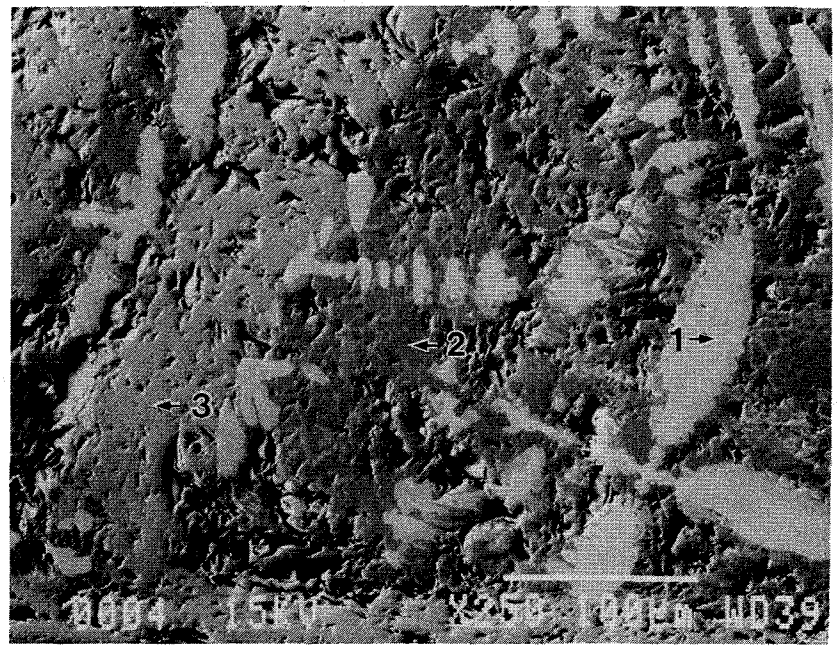

Fig. 62: Fuel rod bundle CORA-W2, cross-section # k (605 mm); SEM/EDX analysis at position # 4 (melt at location d; detailed phase analysis)

Punktanalyse Nr.	Element	Gew. %	Atom %*
1	Be?		
	O	19.0	67.8
	Zr	33.4	20.8
	U	47.6	11.4
2	W	100	100
3	O	11.9	66.7
	U	88.1	33.3

* auf 100 % normalisiert

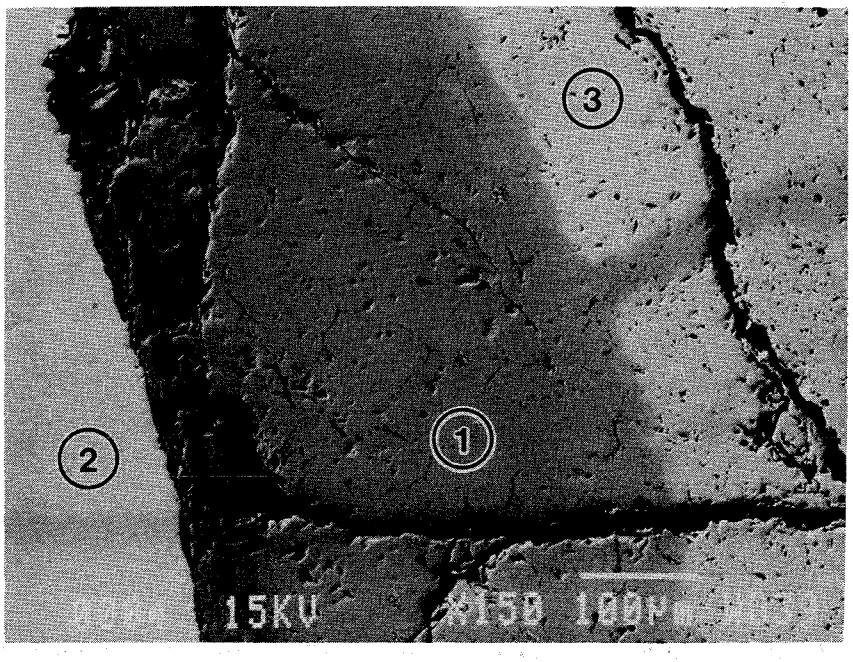

Fig. 63: Fuel rod bundle CORA-W2, cross-section # k (605 mm); SEM/EDX analysis at position # 4 (melt at location e; see Fig. 56; gap between W heater and UO_2 pellet)

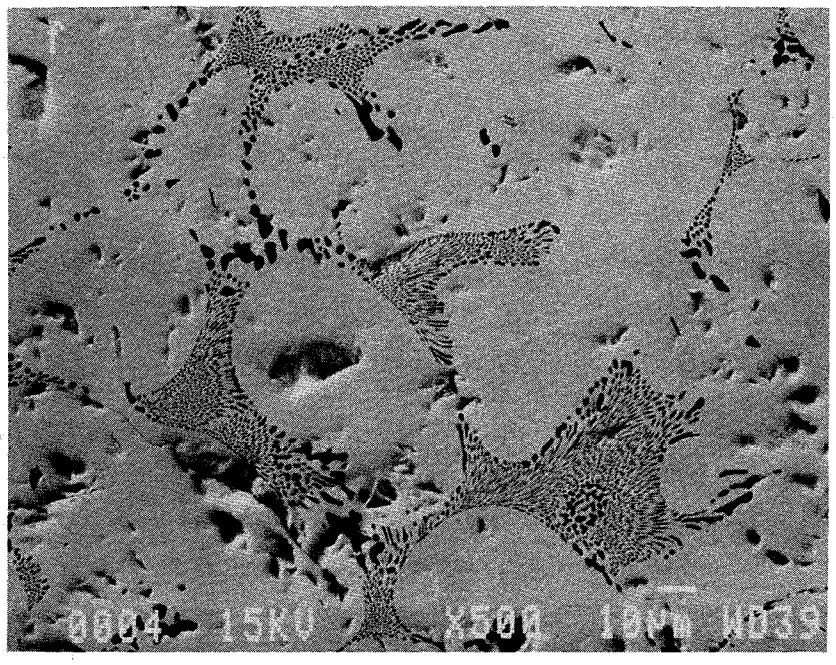

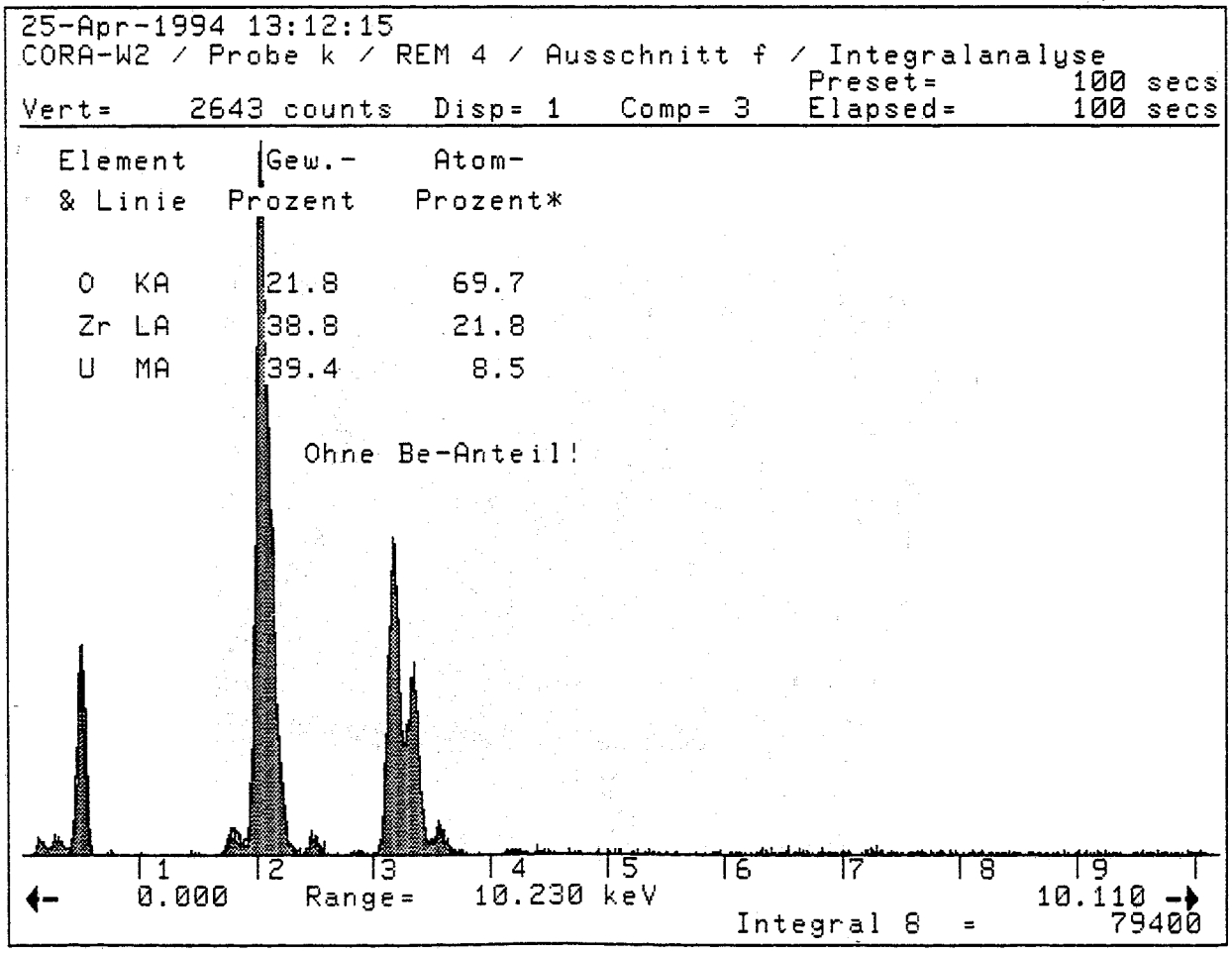

Fig. 64: Fuel rod bundle CORA-W2, cross-section # k (605 mm); SEM/EDX analysis at position # 4 (melt at location f, see Fig. 56)

Punktanalyse Nr.	Element	Gew. %	Atom %*
1	O	17.9	64.3
	Zr	41.1	25.8
	U	41.0	9.9
2	Be	+	+
	O	90	98.5
	Zr	5	1.0
	U	5	0.3
3	Be	+	+
	O	30	79
	Zr	32	15
	U	37	6

* auf 100 % normalisiert
+ Analysenergebnisse ohne Be errechnet
+ Kann nicht mit dem EDX erfaßt werden

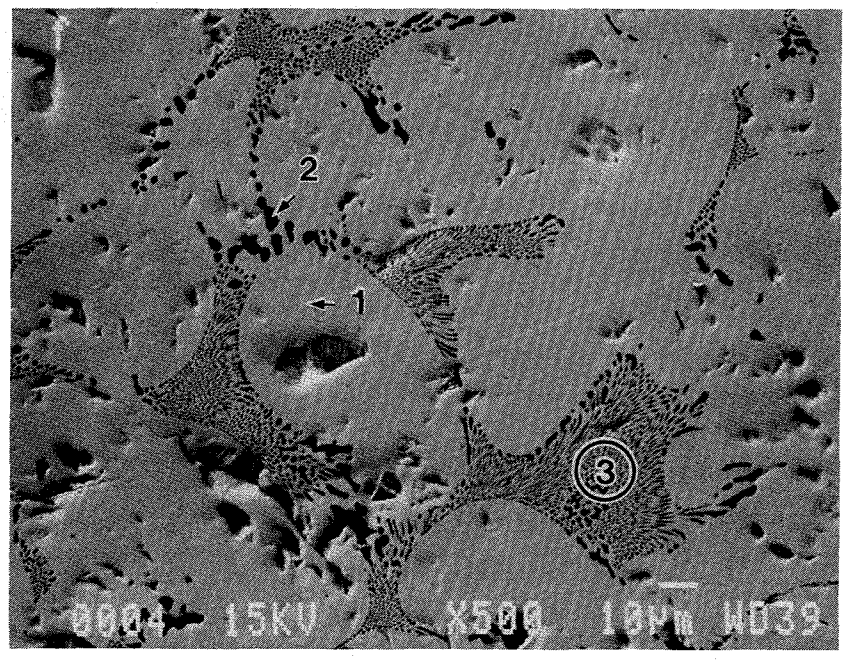

Fig. 65: Fuel rod bundle CORA-W2, cross-section # k (605 mm); SEM/EDX analysis at position # 4 (melt at location f; detailed phase analysis)

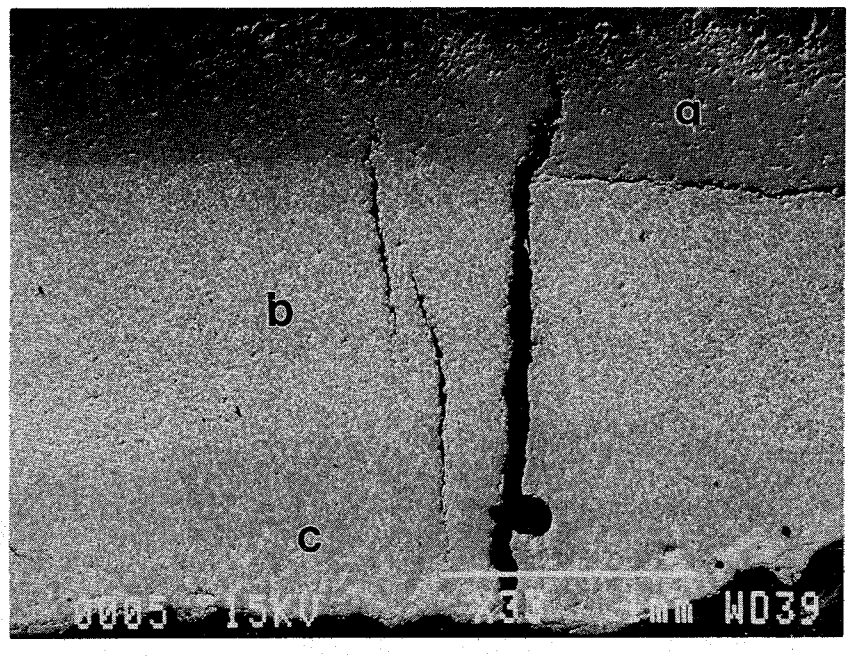

Fig. 66: Fuel rod bundle CORA-W2, cross-section # k (605 mm); General view of position # 5 (shroud; positions of analysis)

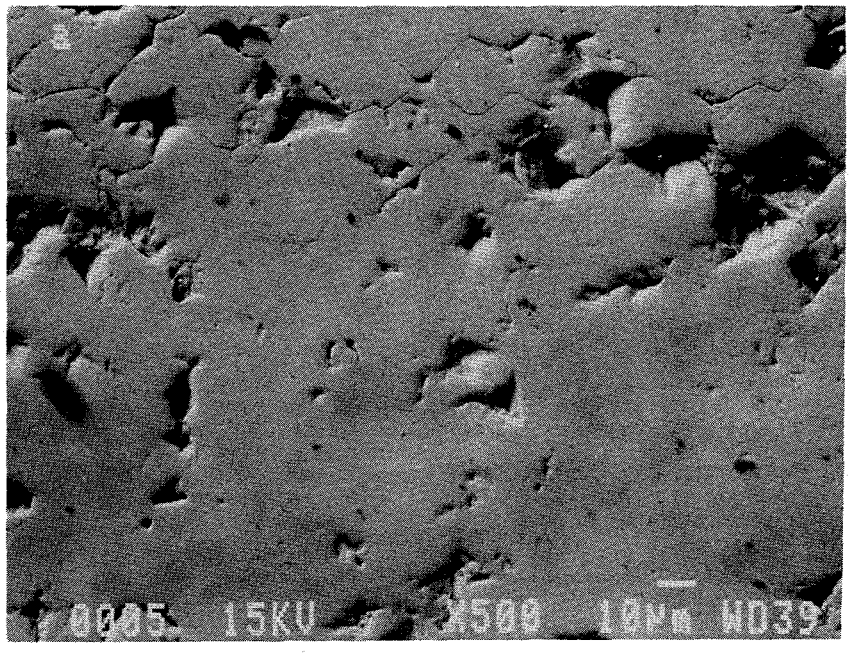

26-Apr-1994 09:19:01
CORA-W2 / Probe k / REM 5 / Ausschnitt a / Integralanalyse

Vert= 4635 counts Disp= 1 Comp= 3 Preset= 100 secs Elapsed= 100 secs

Element & Linie	Gew.-Prozent	Atom-Prozent*	Präzision 3 Sigma	k-Verh.**	Iter.
O KA	28.90	69.85	1.18	0.0616	
Zr LA	71.10	30.15	0.94	0.5616	4
Gesamt	100.00				

*Hinweis: Atom-Prozente sind auf 100 normalisiert
**Hinweis: k-Verhältnis = k.-Verh. x R
Quantex+>mit R = Referenzwert(Std.)/Referenzwert(Probe)

1 2 3 4 5 6 7 8 9
0.000 Range= 10.230 keV 10.110
Integral 8 = 87746

Fig. 67: Fuel rod bundle CORA-W2, cross section # k (605 mm); SEM/EDX analysis at position # 5 location a (shroud)

Punktanalyse Nr.	Element	Gew. %	Atom % *
1	O	7.9	32.8
	Zr	92.1	67.2
2	O	25.8	66.5
	Zr	74.2	33.5

* auf 100 % normalisiert

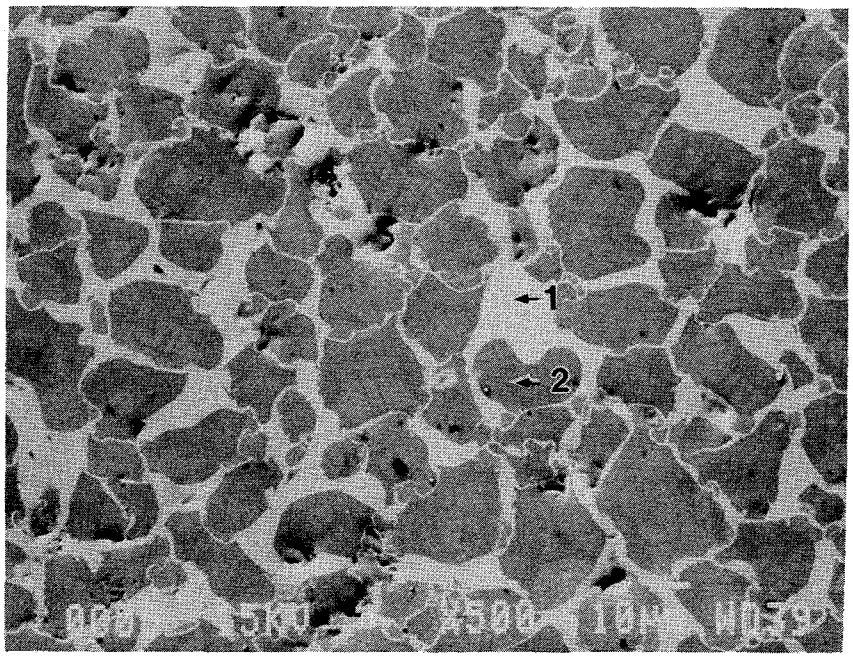

Fig. 68a: Fuel rod bundle CORA-W2, cross section # k (605 mm); SEM/EDX analysis at position # 5 location b (detailed phase analysis of shroud)

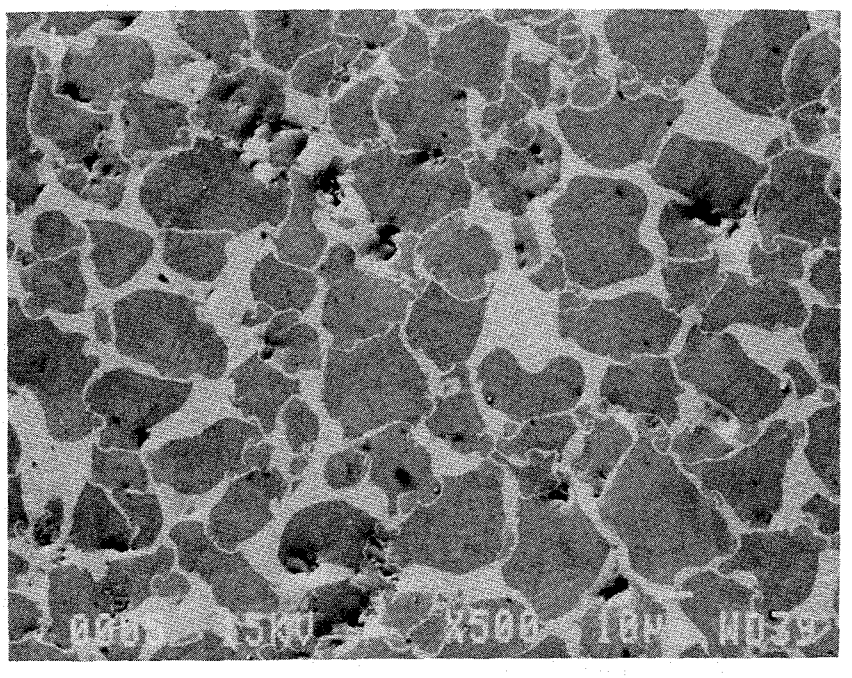

```
26-Apr-1994 09:23:12
CORA-W2 / Probe k / REM 5 / Ausschnitt b / Integralanalyse
                                          Preset=        100 secs
Vert=     5321 counts   Disp= 1    Comp= 3   Elapsed=       100 secs

  Element     Gew.-     Atom-     Präzision
  & Linie   Prozent   Prozent*   3 Sigma  k-Verh.**  Iter.

   O  KA     21.43      60.86      1.04     0.0436
   Zr LA     78.57      39.14      0.97     0.6535       4
   Gesamt   100.00

 *Hinweis: Atom-Prozente sind auf  100 normalisiert
**Hinweis: k-Verhältnis = k.-Verh. x R
Quantex+>mit R = Referenzwert(Std.)/Referenzwert(Probe)
      |1      |2      |3      |4      |5      |6      |7      |8      |9      |
<-    0.000     Range=    10.230 keV                          10.110 ->
                                        Integral 8  =         99557
```

Fig. 68b: Fuel rod bundle CORA-W2, cross section # k (605 mm); SEM/EDX analysis at position # 5 location b (integral analysis of shroud)

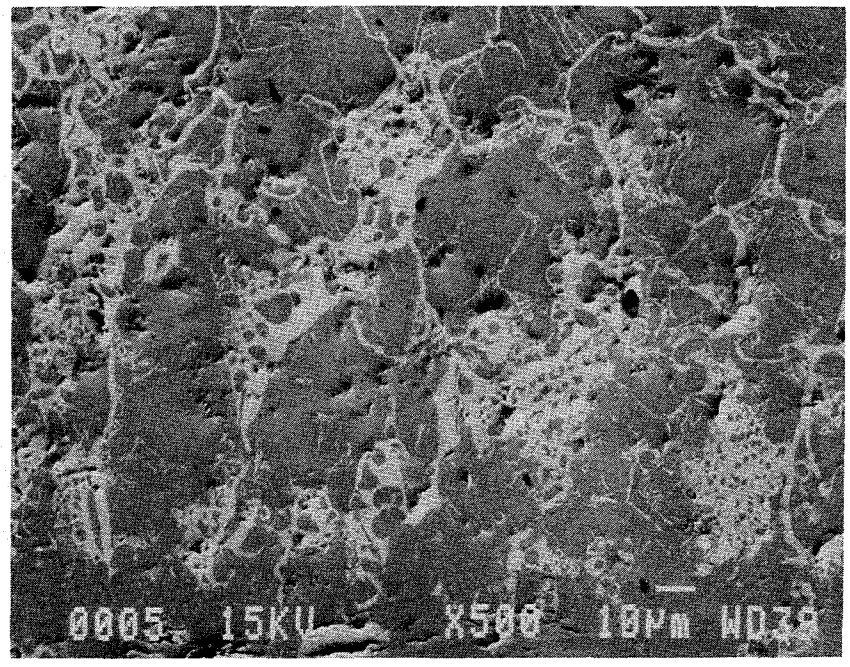

26-Apr-1994 09:27:03
CORA-W2 / Probe k / REM 5 / Ausschnitt c / Integralanalyse

Vert= 5300 counts Disp= 1 Comp= 3 Preset= 100 secs
Elapsed= 100 secs

Element & Linie	Gew.-Prozent	Atom-Prozent*	Präzision 3 Sigma	k-Verh.**	Iter.
O KA	23.54	63.71	1.06	0.0501	
Zr LA	76.46	36.29	0.95	0.6474	4
Gesamt	100.00				

*Hinweis: Atom-Prozente sind auf 100 normalisiert
**Hinweis: k-Verhältnis = k.-Verh. x R
Quantex+>mit R = Referenzwert(Std.)/Referenzwert(Probe)

1 2 3 4 5 6 7 8 9
0.000 Range= 10.230 keV 10.110
Integral 8 = 96632

Fig. 69: Fuel rod bundle CORA-W2, cross section # k (605 mm); SEM/EDX analysis at position # 5 location c (integral analysis of shroud)

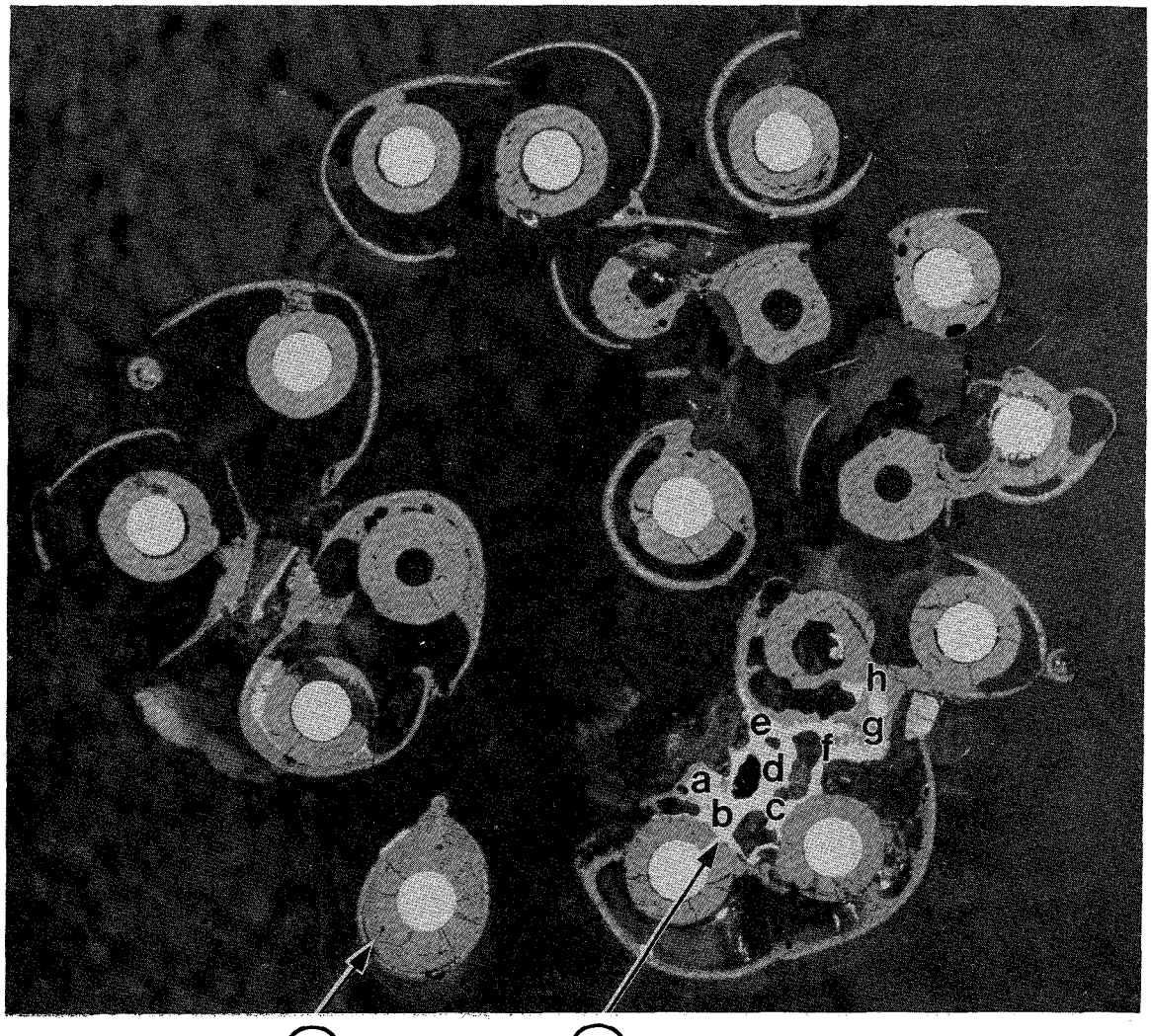

Maßstab 2 : 1

Fig. 70: Fuel rod bundle CORA-W2, cross-section # p (910 mm); Positions of SEM/EDX analysis

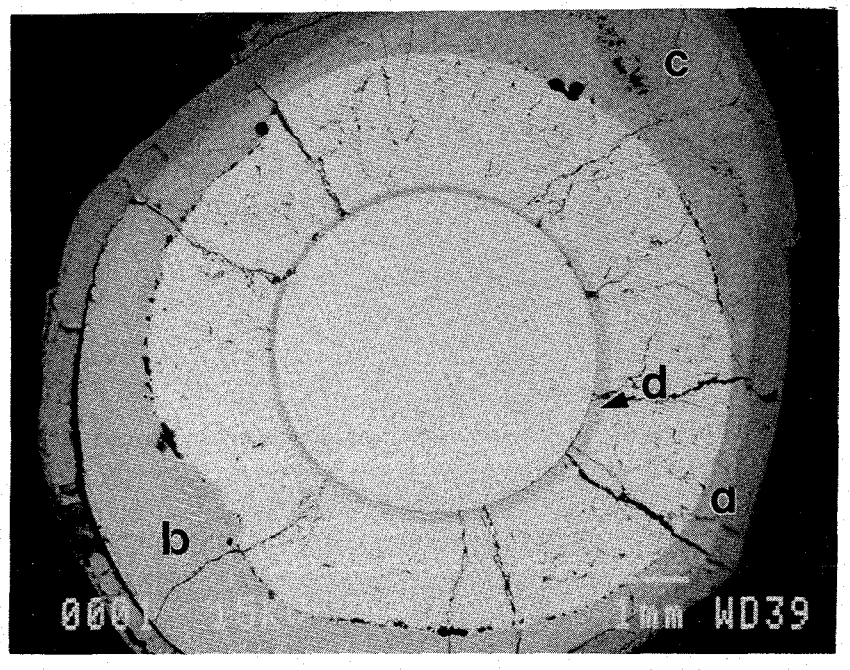

Fig. 71: Fuel rod bundle CORA-W2, cross-section # p (910 mm); General view of position # 1 (fuel rod)

Punktanalyse Nr.	Element	Gew. %	Atom %*
1	O U	11.8 88.2	66.5 33.5
2	O Zr U	15.8 21.0 63.3	66.5 15.5 18.0
3	O Zr U	21.0 49.4 29.6	66.3 27.4 6.3
4	O Zr U	20.1 52.9 27.0	64.5 29.7 5.8
5	O Zr	26.2 73.8	66.9 33.1

* auf 100 % normalisiert

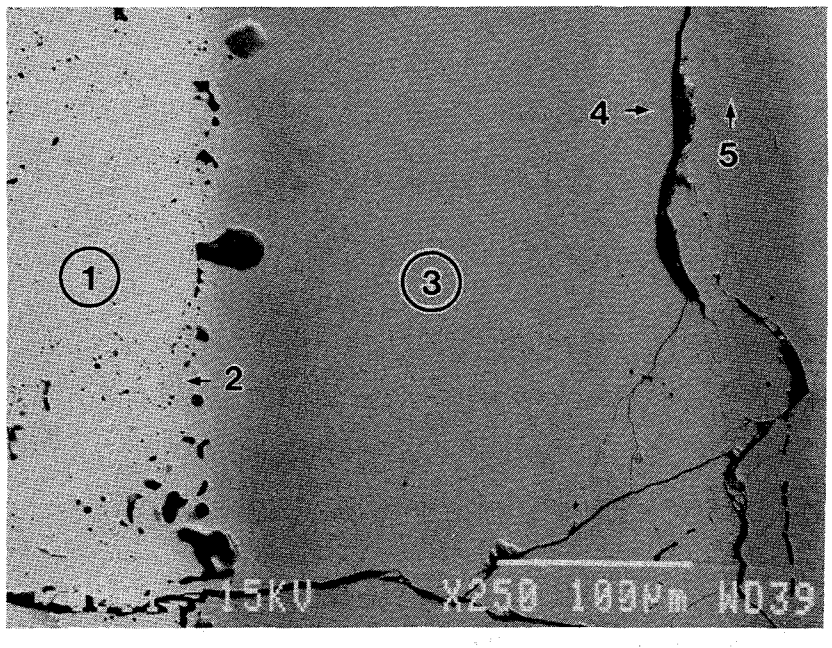

Fig. 72: Fuel rod bundle CORA-W2, cross-section # p (910 mm); SEM/EDX analysis at position # 1 location a (pellet/cladding interface)

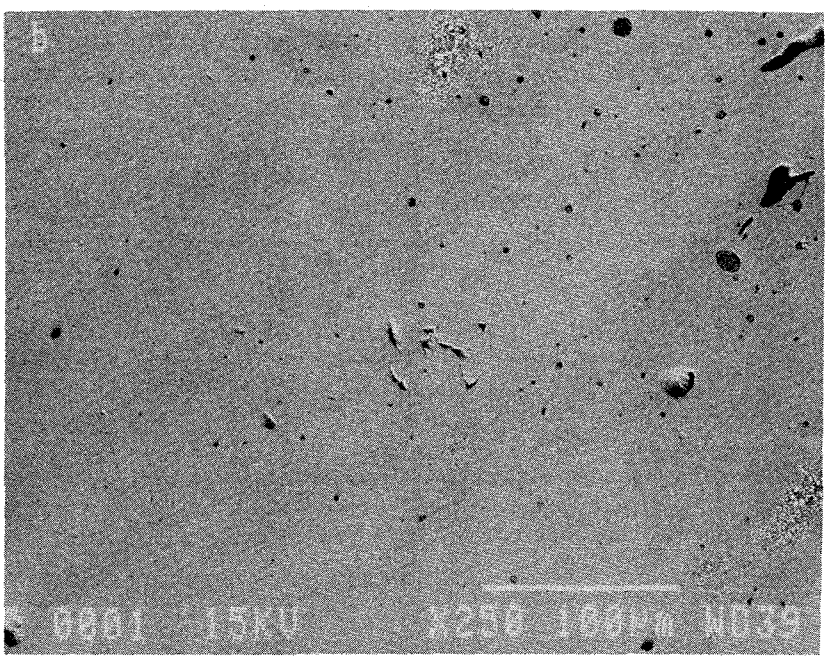

3-May-1994 09:08:24
CORA-W2 / Probe p / REM 1 / Ausschnitt b / Integralanalyse

Vert= 2901 counts Disp= 1 Comp= 3 Preset= 100 secs Elapsed= 100 secs

Element & Linie	Gew.-Prozent	Atom-Prozent*	Präzision 3 Sigma	k-Verh.**	Iter.
O KA	19.61	66.09	0.87	0.0524	
Zr LA	43.04	25.44	0.73	0.3450	
U MA	37.35	8.46	1.04	0.2609	3
Gesamt	100.00				

*Hinweis: Atom-Prozente sind auf 100 normalisiert
**Hinweis: k-Verhältnis = k.-Verh. x R
Quantex+>mit R = Referenzwert(Std.)/Referenzwert(Probe)

1 2 3 4 5 6 7 8 9
0.000 Range= 10.230 keV 10.110
Integral 8 = 81038

Fig. 73: Fuel rod bundle CORA-W2, cross-section # p (910 mm); SEM/EDX analysis at position # 1 location b

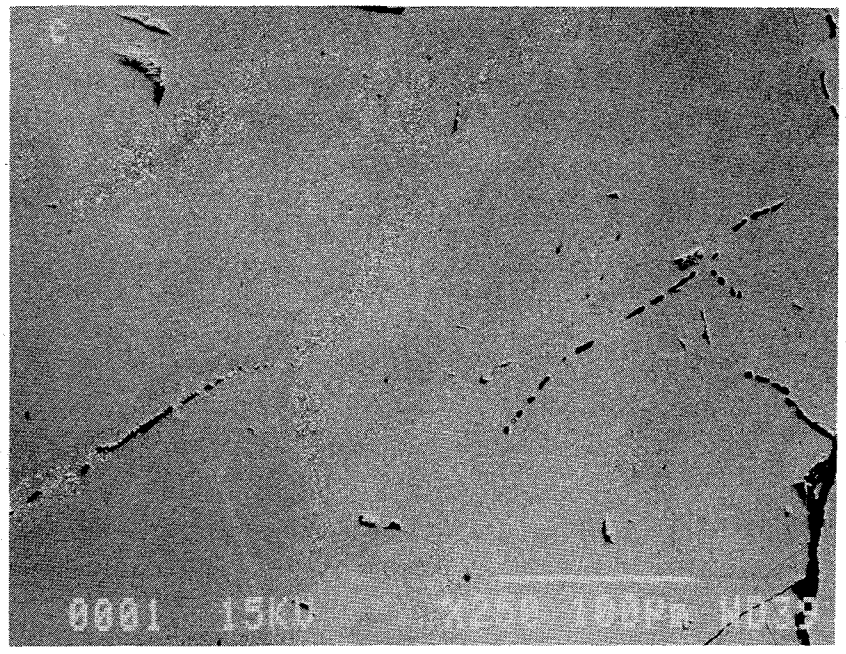

3-May-1994 09:00:50
CORA-W2 / Probe p / REM 1 / Ausschnitt c / Integralanalyse
Preset= 100 secs
Vert= 3332 counts Disp= 1 Comp= 3 Elapsed= 100 secs

Element & Linie	Gew.-Prozent	Atom-Prozent*	Präzision 3 Sigma	k-Verh.**	Iter.
O KA	19.79	65.28	0.87	0.0530	
Zr LA	47.47	27.46	0.75	0.3953	
U MA	32.74	7.26	0.96	0.2323	4
Gesamt	100.00				

*Hinweis: Atom-Prozente sind auf 100 normalisiert
**Hinweis: k-Verhältnis = k.-Verh. x R
Quantex+>mit R = Referenzwert(Std.)/Referenzwert(Probe)

1 2 3 4 5 6 7 8 9
← 0.000 Range= 10.230 keV 10.110 →
Integral 8 = 85364

Fig. 74: Fuel rod bundle CORA-W2, cross-section # p (910 mm); SEM/EDX analysis at position # 1 location c

Punktanalyse Nr.	Element	Gew. %	Atom %*
1	W	100	100
2	O Zr U	18.4 39.7 41.9	65.3 24.7 10.0
3	O Zr U	15.7 21.2 63.0	66.4 15.7 17.9
4	O U	12.0 88.0	67.1 32.9

* auf 100 % normalisiert

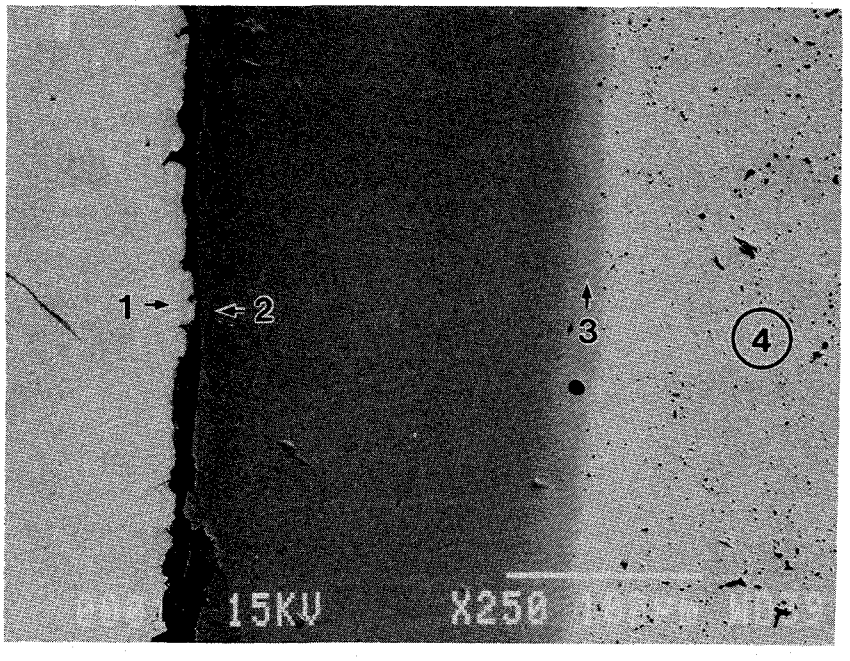

Fig. 75: Fuel rod bundle CORA-W2, cross-section # p (910 mm); SEM/EDX analysis at position # 1 location d

3-May-1994 14:18:36
CORA-W2 / Probe p / REM 2 / Ausschnitt a / Integralanalyse

Vert= 3163 counts Disp= 1 Comp= 3 Preset= 100 secs Elapsed= 100 secs

Element & Linie	Gew.-Prozent	Atom-Prozent*	Präzision 3 Sigma	k-Verh.**	Iter.
B KA	12.59	52.13	1.08	0.0754	
Al KA	0.41	0.68	0.05	0.0032	
Cr KA	2.50	2.16	0.20	0.0248	
Fe KA	14.02	11.24	0.56	0.1406	
Ni KA	2.88	2.20	0.31	0.0294	
Zr LA	42.39	20.80	0.69	0.3710	
Mo LA	21.22	9.90	0.57	0.1577	
W MA	2.36	0.57	0.20	0.0188	
U MA	1.63	0.31	0.22	0.0110	4
Gesamt	100.00				

*Hinweis: Atom-Prozente sind auf 100 normalisiert
**Hinweis: k-Verhältnis = k.-Verh. x R
Quantex+>mit R = Referenzwert(Std.)/Referenzwert(Probe)

1 2 3 4 5 6 7 8 9
0.000 Range= 10.230 keV 10.110
Integral 8 = 87864

Fig. 76: Fuel rod bundle CORA-W2, cross-section # p (910 mm); SEM/EDX analysis at position #2 location a (integral analysis)

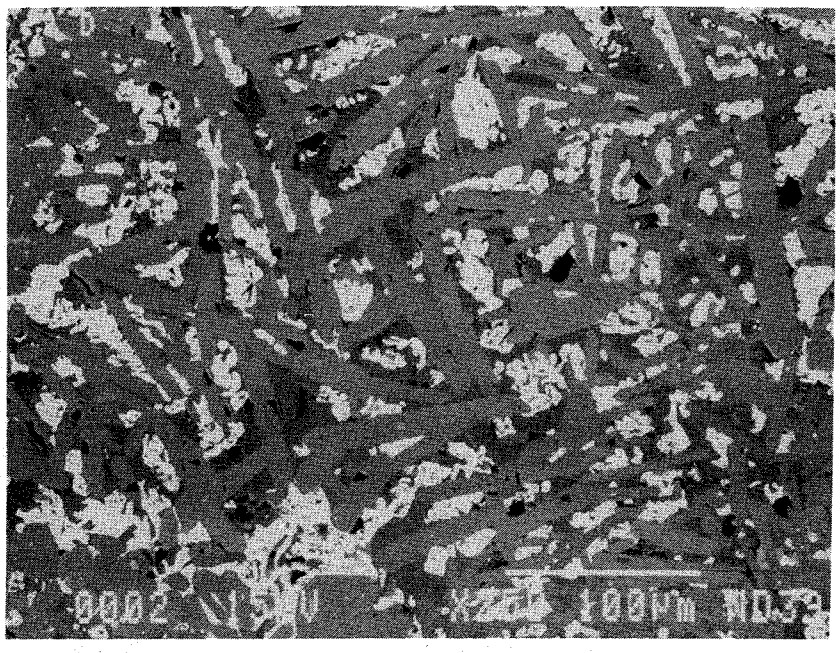

3-May-1994 14:28:36
CORA-W2 / Probe p / REM 2 / Ausschnitt b / Integralanalyse

Vert= 3615 counts Disp= 1 Comp= 3 Preset= 100 secs Elapsed= 100 secs

Element & Linie	Gew.-Prozent	Atom-Prozent*	Präzision 3 Sigma	k-Verh.**	Iter.
B KA	14.26	58.96	1.05	0.1033	
Cr KA	2.85	2.45	0.21	0.0281	
Fe KA	10.51	8.41	0.48	0.1060	
Ni KA	1.87	1.42	0.25	0.0194	
Zr LA	49.64	24.33	0.75	0.4346	
Mo LA	1.83	0.85	0.17	0.0134	
U MA	19.05	3.58	0.73	0.1378	4
Gesamt	100.01				

*Hinweis: Atom-Prozente sind auf 100 normalisiert
**Hinweis: k-Verhältnis = k.-Verh. x R
Quantex+>mit R = Referenzwert(Std.)/Referenzwert(Probe)

1 2 3 4 5 6 7 8 9
0.000 Range= 10.230 keV 10.110
Integral 8 = 81314

Fig. 77: Fuel rod bundle CORA-W2, cross-section # p (910 mm); SEM/EDX analysis at position #2 location b (integral analysis)

Punktanalyse Nr.	Element	Gew. %	Atom %*
1	O	12.1	65.6
	Zr	4.1	3.9
	U	82.8	30.5
2	B	19.0	66.5
	Zr	81.0	33.5
3	Cr	21.2	22.8
	Fe	71.3	71.4
	Ni	4.2	4.0
	Mo	2.7	1.6
	W	0.7	0.2

auf 100 % normalisiert

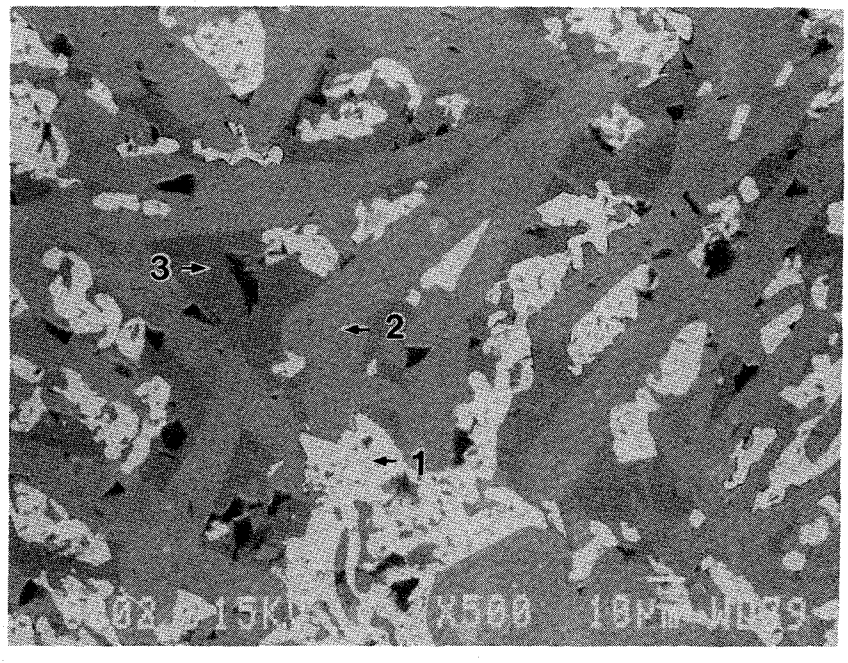

Fig. 78: Fuel rod bundle CORA-W2, cross-section # p (910 mm); SEM/EDX analysis at position #2 location b (detailed phase analysis)

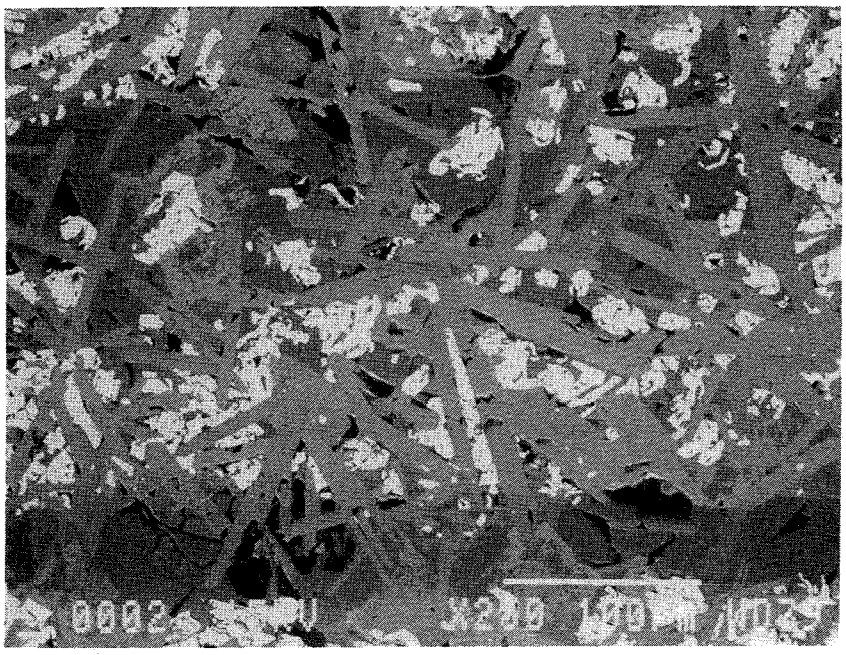

3-May-1994 14:36:04
CORA-W2 / Probe p / REM 2 / Ausschnitt c / Integralanalyse

Vert= 2518 counts Disp= 1 Comp= 3 Preset= 100 secs Elapsed= 100 secs

Element & Linie	Gew.-Prozent	Atom-Prozent*	Präzision 3 Sigma	k-Verh.**	Iter.
B KA	13.78	49.06	1.18	0.0757	
O KA	6.57	15.80	0.46	0.0210	
Cr KA	4.16	3.08	0.25	0.0437	
Fe KA	16.55	11.40	0.59	0.1752	
Ni KA	3.45	2.26	0.33	0.0372	
Zr LA	33.28	14.04	0.60	0.2998	
Mo LA	3.24	1.30	0.21	0.0263	
U MA	18.97	3.07	0.69	0.1503	4
Gesamt	100.00				

*Hinweis: Atom-Prozente sind auf 100 normalisiert
**Hinweis: k-Verhältnis = k.-Verh. x R
Quantex+>mit R = Referenzwert(Std.)/Referenzwert(Probe)

1 2 3 4 5 6 7 8 9

0.000 Range= 10.230 keV 10.110

Integral 8 = 80303

Fig. 79: Fuel rod bundle CORA-W2, cross section # p (910 mm); SEM/EDX analysis at position #2 location c (integral analysis)

3-May-1994 14:43:45
CORA-W2 / Probe p / REM 2 / Ausschnitt d / Integralanalyse

Vert= 3110 counts Disp= 1 Comp= 3 Preset= 100 secs
Elapsed= 100 secs

Element & Linie	Gew.-Prozent	Atom-Prozent*	Präzision 3 Sigma	k-Verh.**	Iter.
B KA	11.33	47.57	0.96	0.0779	
O KA	3.35	9.51	0.37	0.0085	
Cr KA	2.61	2.28	0.20	0.0268	
Fe KA	10.67	8.67	0.48	0.1118	
Ni KA	2.24	1.73	0.26	0.0241	
Zr LA	41.11	20.45	0.67	0.3725	
Mo LA	14.91	7.05	0.47	0.1163	
W MA	1.77	0.44	0.17	0.0145	
U MA	12.01	2.29	0.58	0.0878	3
Gesamt	100.00				

*Hinweis: Atom-Prozente sind auf 100 normalisiert
**Hinweis: k-Verhältnis = k.-Verh. x R
Quantex+>mit R = Referenzwert(Std.)/Referenzwert(Probe)

1 2 3 4 5 6 7 8 9
0.000 Range= 10.230 keV 10.110
Integral 8 = 87666

Fig. 80: Fuel rod bundle CORA-W2, cross section # p (910 mm); SEM/EDX analysis at position #2 location d (integral analysis)

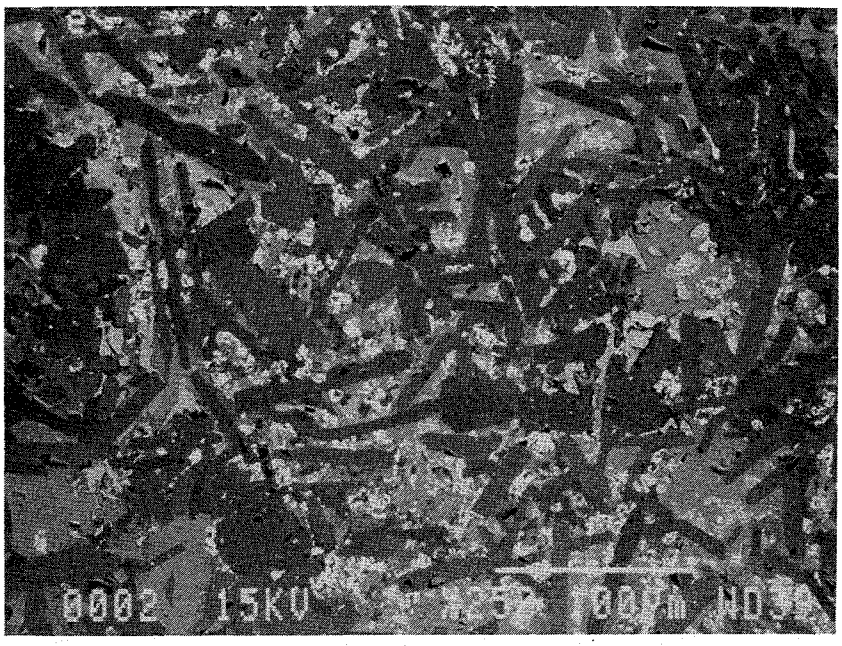

3-May-1994 14:50:28
CORA-W2 / Probe p / REM 2 / Ausschnitt e / Integralanalyse
Vert= 3403 counts Disp= 1 Comp= 3 Preset= 100 secs Elapsed= 100 secs

Element & Linie	Gew.-Prozent	Atom-Prozent*	Präzision 3 Sigma	k-Verh.**	Iter.
B KA	13.65	54.99	1.12	0.0834	
Cr KA	2.99	2.51	0.22	0.0297	
Fe KA	15.35	11.97	0.58	0.1536	
Ni KA	2.66	1.97	0.30	0.0270	
Zr LA	46.48	22.20	0.73	0.4068	
Mo LA	10.67	4.84	0.41	0.0784	
W MA	0.40	0.09	0.08	0.0031	
U MA	7.80	1.43	0.47	0.0546	4
Gesamt	100.00				

*Hinweis: Atom-Prozente sind auf 100 normalisiert
**Hinweis: k-Verhältnis = k.-Verh. x R
Quantex+>mit R = Referenzwert(Std.)/Referenzwert(Probe)

1 2 3 4 5 6 7 8 9
0.000 Range= 10.230 keV 10.110
Integral 8 = 81646

Fig. 81: Fuel rod bundle CORA-W2, cross section # p (910 mm); SEM/EDX analysis at position #2 location e (integral analysis)

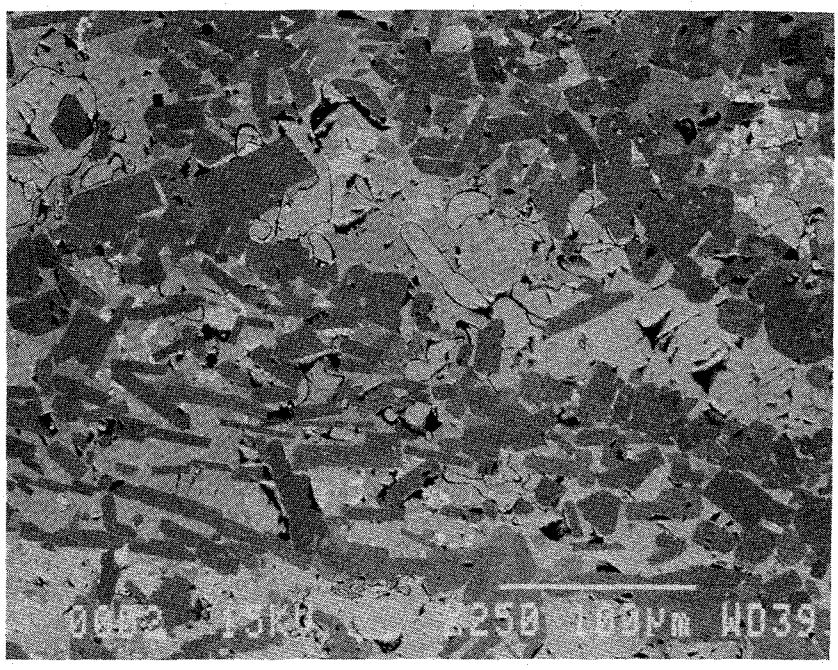

3-May-1994 15:02:44
CORA-W2 / Probe p / REM 2 / Ausschnitt f / Integralanalyse

Vert= 4156 counts Disp= 1 Comp= 3 Preset= 100 secs Elapsed= 100 secs

Element & Linie	Gew.-Prozent	Atom-Prozent*	Präzision 3 Sigma	k-Verh.**	Iter.
B KA	7.69	33.14	0.73	0.0624	
O KA	8.71	25.35	0.65	0.0184	
Cr KA	0.83	0.74	0.12	0.0076	
Fe KA	3.70	3.08	0.29	0.0350	
Ni KA	0.97	0.77	0.18	0.0094	
Zr LA	59.14	30.19	0.83	0.5054	
Mo LA	10.39	5.04	0.42	0.0702	
U MA	8.59	1.68	0.52	0.0553	3
Gesamt	100.02				

*Hinweis: Atom-Prozente sind auf 100 normalisiert
**Hinweis: k-Verhältnis = k.-Verh. x R
Quantex+>mit R = Referenzwert(Std.)/Referenzwert(Probe)

1 2 3 4 5 6 7 8 9
0.000 Range= 10.230 keV 10.110
Integral 8 = 83950

Fig. 82: Fuel rod bundle CORA-W2, cross section # p (910 mm); SEM/EDX analysis at position #2 location f (integral analysis)

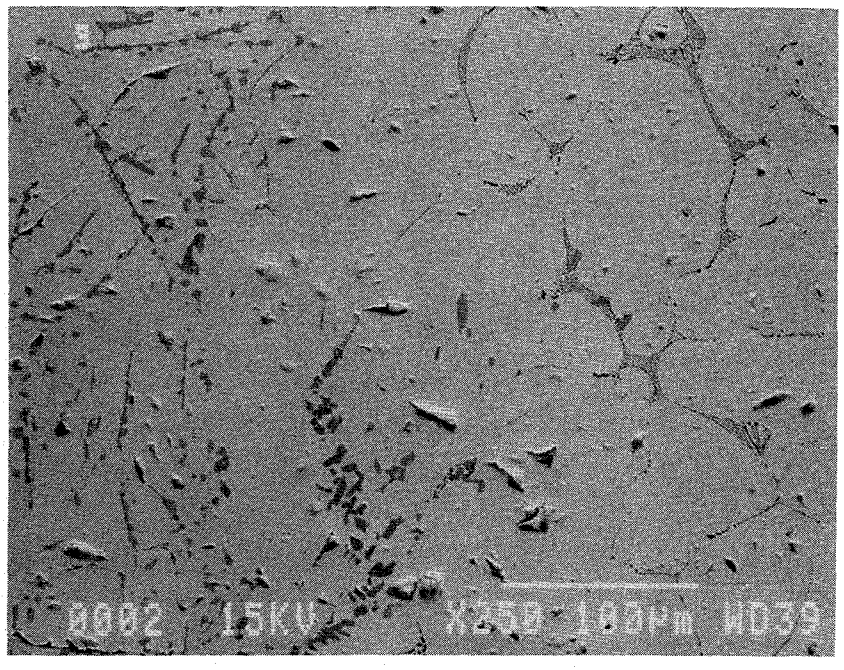

3-May-1994 15:07:08
CORA-W2 / Probe p / REM 2 / Ausschnitt g / Integralanalyse
Preset= 100 secs
Vert= 2827 counts Disp= 1 Comp= 3 Elapsed= 100 secs

Element & Linie	Gew.-Prozent	Atom-Prozent*	Präzision 3 Sigma	k-Verh.**	Iter.
O KA	19.29	66.03	0.85	0.0528	
Zr LA	41.57	24.96	0.71	0.3382	
U MA	39.14	9.01	1.05	0.2799	3
Gesamt	100.00				

Be ?

*Hinweis: Atom-Prozente sind auf 100 normalisiert
**Hinweis: k-Verhältnis = k.-Verh. x R
Quantex+>mit R = Referenzwert(Std.)/Referenzwert(Probe)

1 2 3 4 5 6 7 8 9
0.000 Range= 10.230 keV 10.110
Integral 8 = 83740

Fig. 83: Fuel rod bundle CORA-W2, cross section # p (910 mm); SEM/EDX analysis at position #2 location g (integral analysis)

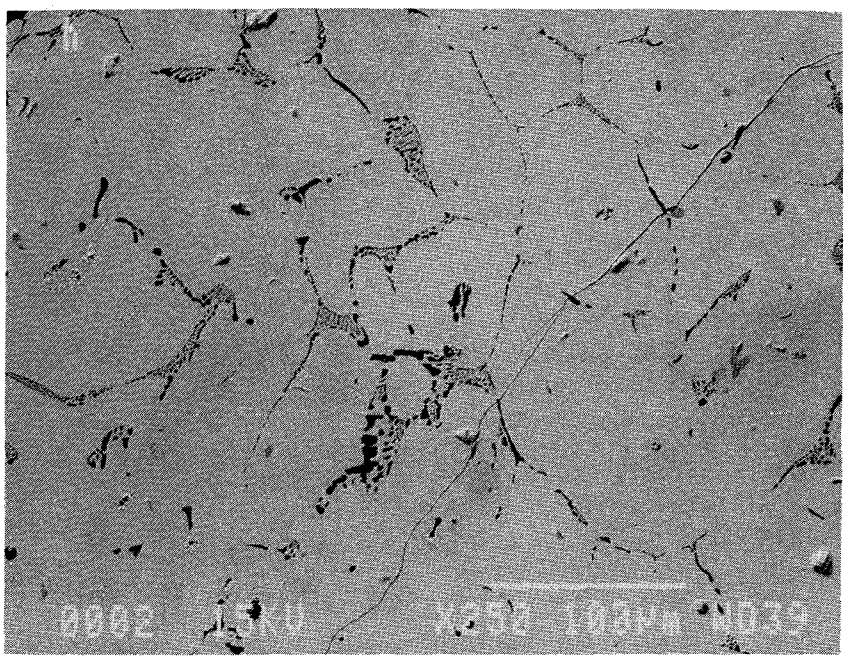

```
 3-May-1994 15:11:11
CORA-W2 / Probe p / REM 2 / Ausschnitt h / Integralanalyse
                                          Preset=        100 secs
Vert=     2294 counts   Disp= 1    Comp= 3   Elapsed=       100 secs

  Element     Gew.-      Atom-     Präzision
  & Linie    Prozent    Prozent*   3 Sigma   k-Verh.**   Iter.
   Be KA   ??
   O  KA      22.17      71.25      0.89      0.0636
   Zr LA      34.32      19.35      0.66      0.2694
   U  MA      43.51       9.40      1.11      0.3097        4

   Ohne Be berechnet!

 *Hinweis: Atom-Prozente sind auf  100 normalisiert
**Hinweis: k-Verhältnis = k.-Verh. x R
Quantex+>mit R = Referenzwert(Std.)/Referenzwert(Probe)
      |1       |2       |3       |4       |5       |6       |7       |8       |9       |
 <-    0.000     Range=    10.230 keV                                    10.110  ->
                                          Integral 8  =          78303
```

Fig. 84: Fuel rod bundle CORA-W2, cross section # p (910 mm); SEM/EDX analysis at position #2 location h (integral analysis)